LOCAL SCALE STRUCTURES IN EARTH'S THERMOSPHERIC WINDS AND THEIR CONSEQUENCES FOR WIND DRIVEN TRANSPORT

By

Manbharat Singh Dhadly

RECOMMENDED:

Dr. Roger Smith

Dr. Donald Hampton

Dr. John Olson

Dr. Richard Collins

Dr. Mark Conde
Advisory Committee Chair

Dr. Renate Wackerbauer
Chair, Department of Physics

APPROVED:

Dr. Paul Layer
Dean, College of Natural Science and Mathematics

Dr. John Eichelberger
Dean of the Graduate School

7 December 2015
Date

LOCAL SCALE STRUCTURES IN EARTH'S THERMOSPHERIC WINDS AND THEIR CONSEQUENCES FOR WIND DRIVEN TRANSPORT

A

DISSERTATION

Presented to the Faculty

of the University of Alaska Fairbanks

in Partial Fulfillment of the Requirements

for the Degree of

DOCTOR OF PHILOSOPHY

By

Manbharat Singh Dhadly, B.Sc., M.Sc.

Fairbanks, Alaska

December 2015

Abstract

In the traditional picture of Earth's upper thermosphere (~190-300 *km*), it is widely presumed that its convective stability and enormous kinematic viscosity attenuate wind gradients, and hence smooth out any structure present in the wind over scale size of several hundreds of kilometers. However, several independent experimental studies have shown that observed upper thermospheric wind fields at high latitudes contain stronger than expected local-scale spatial structures. The motivation of this dissertation is to investigate how the resulting local-scale gradients would distort neutral air masses and complicate thermospheric wind transport.

To achieve this goal, we examined the behavior of a simple parameter that we refer to as the "distortion gradient". It incorporates all of the wind field's departures from uniformity, and is thus capable of representing all resulting contributions to the distortion or mixing of air masses. Climatological analysis of the distortion gradient using 2010, 2011, and 2012 wind data from the All-sky Scanning Doppler Imager (SDI) located at Poker Flat (65.12N, 147.47W) revealed the diurnal and seasonal trends in distortion of thermospheric masses. Distortion was observed to be dependent on geomagnetic activity and orientation of the interplanetary magnetic field.

To understand the time-cumulative influence of these local-scale non-uniformities on thermospheric wind driven transport, time-resolved two-dimensional maps of the thermospheric vector wind fields were used to infer forward and backward air parcel trajectories. Tracing air parcel trajectories through a given geographic location indicates where they came from previously, and where they will go in the future. Results show that wind driven transport is very sensitive to small-scale details of the wind field. Any local-scale spatial wind gradients can significantly complicate air parcel trajectories. Transport of thermospheric neutral species in the presence of the local-scale wind gradients that we observed was found to be far more complicated than what current models typically predict.

To validate these findings, we cross-compared the upper thermospheric neutral winds inferred from a narrow field of view Fabry-Perot interferometer with winds measured by our all-sky SDI. A high degree of correlation was present between their measurements.

This cross-validation study suggests the presence of small-scale short-lived, and previously unobserved wind features in the upper thermosphere, with typical length scales less than ~40 km. The spatially and temporally localized wind features implied by this study represent a new and unexplored regime of dynamics in the thermosphere.

Table of Contents

Page

Page

List of Figures

Page

Page

Page

Page

List of Tables

List of Appendices

Page

Acknowledgements

I dedicate my thesis to my mother Barinder Kaur Dhadly for her endless encouragement, motivation, support, and care. Special thanks to my lovely wife Sandeep Kaur and son Armin Singh Dhadly for their support during my years in graduate school. I would like to acknowledge my family members Jasvir Singh Dhadly, Balwinder Singh Kang, Dalvir Singh Kang, Darshan Singh, and Sukhwinder Kaur for their help and support whenever I needed the most.

I must give my respectful gratitude to my research advisor Dr. Mark Conde for his tireless guidance, support, valuable comments, suggestions, and patience. Thank you for being so understanding and supportive. You are an "awesome" advisor. Thank you from the bottom of my heart for giving me the chance to work with you.

Thank you Dr. Donald Hampton for your support and introducing me to the magical world of auroras. Traveling with you to Svalbard for the C-REX rocket mission was full of fun. Thanks to all other committee members, Dr. Roger Smith, Dr. Richard Collins, and Dr. John Olson for their guidance and essential input during the final stages of the thesis. Thank you for your constructive suggestions in order to improve my thesis work.

Thank you Dr. John Meriwether for providing NFPI wind data for cross-validation study and helping me to understand it. It was my pleasure to work with you.

Finally, a big thank to all of my friends, especially Callum Anderson, Carl Andersen, Matt Cooper, and Peter A Bieniek for their support whenever I needed it.

This work was primarily supported by the grant NSF-397024 from the National Science Foundation with a small contribution from NASA grant NNX13AF28G.

Chapter 1
Introduction to Earth's Upper Atmosphere

1.1 Introduction

Earth's atmosphere is most commonly classified into different regions based on the vertical variation in temperature with altitude. These regions from the surface of the Earth to the highest are the troposphere (0-18 *km*), stratosphere (18-50 *km*), mesosphere (50-90 *km*), thermosphere (90-500 *km*), and exosphere (>500 *km*). The vertical temperature gradient of the troposphere and mesosphere is negative while it is positive for the stratosphere and thermosphere. At the transition between two regions of the atmosphere, the usual nomenclature is to define a "pause" region (e.g. tropopause, stratopause, mesopause, thermopause) in which the vertical temperature gradient is zero. Figure 1.1 shows the temperature variation with altitude in the Earth's atmosphere.

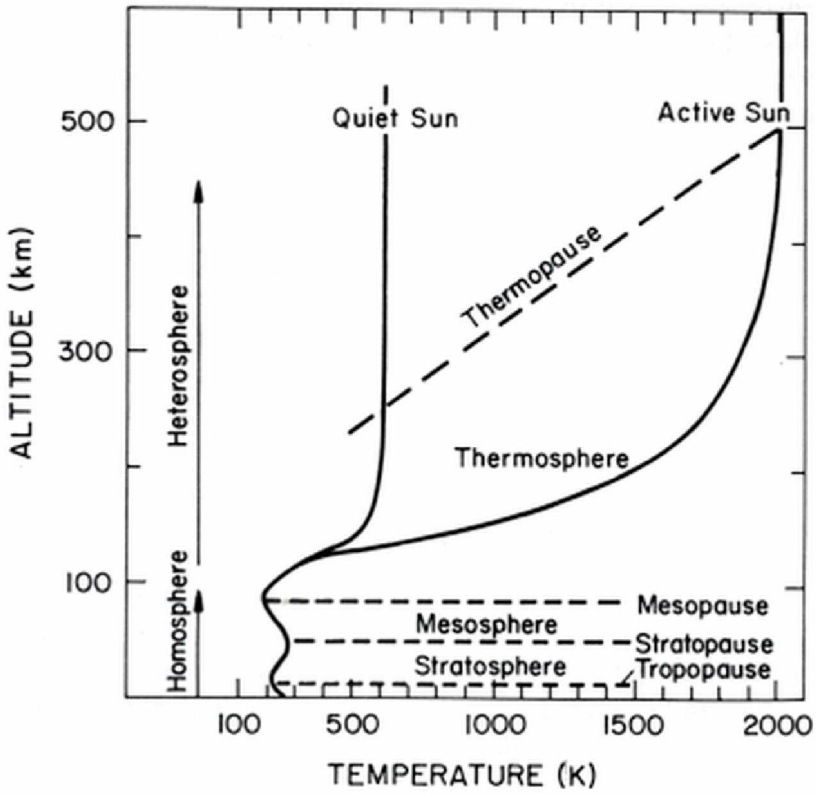

Figure 1.1: The atmospheric temperature profile for quiet and active sun [*Banks and Kockarts*, 1973].

The force due to gravity on air parcels is proportional to their masses, as a consequence, there is a tendency for different atmospheric gases to separate out and form layers under the influence of gravity if there were no competing processes like vertical mixing. The Earth's atmosphere can be classified into two broad regions based on how the gases are distributed: the homosphere and the heterosphere. The homosphere includes the troposphere, stratosphere, and mesosphere. In the homosphere, mixing by small-scale turbulent eddies and unstable convection is strong enough to mix rapidly the constituent gases. These conditions apply to all altitudes below $\sim$100 km. Density in the homosphere decreases almost exponentially with altitude, but the mean molecular mass does not vary significantly with altitude. The upper boundary of the homosphere is called the turbopause or homopause because eddy mixing (by turbulence and unstable convection) is very much less effective above this region. Thus, the heterosphere is a gravitationally settled atmosphere where the major vertical transport process is diffusion. The gases are distributed vertically according to their individual scale height (defined in section 1.2) due to the diffusive separation between heavier and light gases. The resulting layers are formed according to their atomic masses, heavier at the bottom and lighter at the top. Such conditions apply to altitudes above $\sim$100 km. The thermosphere and exosphere together comprise the heterosphere.

This chapter will focus on the Earth's thermosphere (also referred to as Earth's upper atmosphere) and will introduce the fundamental processes involved in the aeronomy of this region. Next chapter will focus on dynamics of the Earth's upper atmosphere. Here we have divided the thermosphere into three regions: lower thermosphere ($\sim$100-150 km), middle thermosphere ($\sim$150-200 km), and upper thermosphere ($\sim$200-500 km).

1.2 Density Distribution and Scale Height

To a first order approximation, the change in atmospheric pressure with the altitude is directly related to mass density of the atmosphere and gravity, and is expressed mathematically as:

$$\frac{\partial p}{\partial z} = -\rho g \tag{1.1}$$

where p denotes the atmospheric pressure ($kg.m^{-1}.s^{-2}$), ρ denotes mass density ($kg.m^{-3}$), and g is the acceleration due to gravity ($m.s^{-2}$). This balance between the vertical pressure gradient and gravity is also known as "hydrostatic or aerostatic" equilibrium. The ideal gas law relates the pressure (p) with temperature (T):

$$p = nkT \tag{1.2}$$

where n is the number density (m^{-3}) and k is the Boltzmann's constant. The mass density (ρ) and number density (n) are related by:

$$\rho = nm \tag{1.3}$$

where m denotes the mean molecular mass (kg). With the help of the above expressions, ρ can be expressed as:

$$\rho = \frac{pm}{kT} \tag{1.4}$$

Assuming an isothermal atmosphere (T constant), substituting the value of ρ from Equation 1.4 into the hydrostatic equilibrium Equation B.1 and integrating:

$$\frac{1}{p}\frac{\partial p}{\partial z} = -\frac{mg}{kT}$$

$$\int_{p_0}^{p} \frac{dp}{p} = -\frac{mg}{kT}\int_{z_0}^{z} dz$$

$$p = p_0 \exp(-\frac{z - z_0}{H}) \tag{1.5}$$

$$H = \frac{kT}{mg} \tag{1.6}$$

In Equation 1.5, p_0 is the pressure at height z_0 and H is called scale height. By using the ideal gas law, Equation 1.5 can further be written in terms of mass density:

$$\rho = \rho_0 \exp(-\frac{z - z_0}{H}) \tag{1.7}$$

where ρ_0 is the mass density at height z_0. Substituting Equation 1.3 into Equation 1.7 gives the number density as a function of height:

$$n = \frac{n_0 m_0}{m} \exp(-\frac{z - z_0}{H}) \tag{1.8}$$

Equations 1.5 and 1.8 show that for an isothermal atmosphere of uniform mean molecular mass, pressure and number density decrease exponentially with altitude. The parameter "scale height" (H) was introduced by Sydney Chapman; it represents the height increment over which density (and pressure) reduces by a factor of 1/e. The scale height is dependent on the mean molecular mass and temperature. For the homosphere, mean molecular mass is constant, therefore:

$$H \propto \frac{T}{g} \tag{1.9}$$

On the other hand, in the heterosphere, atmospheric constituents undergo various chemical reactions (like photodissociation, photoionization, etc) which result in the changes in mean molecular mass. Therefore, scale height for the heterosphere is also a function of mean molecular mass:

$$H \propto \frac{T}{mg} \tag{1.10}$$

Atomic oxygen can be taken as an example. It is produced by photodissociation of O_2 in the middle and upper thermosphere (discussed in detail in section 1.5). The scale height of atomic oxygen in the upper thermosphere can be approximated by using typical thermopause temperature ($T_\infty \sim 1000\ K$), oxygen mass ($m_0 \sim 16 \times 1.67 \times 10^{-27} kg$), and acceleration due to gravity in the upper thermosphere ($\sim 8.8 m.s^{-2}$):

$$H \approx \frac{k\,T_\infty}{m_0\,g} \approx 59\ km \tag{1.11}$$

This means that for every 59 km increase in height in the upper thermosphere, the number density of atomic oxygen decreases by a factor of 1/e.

In the heterosphere, each component gas is distributed vertically according to its scale height. The heavier gases have small scale heights compared to light gases, which means the number density of heavier gases decreases more rapidly with altitude than for lighter gases. That is why heavier species dominate at lower altitudes and lighter species at higher altitudes.

In the thermosphere, temperature increases with the altitude, whereas the acceleration due to gravity decreases with the altitude. Photodissociation of molecules reduces the mean molecular mass with the increase in height. These three factors all combine to

produce an increase in the scale height with altitude above 100 km, which explains why atmospheric density drops faster with altitude in the lower atmosphere than at the top of the atmosphere.

1.3 Vertical Temperature Structure

In the thermosphere, the major source of heat is the absorption of solar ultra-violet (UV), extreme ultra-violet (EUV), and X-ray radiation. The temperature in the thermosphere increases with increasing altitude. The vertical gradient in temperature is stronger in the lower and middle thermosphere (100-200 km) compared to the upper thermosphere (200-500 km).

The decrease in mass density of the thermosphere with altitude decreases the effectiveness of the mechanisms for dissipating the solar ultra-violet radiation absorbed by thermospheric species. This results in the large vertical temperature gradient in the thermosphere. However, above a certain altitude, the thermosphere redistributes heat so efficiently that temperature asymptotically approaches a limiting value. This altitude is referred as thermopause. At the thermopause, the boundary between thermosphere and exosphere, the thermosphere's temperature maximizes. At the exobase, the mean free path of species exceeds its scale height. Above the thermopause altitude ($\sim$600-1000 km), hydrostatic equilibrium begins to break down, collisions become infrequent, gases are no longer in thermal equilibrium and mean free path of the thermospheric neutral constituents exceeds the pressure scale height. As a result, neutral particles tend to follow ballistic trajectories. Within the exosphere, efficient thermal conductivity suppresses any vertical structure in temperature at those heights.

The thermospheric heat budget above 100 km is a strong function of solar activity. The thermopause temperature can rise to 2000 K for an active solar period and drops to 500 K for a quiet solar period. For the lower and middle thermosphere (120-200 km), vertical temperature is frequently approximated by the Bates temperature profile:

$$T(h) = T_\infty - (T_\infty - T(h_0))\exp(-s(h-h_0)) \tag{1.12}$$

In above Equation 1.12, h_0, $T(h_0)$, and s are constants with typical value 120 km, 350 K, and 0.021 km^{-1} respectively. T_∞ is the thermopause temperature.

1.4 Radiative Transfer in the Thermosphere

To understand the dynamics of the thermosphere, a detailed knowledge of energy deposited by solar radiation in the thermosphere as a function of altitude is required. Energy deposition is controlled by the cross-section of atmospheric gases for absorption and ionization, and is a function of wavelength. The discussion given below follows the discussion given in *Liou* [2002] and personal communications with Dr. Mark Conde.

When solar radiation enters the atmosphere, it is attenuated due to absorption by atmospheric species. The Beer-Lambert absorption law describes attenuation of solar flux that enters the upper atmosphere. It states that absorption of solar flux is dependent on the number of absorbing atoms/molecules and their absorption cross-sections. Mathematically, attenuation of the solar flux entering the atmosphere at a zenith angle $\theta_\odot$ is given by:

$$F_{act}(z) = F_\odot \exp(-\frac{\tau(z,\lambda)}{\mu_\odot}) \tag{1.13}$$

where $\mu_\odot = cos(\theta_\odot)$, $F_\odot$ is solar flux at the top of the atmosphere, $\tau(z,\lambda)$ is the vertical optical depth at height z and wavelength λ. The optical depth is the measure of attenuation caused by the atmosphere. Optical depth is a function of altitude and wavelength. It is dependent on the number of atoms/molecules of each species in the atmosphere and their absorption cross-sections; it is a dimensionless parameter. Mathematically, for a single-species atmosphere, it is given by:

$$\tau\,(z,\lambda) = \int_z^\infty n(z)\ \sigma_a(\lambda)\ dz \tag{1.14}$$

where n is the number density (m^{-3}) of an absorbing atoms or molecules, and $\sigma_a(\lambda)$ is the absorption cross-section (m^2) at wavelength λ. F_{act} is the actinic flux, also known as monochromatic radiant flux density. It is spherically integrated radiation flux in the atmosphere. It includes both direct and beam and scattered components. Actinic flux associated with photodissociation is given by:

$$F_{act}(z,\lambda) = \int_{4\pi\ steradians} I(z,\lambda,\theta,\phi)\ d\Omega \tag{1.15}$$

$$F_{act}(z,\lambda) = \int_{\phi=0}^{\phi=2\pi} \int_{\theta=-\pi/2}^{\theta=\pi/2} I(z,\lambda,\theta,\phi)\ sin(\theta)\ d\theta\ d\phi \tag{1.16}$$

where $I(\lambda, \theta, \phi)$ is the monochromatic intensity or radiance with the units of $W.sr^{-1}.nm^{-1}.m^{-2}$. The units of F_{act} are $W.nm^{-1}.m^{-2}$. The relation given by Equation 1.16 is valid for both direct and diffuse beams. Although actinic flux is integrated over the full 4π *steradians*, when the atmosphere is sunlit the only significant contribution to this integral comes from the direction of the sun. Solar UV, EUV, and X-ray photons deposit energy in the thermosphere through photodissociation and photoionization. The solar energy absorbed per unit volume and per unit time along the direction of the solar beam (also referred as volume absorption rate) is expressed mathematically by:

$$q(z, \lambda, \mu_\odot) = -\mu_\odot \frac{dF_{act}(z, \lambda, \mu_\odot)}{dz} \tag{1.17}$$

The factor $\mu_\odot (= cos(\theta_\odot))$ compensates for the longer path length when the sun is not at zenith. Note that rate of photoionization, photodissociation, and heat production are all related to the energy deposition in the atmosphere. Substituting Equation 1.14 and Equation 1.13 into Equation 1.17, the solar absorption rate becomes:

$$\begin{aligned} q(z, \lambda, \mu_\odot) &= -\mu_\odot \frac{d}{dz}\left[F_\odot \exp(-\frac{\tau(z, \lambda)}{\mu_\odot})\right] \\ &= -\mu_\odot \frac{d}{dz}\left[F_\odot \exp(-\frac{\int_z^\infty n(z')\sigma_a(\lambda)dz'}{\mu_\odot})\right] \\ &= n(z)\ \sigma_a(\lambda)\ F_{act}(z, \lambda, \theta_\odot) \\ &= n(z)\ \ J(z, \lambda, \theta_\odot) \end{aligned} \tag{1.18}$$

where $J(z, \lambda, \theta_\odot)$ is known as monochromatic photoabsorption coefficient. The above expression of solar absorption rate is only for the monochromatic flux. The total energy deposited in the atmosphere can be calculated by integrating over all wavelengths:

$$Q(z, \mu_\odot) = n(z) \int_0^\infty J(z, \lambda, \theta_\odot)\ d\lambda \tag{1.19}$$

The parameter $Q(z, \mu_\odot)$ has units of $W.m^{-3}$. So far we have considered the energy deposited in a single-species atmosphere. We can generalize the results given in Equation 1.19 to multi-species atmosphere:

$$Q(z, \mu_\odot) = \sum_i \left[n_i(z) \int_0^\infty J_i(z, \lambda, \theta_\odot)\ d\lambda\right] \tag{1.20}$$

where i denotes the i^{th} species. For an atmosphere containing an absorber whose number density varies exponentially with altitude:

$$n(z) = n_0 \exp(-\frac{z}{H}) \tag{1.21}$$

where n_0 is the number density when z is zero. Substituting Equation 1.21 into Equation 1.18 results in:

$$q(z,\lambda,\mu_\odot) = n_0 \exp(-\frac{z}{H})\, F_{act}(z,\lambda,\theta_\odot) \tag{1.22}$$

By substituting Equation 1.14 and 1.13 into Equation 1.22:

$$q(z,\lambda,\mu_\odot) = n_0\, \sigma_a\, F_\odot \exp(-\frac{z}{H} - \frac{H\, n_0\, \sigma_a}{\mu_\odot} \exp(-\frac{z}{H})) \tag{1.23}$$

It shows that the volume absorption rate (solar energy absorbed per unit volume and per unit time) is a function of altitude, scale height, solar zenith angle, and absorption coefficient. Substituting Equation 1.18 into Equation 1.14 produces:

$$\tau = \int_z^\infty n_0\, \sigma_a \exp(-\frac{z}{H})dz$$

$$\tau = n_0\, \sigma_a\, H \exp(-\frac{z}{H}) \tag{1.24}$$

For an overhead sun ($\theta_\odot = 0$), energy deposition rate with altitude maximizes when optical depth τ is equal to 1. Suppose it happens at an altitude of z_0, then Equation 1.24 can be written in the form:

$$1 = n_0\, \sigma_a\, H \exp(-\frac{z_0}{H})$$

$$n_0\, \sigma_a\, H = \exp(\frac{z_0}{H}) \tag{1.25}$$

In such case, Equation 1.23 using Equation 1.25 can be written in form:

$$q(z = z_0,\ \mu_\odot = 1) = n_0\, \sigma_a\, F_\odot \exp(-\frac{z_0}{H} - 1)$$

Normalized deposition rate can be written as:

$$r = \frac{q(z)}{q(z = z_0,\ \mu_\odot = 1)}$$

$$r = \exp(\ 1 - \frac{(z - z_0)}{H} - \frac{1}{\mu_\odot} \exp(-\frac{(z - z_0)}{H}) \tag{1.26}$$

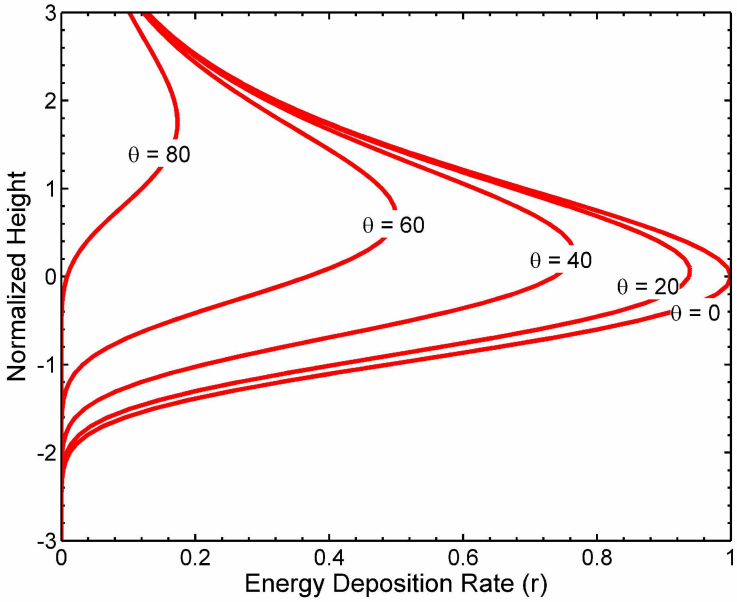

Figure 1.2: Normalized energy deposition rate as a function of altitude.

Let $z' = (z - z_0)/H$ be the normalized height. The behavior of the normalized deposition rate with height is shown in Figure 1.2. It is clear that interaction of solar radiation with the atmosphere leads to deposit maximum energy at a particular altitude. In other words, it forms a layer of maximum absorption. This layer is referred as the "Chapman layer". At high altitudes, energy deposition is limited by the low number density of the atmosphere due to exponential fall off. Below the Chapman layer peak, energy deposition declines rapidly because the absorption at higher altitudes has already attenuated the beam. The altitude of maximum energy deposition is dependent on the nature and concentration of absorbing species, the wavelength of radiation, and solar zenith angle. The real atmosphere has multiple absorbing gases, and polychromatic radiation is incident on the top of the atmosphere. That is why several absorbing layers are found at different altitudes. The maximum energy deposition altitude moves higher with the increase in solar zenith angle.

1.5 Basic Composition

The basic constituents of the thermosphere are O, O_2, N, N_2, H, He, Ar, and NO. Figure 1.3 shows how the number density of thermospheric constituents varies with height. Be-

low the thermosphere, neutral composition is dominated by molecular nitrogen (N_2) and molecular oxygen (O_2). In the thermosphere, O_2 and N_2 behave dramatically differently in the presence of solar ultra-violet radiation. Dissociation of polyatomic molecules by solar UV radiation makes the thermosphere more complex than any other atmospheric region. O_2 photodissociates easily, N_2 by contrast, does not. As a result, nitrogen remains

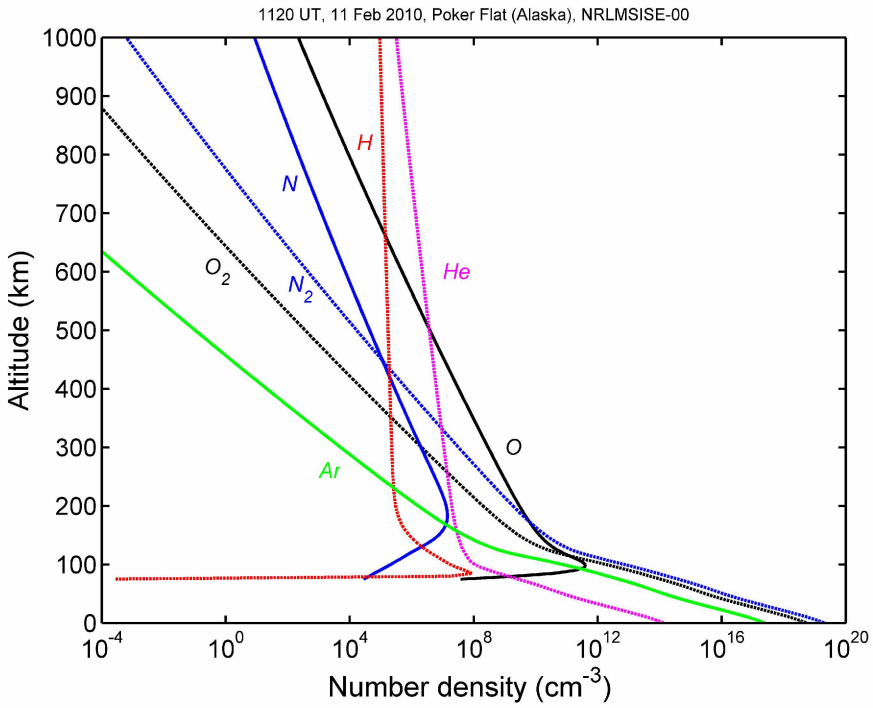

Figure 1.3: Altitude profile of the number density of various principal neutral atmospheric constituents derived from NRL-MSIS00.

almost entirely in the molecular form in the thermosphere. In the lower thermosphere, O and O_2 densities are roughly comparable, whereas in the middle thermosphere, O and N_2 densities become comparable. The O:O_2 ratio increases rapidly with altitude in the thermosphere. Photodissociation of O_2 and scale height of O makes O the dominant species in the upper thermosphere. In general, the O density surpasses the O_2 density in the lower thermosphere at or above $\sim$125km [*Rishbeth and Garriott*, 1969] and the N_2 density at $\sim$200 km [*Rees and Fuller-Rowell*, 1989]. These altitudes vary with the solar UV and X-ray energy inputs [*Hedin et al.*, 1991]. Overall, the thermosphere is dominated by O, O_2, and N_2. The lighter elements like hydrogen and helium start dominating at exospheric heights.

Absorption of solar radiation by thermospheric constituents is the dominant component in the global energy budget. Solar UV, EUV, and X-ray photons are absorbed by thermospheric species primarily via processes of photodissociation and photoionization (depending on the wavelength). There are many other mechanisms (discussed later) that cause excitation of the thermospheric species. Excited species lose their excess energy by photoemission or collisions with other molecules. In the lower thermosphere, loss of energy by collisions (also called quenching) is the dominant process, but in the upper thermosphere energy is mostly lost by the emissions of photons. These photons are responsible for the phenomenon called "airglow"(discussed in detail in chapter 2).

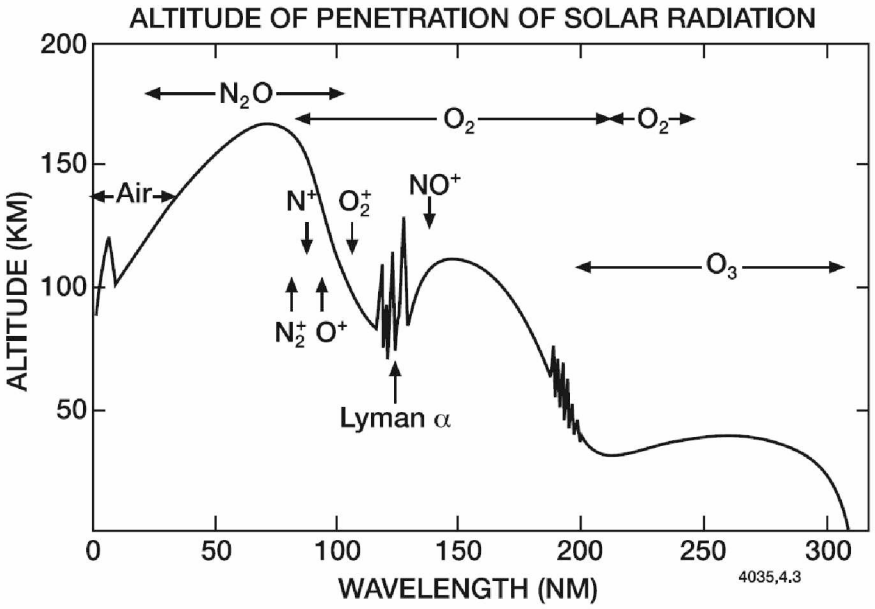

Figure 1.4: Altitude of penetration of solar radiation in the Earth's atmosphere as a function of wavelength. The altitudes correspond to the optical depth equal to one for overhead sun [*Brasseur and Solomon*, 2005].

Absorption of radiation by oxygen and nitrogen molecules is a critical component of Earth's radiation budget. Molecular oxygen has highly variable and structured absorption cross-section between 102.6 *nm* and 130 *nm* [*Roble and Emery*, 1983]. Figure 1.4 illustrates the altitude of penetration of solar radiation as a function of wavelength. The curve represents the altitude where optical depth is unity when the sun is at zenith. It is clear that principal absorbers are nitrogen and oxygen (and compounds of these). UV and

shorter wavelength radiation (EUV and X-rays) are absorbed in the atmosphere so that only the wavelengths with $\lambda \geq 310$ *nm* can reach the earth surface. Wavelengths $\lambda \leq 100$ *nm* are completely absorbed above 100 *km*. X-rays ($\lambda < 10$ *nm*) penetrate to the middle atmosphere and photoionize or indirectly dissociate N_2 and O_2. Photoionization by X-rays is responsible for certain sporadic ionospheric disturbances. Photoionization dominates for $\lambda \leq 100$ *nm* whereas photodissociation dominates at longer wavelengths. Energy

Table 1.1: Energy and wavelength ranges of solar radiation affecting the upper atmosphere.

Spectrum region	Wavelength	Energy
X-ray	0.1 - 10 *nm*	12.4 - 124 keV
EUV	10 - 121 *nm*	124 - 10.2 eV
UV	121 - 200 *nm*	10.2 - 6.2 eV

deposited by radiation in the thermosphere becomes important for $\lambda \leq 175$ *nm*. Flux at longer wavelengths, from 175 to 240 *nm* (Schumann-Runge band and Herberg continuum) is mostly absorbed by molecular oxygen and ozone in the stratosphere. Above 120 *km*, the global mean temperature structure of the thermosphere is basically maintained by the absorption of solar flux by atmospheric species at wavelengths less than 175 *nm*. Energy and wavelength ranges of the solar radiation affecting the upper atmosphere is presented in Table 1.1. Ionization and dissociation threshold energies and wavelengths for primary constituents of the upper atmosphere are presented in Table 1.2.

Absorption of the solar radiation is dependent on the photoabsorption cross-sections of the species. As an example, Figure 1.5 shows the photoabsorption cross-section of molecular oxygen and ozone for $\lambda \leq 800$ *nm*. Photoabsorption cross-sections for primary constituents of the upper atmosphere below $\lambda \leq 110$ *nm* are given in Figure 1.6. Photodissociation of molecular oxygen is the dominant process for the wavelength interval 100-200 *nm* and becomes important above 100 *km* altitude. The Schumann-Runge continuum between 130 to 175 *nm* (as shown in Figure 1.5) is the most important part of the absorption spectrum for photodissociation of O_2. These wavelengths ($\sim$130-175 *nm*)

Table 1.2: Ionization and dissociation threshold energies and wavelengths [*Rees*, 1989].

	Ionization		Dissociation	
Species	eV	λ (nm)	eV	λ (nm)
N_2	15.85	79.6	9.76	127.0
O_2	12.08	102.6	5.12	242.2
O	13.61	91.1		
N	14.54	85.3		
NO	9.25	134	6.51	190.5
H	13.59	91.2		
He	24.58	50.4		

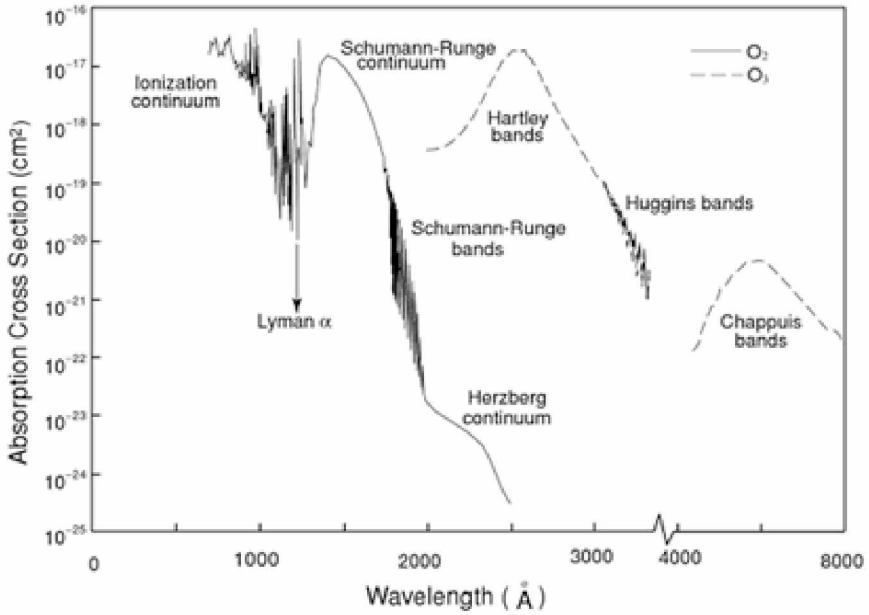

Figure 1.5: Variation in photoabsorption cross-section of ozone and molecular oxygen with wavelength in UV region of electromagnetic spectrum [*Liou*, 2002].

have enough energy to dissociate O_2 molecules but not to ionize them. Absorption in the Schumann-Runge continuum band by O_2 is responsible for a large fraction of the total heat input into the thermosphere. Photoionization of O_2 starts for $\lambda < 102.6$ nm.

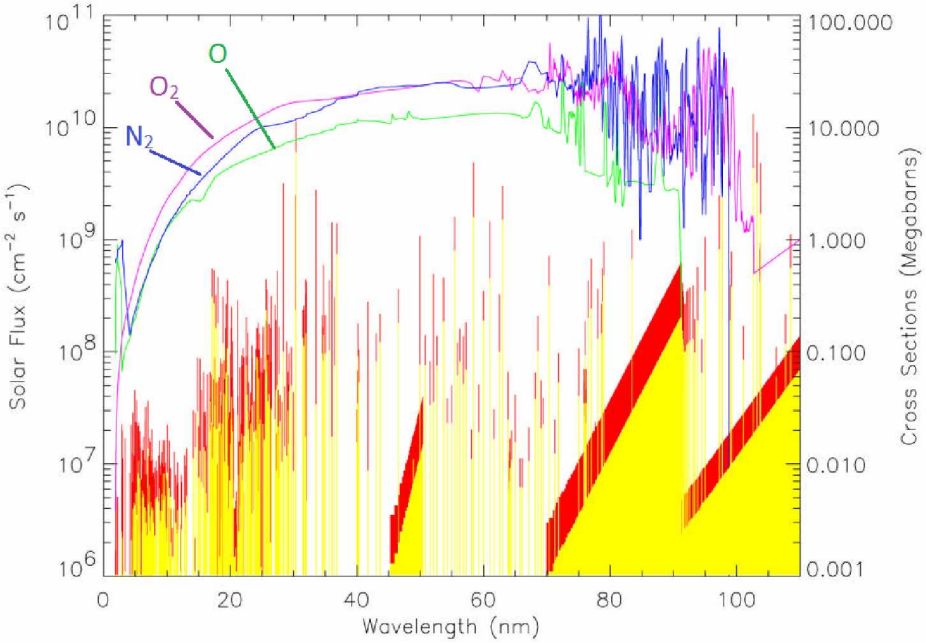

Figure 1.6: Variation in photoabsorption cross-section of the primary constituents of upper atmosphere for $\lambda \leq 110$ *nm* (EUV and X-ray region of electromagnetic spectrum) [*Woods et al.*, 2001].

Photodissociation of molecular oxygen can occur via following two processes:

$$O_2 + h\nu\ (\lambda \leq 240nm) \rightarrow O(^3P)\ +\ O(^3P) \tag{1.27}$$

$$O_2 + h\nu\ (\lambda \leq 174.8nm) \rightarrow O(^3P)\ +\ O(^1D) \tag{1.28}$$

The absorption cross-section of molecular oxygen at wavelengths greater than 200 *nm* is very small. As a result, the chances of photodissociation of molecular oxygen via process shown in Equation 1.27 are minuscule. The photodissociation mechanism shown in Equation 1.28 is responsible for most of the dissociation of molecular oxygen to atomic oxygen.

Atomic oxygen is primarily destroyed by the exothermic three body recombination mechanism:

$$O\ +\ O + M \rightarrow\ O_2 + M + 5.12eV \tag{1.29}$$

$$O_2\ +\ O + M \rightarrow\ O_3 + M \tag{1.30}$$

$$O_3\ +\ O \rightarrow\ 2O_2 \tag{1.31}$$

where M is the third body [*Rees*, 1989] . As the recombination requires a 3-body reaction, this is why O must diffuse downward before it can recombine. Atomic oxygen produced in the upper thermosphere slowly diffuses downward over many days and transported convectively into the lower thermosphere [*Rees*, 1989]. At thermospheric altitudes, molecular nitrogen usually acts as third species in the recombination process of atomic oxygen.

It is clear from above Equations 1.27 to Equations 1.31 that concentrations of O, O_2, O_3 are dependent on each other. Production of atomic oxygen by photodissociation requires sunlight at UV wavelengths or shorter. Due to the scattering and absorption, the intensity of such solar radiation decreases rapidly with decreasing altitude in the thermosphere. On the other hand, the rate of removal of atomic oxygen via three body collisions increases rapidly with decreasing altitude due to the increasing availability of particles for three body collision. The net result is the peak in absolute concentration of atomic oxygen between 85 and 100 *km* as shown in Figure 1.3, whereas the relative abundance of *O* continues to increase throughout the thermosphere.

The lifetime of an oxygen atom is a function of altitude. Recombination requires a 3-body collision, but in the middle and upper thermosphere, the number density is such that the probability of such three body collision is very small. As a consequence, the lifetime of atomic oxygen can be of the order of a month or so. The collision frequency decreases with increasing altitude; as a result, lifetime of atomic oxygen is even much longer than in the lower thermosphere. Before atomic oxygen can recombine to produce molecular oxygen or ozone, it must diffuse downward. At the base of the thermosphere, number densities are large enough for three body collisions to occur at sufficient rates to reduce the atomic oxygen lifetime down to of the order of few hours, which means that any oxygen atom produced during day time will not survive through the following night. This recombination process is exothermic and acts as an important heat source to the bottom of thermosphere [*Rees*, 1989]. Although O is chemically active, in general, loss and production mechanisms have only minor effect on the concentration of O.

Photoionization of the dominant species of the thermosphere (O, O_2, N, N_2) by solar X-rays and extreme UV rays ($\lambda < 102.6\ nm$) produces weakly ionized plasma in the thermosphere. This ionized component in the Earth's thermosphere is commonly referred

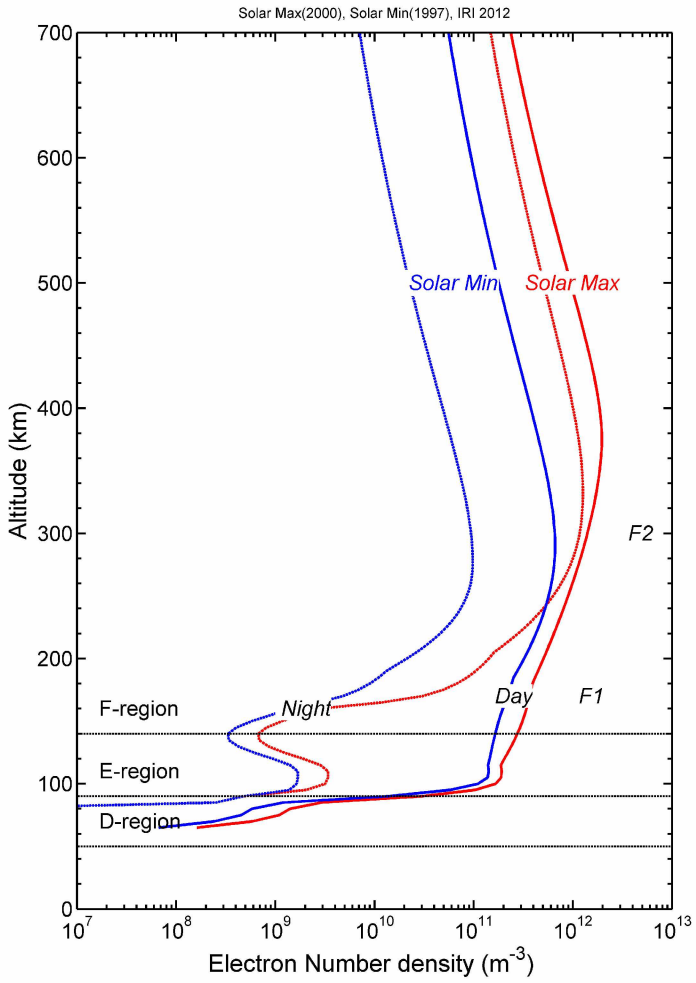

Figure 1.7: Variation of mid-latitude electron density with altitude for day and night and for solar maximum and minimum conditions (data are taken from International Reference Ionosphere Model (IRI) 2012).

to as the "ionosphere". The ionosphere plays an important role in the thermosphere's makeup, especially at high latitudes. The ionosphere is generally characterized by charge neutrality; i.e., total positive charge density exactly cancels to the negative charge density at all locations. The ionosphere is basically divided into various regions based on the altitude variation of the electron density. Those regions are the D-region (∼50-90 *km*), the E-region (∼90-150 *km*), and the F-region (∼150-800 *km*). During day time, the F-region splits into two layers F1 (∼150-200 *km*) and F2 (∼200-800 *km*). Figure 1.7 depicts the variation of mid-latitude ionospheric electron density with altitude for day time and night time.

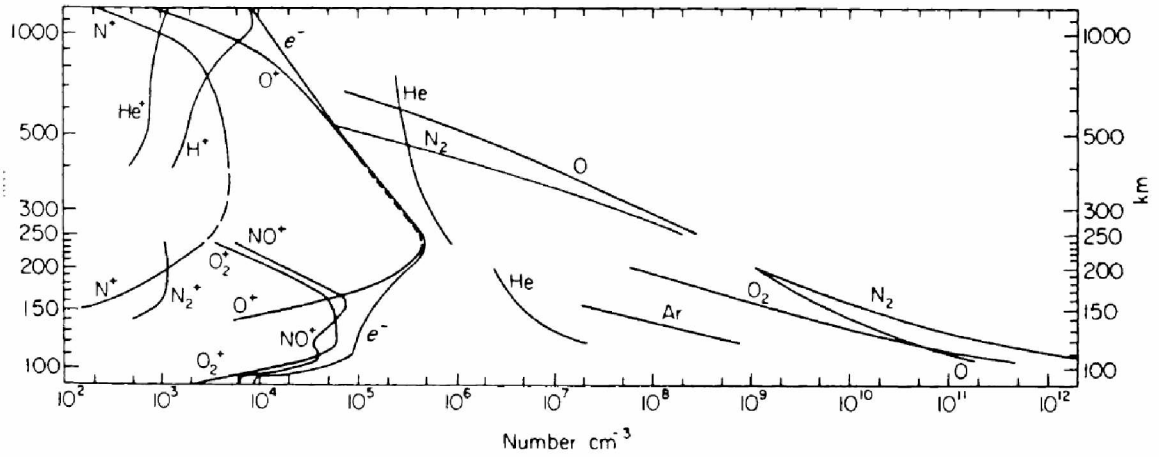

Figure 1.8: Typical mid-latitude daytime density profile of thermospheric and ionospheric constituents above 90 *km* during International Quiet Solar Year (IQSY) based on mass spectrometer measurements above White Sands, New Mexico (32N, 106W) [*Kelly*, 1989].

Solar maximum and solar minimum conditions were taken for comparison. The major regions of the ionosphere are also identified in this figure. The D-region and F1-region vanish at night. NO^+ and O_2^+ are primary ions in E and F1 regions, O^+ is the dominant ion in F2-region, and H^+ and He^+ are the major ions above F-region. The altitude profile of the number density of various primary constituents of the thermosphere and ionosphere is depicted in Figure 1.8.

The photoabsorption cross-section of O_2 is significant between wavelength 80 to 102.6 *nm*, and causes ionization of one of the major constituent of the lower thermospheric species [*Hargraves*, 1995] via:

$$O_2 + h\nu\,(80 \leq \lambda < 102.6nm) \rightarrow O_2^+ + e \tag{1.32}$$

Extreme ultra-violet radiation (~20-90 *nm*) is absorbed in the middle thermosphere (as shown in Figure 1.4). Radiation of wavelengths $\leq$ 66.2 *nm* has enough energy to cause ionization and dissociation of O_2 [*Rees*, 1989]:

$$O_2 + h\nu\,(\lambda \leq 66.2nm) \rightarrow O^+ + O + e \tag{1.33}$$

Molecular oxygen present above the middle thermosphere also undergoes similar ionization and dissociation. Atomic oxygen produced by the ionization-dissociation of O_2

enhances the F1-region ionization. It has strong absorption cross-section for radiation of wavelengths ~10-91.1 *nm* [*Roble and Emery*, 1983]:

$$O + h\nu\,(\lambda < 91.1nm) \rightarrow O^+ + e \tag{1.34}$$

Radiation of wavelengths ~20-79.6 *nm* has sufficient energy to photoionize N_2 [*Roble and Emery*, 1983]:

$$N_2 + h\nu\,(\lambda < 79.6nm) \rightarrow N_2^+ + e \tag{1.35}$$

Radiation of wavelengths $\leq$ 127 *nm* can cause photodissociation of N_2, but absorption cross-section of N_2 is minuscule at such wavelengths. Wavelengths ~80-100 *nm* result in photodissociation:

$$N_2 + h\nu\,(80 \leq \lambda < 100nm) \rightarrow N + N \tag{1.36}$$

It is interesting to note that despite N_2 being a dominant species in the middle thermosphere, atomic nitrogen is only a minor species. The primary reason is that the production and loss of atomic nitrogen are governed more by chemical reactions than by photodissociation of N_2. In general, atomic nitrogen is chemically active and is quickly used up by other thermospheric chemical reaction [*Rees*, 1989]. Another source of atomic nitrogen in the thermosphere is the photoionization and photodissociation of N_2 by radiation of wavelength $\leq$ 51nm:

$$N_2 + h\nu\,(\lambda \leq 51nm) \rightarrow N^+ + N + e \tag{1.37}$$

Many of these above reactions involve the production of the two dominant ionospheric species, NO^+ and O_2^+. Following are the two of the nine chemical reactions responsible for the production of NO^+:

$$O^+(^4S) + N_2 \rightarrow NO^+ + N(^4S) + 1.10eV \tag{1.38}$$

$$N_2^+ + O \rightarrow NO^+ + N(^4S) + 3.08eV \tag{1.39}$$

Following are the two examples responsible for the production of O_2^+

$$O^+(^4S) + O_2 \rightarrow O_2^+ + O + 1.55eV \tag{1.40}$$

$$O^+(^2D) + O_2 \rightarrow O_2^+ + O + 4.87eV \tag{1.41}$$

Collisions with sufficiently energetic electrons can also cause ionization and excitation. The major processes producing ionization are:

$$N_2 + e_p \rightarrow N_2^+ + e_p + e_s \tag{1.42}$$

$$N_2 + e_p \rightarrow N^+ + N + e_p + e_s \tag{1.43}$$

$$O_2 + e_p \rightarrow O_2^+ + e_p + e_s \tag{1.44}$$

$$O_2 + e_p \rightarrow O^+ + O + e_p + e_s \tag{1.45}$$

Collisional processes that cause excitation of the thermospheric species:

$$O_2 + e_p \rightarrow O^* + O + e_p \tag{1.46}$$

$$N_2 + e_p \rightarrow N^* + N + e_p \tag{1.47}$$

where e_p is an electron associated with auroral precipitation or primary photoelectron, and e_s is an ejected secondary electron. O^* and N^* are the species in their excited state. These excited species can undergo collisional de-excitation (quenching) or release excess energy by emitting photons. Quenching is the most favorable process if the excited species are in their forbidden states (or called metastable states). The quenching process occurs via:

$$Q^* + X \rightarrow Q + X^* \tag{1.48}$$

where X can be an atom, molecule, or electron that takes excess energy from species Q via collision. Collisional de-excitation of species in their metastable states plays an important role in the thermal structure of thermosphere. This is because some fraction of the excitation energy is redistributed as heat to the surrounding gas. If the radiative lifetime of the excited state is short or the collision frequency is sufficiently small, the species returns to its ground state by the emission of photons. These photons cause what is known as airglow or aurora (depending on how the state was initially excited):

$$Q^* \rightarrow Q + h\nu \tag{1.49}$$

A notable example is the 630 nm emission from atomic oxygen in ^1D state produced (for example) via equation (1.28). O(^1D) is a metastable state with a radiative lifetime of

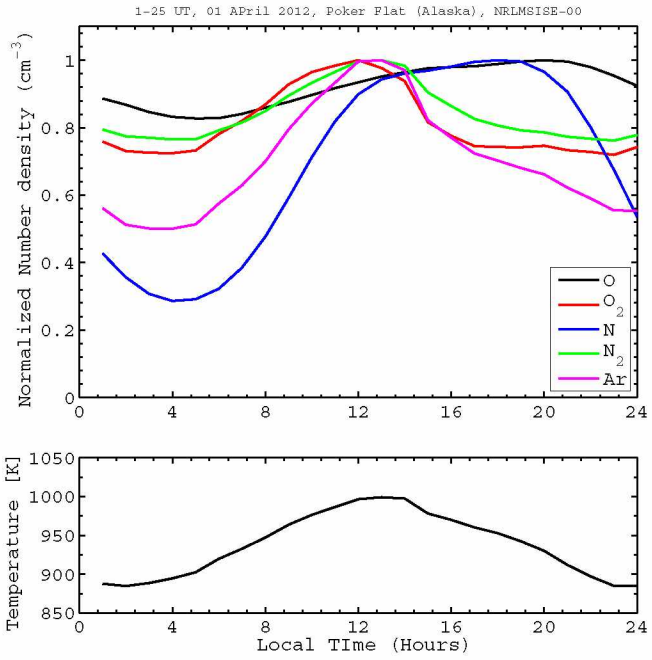

Figure 1.9: Diurnal variation in the thermospheric F-region (250 *km*) composition over Poker Flat Research Range, Alaska (65.12N, 147.47W) with solar tide (data obtained from NRLMSISE-00).

114 seconds. In the F-region, the collision frequency is small enough to allow O(^1D) to return to its ground state O(^3P) by emitting 630 *nm* photon, but below F-region heights this state is severely quenched. The long radiative lifetime of O(^1D) is the primary reason for the diffused appearance of red auroras.

1.6 Variability in Composition

Thermospheric composition changes diurnally with seasons and with geomagnetic activity. Figure 1.9 shows the diurnal variation in thermospheric composition over Poker Flat Research Range (Alaska). Variability in the thermospheric composition is often described by the ratio of atomic oxygen to molecular nitrogen (O/N_2). On the global scale, the O/N_2 ratio is smaller at the solstices and larger at equinoxes [*Strickland et al.*, 2004], which may be due, in part, to greater Joule heating during equinoxes [*Strickland et al.*, 2004]. Observations of ion and neutral velocities and O and N_2 composition from Dy-

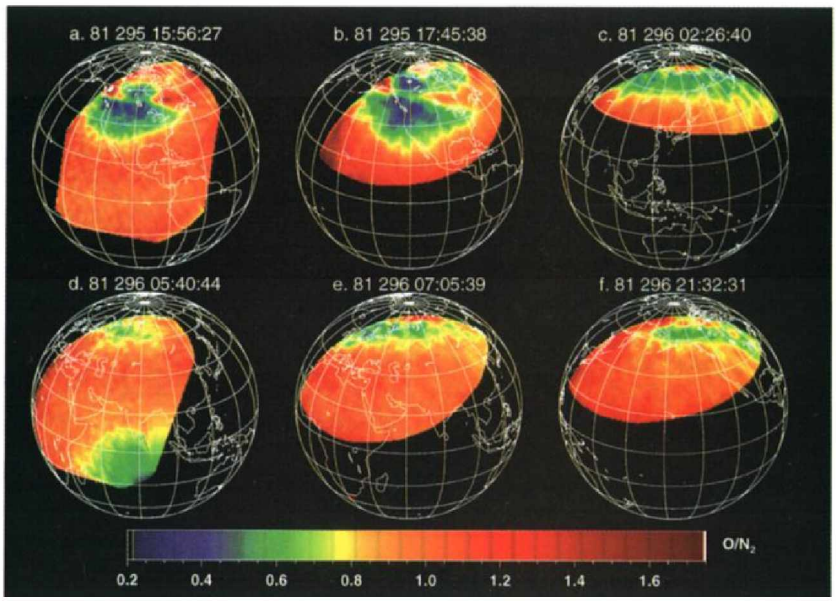

Figure 1.10: O/N_2 ratio at six different times showing dependence on geomagnetic conditions. (a) Quiet conditions, (b-c) thermospheric response several hours after storm onset, and (d-f) next day showing oxygen depleted regions at mid and higher latitudes [*Strickland et al.*, 1999].

namic Explorer-2 (DE2) provided direct evidence of changes in thermospheric composition associated with the Joule heating [*Killeen et al.*, 1984; *Hays et al.*, 1973]. A long known and frequently observed effect of geomagnetic storms is the reduction of O relative to the N_2 at high and middle latitudes. Large geomagnetic storms produce continent-sized regions in which the O/N_2 ratio is reduced at middle to high thermospheric altitudes, as shown for example in Figure 1.10. Significant changes in O/N_2 composition have also been seen from ground-based observations [*Christensen et al.*, 1997] and satellites [*Prölss*, 1980]. Numerous similar examples of storm-related O/N_2 changes have been presented in, for example by *Craven et al.* [1994]; *Burns et al.* [1995]; *Nicholas et al.* [1997]; *Immel et al.* [1997, 2001]; *Zhang and Shepherd* [2004]; *Crowley and Meier* [2013]. *Burns et al.* [1995] suggested upwelling and downwelling of neutral winds as a primary mechanism of the large enhancements of O relative to N_2 on the nightside of winter hemisphere. It has usually been presumed that changes in the mixing ratio are due to large-scale upwelling driven by geomagnetic heating during the storm time. Figure 1.11 from *Conde et al.* [2011] shows

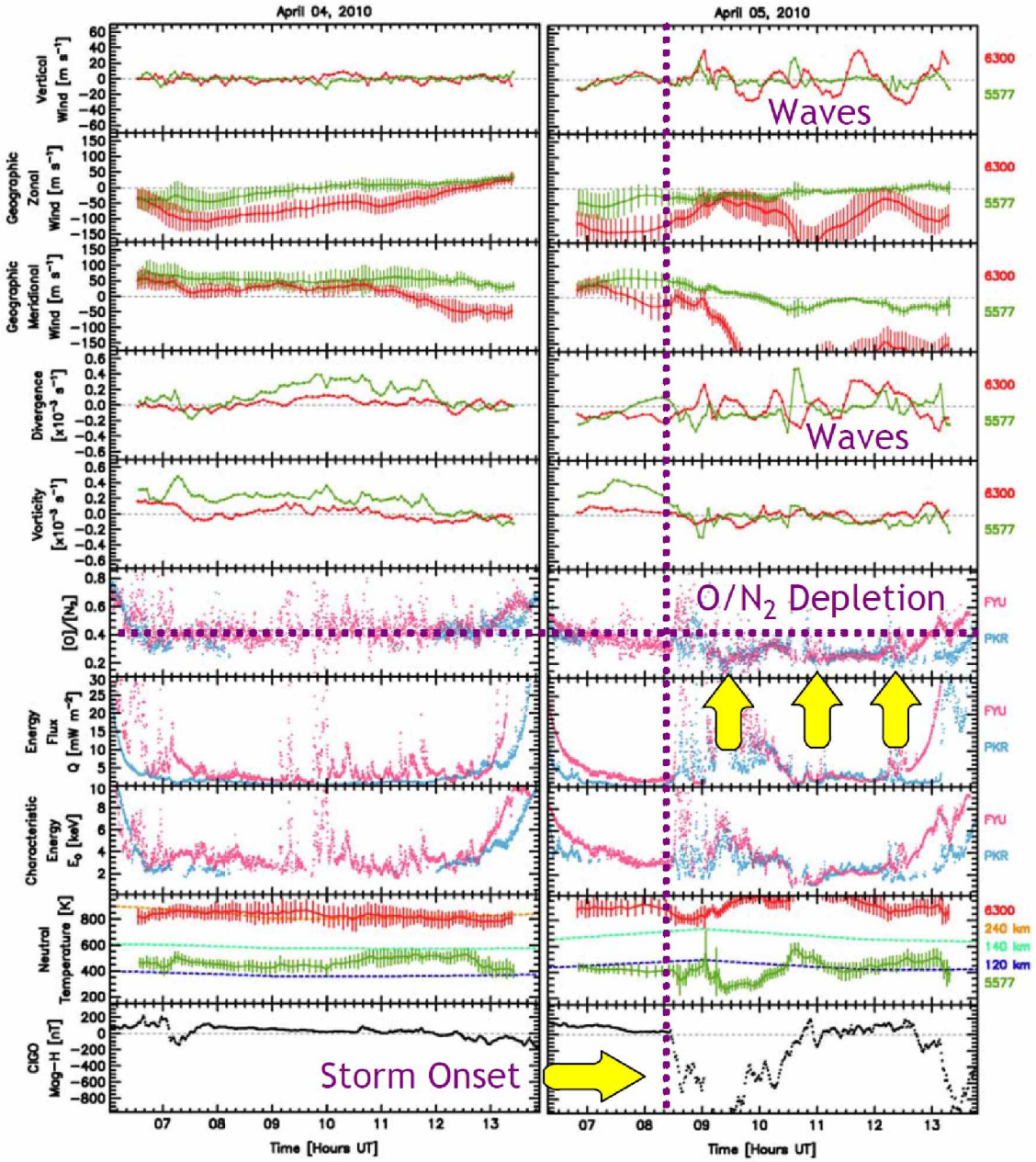

Figure 1.11: Upper atmospheric neutral wind and temperature measurements recorded at Poker Flat on 4th April 2010 (quiet day) and 5th April 2010 (geomagnetic active day) along with O/N_2 data and several other parameters [*Conde et al.*, 2011].

data from two days in April of 2010 (one quiet and other disturbed). The bottom panel shows the magnetic perturbation recorded at College, Alaska; it indicates that April 4 was mostly quiet, whereas a strong storm began at around 8 UT on April 5. The sixth

panel down indicates that the column-integrated thermospheric O/N_2 ratio above Poker Flat and Fort Yukon became depleted (approximately halved) as a result of geomagnetic activity. This study is consistent with expectations based on the studies mentioned above.

Crowley et al. [1989a,b] showed that Joule heating leads to the upwelling of nitrogen rich air which is transported to lower latitudes by meridional winds on the nightside and corotation carries the oxygen depleted air onto dayside. *Fuller-Rowell et al.* [1996] demonstrated the seasonal dependence of these processes. It is now well established that high latitude forcing (heating and convection) can lead to significant thermospheric disturbances on a global scale. When geomagnetic conditions are disturbed, variations in thermospheric composition at high latitudes can be transported to lower latitudes by strong meridional winds, which in turn can affect the lower latitude composition. *Strickland et al.* [1999] have shown the latitudinal motion of the O depleted large-scale patches using DE 1 data. *Pallamraju* [2005] has also discussed such traveling atmospheric composition modifications from high latitudes to lower latitudes during geomagnetic storms by analyzing the substantial variation in 630 *nm* dayglow emissions at a low latitude site (Carmen Alto, Chile) after a geomagnetic storm.

1.7 Heat Budget and Sources

By the law of conservation of energy, energy gain must be equal to energy loss to maintain the thermal structure of the upper atmosphere. The overall process in mathematical form [*Whitten and Poppoff*, 1971] is:

$$\frac{dQ}{dt} = q_T - R - \frac{d\phi}{dz} \tag{1.50}$$

Where Q is the thermal energy, $\frac{dQ}{dt}$ is the rate of energy gain per unit volume at a given height (z), q_T is the rate of energy input (source function), R is rate of energy loss by radiation, and ϕ is the heat energy flux (transport term). The absolute temperature of the upper atmosphere is related to thermal energy Q by:

$$Q = \rho C_p T \tag{1.51}$$

where ρ is the gas density and C_p is the specific heat capacity at constant pressure.

The principal source of thermal energy in the upper atmosphere is the absorption of the solar ultra-violet and extreme ultra-violet radiation by its constituents. At high latitudes, magnetospheric forcing adds a significant amount of energy compared to solar heating via Joule heating and heating by auroral particle precipitation, especially during active or storm conditions. Heat is primarily removed from the upper and lower thermosphere by radiations and heat conduction. In the upper thermosphere, a large fraction of the heat is removed by downward heat conduction [*Burns et al.*, 2013; *Killeen*, 1987]. The radiatively active minor constituents such as NO and CO_2 act as the energy sinks in the thermosphere. A detailed discussion of these various energy sources and sinks of the thermosphere is presented by *Killeen* [1987]. The global thermal balance in the thermosphere (as shown in Figure 1.1) is primarily controlled by a balance between solar heating and weak in-situ cooling. High latitude energy inputs during geomagnetic storms can also make global changes in heating via generation of waves at high latitudes and their dissipation at low and middle latitudes [*Burns et al.*, 2013]. Energy deposited at high latitudes by Joule heating and particle heating perturbs chemistry and dynamics of the thermosphere. A brief discussion of various important sources and sinks of energy in the thermosphere follows:

1.7.1 Solar Heating

Photoabsorption of radiation from the sun is the principal source of thermal energy in the upper atmosphere. Figure 1.12 shows the wavelength-dependent energy deposition in the thermosphere for solar maximum and minimum. This figure depicts the altitude of peak energy deposition, the range of altitudes affected at each wavelength, and the wavelengths where most energy is deposited. Absorption of solar ultra-violet and extreme ultra-violet is primarily responsible for maintaining global high thermospheric temperatures. Interactions of radiation in the thermosphere cause excitation, ionization, and dissociation of thermospheric species. These excited species are then thermalized by collisions with the surrounding gas. The thermal energy deposition rate with altitude in the thermosphere is discussed in section 1.4. Solar heating on the dayside of the thermosphere produces pressure-gradients which in turn drives the basic day-to-night circula-

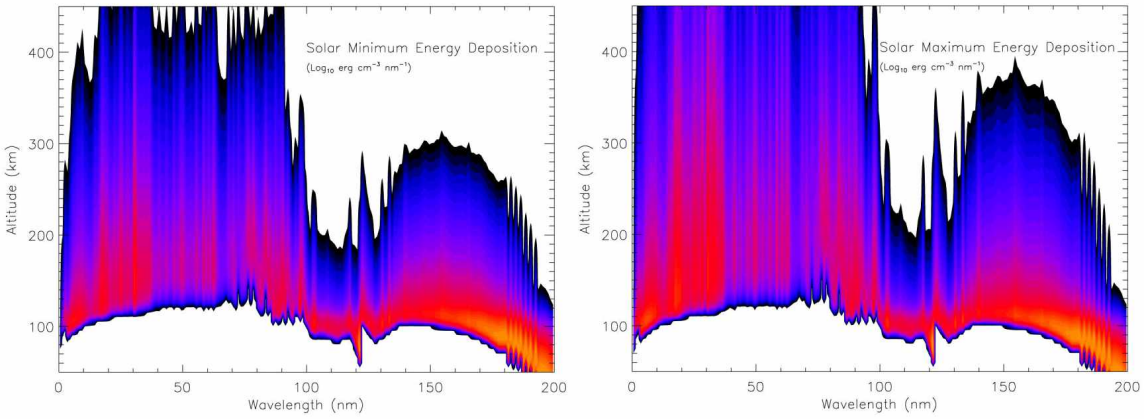

Figure 1.12: Wavelength-dependent deposition of energy in the thermosphere for solar minimum (left) and solar maximum (right) conditions. The colors black through red indicate energy deposition per unit volume [*Woods et al.*, 2001].

tion in the thermosphere (also called solar tide).

Photoionization in the middle or lower thermosphere produces primary electrons that undergo Coulomb collisions with ions and electrons. Electrons also undergo inelastic collisions with neutrals and heat the neutral gas with ~5% efficiency [*Killeen*, 1987]. The energy transfer from ions to the thermosphere is more complicated than the energy transfer of photoelectrons. Various paths occur, including exothermic ion-molecule reactions, via which ions transfer energy to the thermosphere. Much of the chemical potential energy carried by ions goes into heating of the local thermosphere. The remaining chemical potential energy that did not heat the ambient gas, cause dissociation of O_2 into O atoms. These O atoms diffuse downwards and deposit their energy of dissociation into the lower thermosphere.

Absorption of solar radiation in the Schumann-Runge continuum (~130-175 *nm*) is the dominant heat source in the lower thermosphere [*Roble et al.*, 1987]. The photodissociation of the molecular oxygen by the photons in this wavelength range produce atomic oxygen in metastable states (O^1D for example). The excess energy released by these metastable species by collisional quenching heats up the local neutral gas with a heating efficiency of ~33% [*Killeen*, 1987].

Heating of the thermosphere varies with the solar cycle and solar rotation and can

also change as a result of solar flares [e.g., *Qian et al.*, 2006]. The solar decametric flux ($F_{10.7}$) is derived from measurements at radio wavelengths that do not act directly on the upper atmosphere; rather, it is used as a "proxy" indicator of the solar UV and EUV fluxes that do directly influence the Earth's thermosphere. The variation of thermospheric temperature with the change in solar flux was examined by *Hernandez and Roble* [1995] over the Fritz Peak Observatory (39.9N, 105.5W) with a Fabry-Perot spectrometer (FPS). They concluded that temperature at solar maximum was around 500 K greater than at the solar minimum conditions.

1.7.2 Joule Heating

While there are many processes that heat the thermosphere, Joule heating is the primary non-solar energy input high latitudes. Basically, it is the transformation of electric-current energy into thermal energy through neutral collisions with charged particles accelerated by an electric field [*Cole*, 1962]. Joule heating (also called frictional heating or Ohmic heating) is thus caused by a differential velocity between ions and neutral that arise from the different nature of forces acting on neutral gas and plasma.

The thermosphere is weakly ionized plasma with an embedded magnetic field. If no other forcing is present, ions would move under the effect of the Earth's magnetic field. At high latitudes, ionospheric plasma drifts primarily under the combined effect of the convection electric field (mapped down from the magnetosphere along magnetic field lines) and the geomagnetic field. The convection electric fields are solar wind-driven.

When the interplanetary magnetic field (IMF) is southward, reconnection occurs on dayside magnetopause and couples the IMF to the Earth's magnetic field. It creates open magnetic field lines that map into the polar ionosphere. Also, it allows the direct entry of solar wind plasma into the Earth's magnetic field along the opened field lines. These newly opened field lines are swept antisunward by the solar wind dynamic pressure. The field lines moving antisunward become lobe field lines of the magnetosphere on the nightside of earth. These open field lines reconnect again in the tail of magnetosphere. After reconnection, these field lines (now closed) are transported back to the dayside. This complete cycle of transport of magnetic flux from the dayside to the nightside and then

back to the dayside is known as magnetospheric convection. Magnetic flux is transported by the solar wind from the dayside to the nightside over the polar cap and return flow occurs via lower magnetic latitudes. When magnetospheric convection is mapped onto the ionosphere along the magnetic field lines, it develops a plasma convection pattern generally known as "twin cell circulation".

An oval shaped region formed around the boundary of open and closed geomagnetic field lines at high latitudes is called the "auroral oval". Since open field lines exist at high latitudes of both hemispheres, so two auroral ovals are formed: one at northern high latitudes and other at southern high latitudes. They are centered at each geomagnetic pole.

On the dayside, solar wind particles can freely enter the Earth's magnetic field in the cusp region (a region between the lowest-latitude closed field lines and highest-latitude open field lines that map to the nightside magnetosphere). The solar wind plasma is collisionless and induces an electric field ($\boldsymbol{E}_{sw}$)when it is trapped in the cusp region and traversing antisunward through the magnetic field lines. This phenomenon of electric field generation by solar winds is referred to as "dynamo effect" and given by:

$$\boldsymbol{E}_{sw} = -\boldsymbol{V}_{sw} \times \boldsymbol{B}_{sw} \tag{1.52}$$

where $\boldsymbol{V}_{sw}$ is the solar wind speed and $\boldsymbol{B}_{sw}$ is the solar wind magnetic field. The direction of this solar wind induced electric field is from dawn to dusk. The Earth's magnetic field lines are generally considered to be equipotential. When the magnetospheric electric potential between magnetic field lines is mapped back down to the polar cap ionosphere, it results in a dawn to dusk electric field $\boldsymbol{E}_I$, also known as "convection electric field" [*Kelly*, 1989]. A schematic layout of this process is presented in Figure 1.13.This ionospheric convection electric field and the geomagnetic field generates $\boldsymbol{E} \times \boldsymbol{B}$ drift and drives the ionospheric plasma in the antisunward direction across the polar cap. The return flow occurs via lower latitudes and thus forms a two-cell plasma convection pattern. When the IMF is northward, the ionospheric plasma flow pattern is more complicated, often with more than two convection cells. At ionospheric altitudes:

$$\boldsymbol{E}_I = -\boldsymbol{V}_I \times \boldsymbol{B}_I \tag{1.53}$$

Where $\boldsymbol{B}_I$ is the geomagnetic field and $\boldsymbol{V}_I = \frac{\boldsymbol{E}_I \times \boldsymbol{B}_I}{B_I^2}$ is the $\boldsymbol{E} \times \boldsymbol{B}$ drift velocity in ionosphere. For stationary state ($\frac{\partial B}{\partial t} = 0$) state, $\boldsymbol{E} = -\nabla\Phi$, then

$$\begin{aligned} \boldsymbol{V} \cdot \nabla\Phi &= -\boldsymbol{V} \cdot \boldsymbol{E} \\ &= -\boldsymbol{V} \cdot (\boldsymbol{V} \times \boldsymbol{B}) \\ &= 0 \end{aligned} \tag{1.54}$$

This means ionospheric plasma moves along the contours of constant electric potential.

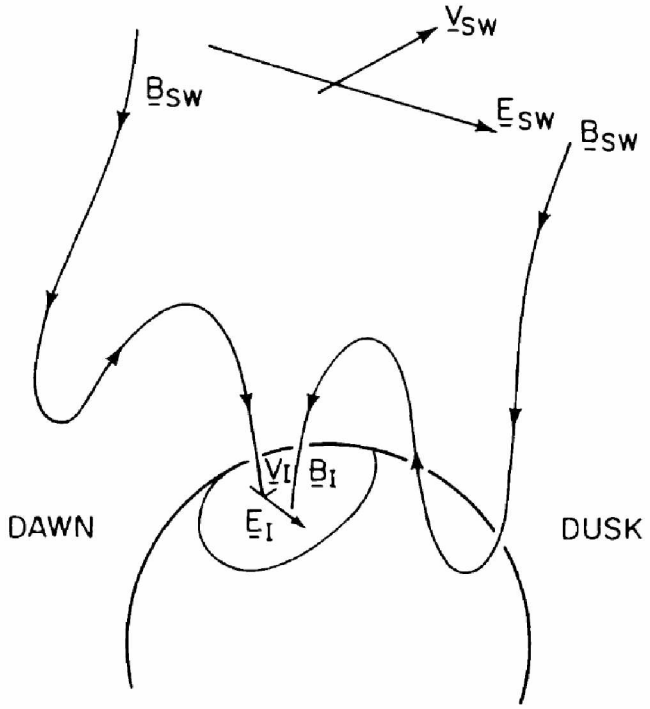

Figure 1.13: Schematic representation of the solar wind dynamo and ionospheric parameters[*Kelly*, 1989].

In practice, the convection patterns are presented in two-dimensional electric potential. The contours of constant potential represents the streamlines of ionospheric plasma. Such an example showing duskside and dawnside convection cells as contours of equipotential lines is presented in Figure 1.14. Typical cross-polar cap potential difference is of the order of 60 kV. Because of reconnection on the night side of Earth during northward IMF, the actual convection pattern is complicated and more than two convection cells are often formed.

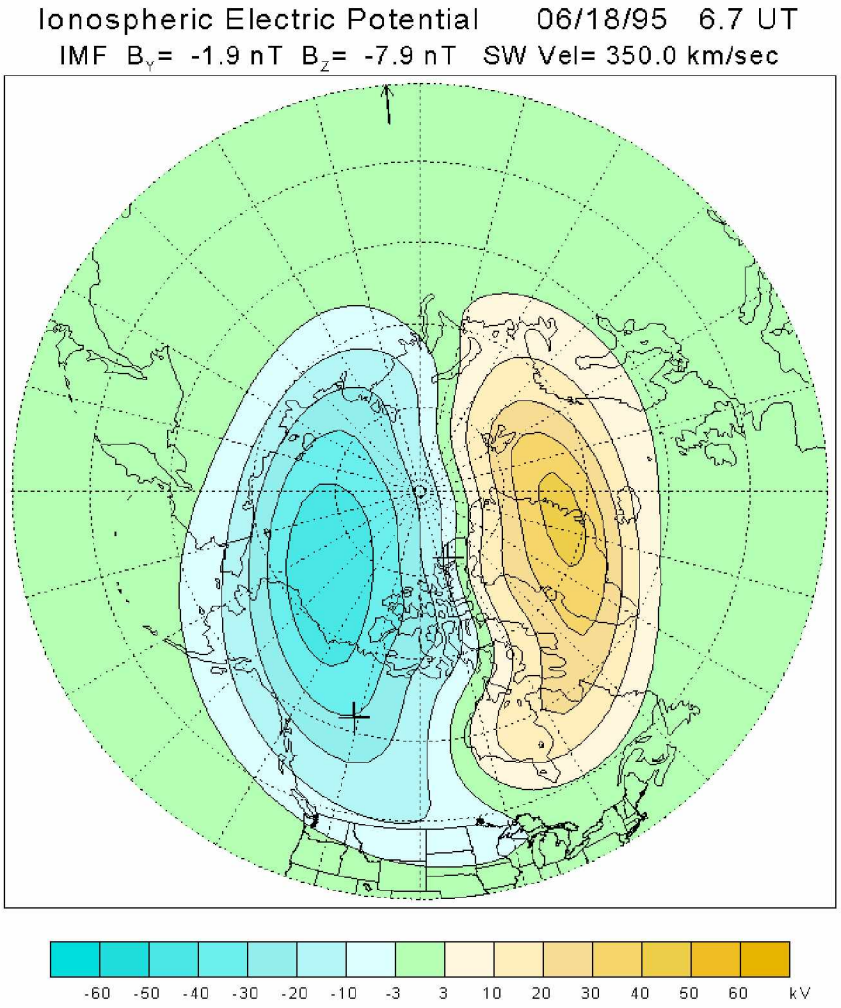

Figure 1.14: Electric potentials (projected in geographic coordinates) obtained from Weimer ionospheric model 1995 by supplying real measured solar wind conditions by WIND spacecraft on 18 June 1995. The arrow indicates the longitude of the sub- solar point at the time of measurement. The + mark close to the geographic north pole shows the location of the geomagnetic pole and the other + marks the location of Fort Simpson, Canada [*Weimer*, 1995].

Momentum exchange occurs between convecting ions and the neutral gas due to collisions. These collisions are sufficiently frequent to generate a significant momentum source for neutrals known as "ion-drag" [*Rees*, 1971; *Meriwether et al.*, 1973; *Nagy et al.*, 1974; *Kelly*, 1989; *Rees and Greenaway*, 1983; *Spencer et al.*, 1982; *Mikkelsen et al.*, 1981; *Killeen et al.*, 1982; *Killeen and Roble*, 1984; *Killeen et al.*, 1984; *Hays et al.*, 1979, 1984; *Fuller-Rowell*,

1995].Thus, magnetospheric plasma convection can, at high latitudes, significantly modify the otherwise mainly pressure-gradient driven neutral wind flow [*Killeen and Roble*, 1988; *Roble et al.*, 1982]. As a result, high latitude neutral winds tend to follow a similar pattern that of convecting plasma and establish a twin cell circulation [*Killeen et al.*, 1982]. The thermospheric circulation cell on the dawnside/duskside of earth is usually called dawnside/duskside circulation cell. Because of the inertia provided by ion-drag to neutral winds, neutral winds can sustain this convection pattern long after magnetospheric/ionospheric forcing dies down, a mechanism known as the "flywheel" effect [*Lyons et al.*, 1985]. The duskside circulation cell is always stronger than the dawnside circulation cell. This is principally because the Coriolis force works against the rotation in the dawnside circulation cell. Even the duskside cell may be very small and weak in mid-winter and on quiet days during solar minimum.

At high altitudes, basic balancing forces are ion drag, pressure, and in some cases viscosity, whereas in the lower thermosphere pressure gradients, tidal forcing, and Coriolis forces are major forces that balance ion drag [*Killeen et al.*, 1984]. Both rocket and unpublished FPI data from Poker Flat at 557.7 *nm* show ion drag can be important down to as low as 120 *km*. In-situ measurements by the DE2 showed that Joule heating is controlled by the combination of temporal and spatial variability of the $\boldsymbol{E} \times \boldsymbol{B}$ ion drifts, local ion and neutral composition, and the time taken for the neutral gas to acquire the available momentum from the drifting ions for any given quasi-stable convection pattern [*Killeen et al.*, 1984].

Joule heating by collisions between plasma and neutrals is proportional to the square of the difference in plasma and neutral bulk flow velocities. As shown in Figure 1.15, when the difference between ion and neutral velocities was large (around time 9483 UT), a strong enhancement in both electron and ion temperature (more than 1000 *K*) was observed. On the other hand, neutrals showed a much smaller increase spread over broader region which is due to the large heat capacity of neutral gas. Generally, collisions of ions with neutrals contribute to Joule heating more than electrons.

Ohm's law for the upper atmosphere is given by:

$$\boldsymbol{J} = \sigma \left(\boldsymbol{E} + \boldsymbol{U}_n \times \boldsymbol{B} \right) \tag{1.55}$$

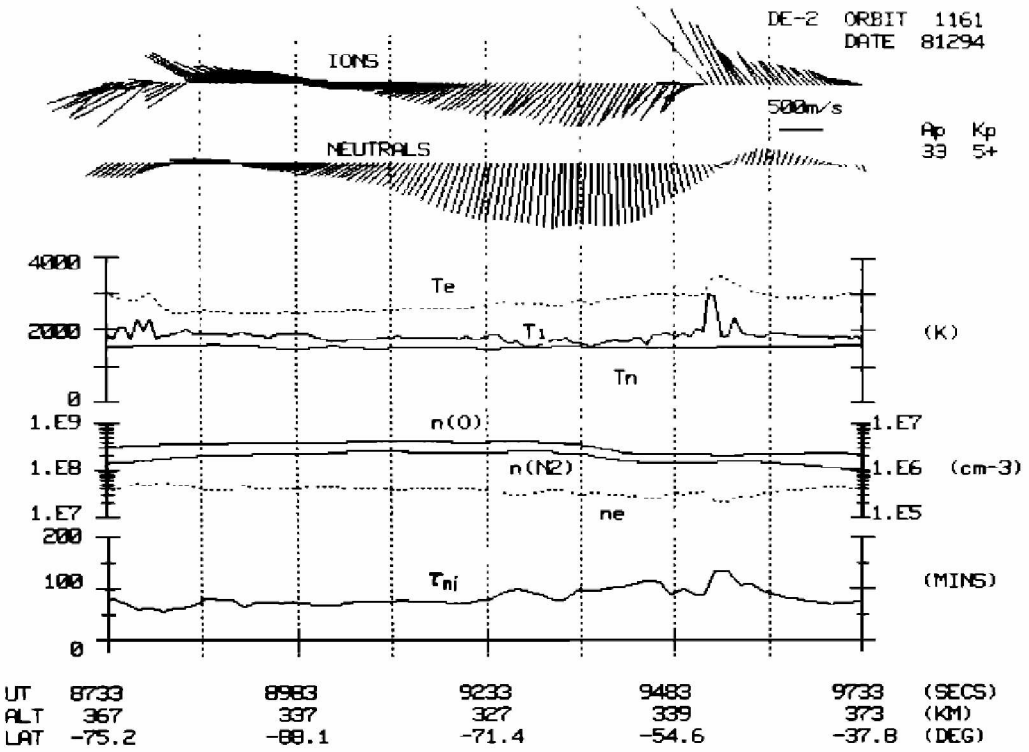

Figure 1.15: Geophysical quantities observed along the track of DE2 during orbit 1174. The first panel shows the ion velocity, second panel shows neutral wind velocity, third panel shows electron, ion, and neutral temperature, fourth panel shows O, N_2, and electron density, and bottom panel shows ion-neutral coupling time constant [*Killeen et al.*, 1984].

where $\boldsymbol{J}$ is the current density, σ is the conductivity tensor, $\boldsymbol{E}$ is the dawn to dusk convection electric field, $\boldsymbol{U}_n$ is the neutral wind velocity, and $\boldsymbol{B}$ is the geomagnetic field. The conductivity tensor has three components: Hall conductivity, Pederson conductivity, and Parallel conductivity. The structure of conductivity tensor is as below:

$$\sigma = \begin{pmatrix} \sigma_P & -\sigma_H & 0 \\ \sigma_H & \sigma_P & 0 \\ 0 & 0 & \sigma_{\parallel} \end{pmatrix} \tag{1.56}$$

where σ_P, σ_H,and $\sigma_{\parallel}$ are the Pederson, Hall, and Parallel conductivities; they are given by [*Maeda*, 1977]:

$$\sigma_P = \left[\frac{em_i v_{in}}{m_i^2 v_{in}^2 + e^2 B^2} + \frac{em_e v_{en}}{m_e^2 v_{en}^2 + e^2 B^2} \right] n_e e \tag{1.57}$$

$$\sigma_H = \left[\frac{-e^2 B}{m_i^2 v_{in}^2 + e^2 B^2} + \frac{e^2 B}{m_e^2 v_{en}^2 + e^2 B^2} \right] n_e e \tag{1.58}$$

$$\sigma_{\parallel} = \left[\frac{n_e e^2}{m_i v_{in}} + \frac{n_e e^2}{m_e v_{en}} \right] \tag{1.59}$$

where e is the electron charge, m_i is the ion mass, m_e is the mass of an electron, n_e is the electron number density, v_{in} is ion-neutral collision frequency, v_{en} is electron-neutral collision frequency, and B is the geomagnetic field. Pederson conductivity corresponds to currents in the direction perpendicular to the magnetic field and parallel to the electric field. Hall conductivity corresponds to the direction perpendicular to both magnetic and electric fields. Hall current is carried by $\boldsymbol{E} \times \boldsymbol{B}$ drift of electrons. In the ionosphere, Hall conductivity maximizes in the E-region because ion drift is suppressed by collisions, whereas electron are still free to drift in the $\boldsymbol{E} \times \boldsymbol{B}$ direction. Parallel conductivity is for the direction parallel to the magnetic field and is far stronger than Hall and Pederson conductivities. These conductivities are dependent on time of the day, location, season, and solar activity. Typical altitude profiles of Pederson conductivity, Hall conductivity, and electron density with altitude is shown in Figure 1.16.

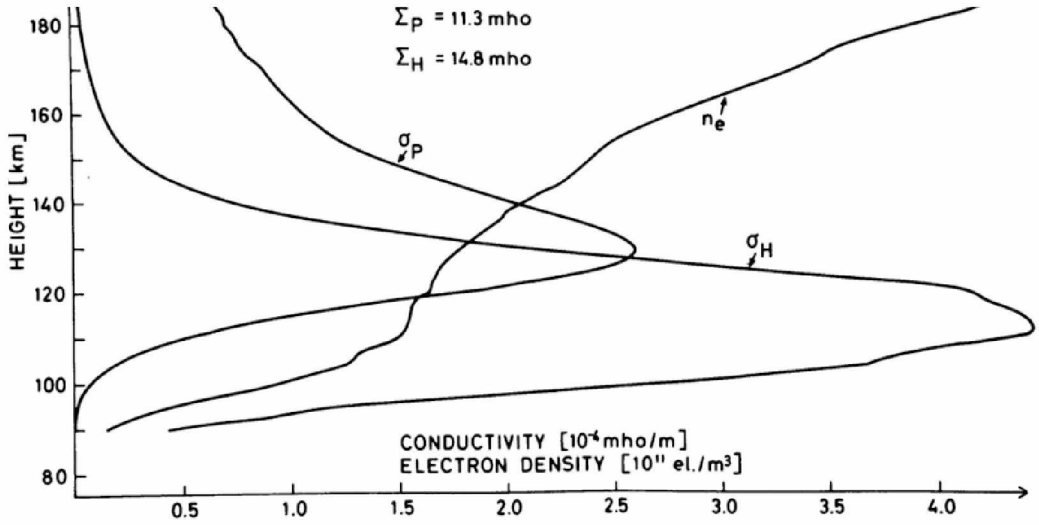

Figure 1.16: Altitude profile of ionospheric conductivities and electron density for a geomagnetically quiet day [*McCormac*, 1974].

The convection electric field ($\boldsymbol{E}$) of magnetospheric origin is the dominant driver of Joule heating. For a uniform $\boldsymbol{E}$, normal to the geomagnetic field ($\boldsymbol{B}$), the heat input per

unit volume and time is given by relation [*McCormac*, 1974]:

$$Q'(h) = \sigma_P(h)\,(\boldsymbol{E}_\perp + \boldsymbol{v}_n \times \boldsymbol{B})^2 = \frac{J_\perp^2}{\sigma_c} \tag{1.60}$$

where $\sigma_c = \sigma_P + \frac{\sigma_H^2}{\sigma_P}$ is the cowling conductivity, $\boldsymbol{E}_\perp$ is the height independent perpendicular (to $\boldsymbol{B}$) electric field, and $\boldsymbol{v}_n$ is the neutral wind velocity. Height integrated Joule heating is:

$$Q = \Sigma_P\,(\boldsymbol{E}_\perp + \boldsymbol{V}_n \times \boldsymbol{B})^2 = \Sigma_P\,(\boldsymbol{E}_\perp + \boldsymbol{E}_W)^2 \tag{1.61}$$

where $\boldsymbol{E}_W$ is the field due to neutral wind and $\boldsymbol{V}_n$ is the height integrated neutral wind. Σ_P and Σ_H are height integrated Pederson and Hall conductivities given by:

$$\Sigma_P = \int \sigma_P\, dh \qquad \Sigma_H = \int \sigma_H\, dh \tag{1.62}$$

Generally σ_P and σ_H (as well as Σ_P and Σ_H) are roughly of the same magnitude. Hall current is largely conducted by ionospheric electrons and it flows low in ionosphere [*McCormac*, 1974]. Equations 1.60 and 1.61 suggest that the maximum Joule heating per unit volume occurs in the most conductive regions of ionosphere.

The magnetosphere and ionosphere are coupled through large-scale DC electric fields and the injection of energetic particles that cause local ionization. Equation 1.61 is often simplified by assuming that the neutral wind is negligible at all altitudes, which reduces the heating to that produced by ion motion only. So, Joule heating in simplistic form is the product of the square of electric field and the Pederson conductivity calculated form ion drift velocity and particle precipitation in the ionosphere [*Foster et al.*, 1983]. This oversimplifies the calculation since both the convection electric fields and neutral winds are permanent features of the high latitude, and therefore Joule heating should always be present [*Rees and Greenaway*, 1983].

Energy deposition per unit volume by Joule heating maximizes around 120 *km* because the current density ($\boldsymbol{J}$) maximizes around this altitude. *Thayer* [1998] studied the effect of neutral wind inclusion in the calculation of height resolved and height-integrated estimates of Joule heating rate in the high latitude E-region using two data sets from Sondrestorm incoherent scatter radar. He found that the inclusion of neutral wind in calculations could decrease the calculated heating rate by 40% or increase it by 400%. He

also observed that when the electric field is directionally steady, the inclusion of neutral wind in calculations typically reduces the calculated Joule heating rate. On the other hand, the inclusion of neutral wind typically enhances the Joule heating rate when directional changes in the electric field are occurring. An analysis by *Aruliah et al.* [2005] using tristatic Fabry-Perot interferometer measurements of the neutral atmosphere and tristatic measurements of the ionosphere by European Incoherent Scatter radar (EISCAT) presented the importance of mesoscale variation in ion velocities when calculating Joule heating. They reported an increase in the estimated Joule heating by 320% when 1 min averages of ion velocity were used, compared to the results if 15 min averages were used instead. This study also highlighted the importance of neutral wind in calculating Joule heating. *Codrescu et al.* [1995] showed that including small-scale electric field variability could increase the calculation of the Joule heating rates by 33%. With the GITM model, *Deng and Ridley* [2007] observed that increasing the latitudinal resolution from 5 degrees to 1.25 degrees increased the estimated Joule heating rate by approximately 20%.

It is well known that Joule heating occurs roughly in an oval pattern at high latitudes with three major heating regions. These regions are: the dayside cleft, the region of sunward convection at dawn and dusk, and the midnight sector. *Foster et al.* [1983] studied the 25000 orbits of Atmospheric explorer satellite (AE-C) and found that Joule heating is dominant in the dawn-dusk and cleft regions. Also, there is no apparent asymmetry in the Joule heating between hemispheres for similar seasons. *Olsson et al.* [2004] studied the dependence of Joule heating on geomagnetic activity (as shown in Figure 1.17) using six months of Poynting flux data from the Astrid-2 satellite. He reported that for nighttime (MLT 18-06), about 1/3 of the total Joule heating occurs in the 65-74 invariant latitude auroral oval. It decreases by a factor of around 1/4 when geomagnetic conditions are quiet. It is because of the expansion of the auroral oval to lower latitudes when geomagnetic conditions are active. Satellite observations have shown that the most significant Joule heating occurs poleward of +/- 50 degrees invariant latitude [*Olsson et al.*, 2004].

Kosch and Nielsen [1995] calculated a mean hemispherical heating of $1.7 \times 10^{11} W$. During disturbed geomagnetic conditions, enormous amount of energy relative to other sources is released from the magnetosphere into auroral regions. It enhances the electric fields

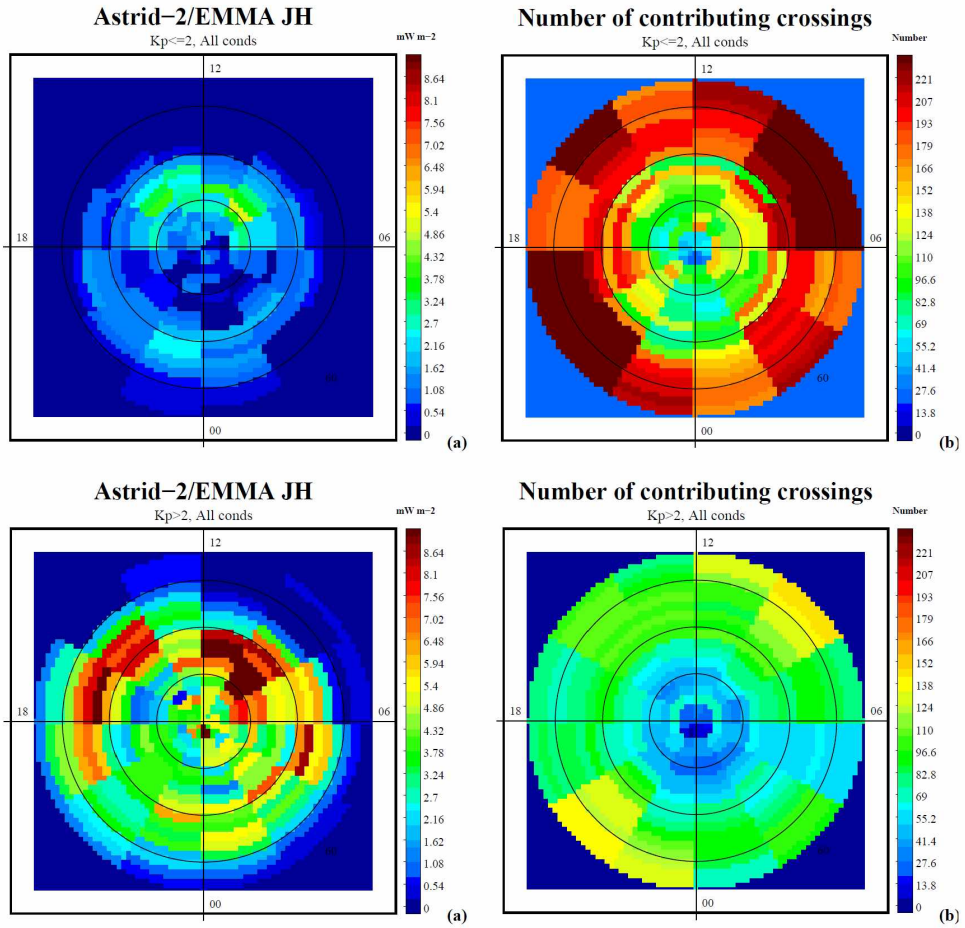

Figure 1.17: Average global Joule heating derived from Astrid-2 satellite measurements of the magnetic and electric field, under conditions of $K_p \leq 2$ (top panels) and $K_p > 2$ (bottom panels). The central circle marks 80 degree invariant latitude, with outer circles at 10 degree increments [*Olsson et al.*, 2004].

and auroral particle precipitation. Increased particle precipitation enhances the conductivity of the thermosphere by heating and ionization [*Buonsanto and Fuller-Rowell*, 1997]. These augmented electric fields and conductivity intensify the hemispheric Joule heating of the thermosphere from tens of gigawatts (quiet time) to hundreds of gigawatts (severe geomagnetic disturbances) [*Buonsanto and Fuller-Rowell*, 1997; *Wang et al.*, 1999]. As a result, dynamical properties of the thermosphere (e.g., wind, temperature, and composition) are significantly affected [*Banks*, 1977]. *Foster et al.* [1983] reported that at eqinox, hemispheric Joule heating is around 25 *GW* for quiet geomagnetic conditions (K_p=1) and

around 85 *GW* for disturbed conditions (K_p=4). Under disturbed geomagnetic conditions, hemispheric Joule heating can be greater than the solar UV absorption during daytime and an order of magnitude larger than during nighttime [*McCormac*, 1974]. In some limited regions, it can be one or even two orders larger. Joule heating is present even during quiet times because there is a substantial and an often seemingly random variability in ionospheric convection. *Foster et al.* [1983] reported a ~50% increase in Joule heating during the summer than during winter, which is primarily due to the enhanced ionospheric conductivities in summer by solar UV and EUV production.

Foster et al. [1983] and *Cosgrove and Thayer* [2006] reported that Joule heating is a linear function of K_p. Studies by *Kosch and Nielsen* [1995] and *Olsson et al.* [2004] both have concluded similar dependence of Joule heating on K_p Index. *Østgaard et al.* [2002] and *Aksnes et al.* [2004] studied the relation between hemispheric integrated Joule heating and *AE* index and found that a nearly linear relationship exit between them.

Joule heating rate is also dependent on the configuration of IMF. The study by *Kosch and Nielsen* [1995] using 173 days of data from coherent scatter radar observed the increase in Joule heating rate with the increase in the southward component of IMF. Using EISCAT radars at Tromso (66.6 GMLAT) and Svalbard (75.4 GMLAT), *Cai et al.* [2014] reported that Joule heating rate is higher for southward than for northward IMF at both stations.

1.7.3 Heating due to Energetic Particle Precipitation (Particle Heating)

Particle heating of the neutral atmosphere occurs at auroral latitudes due to the energy lost by the precipitating energetic auroral particles (basically electrons and protons) through collisions with neutral species as they penetrate lower into the thermosphere [*Bates*, 1951]. Like Joule heating, particle heating is also a permanent feature of the auroral oval and polar cap. The atmospheric heating rate due to the particles is given by [*Banks*, 1977]:

$$Q_P = \varepsilon \alpha n^2 \tag{1.63}$$

where ε is the energy per electron-ion pair deposited locally in the atmosphere as heat, α is the dissociated recombination coefficient, and n is the electron density.

Maximum auroral energy deposition per unit volume occurs between 100 *km* to 200

km. *Banks* [1977] calculated the atmospheric heating rates associated with Joule heating and particle precipitation using Chatanika (Poker Flat) incoherent scatter radar for two 24 hr azimuthal scan experiments (15-16 April 1973 and 15-16 May 1974). On both days,

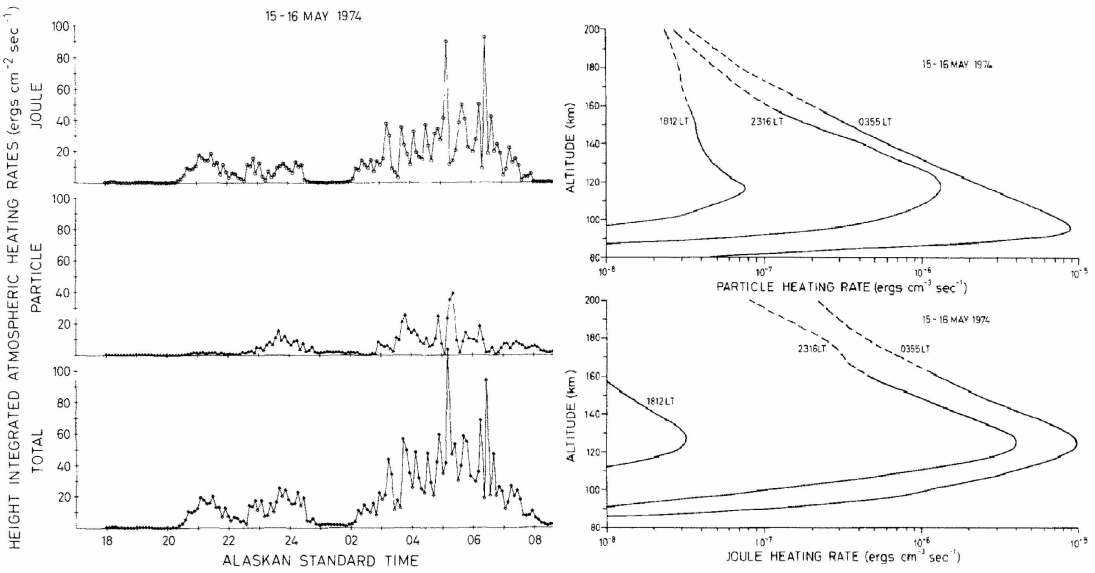

Figure 1.18: Height integrated Joule, particle and total atmospheric heating rates (left) and altitude profile of Joule and particle heating (right) observed with Chatanika (Poker Flat) incoherent scatter radar on 15-16 May 1974 [*Banks*, 1977].

a similar diurnal trend was present in the heating rates. Height integrated (80-200 *km*) Joule heating and particle heating rates for 15-16 May 1974 is shown in Figure 1.18 (left). *Banks* [1977] reported that there is a tendency for height integrated Joule heating rate to be slightly larger than the particle heating rate. The particle precipitation influences the conductivity (by ionizing the neutrals) and hence Joule heating [*Palmroth et al.*, 2006]. *Vickrey et al.* [1982] also used Chatanika incoherent radar and observed that Joule heating generally dominates particle heating in the pre-midnight sector, but daily averages of both are approximately the same. *Banks* [1977] also noted that most of the heating at Chatanika occurred when the radar site was near the auroral oval (1800-0600 Alaska local time). At Chatanika, daytime heating by particle precipitation is not important because this particular site stays equatorward of the auroral oval during the daytime. Figure 1.18 (right) shows example altitude profiles of particle and Joule heating.

Particle heating can at times exceed the Joule heating rate in localized regions within

auroral oval, but over the global scale, Joule heating is more dominant than particle heating. Particle heating occurs mostly in small localized regions of the thermosphere and much more variable than the Joule heating. *Rees and Greenaway* [1983] suggested that particle heating may be the principal cause of the sudden composition changes and temperature enhancements in the non-sunlit polar thermosphere. *Baker et al.* [2004] studied Joule and particle heating rates using Super Dual Auroral Radar Network (SuperDARN) and Global Ultraviolet Imager (GUVI) on the TIMED spacecraft. They found that Joule heating was dominant in the evening sector auroral zone, whereas particle heating was dominant in the morning sector.

1.7.4 Heating by Atmospheric Tides and Gravity Waves

The atmosphere is capable of supporting various types of waves. Atmospheric tides and gravity waves are the most common types of waves that are observed to occur. A brief discussion of tides and gravity waves is given below.

Tides

Oscillations in the atmosphere with time periods that are integral fractions of a lunar or solar day are referred to as "atmospheric tides". An atmospheric tide with 24 hour period is called diurnal tide and with 12 hour period is called semidiurnal tide. An extensive review of atmospheric tides can be found in *Lindzen* [1979]. Atmospheric tides (or solar tides or thermal tides) are primarily forced by the diurnal variation in atmospheric heating by solar radiation. Solar tides drive the basic day-to-night periodic neutral wind circulation, and are generated in-situ in the thermosphere due to the solar heating of O_2 (by the absorption of Schumann-Runge continuum) at 100 *km* to 150 *km* altitude. Such heating of the thermosphere is discussed in the solar heating section 1.7.1. Here we only focus on the energy dissipation by tides and gravity waves traveling to the thermosphere from lower altitudes.

Two modes of tides are observed: migrating and non-migrating. The migrating tides are a function of local time and follow the motion of the sun (that is why they appear to propagate westwards to a stationary ground-based observer), while non-migrating tides

depend on the local time and longitude. A zonally uniform distribution of the absorbing medium around the globe will produce sun synchronous oscillations (migrating tides). Any asymmetry in the longitudinal distribution of absorbing medium will result in non-migrating tides. The migrating solar tides are primarily excited by: 1) solar UV and EUV absorption in the lower and middle thermosphere by O_2 and N_2 (90-200 *km*); 2) absorption of solar radiation by O_3 in the stratosphere (30-60 *km*) and H_2O in the troposphere (0-15 *km*) [*Forbes and Garrett*, 1978, 1979]; and 3) latent heat released by the water content due to deep tropical convection activity in the troposphere [*Lindzen*, 1978; *Forbes and Garrett*, 1979; *Hamilton*, 1981; *Forbes et al.*, 1999]. Any longitudinal asymmetry in the distribution of these sources would excite non-migrating tides (e.g. longitudinal variation in H_2O and O_3 distribution) [*Forbes and Garrett*, 1979; *Williams and Avery*, 1996]. This asymmetry is also caused by the difference in topography (land-sea distribution) with longitude [*Oberheide et al.*, 2006].

At low altitudes, these tides start as small oscillations propagating vertically. With increasing altitude, the oscillation amplitude increases. This is because atmospheric density decreases exponentially with altitude; the oscillation amplitude increases to conserve energy. The amplitude continues to grow until a critical level is reached and wave breaking occur due to convective instability [*Lindzen*, 1981; *Fritts*, 1984]. Their amplitudes can reach more than 50 $m.sec^{-1}$ at mesospheric heights and above. These migrating and non-migrating tides couple the lower atmosphere with the middle and upper atmosphere as they transport heat and horizontal momentum from lower to higher altitudes. *Groves and Forbes* [1985] found that tidal heating was less dominant than solar heating at all higher altitudes (>90 *km*), but below 90 *km*, tidal heating maximizes and solar UV heating become insignificant in comparison. They found global integrated tidal heating of the order of 6×10^9 *Watts* from 150 *km* to 400 *km* and $\sim 7.6 \times 10^{10}$ *Watts* from 90 -150 *km*.

Gravity Waves

A detailed discussion of atmospheric gravity waves is given in *Nappo* [2002]. Gravity waves are oscillations with short horizontal wavelengths (10-1000 *km*) and generated in stably stratified fluid when air parcels are displaced vertically. The buoyancy tries to

restore equilibrium. These waves have oscillations with frequencies less than or equal to the Brunt-Vaisala frequency ω_b given by:

$$\omega_b = \sqrt{\frac{g}{\theta}\frac{\partial\theta}{\partial z}} \tag{1.64}$$

where g is the acceleration due to gravity and θ is called the potential temperature:

$$\theta = T\left(\frac{p_o}{p}\right)^{\frac{\gamma-1}{\gamma}} \tag{1.65}$$

where $\gamma = \frac{C_p}{C_v}$ is the ratio of the specific heat at constant pressure to that at constant volume. θ represents the temperature that an air parcel would have when brought adiabatically to a standard reference pressure p_o. The buoyancy period ($\frac{2\pi}{\omega_b}$) varies with the altitude between approximately 5 min at 100 *km* and up to 25 min in the upper thermosphere [*Yeh and Liu*, 1974].

Upward propagating gravity waves play an important role in dynamics of the mesosphere and above, because they transport significant energy and momentum from high density lower altitudes to the rarefied high altitudes, and then deposit this energy and momentum as they dissipate via viscous or non-linear effects. Depending on the altitude they reach, they can play an important role in plasma and neutral dynamics in the thermosphere. Gravity waves are generated in the troposphere by deep convection, wind flowing over topography, wind shears, front system , or other instabilities. Gravity wave propagation through the atmosphere depends on various factors like wind distribution and thermal structure of the atmosphere. Figure 1.19 shows an example of wave filtering layers in the stratosphere. The wind structure of the stratosphere plays the role of a gravity wave filter, and due to this filtering, gravity waves in mesosphere are eastward propagating in summer and westward propagating in winter. The kinetic energy equation for gravity wave for no damping is:

$$E = \frac{1}{2}\rho|V(z)|^2 \tag{1.66}$$

where $\rho(z)$ is the atmospheric density and $|V(z)|^2$ is the wave amplitude at an altitude z. In the atmosphere, ρ decreases exponentially with z ($\rho = \rho_o \exp(\frac{z}{2H})$). Substituting ρ into

Equation 1.66 and solving for $V(z)$:

$$V(z) = \sqrt{\frac{2E}{\rho_o}} \exp\left(\frac{z}{2H}\right) \tag{1.67}$$

For kinetic energy to remain constant with altitude, the amplitude of the wave must grow exponentially with altitude. At a certain altitude, the amplitude of the gravity wave will grow so large that it will become convectively unstable due to the super adiabatic lapse rate in temperature. This height is the critical height at which wave breaking occurs.

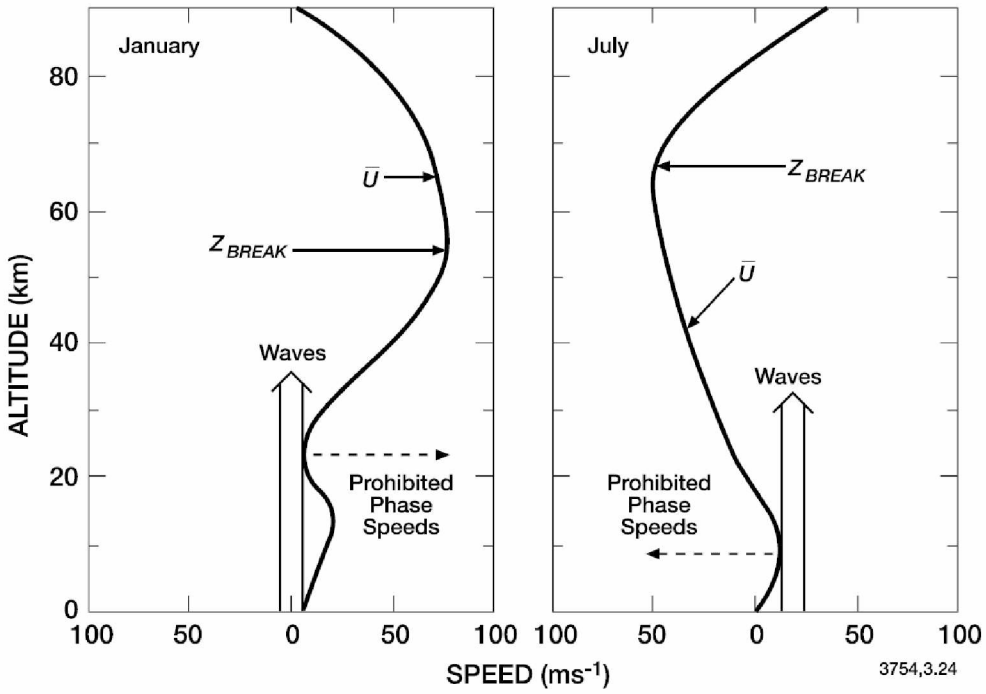

Figure 1.19: Variation of mean zonal winds in winter (left) and summer (right) with altitude. The breaking levels and allowed gravity wave phase speeds are also shown [*Brasseur and Solomon*, 2005].

Most upward traveling gravity waves deposit their energy and momentum in the mesosphere or lower thermosphere, but they can also reach the F-region thermosphere [*Vadas and Fritts*, 2005; *Klostermeyer*, 1969]. *Vadas and Fritts* [2005]; *Klostermeyer* [1969] showed that the gravity waves with high frequencies and larger vertical wavelengths will propagate to higher altitudes because molecular viscosity and thermal diffusivity (which acts as a filter) only allow such gravity waves to propagate higher without dissipation.

Gravity waves dissipating at higher altitudes will have a larger effect on the neutral and plasma dynamics than those that dissipate at lower altitudes because gravity wave momentum fluxes grow exponentially with altitude. Gravity waves with suitable characteristics play an important role in initiating the nighttime equatorial spread F-region plasma bubbles (or equatorial F-region instabilities) [*Hysell et al.*, 1990; *Huang et al.*, 1993; *Sekar et al.*, 1995; *Huang and Kelley*, 1996a,b,c; *Sekar and Kelley*, 1998]. *Hines* [1965] estimated that 50% of the times, an average energy flux of $10^{-4}\ W.m^{-2}$ will reach F-region altitudes. Heat dissipated by gravity waves in the F-region thermosphere estimated by using actual observations of travelling ionospheric disturbances was around $10^{-10}\ W.m^{-3}$ [*Testud*, 1970; *Yeh*, 1972]. They can increase the thermospheric temperatures by 40-80 K [*Klostermeyer*, 1972].

Energy and momentum can be transported within the thermosphere by horizontally propagating gravity waves. Such gravity waves are generated locally in the thermosphere. *Innis and Conde* [2001, 2002] observed gravity waves in vertical thermospheric winds from the DE2 satellite. At high latitudes, it is believed that such gravity waves are excited by the ionospheric processes such as particle precipitation, Joule heating, and Lorentz force associated with auroral electrojets [*Hunsucker*, 1982; *Ford et al.*, 2006] as well as geomagnetic storms and periodic motion of the auroral oval [*Mayr et al.*, 1990; *Innis et al.*, 1996]. These gravity waves play an important role in the dissipating energy from the auroral zone to lower latitudes [*Rees et al.*, 1984a,b].

1.7.5 Thermospheric Cooling

So far we have discussed only the mechanisms that heat the thermosphere, but heat must also be removed in order to maintain thermal equilibrium. Thermospheric heating is primarily balanced by downward molecular heat conduction and radiative cooling. Above 120, heat balance can be written as [*Roble and Emery*, 1983]:

$$C_p \frac{dT_n}{dt} = \frac{d}{dz}\left(K_n \frac{dT_n}{dz} + Q_n - L_n\right) \tag{1.68}$$

where z is the altitude, T_n is the global mean temperature, C_p is the specific heat at constant pressure, K_n is the coefficient of molecular thermal conductivity, Q_n is the mean

global heating rate, and L_n is the radiative cooling rate.

A major source of radiative cooling of the thermosphere (100-240 *km*) is infrared emission at 5.3 μm due to the vibrational transition in nitric oxide molecules [*Gordiets et al.*, 1978; *Kockarts*, 1980]. *NO* vibrational states are excited primarily by collisions with atomic oxygen. Atomic oxygen at 120-180 *km* [*Bates*, 1951; *Craig and Gille*, 1969; *Grossmann and Offermann*, 1978] also contributes in cooling by infrared loss at 6 μm due to transition $O(^3P_1) \rightarrow O(^3P_2)$, but this mechanism is not very efficient. For lower altitudes (90-130 *km*),

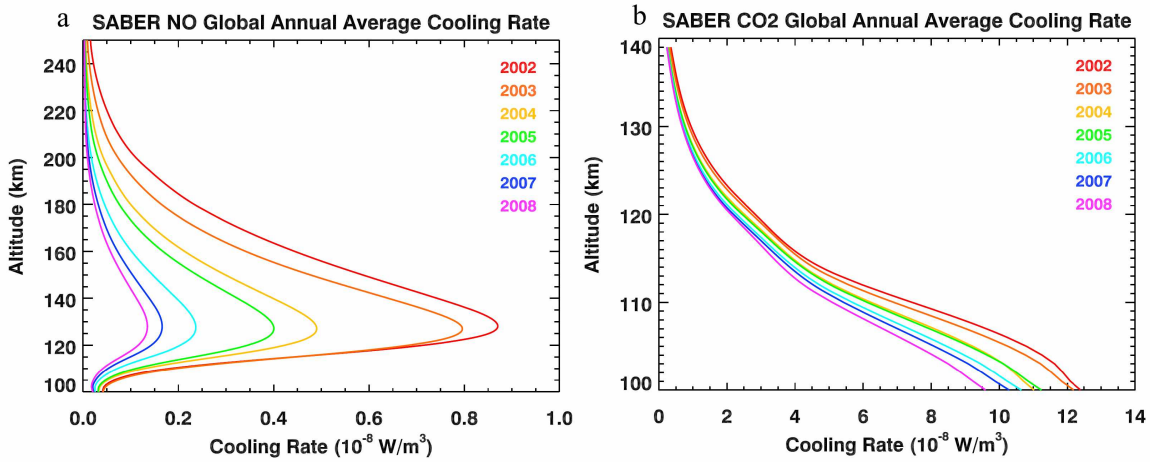

Figure 1.20: Altitude profile of global annual average cooling rate of *NO* (panel a) and CO_2 (panel b) from solar maximum (2002) to solar minimum (2008) derived from the observations of the SABER instrument on the TIMED satellite [*Mlynczak et al.*, 2010].

carbon dioxide (CO_2) [*Curtis and Goody*, 1956] emission at 15 μm is an important source of cooling. *Kockarts* [1980] and *Roble and Emery* [1983] calculated the height profile of the *NO* cooling rates. *Roble and Emery* [1983] showed that cooling by atomic oxygen and *NO* is subtle during a solar minimum. The cooling rate by *NO* is temperature dependent, and the rate of production of *NO* itself is solar activity dependent. A climatological study by *Mlynczak et al.* [2010] used seven years of observations of the radiative cooling in the thermosphere as observed by the SABER instrument on the TIMED mission, to calculate the cooling rates for CO_2 and *NO*. Figure 1.20 shows the global annual average cooling rate profiles for *NO* and CO_2 for solar maximum to solar minimum conditions. They observed that cooling by *NO* was more variable than CO_2 and showed difference latitudinal dependence. They found higher *NO* fluxes and cooling rates at high and polar latitudes.

Maeda et al. [1989] concluded that at high latitudes during aurorally disturbed conditions, predominant cooling occurs during *NO* auroral enhancements.

1.8 References

Aksnes, A., J. Stadsnes, G. Lu, N. Østgaard, R. R. Vondrak, D. L. Detrick, T. J. Rosenberg, G. A. Germany, and M. Schulz (2004), Effects of energetic electrons on the electrodynamics in the ionosphere, *Ann. Geophys.*, *22*(2), 475–496, doi: 10.5194/angeo-22-475-2004.

Aruliah, A. L., E. M. Griffin, A. D. Aylward, E. A. K. Ford, M. J. Kosch, C. J. Davis, V. S. C. Howells, S. E. Pryse, H. R. Middleton, and J. Jussila (2005), First direct evidence of meso-scale variability on ion-neutral dynamics using co-located tristatic FPIs and EISCAT radar in Northern Scandinavia, *Ann. Geophys.*, *23*(1), 147–162, doi: 10.5194/angeo-23-147-2005.

Baker, J. B. H., Y. Zhang, R. A. Greenwald, L. J. Paxton, and D. Morrison (2004), Height-integrated Joule and auroral particle heating in the night side high latitude thermosphere, *Geophys. Res. Lett.*, *31*(9), n/a–n/a, doi: 10.1029/2004GL019535.

Banks, P. (1977), Observations of joule and particle heating in the auroral zone, *J. Atmos. Terr. Phys.*, *39*(2), 179–193, doi: 10.1016/0021-9169(77)90112-X.

Banks, P., and G. Kockarts (1973), *Aeronomy*, 1–31 pp., Elsevier, doi: 10.1016/B978-0-12-077802-7.50006-3.

Bates, D. R. (1951), The Temperature of the Upper Atmosphere, *Proc. Phys. Soc. Sect. B*, *64*(9), 805–821, doi: 10.1088/0370-1301/64/9/312.

Brasseur, G. P., and S. Solomon (2005), *Aeronomy of the Middle Atmosphere, Atmospheric and Oceanographic Sciences Library*, vol. 32, 3 ed., Springer-Verlag, Berlin/Heidelberg, doi: 10.1007/1-4020-3824-0.

Buonsanto, M. J., and T. J. Fuller-Rowell (1997), Strides made in understanding space weather at Earth, *Eos, Trans. Am. Geophys. Union*, *78*(1), 1–7, doi: 10.1029/97eo00002.

Burns, A. G., T. L. Killeen, G. R. Carignan, and R. G. Roble (1995), Large enhancements in the O/N_2 ratio in the evening sector of the winter hemisphere during geomagnetic storms, *J. Geophys. Res.*, *100*(A8), 14,661, doi: 10.1029/94JA03235.

Burns, A. G., W. Wang, S. C. Solomon, and L. Qian (2013), Energetics and composition in the thermosphere, *Geophys. Monogr. Ser.*, *201*, 39–48, doi: 10.1029/2012GM001292.

Cai, L., A. T. Aikio, and T. Nygrén (2014), Solar wind effect on Joule heating in the high-latitude ionosphere, *J. Geophys. Res. Sp. Phys.*, *119*(12), 10,440–10,455, doi: 10.1002/2014JA020269.

Christensen, A. B., J. H. Hecht, R. L. Walterscheid, M. F. Larsen, and W. E. Sharp (1997), Depletion of oxygen in aurora: Evidence for a local mechanism, *J. Geophys. Res.*, *102*(A10), 22,273, doi: 10.1029/97JA01800.

Codrescu, M. V., T. J. Fuller-Rowell, and J. C. Foster (1995), On the importance of E-field variability for Joule heating in the high-latitude thermosphere, *Geophys. Res. Lett.*, *22*(17), 2393–2396, doi: 10.1029/95GL01909.

Cole, K. (1962), Joule Heating of the Upper Atmosphere, *Aust. J. Phys.*, *15*(2), 223, doi: 10.1071/PH620223.

Conde, M., C. Anderson, T. Davies, P. Dyson, and M. Kosch (2011), Ground-based doppler mapping of thermospheric wind and temperature fields with very high Spatial resolution, *CEDAR, POLA-10*.

Cosgrove, R. B., and J. P. Thayer (2006), Parametric dependence of electric field variability in the Sondrestrom database: A linear relation with Kp, *J. Geophys. Res.*, *111*(A10), A10,313, doi: 10.1029/2006JA011658.

Craig, R. A., and J. C. Gille (1969), Cooling of the Thermosphere by Atomic Oxygen, *J. Atmos. Sci.*, *26*(2), 205–209, doi: 10.1175/1520-0469(1969)026<0205:COTTBA>2.0.CO;2.

Craven, J. D., A. C. Nicholas, L. A. Frank, D. J. Strickland, and T. J. Immel (1994), Variations in the FUV dayglow after intense auroral activity, *Geophys. Res. Lett.*, *21*(25), 2793–2796, doi: 10.1029/94GL02458.

Crowley, G., and R. R. Meier (2013), Disturbed O/N_2 ratios and their transport to middle and low latitudes, *Midlatitude Ionos. Dyn. Disturbances*, *181*, 221–234, doi: 10.1029/181gm20.

Crowley, G., B. A. Emery, R. G. Roble, H. C. Carlson, and D. J. Knipp (1989a), Thermospheric dynamics during September 18-19, 1984: 1. Model simulations, *J. Geophys. Res.*, *94*(A12), 16,925, doi: 10.1029/JA094iA12p16925.

Crowley, G., B. A. Emery, R. G. Roble, H. C. Carlson, J. E. Salah, V. B. Wickwar, K. L. Miller, W. L. Oliver, R. G. Burnside, and F. A. Marcos (1989b), Thermospheric dynamics during September 18-19, 1984: 2. Validation of the NCAR Thermospheric General Circulation Model, *J. Geophys. Res.*, *94*(A12), 16,945, doi: 10.1029/JA094iA12p16945.

Curtis, A. R., and R. M. Goody (1956), Thermal Radiation in the Upper Atmosphere, *Proc. R. Soc. A Math. Phys. Eng. Sci.*, *236*(1205), 193–206, doi: 10.1098/rspa.1956.0128.

Deng, Y., and A. J. Ridley (2007), Possible reasons for underestimating Joule heating in global models: E field variability, spatial resolution, and vertical velocity, *J. Geophys. Res.*, *112*(A9), A09,308, doi: 10.1029/2006JA012006.

Forbes, J., M. Hagan, X. Zhang, and J. Hackney (1999), Upper atmosphere tidal variability due to latent heat release in the tropical troposphere, *Adv. Sp. Res.*, *24*(11), 1515–1521, doi: 10.1016/S0273-1177(99)00873-X.

Forbes, J. M., and H. B. Garrett (1978), Thermal excitation of atmospheric tides due to insolation absorption by O_3 and H_2O, *Geophys. Res. Lett.*, *5*(12), 1013–1016, doi: 10.1029/GL005i012p01013.

Forbes, J. M., and H. B. Garrett (1979), Theoretical studies of atmospheric tides, *Rev. Geophys.*, *17*(8), 1951, doi: 10.1029/RG017i008p01951.

Ford, E. A. K., A. L. Aruliah, E. M. Griffin, and I. McWhirter (2006), Thermospheric gravity waves in Fabry-Perot interferometer measurements of the 630.0 nm OI line, *Ann. Geophys.*, *24*(2), 555–566, doi: 10.5194/angeo-24-555-2006.

Foster, J. C., J.-P. St.-Maurice, and V. J. Abreu (1983), Joule heating at high latitudes, *J. Geophys. Res.*, *88*(A6), 4885, doi: 10.1029/JA088iA06p04885.

Fritts, D. C. (1984), Gravity wave saturation in the middle atmosphere: A review of theory and observations, *Rev. Geophys.*, *22*(3), 275, doi: 10.1029/RG022i003p00275.

Fuller-Rowell, T. J. (1995), The dynamics of the lower thermosphere, *Geophys. Monogr. Ser.*, *87*, 23–36.

Fuller-Rowell, T. J., M. V. Codrescu, H. Rishbeth, R. J. Moffett, and S. Quegan (1996), On the seasonal response of the thermosphere and ionosphere to geomagnetic storms, *J. Geophys. Res.*, *101*(A2), 2343, doi: 10.1029/95JA01614.

Gordiets, B., M. Markov, and L. Shelepin (1978), I.R. Radiation of the upper atmosphere, *Planet. Sp. Sci.*, *26*(10), 933–948, doi: 10.1016/0032-0633(78)90076-4.

Grossmann, K. U., and D. Offermann (1978), Atomic oxygen emission at 63 micrometer as a cooling mechanism in the thermosphere and ionosphere, *Nature*, *276*(5688), 594–595, doi: 10.1038/276594a0.

Groves, G., and J. Forbes (1985), Mean zonal and meridional accelerations and mean heating induced by solar tides for equinox and solstice conditions, *Planet. Sp. Sci.*, *33*(3), 283–293, doi: 10.1016/0032-0633(85)90060-1.

Hamilton, K. (1981), Latent Heat Release as a Possible Forcing Mechanism for Atmospheric Tides, *Mon. Weather Rev.*, *109*(1), 3–17, doi: 10.1175/1520-0493(1981)109.

Hargraves, R. B. (1995), The Solar-terrestrial Environment: An Introduction to Geospace, *Cambridge Univ. Press*.

Hays, P., R. Jones, and M. Rees (1973), Auroral heating and the composition of the neutral atmosphere, *Planet. Sp. Sci.*, *21*(4), 559–573, doi: 10.1016/0032-0633(73)90070-6.

Hays, P. B., J. W. Meriwether, and R. G. Roble (1979), Nighttime thermospheric winds at high latitudes, *J. Geophys. Res. Sp. Phys.*, *84*(A5), 1905–1913, doi: 10.1029/JA084iA05p01905.

Hays, P. B., T. L. Killeen, N. W. Spencer, L. E. Wharton, R. G. Roble, B. A. Emery, T. J. Fuller-Rowell, D. Rees, L. A. Frank, and J. D. Craven (1984), Observations of the dynamics of the polar thermosphere, *J. Geophys. Res. Sp. Phys.*, *89*(A7), 5597–5612, doi: 10.1029/JA089iA07p05597.

Hedin, A. E., M. A. Biondi, R. G. Burnside, G. Hernandez, R. M. Johnson, T. L. Killeen, C. Mazaudier, J. W. Meriwether, J. E. Salah, R. J. Sica, R. W. Smith, N. W. Spencer, V. B. Wickwar, and T. S. Virdi (1991), Revised global model of thermosphere winds using satellite and ground-based observations, *J. Geophys. Res.*, *96*(A5), 7657, doi: 10.1029/91JA00251.

Hernandez, G., and R. G. Roble (1995), Thermospheric nighttime neutral temperature and winds over Fritz Peak Observatory: Observed and calculated solar cycle variation, *J. Geophys. Res.*, *100*(A8), 14,647, doi: 10.1029/95JA00565.

Hines, C. O. (1965), Dynamical heating of the upper atmosphere, *J. Geophys. Res.*, *70*(1), 177–183, doi: 10.1029/JZ070i001p00177.

Huang, C., and M. C. Kelley (1996a), Nonlinear evolution of equatorial spread F : 1. On the role of plasma instabilities and spatial resonance associated with gravity wave seeding, *J. Geophys. Res.*, *101*(A1), 283, doi: 10.1029/95JA02211.

Huang, C., and M. C. Kelley (1996b), Nonlinear evolution of equatorial spread F : 2. Gravity wave seeding of Rayleigh-Taylor instability, *J. Geophys. Res.*, *101*(A1), 293, doi: 10.1029/95JA02210.

Huang, C., and M. C. Kelley (1996c), Nonlinear evolution of equatorial spread F : 4. Gravity waves, velocity shear, and day-to-day variability, *J. Geophys. Res.*, *101*(A11), 24,521, doi: 10.1029/96JA02332.

Huang, C., M. C. Kelley, and D. L. Hysell (1993), Nonlinear Rayleigh-Taylor instabilities, atmospheric gravity waves and equatorial spread F, *J. Geophys. Res.*, *98*(A9), 15,631, doi: 10.1029/93JA00762.

Hunsucker, R. D. (1982), Atmospheric gravity waves generated in the high-latitude ionosphere: A review, *Rev. Geophys.*, *20*(2), 293, doi: 10.1029/RG020i002p00293.

Hysell, D. L., M. C. Kelley, W. E. Swartz, and R. F. Woodman (1990), Seeding and layering of equatorial spread F by gravity waves, *J. Geophys. Res.*, *95*(A10), 17,253, doi: 10.1029/JA095iA10p17253.

Immel, T., J. Craven, and L. Frank (1997), Influence of IMF By on large-scale decreases of O column density at middle latitudes, *J. Atmos. Sol. Terr. Phys.*, *59*(6), 725–737, doi: 10.1016/S1364-6826(96)00099-5.

Immel, T. J., G. Crowley, J. D. Craven, and R. G. Roble (2001), Dayside enhancements of thermospheric O/N_2 following magnetic storm onset, *J. Geophys. Res.*, *106*(A8), 15,471, doi: 10.1029/2000JA000096.

Innis, J., P. Greet, and P. Dyson (1996), Fabry-Perot spectrometer observations of the auroral oval/polar cap boundary above Mawson, Antarctica, *J. Atmos. Terr. Phys.*, *58*(16), 1973–1988, doi: 10.1016/0021-9169(96)00007-4.

Innis, J. L., and M. Conde (2001), Thermospheric vertical wind activity maps derived from Dynamics Explorer-2 WATS observations, *Geophys. Res. Lett.*, *28*(20), 3847–3850, doi: 10.1029/2001GL013704.

Innis, J. L., and M. Conde (2002), High-latitude thermospheric vertical wind activity from Dynamics Explorer 2 Wind and Temperature Spectrometer observations: Indications of a source region for polar cap gravity waves, *J. Geophys. Res.*, *107*(A8), 1172, doi: 10.1029/2001JA009130.

Kelly, M. C. (1989), *The Earth's Ionosphere: Plasma Physics & Electrodynamics*, vol. 43, Academic Press.

Killeen, T. L. (1987), Energetics and dynamics of the Earth's thermosphere, *Rev. Geophys.*, *25*(3), 433–454.

Killeen, T. L., and R. G. Roble (1984), An analysis of the high-latitude thermospheric wind pattern calculated by a thermospheric general circulation model: 1. Momentum forcing, *J. Geophys. Res.*, *89*(A9), 7509–7522.

Killeen, T. L., and R. G. Roble (1988), Thermosphere dynamics: Contributions from the first 5 years of the Dynamics Explorer Program, *Rev. Geophys.*, *26*(2), 329–367, doi: 10.1029/RG026i002p00329.

Killeen, T. L., P. B. Hays, N. W. Spencer, and L. E. Wharton (1982), Neutral winds in the polar thermosphere as measured from Dynamics Explorer, *Geophys. Res. Lett.*, *9*(9), 957–960, doi: 10.1029/GL009i009p00957.

Killeen, T. L., P. B. Hays, G. R. Carignan, R. A. Heelis, W. B. Hanson, N. W. Spencer, and L. H. Brace (1984), Ion-neutral coupling in the high-latitude F region: Evaluation of ion heating terms from Dynamics Explorer 2, *J. Geophys. Res.*, *89*(A9), 7495, doi: 10.1029/JA089iA09p07495.

Klostermeyer, J. (1969), Gravity waves in the F-region, *J. Atmos. Terr. Phys.*, *31*(1), 25–45, doi: 10.1016/0021-9169(69)90079-8.

Klostermeyer, J. (1972), Influence of viscosity, thermal conduction, and ion drag on the propagation of atmospheric gravity waves in the thermosphere, *Zeitschr. Geophys.*, *38*, 881–890.

Kockarts, G. (1980), Nitric oxide cooling in the terrestrial thermosphere, *Geophys. Res. Lett.*, *7*(2), 137–140, doi: 10.1029/GL007i002p00137.

Kosch, M. J., and E. Nielsen (1995), Coherent radar estimates of average high-latitude ionospheric Joule heating, *J. Geophys. Res.*, *100*(A7), 12,201, doi: 10.1029/95JA00821.

Lindzen, R. S. (1978), Effect of Daily Variations of Cumulonimbus Activity on the Atmospheric Semidiurnal Tide, *Mon. Weather Rev.*, *106*(4), 526–533, doi: 10.1175/1520-0493.

Lindzen, R. S. (1979), Atmospheric Tides, *Annu. Rev. Earth Planet. Sci.*, *7*(1), 199–225, doi: 10.1146/annurev.ea.07.050179.001215.

Lindzen, R. S. (1981), Turbulence and stress owing to gravity wave and tidal breakdown, *J. Geophys. Res.*, *86*(C10), 9707, doi: 10.1029/JC086iC10p09707.

Liou, K. N. (2002), *An Introduction to Atmospheric Radiation*, 583 pp., Academic Press.

Lyons, L. R., T. L. Killeen, and R. L. Walterscheid (1985), The neutral wind "flywheel" as a source of quiet-time, polar-cap currents, *Geophys. Res. Lett.*, *12*(2), 101–104, doi: 10.1029/GL012i002p00101.

Maeda, K.-I. (1977), Conductivity and drifts in the ionosphere, *J. Atmos. Terr. Phys.*, *39*(9-10), 1041–1053, doi: 10.1016/0021-9169(77)90013-7.

Maeda, S., T. J. Fuller-Rowell, and D. S. Evans (1989), Zonally averaged dynamical and compositional response of the thermosphere to auroral activity during September 18 -24, 1984, *J. Geophys. Res.*, *94*(A12), 16,869, doi: 10.1029/JA094iA12p16869.

Mayr, H., I. Harris, F. Herrero, N. Spencer, F. Varosi, and W. Pesnell (1990), Thermospheric gravity waves: Observations and interpretation using the transfer function model (TFM), *Space Sci. Rev.*, *54*(3-4), doi: 10.1007/BF00177800.

McCormac, B. (1974), Atmosphere of Earth and the Planets, *Proc. summer Adv. study institute, held Univ. Liege, Belgium*, p. 461.

Meriwether, J. W., J. P. Heppner, J. D. Stolarik, and E. M. Wescott (1973), Neutral winds above 200 km at high latitudes, *J. Geophys. Res.*, *78*(28), 6643–6661, doi: 10.1029/JA078i028p06643.

Mikkelsen, I. S., T. S. Jørgensen, M. C. Kelley, M. F. Larsen, E. Pereira, and J. Vickrey (1981), Neutral winds and electric fields in the dusk auroral oval 1. Measurements, *J. Geophys. Res.*, *86*(A3), 1513, doi: 10.1029/JA086iA03p01513.

Mlynczak, M. G., L. A. Hunt, B. Thomas Marshall, F. J. Martin-Torres, C. J. Mertens, J. M. Russell, E. E. Remsberg, M. López-Puertas, R. Picard, J. Winick, P. Wintersteiner, R. E. Thompson, and L. L. Gordley (2010), Observations of infrared radiative cooling in the thermosphere on daily to multiyear timescales from the TIMED/SABER instrument, *J. Geophys. Res.*, *115*(A3), A03,309, doi: 10.1029/2009JA014713.

Nagy, A. F., R. J. Cicerone, P. B. Hays, K. D. McWatters, J. W. Meriwether, A. E. Belon, and C. L. Rino (1974), Simultaneous measurement of ion and neutral motions by radar and optical techniques, *Radio Sci.*, *9*(2), 315–321, doi: 10.1029/RS009i002p00315.

Nappo, C. J. (2002), *An Introduction to Atmospheric Gravity Waves*, 276 pp., Academic Press.

Nicholas, A. C., J. D. Craven, and L. A. Frank (1997), A survey of large-scale variations in thermospheric oxygen column density with magnetic activity as inferred from observations of the FUV dayglow, *J. Geophys. Res.*, *102*(A3), 4493, doi: 10.1029/96JA03464.

Oberheide, J., Q. Wu, T. L. Killeen, M. E. Hagan, and R. G. Roble (2006), Diurnal nonmigrating tides from TIMED Doppler Interferometer wind data: Monthly climatologies and seasonal variations, *J. Geophys. Res.*, *111*(A10), A10S03, doi: 10.1029/2005JA011491.

Olsson, A., P. Janhunen, T. Karlsson, N. Ivchenko, and L. G. Blomberg (2004), Statistics of Joule heating in the auroral zone and polar cap using Astrid-2 satellite Poynting flux, *Ann. Geophys.*, *22*(12), 4133–4142, doi: 10.5194/angeo-22-4133-2004.

Østgaard, N., G. A. Germany, J. Stadsnes, and R. R. Vondrak (2002), Energy analysis of substorms based on remote sensing techniques, solar wind measurements, and geomagnetic indices, *J. Geophys. Res.*, *107*(A9), 1233, doi: 10.1029/2001JA002002.

Pallamraju, D. (2005), First ground-based measurements of OI 6300 Å daytime aurora over Boston in response to the 30 October 2003 geomagnetic storm, *Geophys. Res. Lett.*, *32*(3), L03S10, doi: 10.1029/2004GL021417.

Palmroth, M., P. Janhunen, G. Germany, D. Lummerzheim, K. Liou, D. N. Baker, C. Barth, A. T. Weatherwax, and J. Watermann (2006), Precipitation and total power consumption in the ionosphere: Global MHD simulation results compared with Polar and SNOE observations, *Ann. Geophys.*, *24*(3), 861–872, doi: 10.5194/angeo-24-861-2006.

Prölss, G. W. (1980), Magnetic storm associated perturbations of the upper atmosphere: Recent results obtained by satellite-borne gas analyzers, *Rev. Geophys.*, *18*(1), 183, doi: 10.1029/RG018i001p00183.

Qian, L., R. G. Roble, S. C. Solomon, and T. J. Kane (2006), Calculated and observed climate change in the thermosphere, and a prediction for solar cycle 24, *Geophys. Res. Lett.*, *33*(23), L23,705, doi: 10.1029/2006GL027185.

Rees, D. (1971), Ionospheric wind in auroral zone, *J. Br. Interpanet. Soc*, *24*, 233–246.

Rees, D., and T. J. Fuller-Rowell (1989), Seasonal and geomagnetic response of the thermosphere and ionosphere, *42 AGARD Symp. Ionos. Struct. Var. a Glob. Scale Interact. with Atmos. Magnetos.*

Rees, D., and A. H. Greenaway (1983), Doppler imaging system: an optical device for measuring vector winds. 1: General principles., *Appl. Opt.*, *22*(7), 1078–83.

Rees, D., R. Smith, P. Charleton, F. McCormac, N. Lloyd, and A. Steen (1984a), The generation of vertical thermospheric winds and gravity waves at auroral latitudes-I. Observations of vertical winds, *Planet. Sp. Sci.*, *32*(6), 667–684, doi: 10.1016/0032-0633(84)90092-8.

Rees, D., M. Smith, and R. Gordon (1984b), The generation of vertical thermospheric winds and gravity waves at auroral latitudes-II. Theory and numerical modelling of vertical winds, *Planet. Sp. Sci.*, *32*(6), 685–705, doi: 10.1016/0032-0633(84)90093.

Rees, M. H. (1989), *Physics and Chemistry of the Upper Atmosphere*, Cambridge University Press, Cambridge, doi: 10.1017/CBO9780511573118.

Rishbeth, H., and O. K. Garriott (1969), *Introduction to ionospheric physics*.

Roble, R., and B. Emery (1983), On the global mean temperature of the thermosphere, *Planet. Sp. Sci.*, *31*(6), 597–614, doi: 10.1016/0032-0633(83)90002-8.

Roble, R. G., R. E. Dickinson, and E. C. Ridley (1982), Global circulation and temperature structure of thermosphere with high-latitude plasma convection, *J. Geophys. Res. Sp. Phys.*, *87*(A3), 1599–1614, doi: 10.1029/JA087iA03p01599.

Roble, R. G., E. C. Ridley, and R. E. Dickinson (1987), On the global mean structure of the thermosphere, *J. Geophys. Res.*, *92*(A8), 8745–8758, doi: 10.1029/JA092iA08p08745.

Sekar, R., and M. C. Kelley (1998), On the combined effects of vertical shear and zonal electric field patterns on nonlinear equatorial spread F evolution, *J. Geophys. Res.*, *103*(A9), 20,735, doi: 10.1029/98JA01561.

Sekar, R., R. Suhasini, and R. Raghavarao (1995), Evolution of plasma bubbles in the equatorial F region with different seeding conditions, *Geophys. Res. Lett.*, *22*(8), 885–888, doi: 10.1029/95GL00813.

Spencer, N. W., L. E. Wharton, G. R. Carignan, and J. C. Maurer (1982), Thermosphere zonal winds, vertical motions and temperature as measured from Dynamics Explorer, *Geophys. Res. Lett.*, *9*(9), 953–956, doi: 10.1029/GL009i009p00953.

Strickland, D. J., R. J. Cox, R. R. Meier, and D. P. Drob (1999), Global O/N_2 derived from DE 1 FUV dayglow data: Technique and examples from two storm periods, *J. Geophys. Res.*, *104*(A3), 4251, doi: 10.1029/98JA02817.

Strickland, D. J., R. R. Meier, R. L. Walterscheid, J. D. Craven, A. B. Christensen, L. J. Paxton, D. Morrison, and G. Crowley (2004), Quiet-time seasonal behavior of the thermosphere seen in the far ultraviolet dayglow, *J. Geophys. Res.*, *109*(A1), A01,302, doi: 10.1029/2003JA010220.

Testud, J. (1970), Gravity waves generated during magnetic substorms, *J. Atmos. Terr. Phys.*, *32*(11), 1793–1805, doi: 10.1016/0021-9169(70)90137-6.

Thayer, J. P. (1998), Height-resolved Joule heating rates in the high-latitude E region and the influence of neutral winds, *J. Geophys. Res.*, *103*(A1), 471, doi: 10.1029/97JA02536.

Vadas, S. L., and D. C. Fritts (2005), Thermospheric responses to gravity waves arising from mesoscale convective complexes, *J. Atmos. Sol. Terr. Phys.*, *66*(6-9), 781–804, doi: 10.1016/j.jastp.2004.01.025.

Vickrey, J. F., R. R. Vondrak, and S. J. Matthews (1982), Energy deposition by precipitating particles and Joule dissipation in the auroral ionosphere, *J. Geophys. Res.*, *87*(A7), 5184, doi: 10.1029/JA087iA07p05184.

Wang, W., T. Killeen, A. Burns, and R. Roble (1999), A high-resolution, three-dimensional, time dependent, nested grid model of the coupled thermosphere-ionosphere, *J. Atmos. Sol. Terr. Phys.*, *61*(5), 385–397, doi: 10.1016/S1364-6826(98)00079-0.

Weimer, D. R. (1995), Models of high-latitude electric potentials derived with a least error fit of spherical harmonic coefficients, *J. Geophys. Res.*, *100*(A10), 19,595, doi: 10.1029/95JA01755.

Whitten, R. C., and I. G. Poppoff (1971), *Fundamentals of Aeronomy*, John Wiley & Sons, Inc.

Williams, C. R., and S. K. Avery (1996), Diurnal nonmigrating tidal oscillations forced by deep convective clouds, *J. Geophys. Res.*, *101*(D2), 4079, doi: 10.1029/95JD03007.

Woods, T. N., S. Solomon, and S. Bailey (2001), Solar EUV and X-ray irradiance: Recent results and new prospects, *Am. Geophys. Union (Fall Meet.*, doi: SA41C-08.

Yeh, K. C. (1972), Traveling ionospheric disturbance as a diagnostic tool for thermospheric dynamics, *J. Geophys. Res.*, *77*(4), 709–719, doi: 10.1029/JA077i004p00709.

Yeh, K. C., and C. H. Liu (1974), Acoustic-gravity waves in the upper atmosphere, *Rev. Geophys.*, *12*(2), 193, doi: 10.1029/RG012i002p00193.

Zhang, S. P., and G. G. Shepherd (2004), Solar influence on the O(1D) dayglow emission rate: Global-scale measurements by WINDII on UARS, *Geophys. Res. Lett.*, *31*(7), 1–4, doi: 10.1029/2004GL019447.

Chapter 2
Dynamics of Earth's Upper Atmosphere

2.1 Introduction

The dynamics of Earth's upper atmosphere has attracted considerable theoretical and experimental research for many decades. Studies of upper atmospheric winds started with the observations of chemical trails left by rockets [*Rees*, 1971; *Meriwether et al.*, 1973; *Mikkelsen et al.*, 1981; *Heppner and Miller*, 1982; *Biondi and Sipler*, 1984]. A number of other new instruments and techniques have been devised to study thermospheric wind dynamics including Fabry-Perot spectrometers [*Hernandez and Roble*, 1976; *Hays et al.*, 1979; *Jacka et al.*, 1980; *Sipler et al.*, 1995, 1982; *Rees and Greenaway*, 1983; *Rees et al.*, 1984a; *Burnside and Tepley*, 1989; *Biondi et al.*, 1995; *Conde and Dyson*, 1995a,b; *Nakajima et al.*, 1995], incoherent scatter radars [*Salah and Holt*, 1974; *Wickwar et al.*, 1984; *Buonsanto et al.*, 1989], satellites [*Killeen et al.*, 1982, 1985, 1986; *Hays et al.*, 1984; *Killeen and Roble*, 1988; *Thayer and Killeen*, 1991; *Conde et al.*, 2001], physics-based global thermospheric circulation models [*Geisler*, 1967; *Kohl and King*, 1967; *Fuller-Rowell and Rees*, 1980; *Dickinson et al.*, 1981, 1984; *Richmond et al.*, 1992; *Wang et al.*, 1999; *Ridley et al.*, 2006], and global empirical models such as the horizontal wind model [*Hedin et al.*, 1988, 1991; *Drob et al.*, 2008, 2015; *Emmert et al.*, 2008]. In this chapter, first we will discuss in details of the upper atmospheric winds including their local-scale variability, especially at high latitudes. Second, we will discuss the basic airglow and auroral emissions from the upper atmospheric species and how these emissions are used to infer various geophysical quantities such as winds and temperatures that describe the dynamical state of the upper atmosphere. Finally, we will review numerical modeling studies of the upper atmosphere and discuss various physics-based and empirical models.

2.2 Horizontal Neutral Winds

2.2.1 Basic Drivers

Neutral air parcel motion in the upper atmosphere is predominantly driven by solar heating caused by EUV and UV radiation ($1 < \lambda < 200$ *nm*). This heating results in day-to-night

temperature differences of ~200 K during solar minimum and ~350 K during solar maximum [*Jacchia*, 1965; *Hedin*, 1987]. This solar heating causes thermal expansion of the sunlit part of the thermosphere and develops dayside-to-nightside horizontal solar pressure gradient which in turn drives a horizontal antisunward (day-to-night) tidal wind circulation [e.g., *Kohl and King*, 1967; *Killeen*, 1987]. The solar pressure gradient is also called the "pressure bulge" and the wind circulation driven by it is an example of a "solar thermal tide". At lower altitudes in the thermosphere, atmospheric tides, gravity waves, and inertial forces (e.g., Coriolis force and centrifugal force) play an important role in disturbing the day-to-night pressure driven neutral air parcel flow. However, at higher altitudes, their contribution become negligent.

The thermosphere is commingled with a weakly ionized plasma with an embedded magnetic field. If no other forcing is present, plasma motion would be constrained by the Earth's magnetic field. At high latitudes, ionospheric plasma is primarily driven by the combined effect of the convection electric field generated by solar wind ($\boldsymbol{E}_{sw} = -\boldsymbol{V}_{sw} \times \boldsymbol{B}_{sw}$) mapped down along magnetic field lines from the magnetosphere and the geomagnetic field (details discussed in Joule heating section 1.7.2 of chapter 1). During southward interplanetary magnetic field (IMF), the ionospheric plasma is driven in antisunward across the polar cap by the dawn to dusk electric field. Due to the return flow at lower latitudes, plasma drifting along $\boldsymbol{E} \times \boldsymbol{B}$ forms a two cell convection pattern [*Kelly*, 1989] (details discussed in Joule heating section 1.7.2 of chapter 1).

In the thermosphere, momentum exchange between convecting ions and the neutral gas due to collisions is sufficient to generate a momentum source for neutrals known as ion-drag that can be comparable for even greater in strength than other forces acting on thermospheric air parcels. At high latitudes, ionospheric plasma convection can significantly modify the pressure gradient driven neutral wind flow [e.g., *Roble et al.*, 1982; *Killeen and Roble*, 1988; *Thayer and Killeen*, 1993]. As a result, F-region high latitude thermospheric neutral winds tend to follow a similar pattern that of the convecting plasma and establish a twin cell circulation [*Killeen et al.*, 1982] with dawn and dusk circulation cells. There is always a time lag involved in the momentum transfer from ions to the neutrals which is primarily dependent on the local ion density [*Deng and Ridley*, 2007]. This

time lag varies in the range 0.5 - 6 hours and varies with the geomagnetic activity [*Kosch et al.*, 2001]. An average time lag is ~2 hours for a geomagnetic active and ~3 hours for a geomagnetic quiet period [*Kosch et al.*, 2001]. In practice, the response time at auroral latitudes is often 30 min or less. If neutral air parcels spend sufficient time in the convection region for effective momentum transfer to occur, then they will adopt a flow similar to that of the ion convection. The neutral winds can sustain this flow pattern even long after ionospheric forcing dies down [*Lyons et al.*, 1985]. Although the ionosphere comprises less than one percent of the mass of the upper atmosphere, it has a significant influence on thermospheric dynamics.

High latitude thermospheric wind patterns are dominated by antisunward flow over the polar cap. It is commonly observed that the thermospheric duskside circulation cell is always stronger than the dawnside circulation cell. This is because the Coriolis force acts against counterclockwise rotation in the dawn circulation cell and hence diminishes the vorticity of the dawn circulation cell in the northern hemisphere [*Killeen et al.*, 1984].

Magnetospheric convection provides an energy source (Joule heating and particle heating) and momentum source (ion drag) for the neutral atmosphere. Overall, high latitude thermospheric neutral winds are primarily controlled by the combination of the heating induced pressure gradient (solar heating and Joule heating), momentum exchange between neutrals and the convecting ions (ion drag), and inertial forces [*Kwak and Richmond*, 2007]. The time varying interplay between these drivers results in highly complex thermospheric wind circulation patterns. At higher altitudes, the neutral wind flow is shaped primarily by the interplay between ion drag and heating induced pressure gradient (solar heating and Joule heating); the contribution from inertial forces is small. However, at lower altitudes (for example in the lower thermosphere), tidal and Coriolis forces become increasingly dominant compared to ion drag [*Killeen et al.*, 1984]. Both rocket campaigns and unpublished Scanning Doppler Imager (SDI) data from Poker Flat at 557.7 *nm* show ion drag can be important down to as low as 120 *km*.

2.2.2 Dependence on IMF and Geomagnetic Activity

During disturbed geomagnetic conditions, a large amount of energy is released from the magnetosphere into the auroral thermosphere. Feedback from the thermospheric response in turn enhances the electric fields and auroral particle precipitation. The increased particle precipitation enhances the conductivity of thermosphere by heating and ionization [*Buonsanto and Fuller-Rowell*, 1997]. These augmented electric fields and conductivity intensify the Joule heating (details discussed in Joule heating section 1.7.2 of chapter 1) of the thermosphere from tens of gigawatts (quiet time) to hundreds of gigawatts (severe geomagnetic disturbances). Unsurprisingly, the neutral wind flow is significantly affected [*Buonsanto and Fuller-Rowell*, 1997; *Wang et al.*, 1999].

Ionospheric convection and Joule heating both have strong dependence on the orientation of the interplanetary magnetic field (IMF) and geomagnetic activity [*Cowley et al.*, 1991; *Heppner*, 1972; *Foster et al.*, 1983; *McCormac and Smith*, 1984; *Burch et al.*, 1985; *Heppner and Maynard*, 1987; *Kosch and Nielsen*, 1995; *Weimer*, 1999, 2001; *Papitashvili and Rich*, 2002; *McHarg*, 2005; *Ruohoniemi and Greenwald*, 2005]. Ionospheric convection can expand to lower latitudes with increasing geomagnetic activity. There can also be more than two convection cells depending on the configuration of the IMF [*Kelly*, 1989]. Neutral wind circulation and ionospheric convection are coupled via momentum exchange between ions are neutrals [*Killeen et al.*, 1984; *Thayer and Killeen*, 1993], therefore, any change in the IMF and geomagnetic activity can significantly modify the neutral wind pattern at high latitudes [*Killeen et al.*, 1982, 1985, 1995; *McCormac and Smith*, 1984; *McCormac et al.*, 1985, 1987; *Rees et al.*, 1986; *Sica et al.*, 1986a, 1989; *Meriwether and Shih*, 1987; *Mccormac et al.*, 1991; *Hernandez et al.*, 1991; *Niciejewski et al.*, 1992, 1996; *Richmond et al.*, 2003; *Emmert et al.*, 2006a,b, 2008; *Kwak and Richmond*, 2007, 2014]. There is a time lag involved in the momentum transfer from ions to neutral that is dependent on the local ion density [*Kosch et al.*, 2001; *Deng and Ridley*, 2007], so neutrals are not expected to replicate the changes in ion convection instantaneously or even exactly. The time lag implies that the neutral response will be a smoothed version of the ion convection. Under active geomagnetic conditions, the thermospheric circulation cells (dawn and dusk) expand to lower latitudes. With increasing geomagnetic activity, polar cap antisunward wind speeds and return flow wind

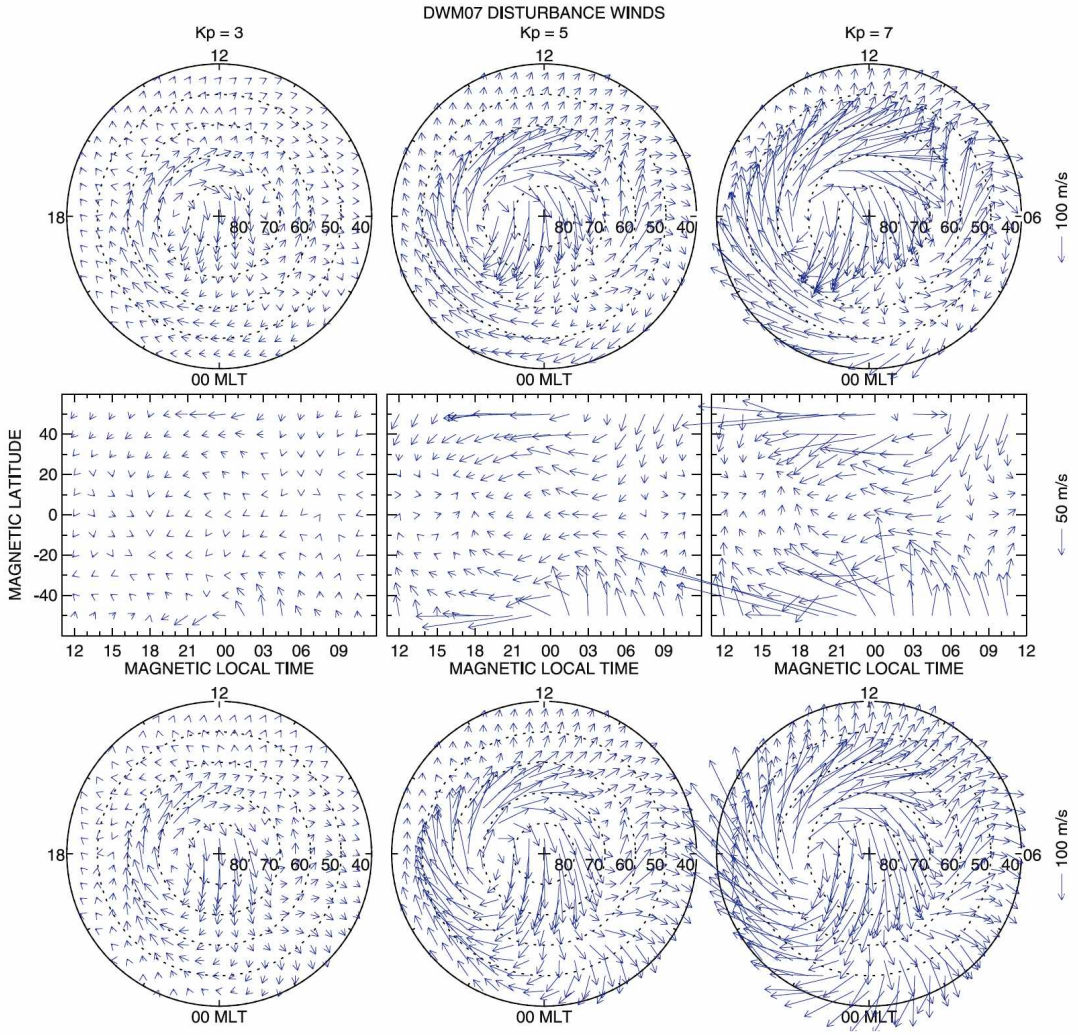

Figure 2.1: Disturbed vector winds as a function of geomagnetic activity (K_p) at high northern latitudes (top row), mid and low latitudes (middle row), and high southern latitudes (bottom row) [*Emmert et al.*, 2008].

speeds (sunward) via lower latitudes also become stronger. The polar cap antisunward wind speeds vary between 300 $m.sec^{-1}$ to 800 $m.sec^{-1}$ for quiet to active geomagnetic conditions [*McCormac et al.*, 1987]. Such dependence of the circulation cells on geomagnetic activity is shown in Figure 2.1.

The IMF influences the ionospheric component of the thermosphere-ionosphere coupled system and drives much of its variability. Ionospheric convection has strong dependence on the IMF and geomagnetic activity. Via the ion-neutral momentum coupling, the thermospheric wind circulation patters are dependent on these quantities. Although

thermospheric winds at high latitudes have been studied for many decades, we still know relatively little about how they respond to the strength and configuration of the interplanetary magnetic field under quiet, moderate, and disturbed geomagnetic conditions. Several independent systematic studies of the dependence of thermospheric neutral wind on the IMF by employing diverse data sets from individual Fabry-Perot interferometer (FPI) observatories around the globe, Wind Imaging Interferometer (WINDII), Challenging minisatellite payload (CHAMP), Dynamic Explorer satellites (DE1 and DE2), physics-based theoretical wind models, and empirical wind models have been done in past [*McCormac and Smith*, 1984; *McCormac et al.*, 1985; *Rees et al.*, 1986; *Sica et al.*, 1989; *Mccormac et al.*, 1991; *Hernandez et al.*, 1991; *Killeen et al.*, 1995; *Richmond et al.*, 2003; *Emmert et al.*, 2006a,b, 2008; *Kwak and Richmond*, 2007, 2014; *Forster et al.*, 2008; *Forster and Cnossen*, 2013; *Forster et al.*, 2011]. The key findings of these studies are discussed below.

The dependence of neutral winds on IMF is non-linear [*Richmond et al.*, 2003]. In the southern hemisphere during summer time, IMF effects on the neutral wind flows are detectable down to $\sim$105 *km* [*Richmond et al.*, 2003]. Above 125 *km*, thermospheric winds show considerable similarity with the ionospheric convection patterns. Around 120 *km* altitude, the dawnside thermospheric convection cell responds strongly to the variations in B_z component of IMF. On the other hand, the duskside thermospheric circulation cell respond to B_z above $\sim$140 *km*. For positive B_z, the dawnside and duskside thermospheric circulation cells remain confined to higher latitudes, but for negative B_z they expand to lower latitudes as a result of the expansion of ionospheric convection cells (in a similar fashion how neutral winds respond to geomagnetic activity as studied in *Emmert et al.* [2008]). The average neutral wind speed often exceeds 300 $m.sec^{-1}$. In the southern hemisphere, the neutral wind flow is anticyclonic for negative B_y and cyclonic for positive B_y. These wind features are depicted in Figure 2.2.

The IMF B_y component exerts a strong influence on the geomagnetically quiet time high latitude wind patterns, particularly in the magnetic midnight sector. An increase in solar irradiance strengthens the high latitude wind response to B_y. The direction of vector winds respond to any changes in the orientation of B_y as shown in Figure 2.3. For positive B_y, the neutral wind flows in the northern (southern) hemisphere are directed

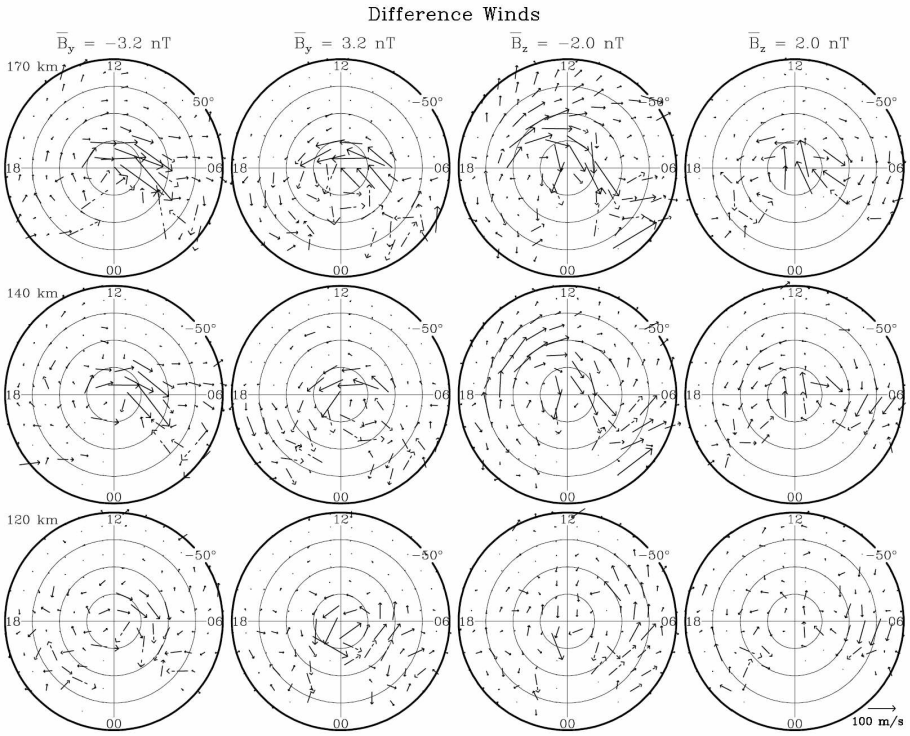

Figure 2.2: Difference winds at various IMF conditions and altitudes. The difference winds were produced by subtracting the wind obtained at mentioned B_y and B_z from the winds obtained at $B_y = B_z = 0$ [*Richmond et al.*, 2003].

more toward the dusk (dawn) sector than the winds for negative B_y. Quiet time wind response to B_y are even detectable as low as 53N magnetic latitude [*Emmert et al.*, 2006b].

During periods of persistent positive B_z and relatively low B_y, neutral winds in the geomagnetic polar cap are sometimes observed to be sunward. Such winds are rarely observed when B_y/B_z ratio exceeds 1, and are not observed for B_z less than 4 nT. In the northern hemisphere polar cap, maximum velocity antisunward winds are observed on the duskside (dawnside) during periods of northward IMF and negative (positive) B_z. Wind speed of the cross polar jet is largest for negative B_z and negative B_y IMF conditions in the northern hemisphere, but for negative B_z and positive B_y IMF conditions in the southern hemisphere. At high southern latitudes, variance in wind speed is larger than for the northern hemisphere, which is presumably due to larger separation between the geomagnetic and geographic pole in the southern hemisphere compared to the northern hemisphere. Such wind features are depicted in Figure 2.4.

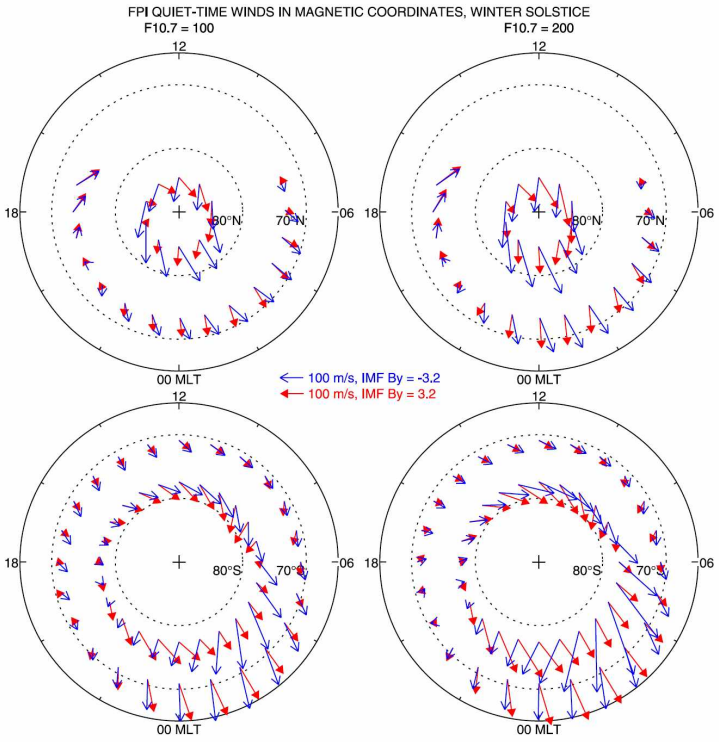

Figure 2.3: High latitude F-region neutral horizontal winds derived from FPI observations from the northern (top row) and southern (bottom row) hemispheres under quiet geomagnetic conditions during winter solstice. Wind dials in left (right) column are for low (high) solar EUV conditions. In the northern hemisphere, outer ring represents data from Sondre Stomfjord FPI and inner ring from Thule. For the southern hemisphere, data is from South Pole FPI [*Emmert et al.*, 2006b].

2.2.3 Seasonal and Solar Cycle Dependence

Many systematic studies of the thermospheric wind flows have investigated their seasonal and solar cycle dependence [e.g., *Hernandez and Roble*, 1984; *Crickmore*, 1994; *Killeen et al.*, 1995; *Aruliah et al.*, 1996; *Griffin et al.*, 2004; *Emmert et al.*, 2006a]. At high latitudes, thermospheric wind speeds tend to increase with increasing solar EUV irradiance. The high latitude thermospheric wind patterns are dominated by antisunward flows over the polar cap. Antisunward wind speeds generally increase with increasing solar extreme ultraviolet (EUV) irradiation (as shown in Figure 2.5), and the winds are generally stronger during equinox than during winter. *Aruliah et al.* [1996] observed an equinoctial asym-

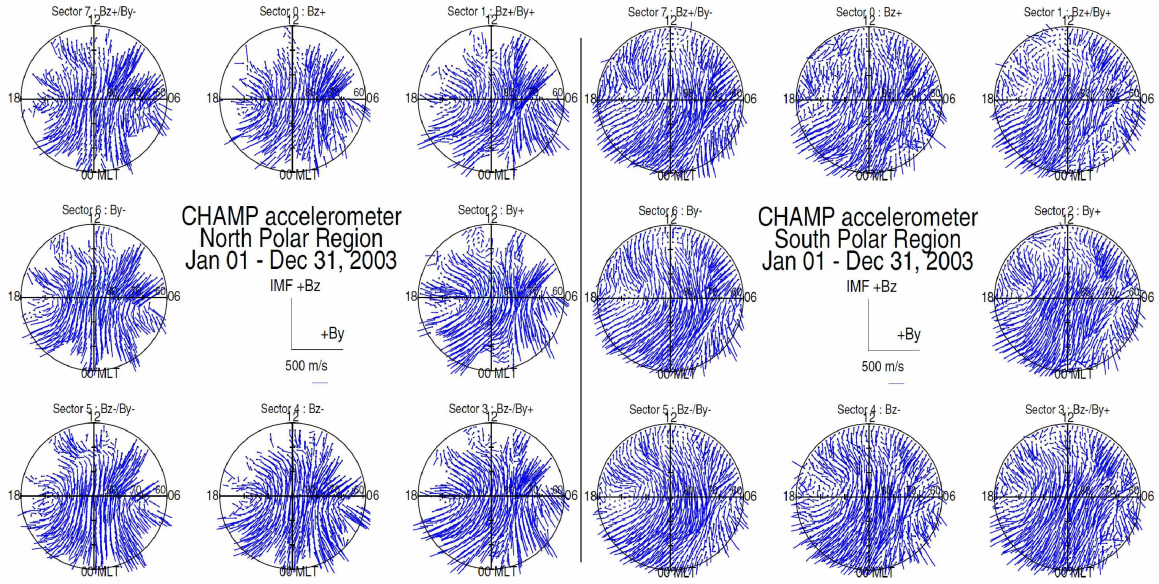

Figure 2.4: Thermospheric horizontal neutral winds for the northern (left panel) and southern (right panel) hemispheres for different B_y and B_z conditions. The outer circle is at 60 degree magnetic latitude. The GSM y-z coordinate directions and scaled vector length is shown at the center of each panel [*Forster et al.*, 2008].

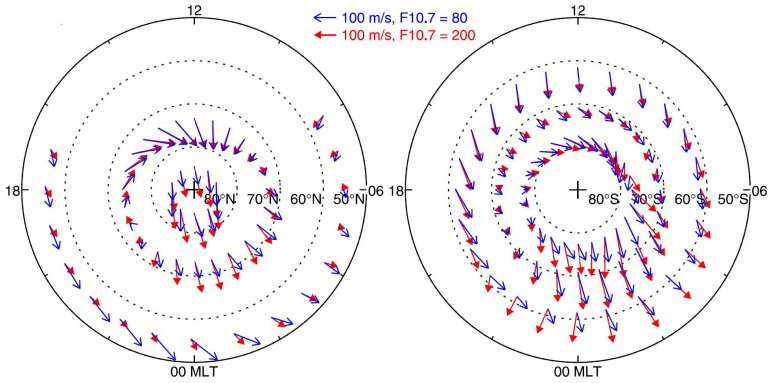

Figure 2.5: High latitude quiet time winter solstice F-region neutral winds derived from FPI measurements in the northern (left panel) and southern (right panel) hemispheres. In the northern hemisphere, FPI data is from three stations: Millstone Hill (outer ring; only north-looking results are shown), Sondre Stromfjord, and Thule (inner ring). In the southern hemisphere, FPI data is from two stations: Halley (outer ring) and South Pole (two inner rings) [*Emmert et al.*, 2006b].

metry in high latitude winds over Kiruna, Sweden. The observed average equatorward velocities were larger during the March equinox than September equinox at both solar maximum and minimum conditions.

2.3 Vertical Winds

The upper atmosphere is stably stratified as discussed in chapter 1, but the presence of vertical winds can significantly disrupt the diffusive equilibrium and transport species from the lower to the upper thermospheric or vice versa. As a consequence, they can disrupt chemical equilibrium at various altitudes in the thermosphere and modify the production and loss mechanism rates of ionospheric and thermospheric species. Usually, vertical winds are expected to be only minor disturbance in the thermospheric dynamics, but they are now known to be playing an important role in the dynamics of the upper atmosphere. Localized heating events cause upwelling of air; for mass continuity, the corresponding downwelling must occur somewhere. Modeling studies by *Killeen et al.* [1984]; *Rishbeth et al.* [1985, 1987] have shown that vertical winds can significantly modify the atmospheric composition, horizontal thermospheric circulation, and energy balance of the upper atmosphere. Upwelling in the thermosphere, for example, lifts molecular nitrogen and nitric oxide from the lower to the upper thermosphere. Increased molecular nitrogen leads to increased recombination rates and hence reduced ion and electron densities, whereas the lifting of nitric oxide causes cooling in the upper thermosphere. A decrease in ion concentration results in weaker ion-neutral coupling and influences other electrodynamical processes.

There exist a number of possible drivers of the vertical winds. A complete detailed discussion of the various potential sources of the vertical winds is given in *Smith* [1998] and recently in *Larsen and Meriwether* [2012]. Both identified diurnal expansion and contraction of the thermosphere due to solar heating, localized heating by Joule and particle precipitation, and wave motions (atmospheric tides and gravity waves) as the primary sources of the vertical winds.

Direct measurements of vertical wind started with the observations by ground-based optical Doppler spectrometers by observing Doppler shift in auroral and airglow emis-

sions [*Smith*, 1980; *Burnside et al.*, 1981; *Hernandez*, 1982; *Rees et al.*, 1984a; *Wardill and Jacka*, 1986; *Price and Jacka*, 1991; *Price et al.*, 1995; *Sipler et al.*, 1995], tracking luminous vapor trails left by rockets [*Rees*, 1969; *Rieger*, 1974], satellites in the upper atmosphere [*Spencer et al.*, 1976, 1982]. These techniques have been in use for a long time, and are still used today. Recently, vertical winds have been measured with incoherent scatter radars [*Oyama et al.*, 2005].

The diurnal cycle of contraction and expansion of the atmosphere due to solar heating is expected to drive vertical winds of small amplitude ($\sim$1-3 $m.sec^{-1}$) [*Smith*, 1998]. *Conde and Dyson* [1995b] used 103 nights of FPI 630 *nm* observations from Mawson (67.6S, 62.9E, Inv 70.5S), Antarctica and concluded that for low geomagnetic activity, the diurnal variation in vertical wind was -2.6 to 3.0 $m.sec^{-1}$. This variation was -6.8 to 4.1 $m.sec^{-1}$ in the case of moderate geomagnetic conditions. *Smith and Hernandez* [1995] measured 40 $m.sec^{-1}$ average diurnal variation in vertical wind amplitude at the South Pole. Vertical winds of the order of 10 $m.sec^{-1}$ are common at low, mid, and high latitudes [*Larsen and Meriwether*, 2012]. Vertical wind magnitude increases slightly with increase in altitude (from E-region to F-region).

Joule and particle heating are two primary sources of energy at auroral latitudes (as discussed in sections 1.7.2 and 1.7.3 of chapter 1). They cause localized heating of the thermosphere that can drive vertical winds of the order of few $m.sec^{-1}$ to $\sim$100 -200 $m.sec^{-1}$. Such larger vertical winds at auroral latitudes have been reported by the observation from both satellites [*Spencer et al.*, 1982] and ground-based Doppler spectrometers [*Rees et al.*, 1984a; *Wardill and Jacka*, 1986; *Price et al.*, 1995; *Innis et al.*, 1999]. A study of vertical winds by *Spencer et al.* [1982] using data from the Wind and Temperature Spectrometer (WATS) on board the DE2 reported vertical winds of the magnitude of 100-250 $m.sec^{-1}$ in the polar cap region and 10-20 $m.sec^{-1}$ at lower latitudes with an estimated uncertainty of 20-30 $m.sec^{-1}$ (due to uncertainty in the spacecraft altitude). They observed that large upwelling vertical winds were in correlation with the increase in temperature, suggesting that temperature enhancement at lower altitudes due to localized Joule heating in the polar cap was likely the driver. *Crickmore et al.* [1991] studied the vertical winds within the vicinity of Halley, Antarctica (75.60S, 26.21W) and observed strong downward vertical winds of

the order of 50 $m.sec^{-1}$ with frequent occurrence when the station was located under the equatorward edge of the auroral oval. Upward vertical winds of the magnitude $\geq$100 $m.sec^{-1}$ were observed poleward of the auroral oval by *Innis et al.* [1999] using 630 *nm* observations with FPI located in Antarctica at Davis (68.6S, 78.0E, Inv 74.6S) and Mawson (67.6S, 62.9E, Inv 70.5S). The separation between these two observatories is $\sim$600 *km*, but Mawson stays mostly under the auroral oval while Davis passes from under the auroral oval into the polar cap.

Price et al. [1995] measured vertical winds in the upper ($\sim$240 *km*) and lower ($\sim$130 *km*) thermosphere by observing 630 *nm* and 557.7 *nm* nightglow auroral and airglow emissions with a high resolution scanning FPI located at Poker Flat, Alaska. Vertical winds and temperature were measured simultaneously for 21 nights. They reported two significant upwelling events that lasted between 15 and 25 min and occurred simultaneously at both altitudes. During active geomagnetic conditions, they observed peak vertical upwelling winds of the order of 42 $m.sec^{-1}$ in the lower thermosphere and 138 $m.sec^{-1}$ in the upper thermosphere. These upwellings were correlated with $\sim$200 *K* temperature increase in the lower thermosphere. On both occasions, the observation locations were located on the poleward side of the auroral oval, and these upwellings were observed during the expansion phase of the substorm.

Ishii et al. [2001] observed vertical winds using two different types of FPIs located at Poker Flat. They observed 557.7 *nm* and 630 *nm* auroral and airglow emissions simultaneously from the lower (E-region) and upper (F-region) thermosphere similar to as discussed in *Price et al.* [1995]. They often observed vertical winds simultaneously at both wavelengths. In the upper thermosphere, upward (downward) vertical winds were often present in the presence of aurora equatorward (poleward) of the observatory. These observations are consistent with observations of other studies discussed above. Vertical winds at different heights showed different behaviors when thin bright aurora passed over the observatory. *Ishii et al.* [2004] observed vertical winds in the lower (E-region) and upper (F-region) thermosphere using FPIs located at Poker Flat and Eagle, Alaska during the Horizontal E-Region Experiment (HEX) campaign in 2003. These observatories are separated by $\sim$300 *km*, but lie at same geographic latitude. From 13 nights of obser-

vations, they found a high correlation between temporal variations in the lower thermospheric vertical winds observed at these two observatories, suggesting that vertical winds in the lower thermosphere were uniform along the auroral arc. On the other hand, they observed a poor correlation between variations in vertical winds observed from the upper thermosphere. *Kosch et al.* [2000] reported only weak coupling between the E-region and F-regions vertical winds using vertical winds data from Ramfjord and Skibotn, which are only by 45 *km* away. They reported an increase in coupling with increasing geomagnetic activity. *Ishii* [2005] studied the relationship between the lower thermospheric vertical wind and location of ionosphere currents in the polar region. He used 557.7 *nm* emissions recorded by a FPI located at Poker Flat to estimate vertical winds from the lower thermosphere (~110-140 *km* altitudes). This height is close to the peak height of the ionospheric currents which is a source of Joule heating. He estimated ionospheric currents using the magnetometer data from Kaktovik, Fort Yukon, Poke Flat, and Gakona. In his single night case study, he found that after 1130 UT, the downwelling wind flow was dominant equatorward of the ionospheric current, while upwelling was dominant poleward of the ionospheric current. This relation was opposite before 1130 UT (Figure 2.6).

In a similar study of vertical winds at high latitudes, *Greet et al.* [2002] calculated mean vertical winds using over four years of data (1997 - 2000) from two southern high latitude stations (Mawson (67.6S, 62.9E, Inv 70.5S) and Davis (68.6S, 78.0E, Inv 74.6S). Although the distance between two stations is ~600 *km*, they recorded quite different mean thermospheric vertical winds. Mean hourly vertical winds at Mawson were between -10 $m.sec^{-1}$ to +4 $m.sec^{-1}$ and showed little dependence on K_p index. On the other hand, mean hourly vertical wind at Davis varied between -10 $m.sec^{-1}$ to 10 $m.sec^{-1}$ and showed a significant dependence on K_p. They found that the location of the observatory relative to the auroral oval had a major influence on the estimated mean vertical winds. They observed small amplitude mean vertical winds within the auroral oval, downward winds on the equatorward boundary of the auroral oval, and large vertical winds poleward of the auroral oval (downward in early magnetic evening and upward around magnetic midnight). This behavior of the vertical winds relative to the position of the auroral oval was in agreement with the studies mentioned above. Such vertical wind behavior is shown in Figure 2.7.

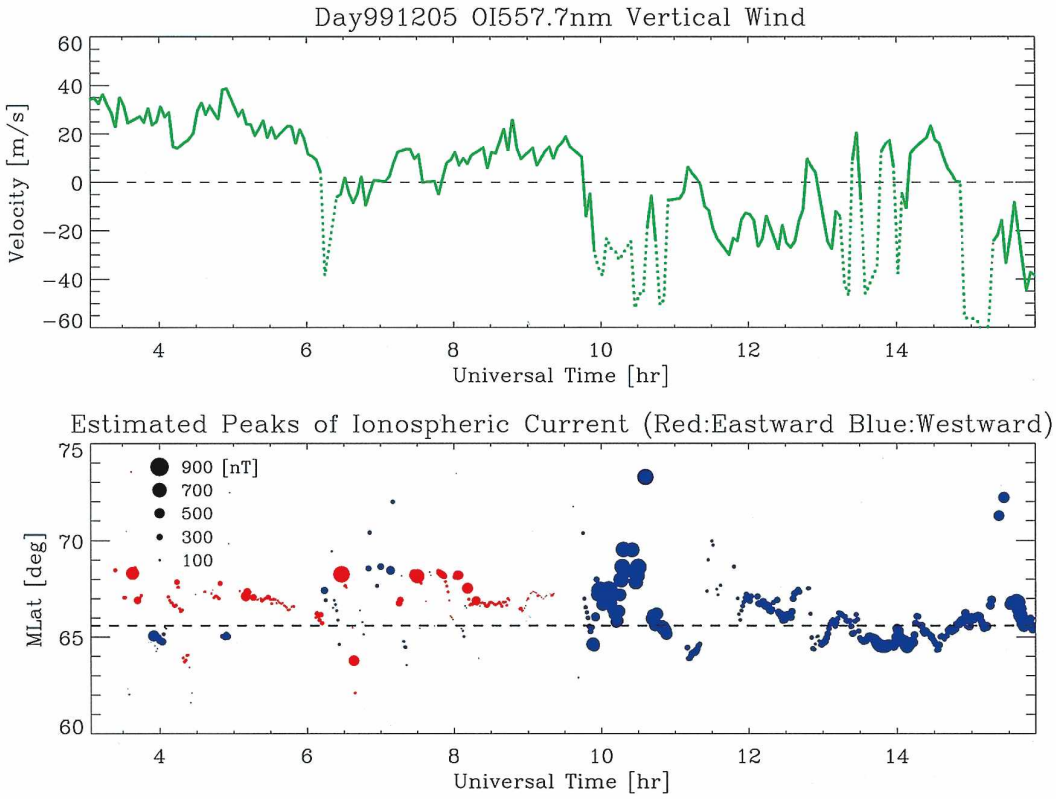

Figure 2.6: Vertical wind velocity as function of universal time (UT) observed with FPI at zenith of Poker Flat, Alaska on 05 Dec 1999 (Top panel). Estimated peaks of the ionospheric currents derived from ground-based magnetometers located in Alaska, as function of magnetic latitude and universal time (Bottom panel). Red (blue) circles represent currents in Eastward (westward) direction. The size and color of circles represent the magnitude and the direction of the ionospheric current [*Ishii*, 2005].

Gravity waves transfer energy and momentum from the lower to the upper atmosphere and play an important role in driving the thermospheric vertical winds. *Spencer et al.* [1976] studied variations in the neutral vertical winds and temperatures using N_2 measurements from the Atmospheric Explorer-C. They concluded that the observed variations in the vertical winds and temperatures were due to gravity waves in the auroral zone. *Wardill and Jacka* [1986] observed oscillatory behavior of vertical winds derived from 630 *nm* emissions from Mawson, Antarctica for both quiet time and disturbed geomagnetic conditions. They linked this oscillatory behavior of vertical winds with the thermospheric gravity waves. *Johnson and Killeen* [1995] observed perturbation of the or-

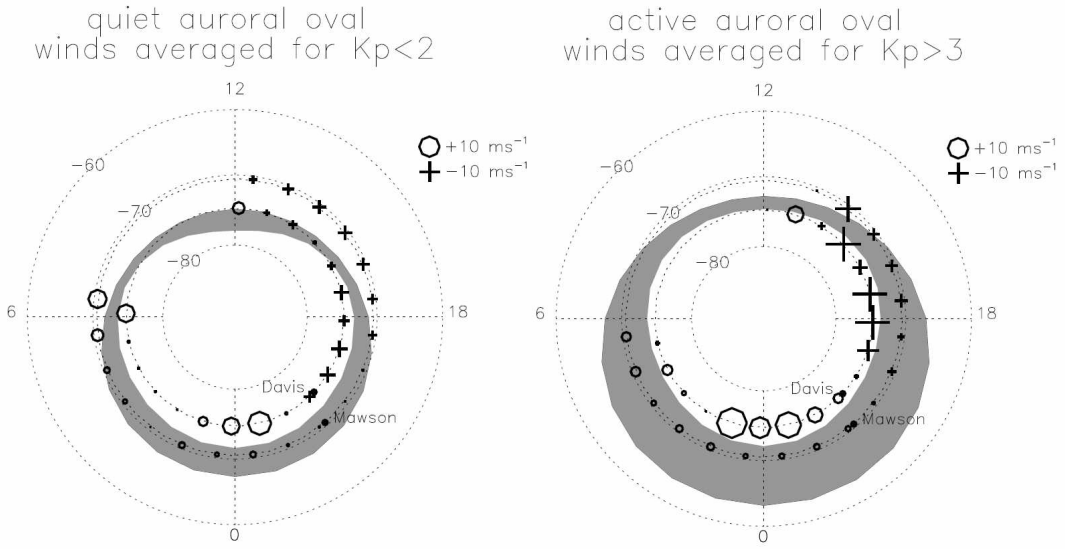

Figure 2.7: Hourly mean vertical winds from two southern hemisphere stations (Davis and Mawson) for quiet (K_p < 2, left panel) and active (K_p < 3, right panel) geomagnetic conditions. The locations and magnitude of upward and downward vertical winds with respect to the auroral oval is represented by "circles" and "crosses" markers respectively [*Greet et al.*, 2002].

der of 100 $m.sec^{-1}$ in the vertical winds measured by the DE2 at altitudes above 250 *km*. These perturbations were caused by the gravity waves with horizontal wavelength (along the satellite path) of about 500 *km*. Such features were also recorded in the ion vertical velocity and temperatures. They inferred vertical displacement of the order of 10 *km* with a time period of 1000 seconds and horizontal phase progression from nightside to dayside. In most of the events, they observed gravity waves extended all the way across the polar cap.

Innis and Conde [2001, 2002] studied vertical winds from 250 to 650 *km* altitude using the WATS spectrometer observations on the DE3 satellite. They selected a sliding window of 120 sec which was equivalent to ∼900 *km* in the distance and then mapped the standard deviation of vertical winds in local time and invariant latitude. Results were separated by altitude, AE index, and solar zenith angle. No significant differences in the high latitude vertical wind activity in between hemispheres were observed and vertical wind activity showed no correlation with solar zenith angle. Vertical wind activity

changed slightly with the increase in altitude. However, this study found a clear relationship between the vertical wind activity and geomagnetic activity (indicated by AE index). At high altitudes, they found an increase in the vertical wind activity with the increase in geomagnetic activity as depicted in Figure 2.8. The authors related this vertical wind

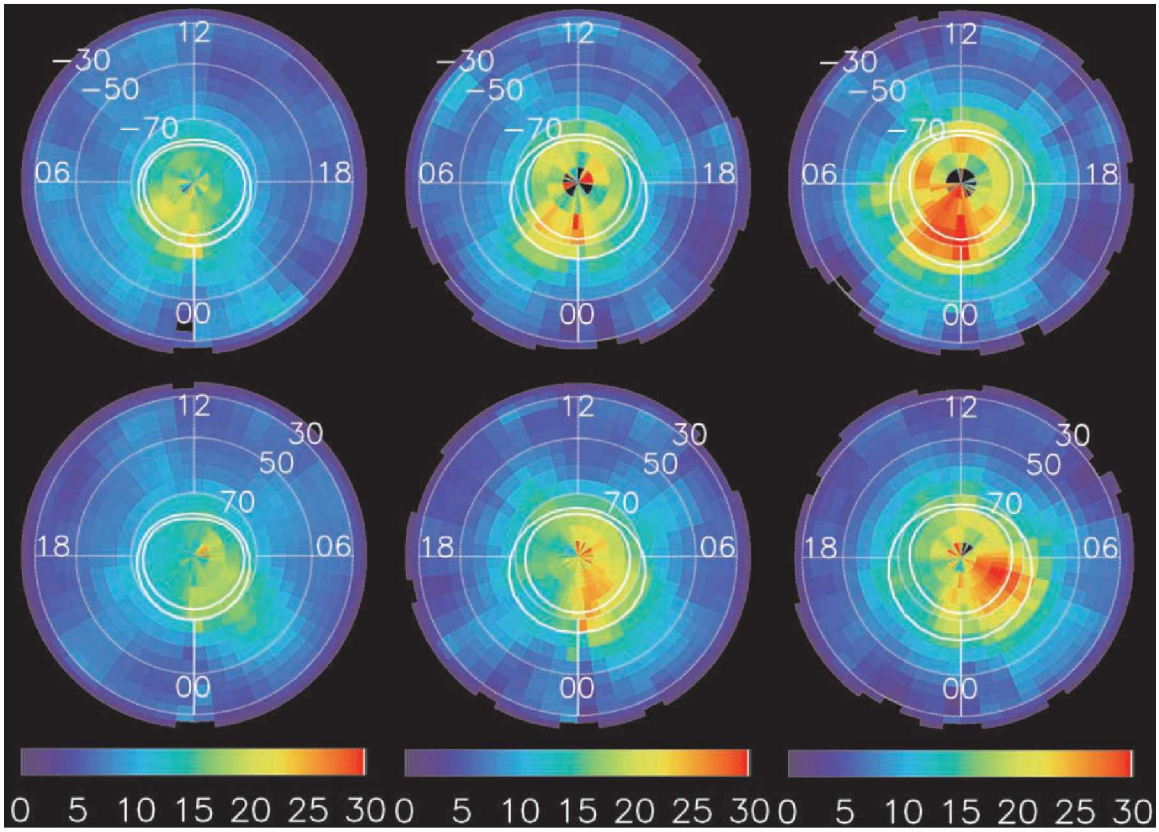

Figure 2.8: Vertical wind standard deviation ($\sigma(V_z)$ in $m.sec^{-1}$) derived from the WATS spectrometer observations on the DE3 satellite presented on southern (top row) and northern (bottom row) polar maps (bins of 0.5 h LMT and 5° invariant latitude) for $AE < 250\ nT$ (first column), $250\ nT \leq AE < 500\ nT$ (second column), and $AE \geq 500\ nT$ [*Innis and Conde*, 2002].

behavior to the activity of gravity waves in the polar region, which also changes with the change in geomagnetic activity. A study by *Johnson and Killeen* [1995] also recorded many wavelike structures in the WATS vertical wind time series. A study by *Mayr et al.* [1990] using DE2 data concluded that the auroral oval is likely the cause of gravity waves in the polar cap. A study of vertical and horizontal winds using two different types of

FPI instruments located at Ramfjord, Norway by *Ishii et al.* [1999] also reported wave-like structures in the vertical winds in the lower and upper thermosphere. However, in this study these structures were not always in phase.

Horizontal and vertical winds are coupled by the mass continuity

$$\frac{\partial \rho}{\partial t} + \overrightarrow{\nabla} . (\rho \overrightarrow{U}) = 0 \tag{2.1}$$

where ρ is the density and $\overrightarrow{U}$ is the neutral wind velocity. This equation states that temporal change in mass density is solely related to divergence of the mass flux. Using the treatment given in *Burnside et al.* [1981] for incompressible atmosphere, the above expression can be reduced to:

$$w = H (\overrightarrow{\nabla_h} . \overrightarrow{U}) \tag{2.2}$$

$$w = H \left(\frac{\partial u}{\partial x} + \frac{\partial v}{\partial y} \right) \tag{2.3}$$

where H is the atmospheric scale height of the layer in consideration and $\overrightarrow{\nabla_h} \cdot U$ is the horizontal divergence; w, u, and v are the vertical, zonal, and meridional components of wind field respectively. The above relation shows that vertical wind can be estimated from divergence and vice versa if scale height H is known. *Burnside et al.* [1981] suggested that vertical winds drive horizontal divergent flows. *Crickmore* [1993] used thermospheric density data recorded by DE2 to study the assumption of atmosphere incompressibility for calculating vertical winds from horizontal divergence and found this assumption acceptable in most of the cases.

Smith and Hernandez [1995] studied thermospheric winds over the South Pole and investigated the relationship between vertical winds and divergence in horizontal winds. The calculated divergence of the horizontal wind was of the order of $10^{-3} sec^{-1}$. They found that vertical winds were driven by divergence in the horizontal winds. Also, vertical winds were proportional to the calculated divergences in the horizontal winds, but the proportionality constant was found to be twice the typical scale height at the altitude of measurement. Upward vertical winds were driven by horizontal convergence (negative divergence), and downward vertical winds were driven by positive horizontal divergence as shown in Figure 2.9. Vertical wind and divergence exhibited similar behaviors in both the lower and upper thermosphere.

This behavior of vertical wind with divergence observed by *Smith and Hernandez* [1995] was opposite to what was suggested by *Burnside et al.* [1981]. *Anderson et al.* [2011] reached similar conclusions as of *Burnside et al.* [1981] based on analysis of FPI data from Mawson and Davis, Antarctica. *Smith and Hernandez* [1995] and *Rees et al.* [1984b] suggest that divergence (for example imposed by ion drag) in the horizontal winds was the driving force for vertical winds, not the other way around as suggested by *Burnside et al.* [1981] and *Anderson et al.* [2011].

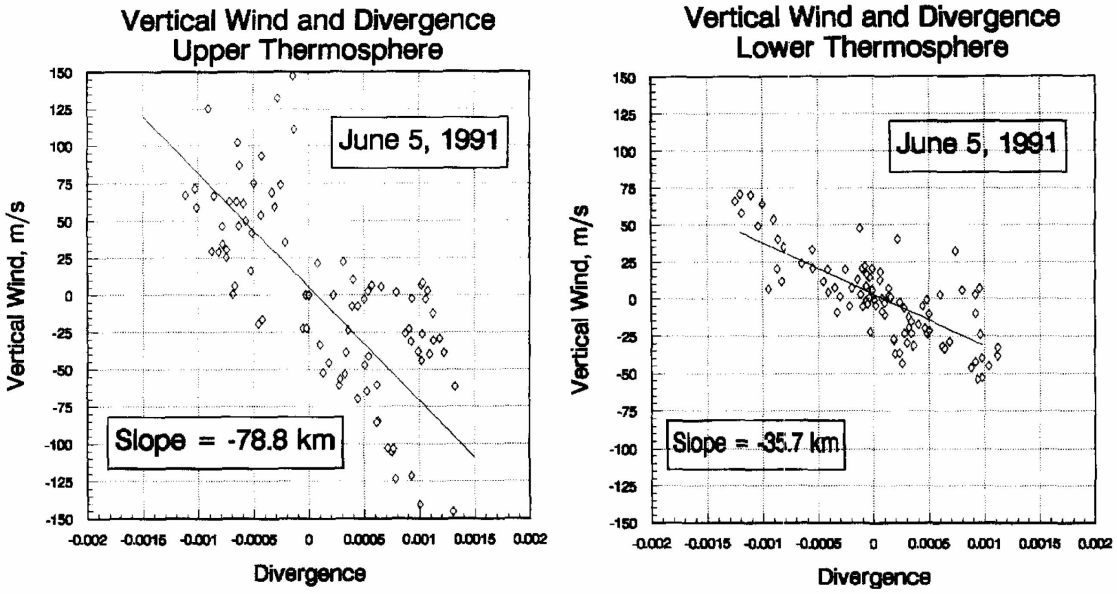

Figure 2.9: Variation of vertical wind with divergence in the horizontal wind for the upper (left panel) and lower (right panel) thermosphere [*Smith and Hernandez*, 1995].

Analysis by *Guo and McEwen* [2003] of vertical wind data from five winters recorded by FPIs in the northern hemisphere polar cap suggests that vertical winds are driving horizontal divergences. Although *Guo and McEwen* [2003] found a linear relationship between horizontal divergence and vertical wind, saturation in divergence associated with the strong upward vertical wind events was also reported. *Ishii et al.* [1999] investigated the correlation coefficient between vertical wind and horizontal divergence using two different types of FPIs located at Ramfjord, Norway. Although the correlation between the horizontal wind divergence and vertical wind varied with time, the sign of coefficient was negative for most of the time. On the basis of the sign of correlation, *Ishii et al.* [1999] sug-

gested that most of the time vertical motion was driven by divergence in the horizontal wind that is in agreement with the studies of *Rees et al.* [1984b] and *Smith and Hernandez* [1995].

The thermospheric vertical wind component is often used to determine the zero-velocity baseline for the ground-based spectroscopic observations. For deriving Doppler shift from recorded spectra, it is commonly assumed that average vertical wind over the entire night should be zero. A study by *Aruliah and Rees* [1995] discussed the trouble with using this assumption for obtaining zero Doppler shift. They investigated 1242 nights of data from the high latitude FPI observatory located at Kiruna, Sweden (68N, 20E) and found that mean vertical winds have dependence on universal time (UT), season, solar activity, and geomagnetic activity. The use of zero vertical wind assumption would add a systematic bias in calculated Doppler shifts, which can be of the order of 5 $m.sec^{-1}$ for quiet geomagnetic conditions and 10-20 $m.sec^{-1}$ for active geomagnetic conditions. However, the zero vertical wind assumption can only be used when observation periods are long (typically in mid-winter), and geomagnetic conditions are quiet.

2.4 Small-scale Structures

In the traditional picture of Earth's thermosphere, it is widely presumed that its convective stability and enormous kinematic viscosity attenuate wind gradients, and hence smooth out any structure present in the wind over scale sizes of several hundreds of kilometers. Also, the neutral gas is assumed to respond very slowly to magnetospheric forcing because of its large inertia. That is why it is most commonly treated as a background and easily predictable medium. For such a medium, air parcel trajectories would be relatively simple and transport processes would only slowly disperse and mixes air masses. This means that regions of perturbed chemical composition formed for example by an intense aurora or any other processes, would be expected to remain intact for many hours or even days. However, independent systematic studies have shown that this simple picture does not hold in practice [e.g., *Meriwether et al.*, 1973, 1988; *Conde and Smith*, 1995, 1998a,b; *Killeen et al.*, 1995; *Greet et al.*, 1999; *Aruliah and Griffin*, 2001; *Aruliah et al.*, 2004]. Thermospheric dynamics is quite complex especially at high latitudes, and

thermospheric wind fields have much more local spatial scale structures than expected from simple considerations.

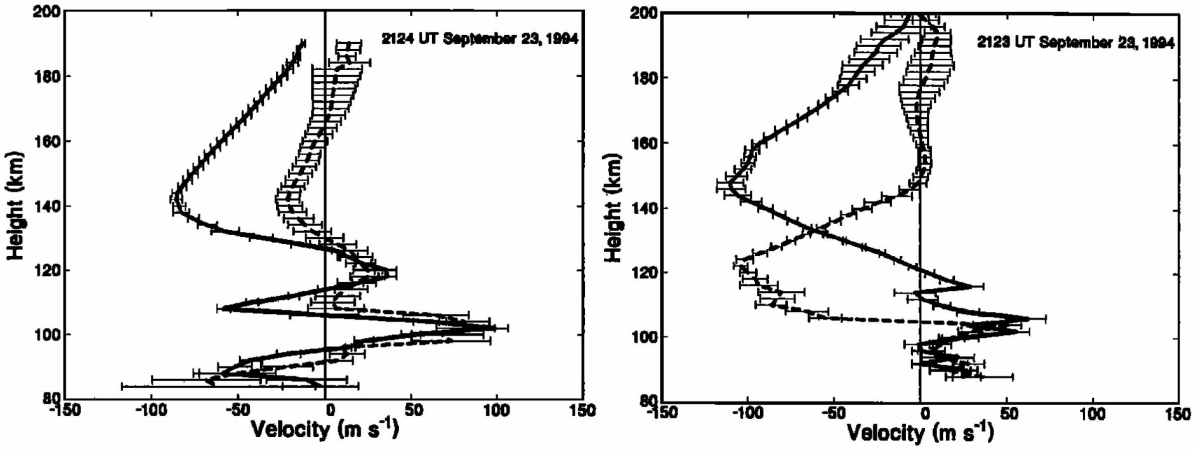

Figure 2.10: Zonal (solid line) and meridional (dashed line) wind profiles at magnetic equator (left panel) and 480 *km* north along the magnetic meridian (right panel) near sunset on 23 September 1994 [*Larsen and Odom*, 1997].

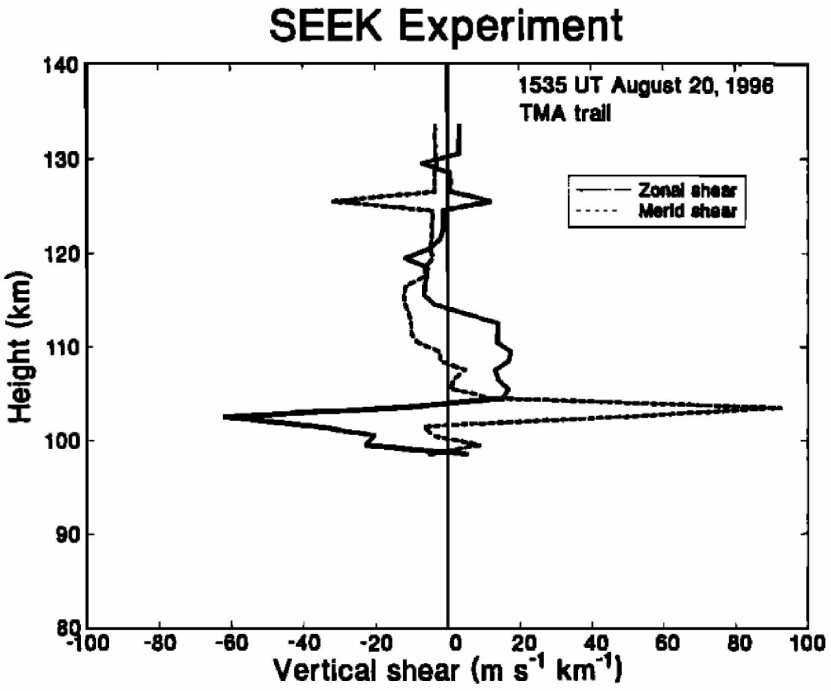

Figure 2.11: Zonal (solid line) and meridional (dashed line) wind shears at Kyushu (33N, 131E) from chemical release on 20 Aug 1996 [*Larsen et al.*, 1998].

2.4.1 Vertical Structures

Sounding rocket chemical releases provide the most direct measurements of the neutral wind altitude profile, but with a very limited temporal coverage. Since 1958, more than 400 such in-situ measurements of the wind profiles of the upper atmosphere that cover a wide range of latitudes, longitudes, seasons, and local times have been made [*Larsen*, 2002]. A number of chemical release studies observed the presence of large vertical shears in the lower thermosphere (bottom side of E-region). For example, a study of E-region thermosphere by *Larsen and Odom* [1997] in the vicinity of magnetic equator reported maximum wind speeds of the order of 80-100 $m.sec^{-1}$ and wind direction reversal over the altitude scales of 10-15 km. Such a wind behavior is shown in Figure 2.10. At an altitude of $\sim$105 km, *Larsen et al.* [1998] reported wind maximum of around 150 $m.sec^{-1}$ and strong shears in zonal wind ($\sim$50 $m.sec^{-1}.km^{-1}$) as shown in Figure 2.11. In a similar study, *Rees et al.* [1976] observed wind speeds of 130 $m.sec^{-1}$ near 104 km altitude and wind shears of the same order as measured by *Larsen et al.* [1998]. *Larsen* [2002] combined the four decades of wind measurements obtained with the chemical release technique. The combined results showed three consistent features: 1. wind maximum of the order of 100 $m.sec^{-1}$ in the altitude range 100-110 km, 2. large shears (maximum 100 $m.sec^{-1}.km^{-1}$) at the bottom side of the E-region, and 3. strong shears at vertical scales of $\sim$10 km or less. In 60% of the cases, wind measurements exceeded 100 $m.sec^{-1}$. The shear magnitudes obtained from this study are presented in Figure 2.12; both zonal and meridional shears are presented in Figure 2.13.

The in-situ measurements obtained by tracing chemical releases provide an extended altitude coverage, but with limited temporal coverage at high cost and technical complexity. On the other hand, ground-based optical techniques provide limited altitude range, but with extensive temporal coverage. That is why the most extensive horizontal wind measurements have come from ground-based optical techniques. F-region thermospheric winds and temperatures are most commonly observed using the 630 nm red line emission, and E-region winds and temperatures using the 557 nm green line emission.

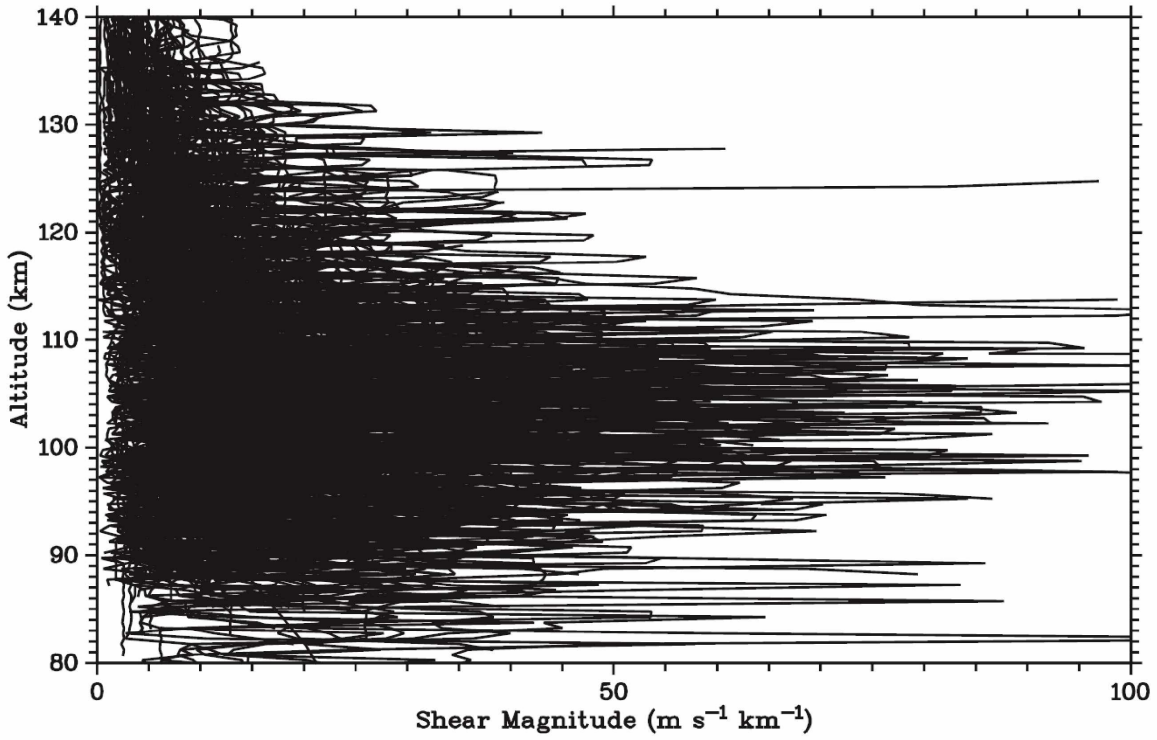

Figure 2.12: Altitude profile of shear magnitudes for all the low and mid-latitude data accumulated during the last four decades [*Larsen*, 2002].

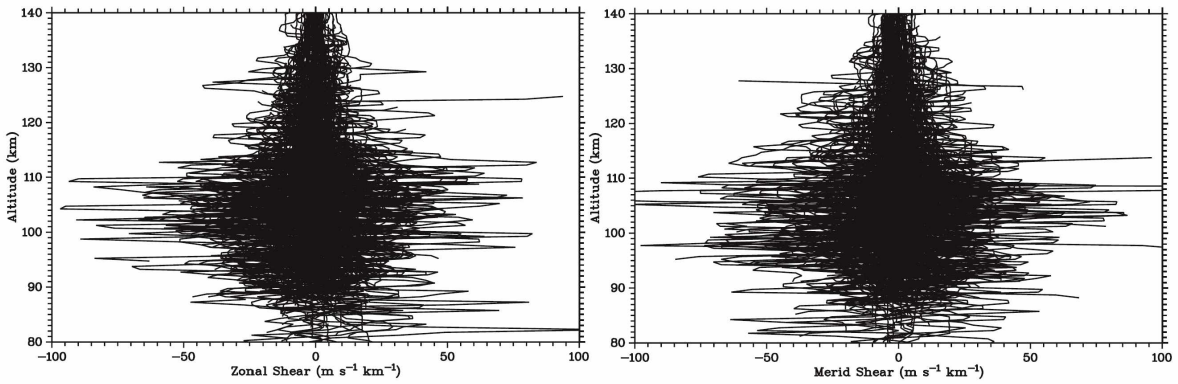

Figure 2.13: Altitude profile of zonal (left panel) and meridional (right panel) shears for all the low and mid-latitude data obtained from last four decades [*Larsen*, 2002].

2.4.2 Horizontal Structures

Any low cadence point measurements of a wind field that has significant spatial structure will fail to fully describe the dynamics of that wind field. This is the case for narrow field Fabry-Perot Interferometers (FPIs). It is difficult to resolve localized and short period

fluctuations with them. This is due to their limited spatial resolution and time required to complete an observation sequence. *Rees and Greenaway* [1983] and *Rees et al.* [1984a] described the use of a wide angle viewing FPI (called Doppler Imaging System (DIS)) to detect small-scale short living structures in the horizontal thermospheric wind fields by observing thermospheric winds over a wide geographic area at high temporal resolution. *Rees et al.* [1984a] used DIS located at Kiruna, Sweden (67.8N, 21.2E) in conjunction with a collocated traditional FPI on a geomagnetically active night, and observed fluctuations of the order of $\pm$ 150 $m.sec^{-1}$ with associated spatial scale of 100-200 km in the F-region horizontal wind flows within an 800 km diameter region of observation. *Batten and Rees* [1990] used the DIS data sets from 1987-1988 winter and confirmed the highly dynamical behavior of thermosphere at high latitudes. They reported high variability at small spatial scales ($\sim$50 km) and small temporal scales ($\sim$10 min) in the thermospheric horizontal wind fields. Rapid spatial wind reversals at the equatorward edge of the auroral oval within less than 100 km were regularly observed, particularly during active geomagnetic conditions. They also reported regular short period convergence and divergence events in the horizontal wind fields during active geomagnetic conditions. Some of the events were related to rapid changes in local auroral brightness. *Rees et al.* [1998] used 630 nm emissions with two advanced DISs located in Kiruna, Sweden and Longyearbyen, Svalbard and observed a significant amount of spatial variability within a 400 km diameter. A line-of-sight (LOS) wind difference of $\sim$100 $m.sec^{-1}$ was observed between the opposite cardinal look directions separated by $\sim$400 km.

Aruliah and Griffin [2001] studied the response of thermospheric F-region horizontal neutral winds and temperatures to ionospheric changes over the meso-scales (spatial and temporal) by utilizing neutral wind data from three northern Scandinavian FPIs (located at Kiruna, Sweden (67.8N, 20.4E), Kilpisjarvi, Finland (69.2N, 20.8E), Longyearbyen, Svalbard (78.2N, 15.6E)), and ionospheric plasma convection measurements from the EISCAT radar. Significant gradients in the average neutral zonal winds were present near Kiruna. They observed a change in wind speed of the order of 150 $m.sec^{-1}$ in a time period shorter than 40 min. The neutral wind behavior changed with the change in geomagnetic activity. Results of this study showed that neutrals are capable of responding to ionospheric

variations with spatial scale sizes less than a few hundred kilometers and temporal scales of tens of minutes. Another study by *Aruliah et al.* [2005] using tristatic winds reported similar results. *Griffin et al.* [2008] used a Scanning Doppler Imager (SCANDI) located at Nordlysstasjonen optical observatory near Longyearbyen and reported strong enhancement in the LOS winds, and LOS wind speed differences of $\sim$100 $m.sec^{-1}$ at two different regions of the thermosphere separated by $\sim$200 km. Simultaneous measurements of vertical winds and temperatures showed that the regions of strong enhancements were dominated by Joule heating at that time.

McCormac et al. [1985] studied high latitude thermospheric winds from the upper thermosphere obtained with DE2 along its track and illustrated the presence of sharp wind gradients near the equatorward edge of the auroral oval. Narrow wind reversals were observed most of the time on the duskside of thermospheric circulation. They reported antisunward polar cap wind flows of the order of 500 $m.sec^{-1}$ and return flow via duskside cell of the order of 400 $m.sec^{-1}$. Large wind gradients were often observed along the track of DE2 at high latitudes, which suggest that these sharp wind gradients are a persistent feature of the high latitude upper thermospheric wind flows. An example of four such orbits showing significant wind gradients along the track of the satellite is presented in Figure 2.14. The investigations of [*McCormac et al.*, 1987] showed that the wind gradients present along the duskside auroral oval become more stronger and move to lower latitudes with increasing geomagnetic activity. *Killeen and Roble* [1988] combined the simultaneous measurements of the global scale auroral luminosity from DE1 and neutral winds over the northern polar cap (winter time) derived from DE2. These simultaneous measurements provided the direct evidence of the relationship between spatial distribution of aurora and F-region neutral wind circulation at high latitude. According to this study, spatially narrow wind reversals were often present at the poleward edge of the duskside auroral oval. Such an example is shown in Figure 2.15.

Conde and Smith [1995, 1998b]; *Conde et al.* [2001]; *Anderson et al.* [2012]; *Dhadly et al.* [2015] used a newly developed wavelength scanning Doppler imaging FPI, known as "SDI" (refer to appendix A for details of SDI) located at Poker Flat (Alaska) to map thermospheric wind fields at high spatial and temporal resolution. The biggest advantage of

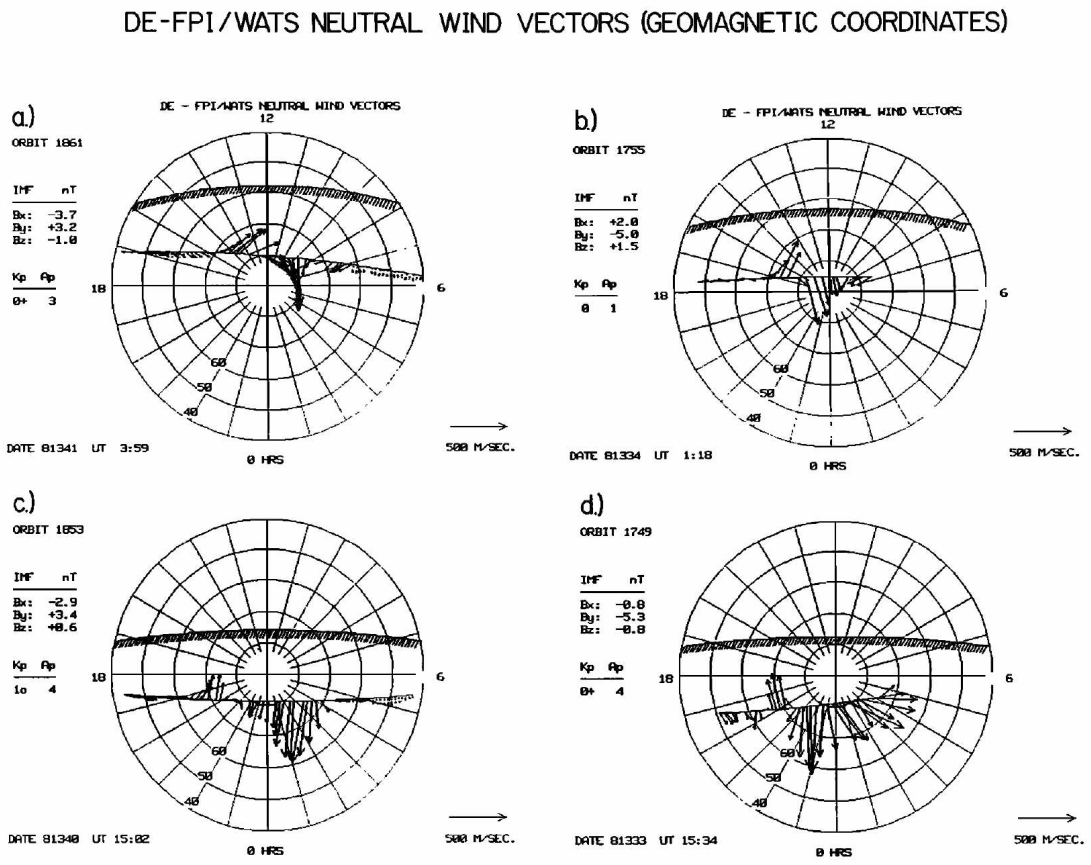

Figure 2.14: Vector neutral wind measurements (in geomagnetic polar coordinates) along the track of DE2 during a) orbit 1861, b) orbit 1755, c) orbit 1853 and d) orbit 1749. The curved hatched line represents the solar terminator [*McCormac et al.*, 1985].

using SDI compared to DIS was its wavelength scanning etalon, because multiple etalon scans would suppress any distortion in the spectra resulted from any spatial auroral intensity gradients present in the sky. This allowed simultaneous optical measurements of airglow from many tens of locations across the sky (~144 full field of view) at a spatial resolution of the order of ~50 *km* (at an altitude of the 630.0 *nm* emission), and with integration times as low as 1-2 minutes during aurorally active conditions (and 3-5 minutes during normal viewing conditions) with minimal distortion in spectra. These studies investigated the behavior of horizontal neutral winds over a geographic latitudinal range of around 60N to 70N with aurora and ionospheric plasma convection. These studies revealed the presence of strong latitudinal gradients in the F-region horizontal winds associated with ion drag and diurnal pressure gradient. The latitudinal wind gradients

were stronger in the pre-magnetic midnight sector than the post-magnetic midnight sector above Alaska. These strong gradients were associated with the equatorward and poleward boundaries of the discrete aurora. In our recent study *Dhadly et al.* [2015], discussed in chapter 5, suggests the presence of structures with spatial size smaller than 40 *km* in the upper thermosphere. Such small-scale structures have not been reported before.

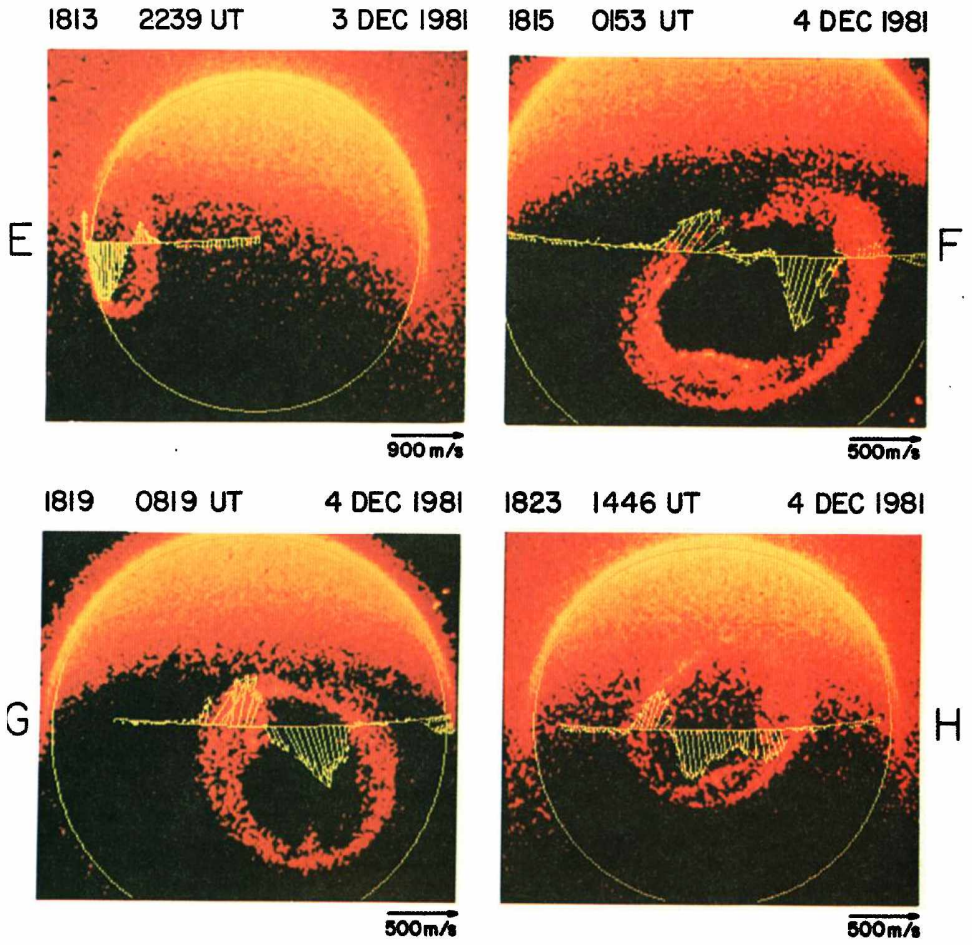

Figure 2.15: Vector neutral winds (yellow) from DE2 superposed on auroral UV images from DE1. For each panel, sun is at the top pf the figure and dusk to the left. The orbit number of DE2 is given at the top of each panel [*Killeen and Roble*, 1988].

In the traditional picture of Earth's thermosphere, it is widely presumed that its convective stability and enormous kinematic viscosity attenuate wind gradients, and hence smooth out any structure present in the wind over scale sizes of several hundreds of kilometers. However, above discussed experimental studies shows that thermosphere can re-

spond quickly to magnetospheric forcing and have much more dynamical structure than predicted by models. There are only a few modeling studies [e.g., *Walterscheid et al.*, 1985; *Keskinen and Satyanarayana*, 1993] that have predicted the development of strong shears in the vicinity of auroral arcs of on spatial scales of the order of tens of hundred kilometers.

2.5 Thermospheric Spectroscopic Emissions: Airglow and Aurora

Airglow is the faint emission of light from electronically and/or vibration-rotationally excited atoms and molecules in the Earth's upper atmosphere. Airglow is generally diffuse and unstructured. Solar X-rays, UV, and EUV photons supply energy to upper atmospheric species, causing their photoionization and photodissociation, which often leaves the atoms and molecules in unstable excited states that will re-radiate after spending some lifetime in the excited state. During this lifetime, the excited atoms/molecules may undergo collisions and distribute their energy (quenching). If excited species are not quenched before their radiative lifetimes, they return to their ground states by releasing excess energy in the form of photons at particular wavelengths. The photochemical sources of the excited states that are responsible for airglow emissions are present everywhere; that is why airglow is always diffuse and is a global phenomenon that occurs at all latitudes. At lower altitudes, the collision frequencies are so high (due to increased particle number density) that it leads to the quenching of excited states long before the atoms and molecules can re-radiate. This is why airglow does not occur in the lower atmosphere.

Airglow is most commonly separated into three categories: Dayglow, twilightglow and nightglow. The distinction arises because of the varying role of sunlight in exciting the emissions. As expected, dayglow describes airglow during the daytime, while nightglow describes night time airglow. Twilightglow occurs during twilight hours when sunlight illuminates the upper atmosphere. Daytime airglow is produced by resonant and fluorescent scattering of sunlight, as well as by photochemical reactions. Nightglow, by contrast, is only produced by recombination of the species that were photodissociated or photoionized by sunlight during daytime. Twilightglow and nightglow are much easier to observe than dayglow because of the direct and Rayleigh scattering of sunlight dur-

ing daytime by the lower atmosphere which is so bright that it overwhelms the weaker airglow signal.

The most commonly and easily observed nightglow emissions are from atomic oxygen (at wavelengths 557.7 *nm*, 630 *nm*, 636.4 *nm*), sodium (at wavelengths 589-589.6 *nm*), and Meinel hydroxyl bands. During the twilight period, certain spectral emissions for example sodium at 589 *nm* and 589.3 *nm* are much stronger than during nighttime.

Although aurora is also emission of light from electronically and/or vibration-rotationally excited atoms and molecules in the Earth's upper atmosphere, it is regarded as a separate phenomenon to airglow because it is excited by collisions with precipitating auroral particles. Aurora occurs most commonly in diffuse, pulsating patches, and highly structured bright and localized arcs. Auroral emissions occur at high latitudes in the auroral oval (near the boundary region between open and closed field lines of the Earth's magnetic field). Energetic particles (in most cases electrons) accelerated in the magnetosphere can penetrate deep ($\sim$100 *km*) into the Earth's upper atmosphere along (mostly) open magnetic field lines and collide (inelastic collision) with other upper atmospheric species. It results in their ionization, dissociation, or excitation. These excited species then release excess energy in the form of optical radiation (auroral emissions). Quenching of the excited species occurs in similar manner to airglow as discussed above. Auroral precipitating particles (with energy well above the ambient thermal energy) excite a considerable number of spectral emissions and bands from upper atmospheric constituents, out of which 557.7 *nm* and 630 *nm* are among the strongest features of visible airglow and auroral spectrum.

The so called oxygen "red line" (630 *nm*) and "green line" emissions (557.7 *nm*) come from the upper and lower thermosphere respectively, and are probably the two most studied of all airglow and auroral emissions for remote sensing the upper and lower thermospheric dynamics. Airglow emissions from Meinel hydroxyl bands at various wavelengths (between 300 *nm* to 4000 *nm*) are widely used for remote sensing the mesopause dynamics.

The work presented here in chapters 3, 4, and 5 is based solely on observations at 630 *nm* wavelength. The research work presented in appendix B is based on using OH

emission observations from (6,2) Meinel band at 843 *nm* (also known as $P_1(3)$ emission line) from the mesopause (~85 *km*). So, in the following discussion, we will focus only on the emissions at 630 *nm* and 843 *nm* wavelengths.

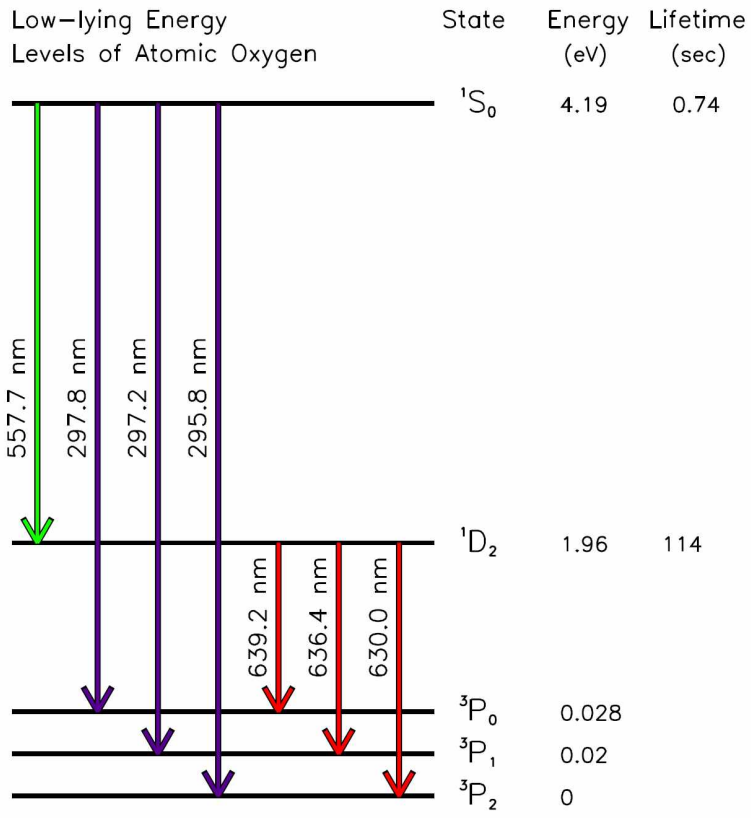

Figure 2.16: Lower energy levels of atomic oxygen and various possible transitions between them leading to the red, blue, and green emissions [*Anderson*, 2011].

2.5.1 Red Line Emission (λ = 630 *nm*)

The red line emission emanates from the upper thermosphere when an atomic oxygen in the ^1D state transitions to its ground state ^3P. As shown in Figure 2.16, this transition produces a triplet (630 *nm*, 636.4 *nm*, and 639.2 *nm*) which means there are three possible pathways by which atomic oxygen in the ^1D state reach the ^3P ground state [*Banks and Kockarts*, 1973; *Whitten and Poppoff*, 1971]. The 639.2 *nm* emission is too weak to be observed, and the probability of 630 *nm* occurrence is three times that of 636.4 *nm* [*Rishbeth and Garriott*, 1969]. It means 630 *nm* is the dominant emission out of this triplet. Vari-

Table 2.1: Various possible mechanisms leading to the production of atomic oxygen in the ^1D state [*Anderson*, 2011].

Type	Reaction
(1) Photodissociation	$O_2 + h\nu \rightarrow O(^1D) + O(^3P)$
(2) Dissociative Recombination	$O_2^+ + e \rightarrow O(^1D) + O$
(3) Electron Impact	$O(^3P) + e^* \ (E > 1.96\ eV) \rightarrow O(^1D) + e$
(4) Cascade	$O(^1S) \rightarrow O(^1D) + h\nu(\lambda = 557.7nm)$
(5) Ion-Atom Interchange	$N^+ + O_2 \rightarrow O(^1D) + NO^+$
(6) Quenching	$N^* + O \rightarrow O(^1D) + N(^4S)$
(7) Impact Dissociation	$O_2 + e^* \rightarrow O(^1D) + O + e$
(8) Atom interchange	$N(^2D) + O_2 \rightarrow O(^1D) + NO$

ous possible mechanisms can excite atomic oxygen into the ^1D state. A list of the major mechanisms for the production of atomic oxygen in the ^1D state is given in Table 2.1.

According to the atomic selection rules, the transition from the ^1D state to the ^3P state is forbidden, which makes the ^1D state "metastable" with a very long radiative lifetime of ~114 *sec*. Due to this long radiative lifetime of the ^1D metastable state, it is likely to be quenched by collision with other atmospheric species (particularly N_2 , O, and O_2) if the collision frequency is high. The radiative lifetime of the aurorally generated population of atomic oxygen (in ^1D state) is sufficient to allow its population to diffuse spatially from the regions in which the auroral processes generated it. Also, red emissions are the product of low energy electrons which typically are not formed by well structured acceleration mechanisms. That is why red auroras are often diffuse. The 630 *nm* emissions emanate from a broad vertical extent ~100-400 *km* of the thermosphere with maximum volume emission rate ~240 *km*. Above 200 *km*, the atmospheric number density is such that it allows the radiative transition from the ^1D state to ^3P state [*Sandholt et al.*, 2002], but below 200 *km*, the quenching of ^1D state rapidly increases. The volume emission rate of 630 *nm* dayglow as measured by the WINDII instrument on the UARS spacecraft

is shown in Figure 2.17. *Sica et al.* [1986b] studied the variation in 630 *nm* maximum volume emission layer altitude using variations in thermospheric temperature observed by a ground-based FPI located at College (64.8*N*, 147.8*W*), Alaska. This study showed that the 630 *nm* airglow layer peaks around 240-250 *km* in the presence of soft auroral precipitation. With very soft or no auroral precipitation, the emission layer can peak higher than this, whereas very hard precipitation can move the emission layer peak many tens of kilometers lower.

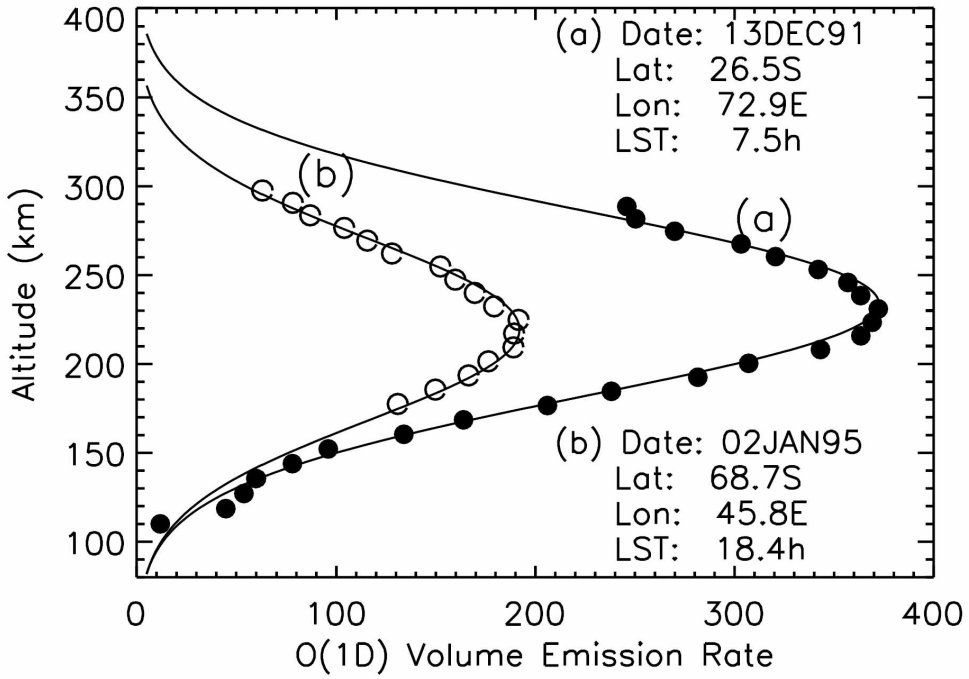

Figure 2.17: Two samples of measured red line volume emission rate (circles) fitted with Gaussian profile (solid line) [*Zhang and Shepherd*, 2004].

The various possible mechanisms for the production of oxygen in the ^1D are listed in Table 2.1. Out of them, photodissociation of molecular oxygen by solar radiations at daytime is the most dominant mechanism. At night time, however, dissociative recombination is the dominant mechanism when auroral precipitation is negligible. In the presence of auroral precipitation, oxygen atoms in the ground state undergo inelastic collisions with the auroral electrons. Colliding electrons with energy above the threshold 1.97 *eV* can excite atomic oxygen in the ^3P state to the ^1D state. This electron impact excitation mechanism is dominant at polar latitudes (as compared to other latitudes) and leads to

the formation of red auroral arcs. Under special circumstances, the red aurora can be excited thermally. When plasma temperature is high, the electrons from the higher end of the energy distribution (hot electrons with Temperature > 3000 K) have enough energy to excite lower energy states of atomic oxygen. Such conditions produce stable red auroras (also known as stable auroral red (SAR) arcs) just equatorward of the auroral zone [*Cole*, 1965; *Sandholt et al.*, 2002]. The brightness of these SARs can be ~13 kilo-Rayleighs [*Baumgardner et al.*, 2007], where 1 Rayleigh is equivalent to 10^{10} $photon.m^{-2}.s^{-1}$. The typical altitude of thermally excited aurora is 300-500 km in contrast to the electron impact excitation 200-300 km. The probability of excitation by electron impact is very small for electrons with energy $\gg$1 keV, but high for electrons with energy < 500 eV [*Sandholt et al.*, 2002].

All the other listed mechanisms of O(^1D) production (discussed below) listed in Table 2.1 are minor sources. Atomic oxygen in the ^1S state can make a direct transition to the ^3P state via emission of 297.2 nm photon (blue line emission), but such emissions are rarely observed. Another way is a two-step cascade process: first transition from the ^1S to ^1D by the emission of a 557.7 nm photon and then ^1D to ^3P by the emission of a 630 nm photon. Other minor mechanisms include ion-atom interaction between nitrogen ions and molecular oxygen, production via quenching of excited nitrogen, impact dissociation, and atom exchange.

In the real atmosphere, quenching of the excited states of atomic oxygen is always present. The possible primary thermospheric sources that cause quenching of O(^1D) are N_2 and O_2. Minor sources of quenching are N and $O(^3P)$. Quenching rates and various mechanisms that lead to quenching of the ^1D state are discussed in *Streit* [1976]; *Hays et al.* [1978]; *Solomon et al.* [1988]; *Sobral et al.* [1992].

2.5.2 Hydroxyl Emission

Although, hydroxyl (OH) is a minor constituent and present throughout the Earth's lower and middle atmosphere, OH emissions have been used extensively to study temperatures and dynamical processes occurring at the mesospheric heights. *Meinel* [1950a,b] discovered the OH emissions in the nightglow. Rocket-borne and satellite [*Baker and Stair*, 1988;

Offermann and Gerndt, 1990; *Sivjee*, 1992; *Zhang and Shepherd*, 1999; *Liu and Shepherd*, 2006; *French and Mulligan*, 2010] observations have shown that the mean altitude of OH airglow emission layer is 87 *km* with a mean thickness of 8 *km* centered at the mesopause. It is produced chemically in excited quantum states which are short-lived (metastable with a lifetime $10^{-3} sec$) and collisionally deactivated or quenched at the altitudes below mesopause (~87 km). At the mesopause and above, collision frequency is such that a significant fraction of the excited OH molecules survive from collisional deactivation long enough to undergo radiative relaxation, and thus form an emitting layer. This is the probable reason why the OH emission layer has a sharp lower border and extended high altitude tail.

The OH emission is one of the brightest in the night sky, and it occurs in a number of bands. The most widely accepted mechanism for the production of excited OH molecules is the Bates-Nicolet process [*Bates and Nicolet*, 1950]:

$$O_3 + H \longrightarrow OH^* (\nu^{'} \leq 9) + O_2 + 3.34\, ev \tag{2.4}$$

where ν is the vibration state of excited OH molecule. The relative yields of Bates-Nicolet process for the sixth, seventh, eighth, and ninth vibrational levels are 0.04, 0.07, 0.34, and 0.55 respectively [*Llewellyn and Long*, 1978]. The excited OH molecules undergo deexcitation either via radiative relaxation or collisional deactivation. OH emissions cover a broad range of wavelengths from visible to infrared region (~300 *nm* to 1000 *nm*) depending on the vibration state of the excited OH molecules.

$$\textit{Radiative relaxation}: \; OH^*(\nu^{'}) \longrightarrow OH(v^{''}) + hv$$

$$\textit{Collisional deactivation}: \; OH^*(\nu^{'}) + M \longrightarrow OH(v^{''}) + M + E$$

where M can be O_2 , N_2, or O and E is the energy produced during this collisional deactivation. *McDade and Llewellyn* [1987] proposed sudden death of excited OH molecules rather than stepwise deactivation via

$$OH^*(\nu^{'}) \longrightarrow OH\,(v^{'} = 0) + M \tag{2.5}$$

where M can be O_2 , N_2, or O. Simultaneous measurement of the volume emission rates of $\nu > 6$ (high vibrational state) and $\nu < 6$ (low vibrational state) showed that high vibrational

state populations are generally higher in altitude than low vibrational state population [*Baker*, 1978] as shown in Figure 2.18.

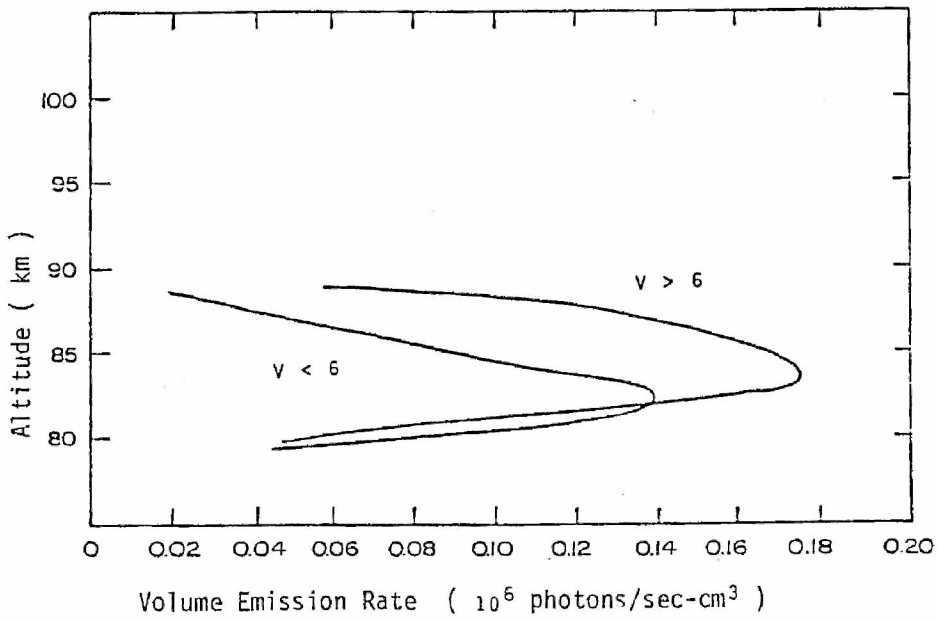

Figure 2.18: Typical simultaneous emission profiles of OH [*Baker*, 1978].

Different vibrational OH transitions produce different emission bands (known as Meinel bands) [*Meinel*, 1950a,b]. Each OH vibrational level is split into few rotational levels. Thus, each band corresponds to a series of rotational transitions, occupying a certain range of wavelengths in the visible or infrared region. The OH bands principally result from the rotational transitions within either the ground or first excited electronic state of the OH molecule. A complete nomenclature of OH line emissions in discussed in *Osterbrock and Martel* [1992]; *Osterbrock et al.* [1996].

Each rotational emission line inside a vibrational-rotational band is assigned a letter (P, Q, or R) depending on the selection rules. Q-branch occurs at the center of the vibrational-rotational band whereas P-branch and R-branch occur on lower frequency and higher frequency side of the vibrational-rotational band, respectively. OH emission bands extend from the visible region (~300 *nm*) to infrared region (~4000 *nm*). In our mesospheric study (discussed in appendix B), we used OH emissions from the (6,2) Meinel band at 843 *nm*, also known as $P_1(3)$ doublet emission line. Here, subscript '1' implies to a rotational

transition in the ground state (subscript '2' would imply to a rotational transition in the first excited state) and '3' in the bracket implies to a rotational quantum number. Figure 2.19 shows few of the emission lines from OH (6,2) Meinel band.

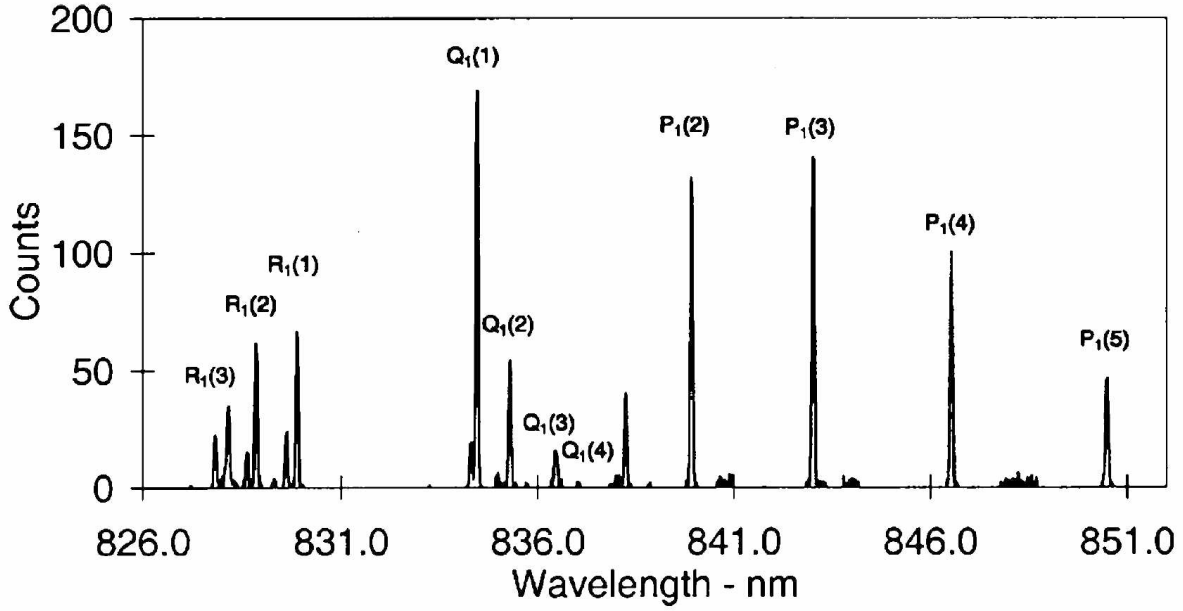

Figure 2.19: Major OH emission lines in (6,2) Meinel band [*French et al.*, 2000].

Due to nuclear spin of the OH molecules, emissions are subject to lambda doublet splitting. All branch lines of the (6,2) Meinel band are given in Table 1 in *Greet et al.* [1997]. The peaks of $P_1(3)$ doublet exist at 843.007 *nm* and 843.026 *nm*, which are only 0.019 *nm* apart. These components are spectrally very close and can be distinguished only with a high resolution spectrometer. The spectrum of $P_1(3)$ emission line with doublet structure is shown in Figure 2.20. This doublet introduces distortion in the $P_1(3)$ emission spectrum and cannot be used to estimate wind and temperature without careful analysis. For avoiding this doublet, a common procedure is to choose the etalon spacing in FPIs specifically to make these two peaks actually fall on top of each other as discussed in *Rees et al.* [1990] and *East et al.* [1995].

2.6 Temperature and Wind Measurements from Spectroscopic Analysis

Spectroscopic emissions from several different thermospheric species (discussed in section 2.5) are used to infer various geophysical quantities of the thermosphere, most com-

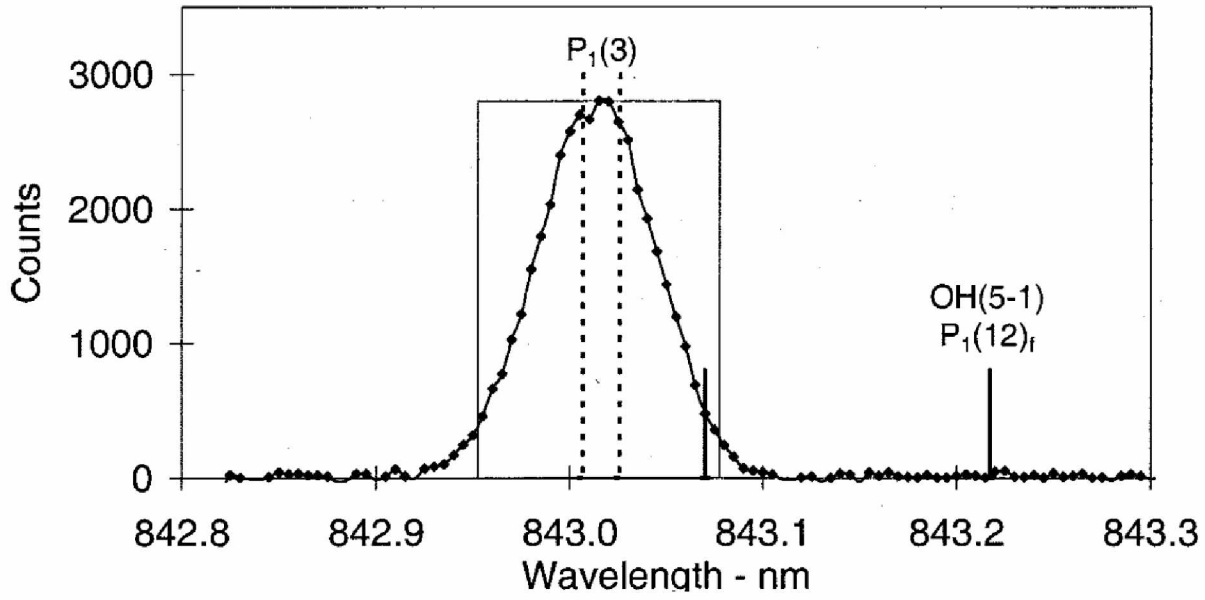

Figure 2.20: Spectrum of $P_1(3)$ OH emission line showing doublet structure [*French et al.*, 2000].

monly winds and temperatures. While determining these quantities, it is usually presumed that the excited species are in thermal equilibrium with the ambient neutral gas and that their properties represent those of the ambient neutral gas.

If all emitting particles are stationary, we would observe a very narrow line spectrum. If the emitting particles are undergoing random thermal motion, there will be a statistical spread of speeds along the observer's line-of-sight (LOS) that will cause broadening in the observed spectrum, referred to as "Doppler broadening". The higher the temperature, the wider the distribution of LOS wind speeds, and hence the broader the observed spectral line. In the realistic thermosphere, Doppler broadening is always present. Furthermore, if there is an overall flow of the bulk gas along the observer's LOS then there will be a non-zero bias introduced into the distribution of LOS speeds, resulting in a net Doppler shift in the observed spectrum. Measuring the Doppler broadening provides a temperature estimate and measuring the Doppler shift provides an estimate of the LOS wind component (sample spectrum in Figure 2.21). The recorded spectrum with FPI is usually Gaussian in shape. The Doppler width at half maxima of the recorded spectrum

is related to the temperature [*Jacka*, 1985] by:

$$\delta\lambda = \frac{2\lambda_o}{c}\sqrt{\frac{2\,k\,T\,ln(2)}{M}} = 7.16 \times 10^{-7}\,\lambda_o\sqrt{\frac{T}{M}} \tag{2.6}$$

where λ_o is the rest (zero velocity) wavelength (center wavelength), M is atomic mass and T is the kinetic temperature of emitting species, c is the speed of light, and k is the Boltzmann constant. This equation allows the estimation of the thermospheric temperature. The LOS component of the wind velocity is calculated from the Doppler shift by:

$$v = c\,\frac{\lambda - \lambda_o}{\lambda} \tag{2.7}$$

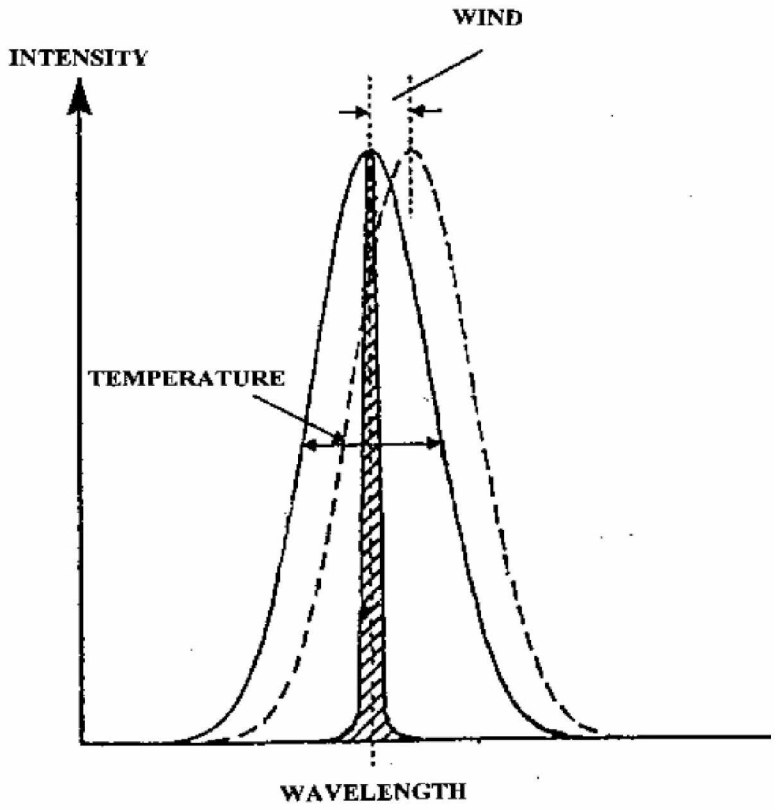

Figure 2.21: A sample spectrum observed with FPI. The solid curve represents the observed spectrum and dashed curve represents the zero velocity spectrum [*Griffin et al.*, 2002].

It is important to note that pressure broadening (also called collisional broadening, which occurs if emitting atoms are suffering frequent collisions with other atoms or ions

that can distort their energy levels) is negligible at thermospheric heights. Natural line broadening is governed by the Heisenberg uncertainty principal ($\Delta E \Delta t \sim \frac{h}{2\pi}$). In the case of 630 *nm* emission, the excited state is a metastable state with a radiative lifetime of ~114 sec that makes natural line broadening also negligible.

630 *nm* emissions have been used extensively to monitor the upper thermospheric temperatures and winds remotely. As discussed in the beginning of this section, the temperature determination assumes thermal equilibrium between emitting species and the ambient neutral gas. But, the newly created $O(^1D)$ population does not have a Maxwellian velocity distribution because the primary source of $O(^1D)$ is dissociative recombination (Reaction 2 in Table 2.1) which is an exothermic process [*Schmitt et al.*, 1981]. The energy released is much greater than the thermal energy of ambient neutrals. This energy is either carried as kinetic energy by the product atoms or excitation energy. The amount of kinetic energy is dependent on the electronic state (^1S, ^1D, or ^3P) of the other oxygen atom produced during the dissociative recombination [*Schmitt et al.*, 1981].

The presence of the non-thermalized population as a propotion of the overall population of excited atomic oxygen in the thermosphere has been the subject of many theoretical studies over the years [*Hays and Walker*, 1966; *Yee and Hays*, 1980] and attempts have been made to detect non-thermalized atoms from the ground-based observation [*Biondi and Feibelman*, 1968; *Hernandez*, 1971]. The degree of thermalization depends upon the chemical lifetime of the excited state, the collision frequency with ambient species (predominantly O and N_2 in the F-region), and the velocity distribution of the newly created $O(^1D)$ population [*Yee*, 1988]. *Jacka* [1985] suggested that, because of ~114 *sec* radiative lifetime of $O(^1D)$ the temperature inferred from the 630 *nm* emission line width is a good measure of bulk neutral gas temperature at all levels. But, the modeling studies by *Yee* [1988] showed that the non-thermalized population could systematically overestimate the temperatures between 50-100 K.

2.7 Atmospheric Modeling

Upper atmospheric models are used to study atmospheric composition, temperature, and wind dynamics on local and global scales. They are primarily divided into two categories:

1) Physics-based numerical models and 2) Empirical models. The physics-based theoretical models use first principles to simulate the observed conditions by solving various fundamental nonlinear primitive coupled equations governing energy and momentum exchange, and mass conservation. On the other hand, empirical models use observational data and organize databases in a form suitable for geophysical interpretation. The empirical model encapsulates all available historical information and measurements to describe the various geophysical quantities of the atmosphere as a function of latitude, longitude, altitude, day of year, and time of day. A brief discussion of various physics-based and empirical models is given below.

2.7.1 Physics-based Numerical Models

Geisler [1967] and *Kohl and King* [1967] were the first to successfully model the underlying behavior of thermospheric winds at low and mid-latitudes from first principles. Since then many generations of physics-based numerical models have been developed to study spatial and temporal variations in the thermospheric dynamics on the global scales. TIEGCM (Thermosphere Ionosphere Electrodynamics General Circulation) is a three dimensional, time dependent numerical model of the earth's neutral upper atmosphere developed by National Centre for Atmospheric Research (NCAR). It simulates the full three dimensional neutral wind, neutral and ion composition, and neutral, ion, and electron temperatures at a high resolution of 5 degrees in both longitude and latitude. Originally it was called TGCM (Thermospheric General Circulation Model), developed by *Dickinson et al.* [1981]. *Dickinson et al.* [1984] improved this model by incorporating coupled dynamics and compositions. Computation domain spans from nearly 95 to 500 *km* in altitude with 25 constant pressure surfaces and vertical resolution of 2 grid points per scale height. Early versions of this model family were basically designed to study the upper thermospheric dynamics. Further development was done by *Roble et al.* [1988], extending TGCM to TIGCM (Thermosphere Ionosphere General Circulation Model) by including a self-consistent aeronomic scheme of the thermosphere and ionosphere. *Richmond et al.* [1992] updated TIGCM to TIE-GCM (Thermosphere Ionosphere Electrodynamics General Circulation Model) which uses the resultant electric field and

currents (replacing the empirical models of the electric field and ion drifts) computed self-consistently from dynamo effects of thermospheric winds. The altitude range of this model is 95-500 *km*. *Ridley et al.* [1994] developed the most recent version of TIE-GCM, which is TIME-GCM (Thermosphere Ionosphere Mesosphere Electrodynamics General Circulation Model). The altitude range of this model is 30-500 *km*. Basic additions to produce this model were the inclusion of physical and chemical processes appropriate for mesosphere and upper stratosphere and extending the lower boundary to 30 *km* instead of 95 *km*.

TIGCM and TIEGCM use a resolution of 5 degrees in both longitude and latitude. Such spatial resolution is adequate for global scale studies of the upper atmosphere, but not for local-scale studies. As discussed in section 2.4, thermospheric wind dynamics is quite complex especially at high latitudes, and thermospheric wind fields have much more local spatial scale structures than predicted by models. For studying local-scale thermospheric dynamics, *Wang et al.* [1999] developed a three dimensional high resolution nested grid model TING (Thermosphere Ionosphere Nested Grid) which is an extension of TIGCM. TING is basically a global TIGCM with an adjustable nested grid that has higher spatial and temporal resolution than the coarse resolution of TIGCM. The size, location, and resolution of the nested grid are adjustable.

Millward et al. [1996] developed time-dependent global coupled thermosphere ionosphere plasmasphere model (CTIP) by including mid and lower latitude plasmasphere model with a global ionosphere and thermosphere model. This model couples the thermosphere development by *Fuller-Rowell and Rees* [1980] and *Rees et al.* [1980], the high latitude ionosphere development by *Quegan* [1982] and *Quegan et al.* [1982], the low and mid-latitude plasmasphere by *Bailey* [1983], and the electrodynamics by *Richmond et al.* [1992]. Latitude resolution is 2 degrees and the longitude resolution is 18 degrees. Recently, electrodynamical calculation of the global dynamo electric field was included in CTIP and named it CTIPe (Coupled Thermosphere Ionosphere Plasmasphere Electrodynamics Model). The model output includes neutral temperature, wind, and density; and ion electron number density.

Ridley et al. [2006] developed the Global Ionosphere Thermosphere Model (GITM). It

is different to other upper atmospheric models as it uses an altitude grid instead of a pressure grid. The grid pattern and resolution of this model are flexible. The model output includes neutral, ion, and electron temperatures; neutral and plasma velocities; neutral mass density and neutral number density; and number density of major ionospheric species.

2.7.2 Empirical Models

Among the empirical wind models, the Horizontal Wind Model (HWM) is most popular with the aeronomy community. *Hedin et al.* [1988] first developed the model as HWM87 using thermospheric data obtained from Atmospheric Explorer (AE) and DE2 satellites. This model was only developed for heights above 220 *km* because the wind data from these two satellites was of suitable only for the upper thermosphere. HWM90, HWM93, HWM07, and HWM14 are the successors of this model [*Hedin et al.*, 1991, 1996; *Drob et al.*, 2008, 2015; *Emmert et al.*, 2008]. Lower and middle thermospheric winds were first included in HWM93 and thereafter. The latest HWM14 uses a suite of wind measurements spanning past 50 years from the ground-based thermospheric wind measuring observatories around the globe, rockets, and many satellite missions. The output of this model is a function of latitude, longitude, altitude, day of year, local solar time, and geomagnetic activity. The advantage of the HWM model is that it encapsulates all diverse thermospheric neutral wind data sets and provides the dynamical information of the thermosphere to facilitate our quantitative understanding of global thermosphere. However, many issues with HWM remain unexplored including dependence of the predicted winds on the IMF strength and orientation, seasonal and altitude dependence of disturbed winds, and solar cycle dependence.

NRL-MSIS (Mass Spectrometer and Incoherent Scatter Radar)is an empirical model of thermospheric temperature, density, and composition that is widely used by aeronomy community. It describes the neutral temperature and number densities of various species in the Earth's atmosphere from ground to thermospheric heights. MSIS-86 [*Hedin*, 1987] was the first stable and reliable version of the original MSIS [*Hedin et al.*, 1977a,b]. The original idea of MSIS was to synthesize results from various mass spectrometers that had

been flown, together with ground-based incoherent scatter radars. The recent version of MSIS is NRLMSIS-00, which is developed by *Picone* [2002].

Current models (both physics-based and empirical) cannot describe local details of the thermospheric wind fields, especially at auroral latitudes. This is because, at high latitudes, thermospheric wind drivers are highly variable; and the time varying interplay between these drivers leads to the substantial variations in thermospheric circulations at the local and synoptic scales. Thermospheric transport driven by wind fields at high latitudes is a key component of the global thermospheric wind transport. In order to understand details of how high latitude wind driven transport influences the lower latitude thermosphere, the precise knowledge of high latitude wind system is required. Current models will require better specifications of thermospheric wind drivers and higher spatial resolutions for simulating thermospheric wind transport accurately, especially at high latitudes.

2.8 References

Anderson, C. (2011), Optical remote sensing of local-scale thermospheric dynamics above Antarctica, *Thesis*.

Anderson, C., T. Davies, M. Conde, P. Dyson, and M. J. Kosch (2011), Spatial sampling of the thermospheric vertical wind field at auroral latitudes, *J. Geophys. Res. Sp. Phys.*, *116*(A6), A06,320, doi: 10.1029/2011ja016485.

Anderson, C., M. Conde, and M. G. McHarg (2012), Neutral thermospheric dynamics observed with two scanning Doppler imagers: 1. Monostatic and bistatic winds, *J. Geophys. Res. Sp. Phys.*, *117*(A3), A03,304, doi: 10.1029/2011ja017041.

Aruliah, A. L., and E. Griffin (2001), Evidence of meso-scale structure in the high-latitude thermosphere, *Ann. Geophys.*, *19*(1), 37–46, doi: 10.5194/angeo-19-37-2001.

Aruliah, A. L., and D. Rees (1995), The trouble with thermospheric vertical winds: Geomagnetic, seasonal and solar cycle dependence at high latitudes, *J. Atmos. Terr. Phys.*, *57*(6), 597–609, doi: 10.1016/0021-9169(94)00100-3.

Aruliah, A. L., A. D. Farmer, D. Rees, and U. Brändström (1996), The seasonal behavior of high-latitude thermospheric winds and ion velocities observed over one solar cycle, *J. Geophys. Res.*, *101*(A7), 15,701, doi: 10.1029/96JA00360.

Aruliah, A. L., E. M. Griffin, I. McWhirter, A. D. Aylward, E. A. K. Ford, A. Charalambous, M. J. Kosch, C. J. Davis, and V. S. C. Howells (2004), First tristatic studies of meso-scale ion-neutral dynamics and energetics in the high-latitude upper atmosphere using collocated FPIs and EISCAT radar, *Geophys. Res. Lett.*, *31*(3), L03,802, doi: 10.1029/2003gl018469.

Aruliah, A. L., E. M. Griffin, A. D. Aylward, E. A. K. Ford, M. J. Kosch, C. J. Davis, V. S. C. Howells, S. E. Pryse, H. R. Middleton, and J. Jussila (2005), First direct evidence of meso-scale variability on ion-neutral dynamics using co-located tristatic FPIs and EISCAT radar in Northern Scandinavia, *Ann. Geophys.*, *23*(1), 147–162, doi: 10.5194/angeo-23-147-2005.

Bailey, G. (1983), The effect of a meridional $E \times B$ drift on the thermal plasma at L = 1.4, *Planet. Sp. Sci.*, *31*(4), 389–409, doi: 10.1016/0032-0633(83)90154-X.

Baker, D. J. (1978), Studies of atmospheric infrared emissions rep. AFGL-TR-78-0251, Air Force Geophysics Lab. Bedford, Massachusetts.

Baker, D. J., and A. T. Stair (1988), Rocket measurements of the altitude distributions of the hydroxyl airglow, *Phys. Scr.*, *37*(4), 611–622, doi: 10.1088/0031-8949/37/4/021.

Banks, P., and G. Kockarts (1973), *Aeronomy*, 1–31 pp., Elsevier, doi: 10.1016/B978-0-12-077802-7.50006-3.

Bates, D., and M. Nicolet (1950), The photochemistry of atmospheric water vapor, *J. Geophys. Res.*, *55*(3), 301–327.

Batten, S., and D. Rees (1990), Thermospheric winds in the auroral oval: Observations of small scale structures and rapid fluctuations by a Doppler Imaging System, *Planet. Sp. Sci.*, *38*(5), 675–694, doi: 10.1016/0032-0633(90)90074-Z.

Baumgardner, J., J. Wroten, J. Semeter, J. Kozyra, M. Buonsanto, P. Erickson, and M. Mendillo (2007), A very bright SAR arc: implications for extreme magnetosphere-ionosphere coupling, *Ann. Geophys.*, *25*(12), 2593–2608, doi: 10.5194/angeo-25-2593-2007.

Biondi, M. A., and W. A. Feibelman (1968), Twilight and nightglow spectral line shapes of oxygen λ6300 and λ5577 radiation, *Planet. Sp. Sci.*, *16*(4), 431–443, doi: 10.1016/0032-0633(68)90158-X.

Biondi, M. A., and D. P. Sipler (1984), Studies of equatorial 630.0 nm airglow enhancements produced by a chemical release in the F-region, *Planet. Sp. Sci.*, *32*(12), 1605–1610, doi: 10.1016/0032-0633(84)90029-1.

Biondi, M. A., D. P. Sipler, M. E. Zipf, and J. L. Baumgardner (1995), All-sky Doppler interferometer for thermospheric dynamics studies, *Appl. Opt.*, *34*(10), 1646–1654.

Buonsanto, M. J., and T. J. Fuller-Rowell (1997), Strides made in understanding space weather at Earth, *Eos, Trans. Am. Geophys. Union*, *78*(1), 1–7, doi: 10.1029/97eo00002.

Buonsanto, M. J., J. E. Salah, K. L. Miller, W. L. Oliver, R. G. Burnside, and P. G. Richards (1989), Observations of neutral circulation at mid-latitudes during the equinox transition study, *J. Geophys. Res.*, *94*(A12), 16,987, doi: 10.1029/JA094iA12p16987.

Burch, J. L., P. H. Reiff, J. D. Menietti, R. A. Heelis, W. B. Hanson, S. D. Shawhan, E. G. Shelley, M. Suguira, D. R. Weimer, and J. D. Winningham (1985), IMF By-dependent plasma flow and Birkeland currents in the dayside magnetosphere, 1, Dynamics Explorer observations, *J. Geophys. Res.*, *90*.

Burnside, R. G., and C. A. Tepley (1989), Optical observations of thermospheric neutral winds at Arecibo between 1980 and 1987, *J. Geophys. Res.*, *94*(A3), 2711, doi: 10.1029/JA094iA03p02711.

Burnside, R. G., F. A. Herrero, J. W. Meriwether, and J. C. G. Walker (1981), Optical observations of thermospheric dynamics at Arecibo, *J. Geophys. Res. Sp. Phys.*, *86*(A7), 5532–5540, doi: 10.1029/JA086iA07p05532.

Cole, K. D. (1965), Stable auroral red arcs, sinks for energy of D_{st} main phase, *J. Geophys. Res.*, *70*(7), 1689–1706, doi: 10.1029/JZ070i007p01689.

Conde, M., and P. Dyson (1995a), Thermospheric horizontal winds above Mawson, Antarctica, *Adv. Sp. Res.*, *16*(5), 41–52, doi: 10.1016/0273-1177(95)00171-A.

Conde, M., and P. Dyson (1995b), Thermospheric vertical winds above Mawson, Antarctica, *J. Atmos. Terr. Phys.*, *57*(6), 589–596, doi: 10.1016/0021-9169(94)00099-A.

Conde, M., and R. W. Smith (1995), Mapping thermospheric winds in the auroral zone, *Geophys. Res. Lett.*, *22*(22), 3019–3022, doi: 10.1029/95GL02437.

Conde, M., and R. W. Smith (1998a), Simultaneous observations of the aurora and of non-uniform thermospheric winds, from Poker Flat, Alaska, *Proc NIPR Symp Up Atmos Phys (Nat Inst Polar Res)*, *12*, 30–38.

Conde, M., and R. W. Smith (1998b), Spatial structure in the thermospheric horizontal wind above Poker Flat, Alaska, during solar minimum, *J. Geophys. Res.*, *103*(A5), 9471–9949, doi: 10.1029/97JA03331.

Conde, M., J. D. Craven, T. Immel, E. Hoch, H. Stenbaek-Nielsen, T. Hallinan, R. W. Smith, J. Olson, W. Sun, L. A. Frank, and J. Sigwarth (2001), Assimilated observations of thermospheric winds, the aurora, and ionospheric currents over Alaska, *J. Geophys. Res. Sp. Phys.*, *106*(A6), 10,493–10,508, doi: 10.1029/2000JA000135.

Cowley, S. W., J. P. Morelli, and M. Lockwood (1991), Dependence of convective flows and particle precipitation in the high-latitude dayside ionosphere on the X and Y components of the interplanetary magnetic field, *J. Geophys. Res.*, *96*, 5557.

Crickmore, R., J. Dudeney, and A. Rodger (1991), Vertical thermospheric winds at the equatorward edge of the auroral oval, *J. Atmos. Terr. Phys.*, *53*(6-7), 485–492, doi: 10.1016/0021-9169(91)90076-J.

Crickmore, R. I. (1993), A comparison between vertical winds and divergence in the high-latitude thermosphere, *Ann. Geophys.*, *11*, 728–733.

Crickmore, R. I. (1994), Mean thermospheric winds observed from Halley, Antarctica, *Ann. Geophys.*, *12*(10/11), 1101–1113, doi: 10.1007/s00585-994-1101-5.

Deng, Y., and A. J. Ridley (2007), Possible reasons for underestimating Joule heating in global models: E field variability, spatial resolution, and vertical velocity, *J. Geophys. Res.*, *112*(A9), A09,308, doi: 10.1029/2006JA012006.

Dhadly, M. S., J. Meriwether, M. Conde, and D. Hampton (2015), First ever cross comparison of thermospheric wind measured by narrow- and wide-field optical Doppler spectroscopy, *J. Geophys. Res. Sp. Phys.*, doi: 10.1002/2015JA021316.

Dickinson, R. E., E. C. Ridley, and R. G. Roble (1981), A three-dimensional general circulation model of the thermosphere, *J. Geophys. Res.*, *86*(A3), 1499–1512, doi: 10.1029/JA086iA03p01499.

Dickinson, R. E., E. C. Ridley, and R. G. Roble (1984), Thermospheric general circulation with coupled dynamics and composition, *J. Atmos. Sci.*, *41*(2), 205–219, doi: 10.1175/1520-0469.

Drob, D. P., J. T. Emmert, G. Crowley, J. M. Picone, G. G. Shepherd, W. Skinner, P. Hays, R. J. Niciejewski, M. Larsen, C. Y. She, J. W. Meriwether, G. Hernandez, M. J. Jarvis, D. P. Sipler, C. A. Tepley, M. S. O'Brien, J. R. Bowman, Q. Wu, Y. Murayama, S. Kawamura, I. M. Reid, and R. A. Vincent (2008), An empirical model of the Earth's horizontal wind fields: HWM07, *J. Geophys. Res. Sp. Phys.*, *113*(12), 1–18, doi: 10.1029/2008JA013668.

Drob, D. P., J. T. Emmert, J. W. Meriwether, J. J. Makela, E. Doornbos, M. Conde, G. Hernandez, J. Noto, K. A. Zawdie, S. E. McDonald, J. D. Huba, and J. H. Klenzing (2015), An update to the Horizontal Wind Model (HWM): The quiet time thermosphere, *Earth Sp. Sci.*, *2*, doi: 10.1002/2014EA000089.

East, S., N. Meredith, M. Harris, D. Rees, V. Wickwar, I. K. Monson, and H. G. Muller (1995), First summer results on winds in the upper mesosphere derived from the 843 nm hydroxyl emissions measured from the Bear Lake Observatory, Utah, *J. Atmos. Terr. Phys.*, *57*(9), 995–1008, doi: 10.1016/0021-9169(94)00086-4.

Emmert, J. T., M. L. Faivre, G. Hernandez, M. J. Jarvis, J. W. Meriwether, R. J. Niciejewski, D. P. Sipler, and C. A. Tepley (2006a), Climatologies of nighttime upper thermospheric winds measured by ground-based Fabry-Perot interferometers during geomagnetically quiet conditions: 1. Local time, latitudinal, seasonal, and solar cycle dependence, *J. Geophys. Res.*, *111*(A12), A12,302, doi: 10.1029/2006JA011948.

Emmert, J. T., G. Hernandez, M. J. Jarvis, R. J. Niciejewski, D. P. Sipler, and S. Vennerstrom (2006b), Climatologies of nighttime upper thermospheric winds measured by ground-based Fabry-Perot interferometers during geomagnetically quiet conditions: 2. High-latitude circulation and interplanetary magnetic field dependence, *J. Geophys. Res.*, *111*(A12), A12,303, doi: 10.1029/2006JA011949.

Emmert, J. T., D. P. Drob, G. G. Shepherd, G. Hernandez, M. J. Jarvis, J. W. Meriwether, R. J. Niciejewski, D. P. Sipler, and C. A. Tepley (2008), DWM07 global empirical model of upper thermospheric storm-induced disturbance winds, *J. Geophys. Res.*, *113*(A11), A11,319, doi: 10.1029/2008JA013541.

Forster, M., and I. Cnossen (2013), Upper atmosphere differences between northern and southern high latitudes: The role of magnetic field asymmetry, *J. Geophys. Res. Sp. Phys.*, *118*(9), 5951–5966, doi: 10.1002/jgra.50554.

Forster, M., S. Rentz, W. Köhler, H. Liu, and S. E. Haaland (2008), IMF dependence of high-latitude thermospheric wind pattern derived from CHAMP cross-track measurements, *Ann. Geophys.*, *26*(6), 1581–1595, doi: 10.5194/angeo-26-1581-2008.

Forster, M., S. E. Haaland, and E. Doornbos (2011), Thermospheric vorticity at high geomagnetic latitudes from CHAMP data and its IMF dependence, *Ann. Geophys.*, *29*(1), 181–186, doi: 10.5194/angeo-29-181-2011.

Foster, J. C., J.-P. St.-Maurice, and V. J. Abreu (1983), Joule heating at high latitudes, *J. Geophys. Res.*, *88*(A6), 4885, doi: 10.1029/JA088iA06p04885.

French, W. J. R., and F. J. Mulligan (2010), Stability of temperatures from TIMED/SABER v1.07 (2002-2009) and Aura/MLS v2.2 (2004-2009) compared with OH(6-2) temperatures observed at Davis Station, Antarctica, *Atmos. Chem. Phys. Discuss.*, *10*(9), 21,547–21,565, doi: 10.5194/acpd-10-21547-2010.

French, W. J. R., G. B. Burns, K. Finlayson, P. A. Greet, R. P. Lowe, and P. F. B. Williams (2000), Hydroxyl (6-2) airglow emission intensity ratios for rotational temperature determination, *Ann. Geophys.*, *18*(10), 1293–1303, doi: 10.1007/s005850000260.

Fuller-Rowell, T. J., and D. Rees (1980), A Three-Dimensional Time-Dependent Global Model of the Thermosphere, *J. Atmos. Sci.*, *37*, 2545–2567, doi: 10.1175/1520-0469(1980)037.

Geisler, J. (1967), A numerical study of the wind system in the middle thermosphere, *J. Atmos. Terr. Phys.*, *29*(12), 1469–1482, doi: 10.1016/0021-9169(67)90100-6.

Greet, P. A., W. J. R. French, G. B. Burns, P. F. B. Williams, R. P. Lowe, and K. Finlayson (1997), OH(6-2) spectra and rotational temperature measurements at Davis, Antarctica, *Ann. Geophys.*, *16*(1), 77, doi: 10.1007/s005850050581.

Greet, P. A., M. G. Conde, P. L. Dyson, J. L. Innis, A. M. Breed, and D. J. Murphy (1999), Thermospheric wind field over Mawson and Davis, Antarctica; simultaneous observations by two Fabry-Perot spectrometers of λ630 nm emission, *J. Atmos. Sol. Terr. Phys.*, *61*(14), 1025–1045, doi: http://dx.doi.org/10.1016/S1364-6826(99)00059-0.

Greet, P. A., J. L. Innis, and P. L. Dyson (2002), Thermospheric vertical winds in the auroral oval/polar cap region, *Ann. Geophys.*, *20*(12), 1987–2001.

Griffin, E. M., A. L. Aruliah, I. McWhirter, and T. Yeoman (2002), Thermospheric neutral temperature measurements from the University College London Fabry-Perot interferometers, *Sadankyla Geophys. Obs. Publ.*, *92*, 117–120.

Griffin, E. M., A. Aruliah, I. C. F. Müller-Wodarg, and A. Aylward (2004), Comparison of high-latitude thermospheric meridionalwinds II: combined FPI, radar and model Climatologies, *Ann. Geophys.*, *22*(3), 863–876, doi: 10.5194/angeo-22-863-2004.

Griffin, E. M., A. L. Aruliah, I. McWhirter, H. C. I. Yiu, A. Charalambous, and I. McCrea (2008), Upper thermospheric neutral wind and temperature measurements from an extended spatial field, *Ann. Geophys.*, *26*(9), 2649–2655, doi: 10.5194/angeo-26-2649-2008.

Guo, W., and D. McEwen (2003), Vertical winds in the central polar cap, *Geophys. Res. Lett.*, *30*(14), 1–4, doi: 10.1029/2003GL017124.

Hays, P., and J. Walker (1966), Doppler profiles of the 5577 Å airglow, *Planet. Sp. Sci.*, *14*(12), 1331–1337, doi: 10.1016/0032-0633(66)90085-7.

Hays, P. B., D. W. Rusch, R. G. Roble, and J. C. G. Walker (1978), The O I (6300 Å) airglow, *Rev. Geophys.*, *16*(2), 225, doi: 10.1029/RG016i002p00225.

Hays, P. B., J. W. Meriwether, and R. G. Roble (1979), Nighttime thermospheric winds at high latitudes, *J. Geophys. Res. Sp. Phys.*, *84*(A5), 1905–1913, doi: 10.1029/JA084iA05p01905.

Hays, P. B., T. L. Killeen, N. W. Spencer, L. E. Wharton, R. G. Roble, B. A. Emery, T. J. Fuller-Rowell, D. Rees, L. A. Frank, and J. D. Craven (1984), Observations of the dynamics of the polar thermosphere, *J. Geophys. Res. Sp. Phys.*, *89*(A7), 5597–5612, doi: 10.1029/JA089iA07p05597.

Hedin, A., E. Fleming, A. Manson, F. Schmidlin, S. Avery, R. Clark, S. Franke, G. Fraser, T. Tsuda, F. Vial, and R. Vincent (1996), Empirical wind model for the upper, middle and lower atmosphere, *J. Atmos. Terr. Phys.*, *58*(13), 1421–1447, doi: 10.1016/0021-9169(95)00122-0.

Hedin, A. E. (1987), MSIS-86 Thermospheric Model, *J. Geophys. Res.*, *92*(A5), 4649, doi: 10.1029/JA092iA05p04649.

Hedin, A. E., J. E. Salah, J. V. Evans, C. A. Reber, G. P. Newton, N. W. Spencer, D. C. Kayser, D. Alcaydé, P. Bauer, L. Cogger, and J. P. McClure (1977a), A global thermospheric model based on mass spectrometer and incoherent scatter data MSIS, 1. N_2 density and temperature, *J. Geophys. Res.*, *82*(16), 2139–2147, doi: 10.1029/JA082i016p02139.

Hedin, A. E., C. A. Reber, G. P. Newton, N. W. Spencer, H. C. Brinton, H. G. Mayr, and W. E. Potter (1977b), A global thermospheric model based on mass spectrometer and incoherent scatter data MSIS. II - Composition, *J. Geophys. Res.*, *82*(16).

Hedin, A. E., N. W. Spencer, and T. L. Killeen (1988), Empirical global model of upper thermosphere winds based on Atmosphere and Dynamics Explorer satellite data, *J. Geophys. Res.*, *93*(A9), 9959, doi: 10.1029/JA093iA09p09959.

Hedin, A. E., M. A. Biondi, R. G. Burnside, G. Hernandez, R. M. Johnson, T. L. Killeen, C. Mazaudier, J. W. Meriwether, J. E. Salah, R. J. Sica, R. W. Smith, N. W. Spencer, V. B. Wickwar, and T. S. Virdi (1991), Revised global model of thermosphere winds using satellite and ground-based observations, *J. Geophys. Res.*, *96*(A5), 7657, doi: 10.1029/91JA00251.

Heppner, J. P. (1972), Polar-cap electric field distributions related to the interplanetary magnetic field direction, *J. Geophys. Res.*, *77*(25), 4877–4887, doi: 10.1029/JA077i025p04877.

Heppner, J. P., and N. C. Maynard (1987), Empirical high-latitude electric field models, *J. Geophys. Res.*, *92*(A5), 4467, doi: 10.1029/JA092iA05p04467.

Heppner, J. P., and M. L. Miller (1982), Thermospheric winds at high latitudes from chemical release observations, *J. Geophys. Res.*, *87*(A3), 1633, doi: 10.1029/JA087iA03p01633.

Hernandez, G. (1971), The signature profiles of In the airglow, *Planet. Sp. Sci.*, *19*(5), 467–476, doi: 10.1016/0032-0633(71)90162-0.

Hernandez, G. (1982), Vertical motions of the neutral thermosphere at midlatitude, *Geophys. Res. Lett.*, *9*(5), 555–557, doi: 10.1029/GL009i005p00555.

Hernandez, G., and R. G. Roble (1976), Direct measurements of nighttime thermospheric winds and temperatures, 1. Seasonal variations during geomagnetic quiet periods, *J. Geophys. Res.*, *81*(13), 2065–2074, doi: 10.1029/JA081i013p02065.

Hernandez, G., and R. G. Roble (1984), The geomagnetic quiet nighttime thermospheric wind pattern over Fritz Peak observatory during solar cycle minimum and maximum, *J. Geophys. Res.*, *89*(A1), 327–337, doi: 10.1029/JA089iA01p00327.

Hernandez, G., F. G. McCormac, and R. W. Smith (1991), Austral thermospheric wind circulation and interplanetary magnetic field orientation, doi: 10.1029/90JA02458.

Innis, J., P. Greet, D. Murphy, M. Conde, and P. Dyson (1999), A large vertical wind in the thermosphere at the auroral oval/polar cap boundary seen simultaneously from Mawson and Davis, Antarctica, *J. Atmos. Sol. Terr. Phys.*, *61*(14), 1047–1058, doi: 10.1016/S1364-6826(99)00060-7.

Innis, J. L., and M. Conde (2001), Thermospheric vertical wind activity maps derived from Dynamics Explorer-2 WATS observations, *Geophys. Res. Lett.*, *28*(20), 3847–3850, doi: 10.1029/2001GL013704.

Innis, J. L., and M. Conde (2002), High-latitude thermospheric vertical wind activity from Dynamics Explorer 2 Wind and Temperature Spectrometer observations: Indications of a source region for polar cap gravity waves, *J. Geophys. Res.*, *107*(A8), 1172, doi: 10.1029/2001JA009130.

Ishii, M. (2005), Relationship between thermospheric vertical wind and the location of ionospheric current in the polar region, *Adv. polar Up. Atmos. Res.*, *19*, 63–70.

Ishii, M., S. Oyama, S. Nozawa, R. Fujii, E. Sagawa, S. Watari, and H. Shinagawa (1999), Dynamics of Neutral Wind in the polar region observed with two Fabry-Perot Interferometers, *Earth Planets Sp.*, *51*(7-8), 833–844, doi: 10.1186/BF03353242.

Ishii, M., M. Conde, R. W. Smith, M. Krynicki, E. Sagawa, and S. Watari (2001), Vertical wind observations with two Fabry-Perot interferometers at Poker Flat, Alaska, *J. Geophys. Res. Sp. Phys.*, *106*(A6), 10,537–10,551, doi: 10.1029/2000ja900148.

Ishii, M., M. Kubota, M. Conde, R. W. Smith, and M. Krynicki (2004), Vertical wind distribution in the polar thermosphere during Horizontal e Region Experiment (HEX) campaign, *J. Geophys. Res. Sp. Phys.*, *109*(A12), 1–9, doi: 10.1029/2004JA010657.

Jacchia, L. G. (1965), Static diffusion models of the upper atmosphere with empirical temperature profiles, *Smithson. Contrib. to Astrophys.*, *8*.

Jacka, F. (1985), Application of Fabry-Perot spectrometers for measurement of upper atmosphere temperatures and winds, *Int. Counc. Sci. Unions Middle Atmos. Handb.*, *13*, 19–40.

Jacka, F., A. R. D. Bower, D. F. Creighton, and P. A. Wilksch (1980), A large-aperture high-resolution Fabry-Perot spectrometer for airglow studies, *J. Phys. E.*, *13*(5), 562–568, doi: 10.1088/0022-3735/13/5/023.

Johnson, R. M., and T. L. Killeen (Eds.) (1995), *The Upper Mesosphere and Lower Thermosphere: A Review of Experiment and Theory*, *Geophysical Monograph Series*, vol. 87, American Geophysical Union, Washington, D. C., doi: 10.1029/GM087.

Kelly, M. C. (1989), *The Earth's Ionosphere: Plasma Physics & Electrodynamics*, vol. 43, Academic Press.

Keskinen, M. J., and P. Satyanarayana (1993), Nonlinear unstable auroral-arc driven thermospheric winds in an ionosphere-magnetosphere coupled model, *Geophys. Res. Lett.*, *20*(23), 2687–2690, doi: 10.1029/93GL01978.

Killeen, T. L. (1987), Energetics and dynamics of the Earth's thermosphere, *Rev. Geophys.*, *25*(3), 433–454.

Killeen, T. L., and R. G. Roble (1988), Thermosphere dynamics: Contributions from the first 5 years of the Dynamics Explorer Program, *Rev. Geophys.*, *26*(2), 329–367, doi: 10.1029/RG026i002p00329.

Killeen, T. L., P. B. Hays, N. W. Spencer, and L. E. Wharton (1982), Neutral winds in the polar thermosphere as measured from Dynamics Explorer, *Geophys. Res. Lett.*, *9*(9), 957–960, doi: 10.1029/GL009i009p00957.

Killeen, T. L., P. B. Hays, G. R. Carignan, R. A. Heelis, W. B. Hanson, N. W. Spencer, and L. H. Brace (1984), Ion-neutral coupling in the high-latitude F region: Evaluation of ion heating terms from Dynamics Explorer 2, *J. Geophys. Res.*, *89*(A9), 7495, doi: 10.1029/JA089iA09p07495.

Killeen, T. L., P. B. Hays, R. A. Heelis, W. B. Hanson, and N. W. Spencer (1985), Neutral motions in the polar thermosphere for northward Interplanetary Magnetic Field, *Geophys. Res. Lett.*, *12*(4), 159–162, doi: 10.1029/GL012i004p00159.

Killeen, T. L., R. G. Roble, R. W. Smith, N. W. Spencer, J. W. Meriwether, D. Rees, G. Hernandez, P. B. Hays, L. L. Cogger, D. P. Sipler, M. A. Biondi, and C. A. Tepley (1986), Mean neutral circulation in the winter polar F region, *J. Geophys. Res. Sp. Phys.*, *91*(A2), 1633–1649, doi: 10.1029/JA091iA02p01633.

Killeen, T. L., Y.-I. Won, R. J. Niciejewski, and A. G. Burns (1995), Upper thermosphere winds and temperatures in the geomagnetic polar cap: Solar cycle, geomagnetic activity, and interplanetary magnetic field dependencies, *J. Geophys. Res.*, *100*(A11), 21,327, doi: 10.1029/95JA01208.

Kohl, H., and J. King (1967), Atmospheric winds between 100 and 700 km and their effects on the ionosphere, *J. Atmos. Terr. Phys.*, *29*(9), 1045–1062, doi: 10.1016/0021-9169(67)90139-0.

Kosch, M. J., and E. Nielsen (1995), Coherent radar estimates of average high-latitude ionospheric Joule heating, *J. Geophys. Res.*, *100*(A7), 12,201, doi: 10.1029/95JA00821.

Kosch, M. J., M. Ishii, A. Kohsiek, D. Rees, K. Schlegel, T. Hagfors, and K. Cierpka (2000), A comparison of vertical thermospheric winds from Fabry-Perot interferometer measurements over a 50 km baseline, *Adv. Sp. Res.*, *26*(6), 985–988, doi: 10.1016/S0273-1177(00)00042-9.

Kosch, M. J., K. Cierpka, M. T. Rietveld, T. Hagfors, and K. Schlegel (2001), High-latitude ground-based observations of the thermospheric ion-drag time constant, *Geophys. Res. Lett.*, *28*(7), 1395–1398, doi: 10.1029/2000GL012380.

Kwak, Y. S., and A. D. Richmond (2007), An analysis of the momentum forcing in the high-latitude lower thermosphere, *J. Geophys. Res.*, *112*(A1), A01,306, doi: 10.1029/2006JA011910.

Kwak, Y. S., and A. D. Richmond (2014), Dependence of the high-latitude lower thermospheric wind vertical vorticity and horizontal divergence on the interplanetary magnetic field, *J. Geophys. Res. Sp. Phys.*, *119*(2), 1356–1368, doi: 10.1002/2013JA019589.

Larsen, M. F. (2002), Winds and shears in the mesosphere and lower thermosphere: Results from four decades of chemical release wind measurements, *J. Geophys. Res. Sp. Phys.*, *107*(A8), SIA 28–1–SIA 28–14, doi: 10.1029/2001ja000218.

Larsen, M. F., and J. W. Meriwether (2012), Vertical winds in the thermosphere, *J. Geophys. Res.*, *117*(A9), A09,319, doi: 10.1029/2012JA017843.

Larsen, M. F., and C. D. Odom (1997), Observations of altitudinal and latitudinal E-region neutral wind gradients near sunset at the magnetic equator, *Geophys. Res. Lett.*, *24*(13), 1711–1714, doi: 10.1029/97GL01469.

Larsen, M. F., S. Fukao, M. Yamamoto, R. Tsunoda, K. Igarashi, and T. Ono (1998), The SEEK Chemical Release Experiment: Observed neutral wind profile in a region of sporadic E, *Geophys. Res. Lett.*, *25*(11), 1789–1792, doi: 10.1029/98GL00986.

Liu, G., and G. G. Shepherd (2006), An empirical model for the altitude of the OH nightglow emission, *Geophys. Res. Lett.*, *33*(9), L09,805, doi: 10.1029/2005GL025297.

Llewellyn, E. J., and B. H. Long (1978), The OH Meinel bands in the airglow-the radiative lifetime, *Can. J. Phys.*, *56*(5), 581–586, doi: 10.1139/p78-076.

Lyons, L. R., T. L. Killeen, and R. L. Walterscheid (1985), The neutral wind "flywheel" as a source of quiet-time, polar-cap currents, *Geophys. Res. Lett.*, *12*(2), 101–104, doi: 10.1029/GL012i002p00101.

Mayr, H., I. Harris, F. Herrero, N. Spencer, F. Varosi, and W. Pesnell (1990), Thermospheric gravity waves: Observations and interpretation using the transfer function model (TFM), *Space Sci. Rev.*, *54*(3-4), doi: 10.1007/BF00177800.

McCormac, F. G., and R. W. Smith (1984), The influence of the interplanetary magnetic field Y component on ion and neutral motions in the polar thermosphere, *Geophys. Res. Lett.*, *11*(9), 935–938, doi: 10.1029/GL011i009p00935.

McCormac, F. G., T. L. Killeen, E. Gombosi, P. B. Hays, and N. W. Spencer (1985), Configuration of the high-latitude thermosphere neutral circulation for IMF By negative and positive, *Geophys. Res. Lett.*, *12*(4), 155–158, doi: 10.1029/GL012i004p00155.

McCormac, F. G., T. L. Killeen, J. P. Thayer, G. Hernandez, C. R. Tschan, J.-J. J. Ponthieu, and N. W. Spencer (1987), Circulation of the polar thermosphere during geomagnetically quiet and active times as observed by Dynamics Explorer 2, *J. Geophys. Res. Sp. Phys.*, *92*(A9), 10,133–10,139, doi: 10.1029/JA092iA09p10133.

Mccormac, F. G., T. L. Killeen, and J. P. Thayer (1991), The influence of IMF B(y) on the high-latitude thermospheric circulation during northward IMF, *J. Geophys. Res.*, *96*(A1), 115, doi: 10.1029/90JA01996.

McDade, I. C., and E. J. Llewellyn (1987), Kinetic parameters related to sources and sinks of vibrationally excited OH in the nightglow, *J. Geophys. Res.*, *92*(A7), 7643, doi: 10.1029/JA092iA07p07643.

McHarg, M. (2005), High-latitude Joule heating response to IMF inputs, *J. Geophys. Res.*, *110*(A8), A08,309, doi: 10.1029/2004JA010949.

Meinel, A. B. (1950a), OH emission bands in the spectrum of the night sky. I, *Astrophys. J.*, *111*, 555, doi: 10.1086/145296.

Meinel, A. B. (1950b), OH emission bands in the spectrum of the night sky. II, *Astrophys. J.*, *112*, 120, doi: 10.1086/145321.

Meriwether, J. W., and P. Shih (1987), On the nighttime signatures of thermospheric winds observed at Sondrestrom, Greenland, as correlated with interplanetary magnetic field parameters, *URSI High Alt. Obs.*, *5*, 329–336.

Meriwether, J. W., J. P. Heppner, J. D. Stolarik, and E. M. Wescott (1973), Neutral winds above 200 km at high latitudes, *J. Geophys. Res.*, *78*(28), 6643–6661, doi: 10.1029/JA078i028p06643.

Meriwether, J. W., T. L. Killeen, F. G. McCormac, A. G. Burns, and R. G. Roble (1988), Thermospheric winds in the geomagnetic polar cap for solar minimum conditions, *J. Geophys. Res.*, *93*(A7), 7478, doi: 10.1029/JA093iA07p07478.

Mikkelsen, I. S., T. S. Jørgensen, M. C. Kelley, M. F. Larsen, E. Pereira, and J. Vickrey (1981), Neutral winds and electric fields in the dusk auroral oval 1. Measurements, *J. Geophys. Res.*, *86*(A3), 1513, doi: 10.1029/JA086iA03p01513.

Millward, G. H., R. J. Moffet, S. Quegan, and T. J. Fuller-Rowell (1996), A coupled thermoshere-ionosphere-plasmasphere model CTIP, *STEP Handb. Ionos. Model.*, p. 239.

Nakajima, H., S. Okano, H. Fukunishi, and T. Ono (1995), Observations of thermospheric wind velocities and temperatures by the use of a Fabry-Perot Doppler imaging system at Syowa Station, Antarctica, *Appl. Opt.*, *34*(36), 8382–8395, doi: 10.1364/AO.34.008382.

Niciejewski, R., T. Killeen, R. Johnson, and J. Thayer (1992), The behavior of the high-latitude F-region neutral thermosphere in relation to IMF parameters, *Adv. Sp. Res.*, *12*(6), 215–218, doi: 10.1016/0273-1177(92)90058-6.

Niciejewski, R. J., T. L. Killeen, and S. C. Solomon (1996), Observations of thermospheric horizontal neutral winds at Watson Lake, Yukon Territory (Λ = 65N), *J. Geophys. Res. Sp. Phys.*, *101*(A1), 241–259, doi: 10.1029/95JA02683.

Offermann, D., and R. Gerndt (1990), Upper mesosphere temperatures from OH-emissions, *Adv. Sp. Res.*, *10*(12), 217–221, doi: 10.1016/0273-1177(90)90399-K.

Osterbrock, D. E., and A. Martel (1992), Sky spectra at a light-polluted site and the use of atomic and OH sky emission lines for wavelength calibration, *Publ. Astron. Soc. Pacific*, *104*, 76, doi: 10.1086/132961.

Osterbrock, D. E., J. P. Fulbright, A. R. Martel, M. J. Keane, S. C. Trager, and G. Basri (1996), Night-sky high-resolution spectral atlas of OH and O_2 emission lines for echelle spectrograph wavelength calibration, *Publ. Astron. Soc. Pacific*, *108*, 277, doi: 10.1086/133722.

Oyama, S., B. J. Watkins, S. Nozawa, S. Maeda, and M. Conde (2005), Vertical ion motion observed with incoherent scatter radars in the polar lower ionosphere, *J. Geophys. Res. Sp. Phys.*, *110*(A4), 1–14, doi: 10.1029/2004JA010705.

Papitashvili, V. O., and F. J. Rich (2002), High-latitude ionospheric convection models derived from Defense Meteorological Satellite Program ion drift observations and parameterized by the interplanetary magnetic field strength and direction, *J. Geophys. Res.*, *107*(A8), 1198, doi: 10.1029/2001JA000264.

Picone, J. M. (2002), NRLMSISE-00 empirical model of the atmosphere: Statistical comparisons and scientific issues, *J. Geophys. Res.*, *107*(A12), 1468, doi: 10.1029/2002JA009430.

Price, G., and F. Jacka (1991), The influence of geomagnetic activity on the upper mesosphere/lower thermosphere in the auroral zone. I. Vertical winds, *J. Atmos. Terr. Phys.*, *53*(10), 909–922, doi: 10.1016/0021-9169(91)90004-Q.

Price, G., R. Smith, and G. Hernandez (1995), Simultaneous measurements of large vertical winds in the upper and lower thermosphere, *J. Atmos. Terr. Phys.*, *57*(6), 631–643, doi: 10.1016/0021-9169(94)00103-U.

Quegan, S. (1982), Theoretical studies of large-scale features of the Earth's mid- to high-latitude ionosphere, *Ph.D. Thesis Sheff. Univ. (England).*

Quegan, S., G. Bailey, R. Moffett, R. Heelis, T. Fuller-Rowell, D. Rees, and R. Spiro (1982), A theoretical study of the distribution of ionization in the high-latitude ionosphere and the plasmasphere: first results on the mid-latitude trough and the light-ion trough, *J. Atmos. Terr. Phys.*, *44*(7), 619–640, doi: 10.1016/0021-9169(82)90073-3.

Rees, D. (1969), Vertical Winds in the lower ionosphere, *J. Br. Interplanet. Soc.*, *22*.

Rees, D. (1971), Ionospheric wind in auroral zone, *J. Br. Interpanet. Soc*, *24*, 233–246.

Rees, D., and A. H. Greenaway (1983), Doppler imaging system: an optical device for measuring vector winds. 1: General principles., *Appl. Opt.*, *22*(7), 1078–83.

Rees, D., E. Dorling, K. Lloyd, and C. Low (1976), The role of neutral winds and ionospheric electric field in forming stable sporadic E-layers, *Planet. Sp. Sci.*, *24*(5), 475–478, doi: 10.1016/0032-0633(76)90092-1.

Rees, D., T. Fuller-Rowell, and R. Smith (1980), Measurements of high latitude thermospheric winds by rocket and ground-based techniques and their interpretation using a three-dimensional, time-dependent dynamical model, *Planet. Sp. Sci.*, *28*(9), 919–932, doi: 10.1016/0032-0633(80)90064-1.

Rees, D., R. Smith, P. Charleton, F. McCormac, N. Lloyd, and A. Steen (1984a), The generation of vertical thermospheric winds and gravity waves at auroral latitudes-I. Observations of vertical winds, *Planet. Sp. Sci.*, *32*(6), 667–684, doi: 10.1016/0032-0633(84)90092-8.

Rees, D., M. Smith, and R. Gordon (1984b), The generation of vertical thermospheric winds and gravity waves at auroral latitudes-II. Theory and numerical modelling of vertical winds, *Planet. Sp. Sci.*, *32*(6), 685–705, doi: 10.1016/0032-0633(84)90093.

Rees, D., T. Fuller-Rowell, R. Gordon, M. Smith, N. Maynard, J. Heppner, N. Spencer, L. Wharton, P. Hays, and T. Killeen (1986), A theoretical and empirical study of the response of the high latitude thermosphere to the sense of the "Y" component of the interplanetary magnetic field, *Planet. Sp. Sci.*, *34*(1), 1–40, doi: 10.1016/0032-0633(86)90100-5.

Rees, D., A. Aruliah, T. J. Fuller-Rowell, V. B. Wickwar, and R. J. Sica (1990), Winds in the upper mesosphere at mid-latitude: First results using an imaging Fabry-Perot Interferometer, *Geophys. Res. Lett.*, *17*(9), 1259–1262, doi: 10.1029/GL017i009p01259.

Rees, D., R. W. Smith, F. Signernes, K. Henriksen, U. Brandstrom, M. Harris, and G. Maskall (1998), Observations of thermospheric neutral winds within the polar cusp and the auroral oval using a Doppler imaging system (DIS), *Ann. Geophys.*, *16*(11), 1461–1474, doi: 10.1007/s00585-998-1461-3.

Richmond, A. D., E. C. Ridley, and R. G. Roble (1992), A thermosphere/ionosphere general circulation model with coupled electrodynamics, *Geophys. Res. Lett.*, *19*(6), 601–604, doi: 10.1029/92gl00401.

Richmond, A. D., C. Lathuillere, and S. Vennerstroem (2003), Winds in the high-latitude lower thermosphere: Dependence on the interplanetary magnetic field, *J. Geophys. Res.*, *108*(A2), 1066, doi: 10.1029/2002JA009493.

Ridley, A. J., Y. Deng, and G. Tóth (2006), The global ionosphere-thermosphere model, *J. Atmos. Sol. Terr. Phys.*, *68*(8), 839–864, doi: 10.1016/j.jastp.2006.01.008.

Ridley, E. C., R. G. Roble, and E. C. Ridley (1994), A thermosphere-ionosphere-mesosphere-electrodynamics general circulation model (time-GCM): Equinox solar cycle minimum simulations (30-500 km), *Geophys. Res. Lett.*, *21*(6), 417–420.

Rieger, E. (1974), Neutral air motions deduced from barium releases experiments-I. Vertical winds, *J. Atmos. Terr. Phys.*, *36*(8), 1377–1385, doi: 10.1016/0021-9169(74)90214-1.

Rishbeth, H., and O. K. Garriott (1969), *Introduction to ionospheric physics*.

Rishbeth, H., R. Gordon, D. Rees, and T. Fuller-Rowell (1985), Modelling of thermospheric composition changes caused by a severe magnetic storm, *Planet. Sp. Sci.*, *33*(11), 1283–1301, doi: 10.1016/0032-0633(85)90007-8.

Rishbeth, H., T. Fuller-Rowell, and D. Rees (1987), Diffusive equilibrium and vertical motion in the thermosphere during a severe magnetic storm : A computational study, *Planet. Sp. Sci.*, *35*(9), 1157–1165, doi: 10.1016/0032-0633(87)90022-5.

Roble, R. G., R. E. Dickinson, and E. C. Ridley (1982), Global circulation and temperature structure of thermosphere with high-latitude plasma convection, *J. Geophys. Res. Sp. Phys.*, *87*(A3), 1599–1614, doi: 10.1029/JA087iA03p01599.

Roble, R. G., E. C. Ridley, A. D. Richmond, and R. E. Dickinson (1988), A coupled thermosphere/ionosphere general circulation model, *Geophys. Res. Lett.*, *15*(12), 1325–1328, doi: 10.1029/GL015i012p01325.

Ruohoniemi, J. M., and R. A. Greenwald (2005), Dependencies of high-latitude plasma convection: Consideration of interplanetary magnetic field, seasonal, and universal time factors in statistical patterns, *J. Geophys. Res.*, *110*(A9), A09,204, doi: 10.1029/2004JA010815.

Salah, J. E., and J. M. Holt (1974), Midlatitude thermospheric winds from incoherent scatter radar and theory, *Radio Sci.*, *9*(2), 301–313, doi: 10.1029/RS009i002p00301.

Sandholt, P. E., H. C. Carlson, and A. Egeland (2002), *Dayside and Polar Cap Aurora*, vol. 270, 278 pp., Springer Netherlands.

Schmitt, G. a., V. J. Abreu, and P. B. Hays (1981), Non-thermal O(1D) produced by dissociative recombination of O_2^+: A theoretical model and observational results, *Planet. Sp. Sci.*, *29*(10), 1095–1099, doi: 10.1016/0032-0633(81)90008-8.

Sica, R. J., M. H. Rees, G. J. Romick, G. Hernandez, and R. G. Roble (1986a), Auroral zone thermospheric dynamics: 1. Averages, *J. Geophys. Res. Sp. Phys.*, *91*(A3), 3231–3244, doi: 10.1029/JA091iA03p03231.

Sica, R. J., M. H. Rees, R. G. Roble, G. Hernandez, and G. J. Romick (1986b), The altitude region sampled by ground-based Doppler temperature measurements of the OI 15867 K emission line in aurorae, *Planet. Sp. Sci.*, *34*(5), 483–488, doi: http://dx.doi.org/10.1016/0032-0633(86)90035-8.

Sica, R. J., G. Hernandez, B. A. Emery, R. G. Roble, R. W. Smith, and M. H. Rees (1989), The control of auroral zone dynamics and thermodynamics by the interplanetary magnetic field dawn-dusk (Y) component, *J. Geophys. Res.*, *94*(A9), 11,921, doi: 10.1029/JA094iA09p11921.

Sipler, D., M. Biondi, and M. Zipf (1995), Vertical winds in the midlatitude thermosphere from Fabry-Perot interferometer measurements, *J. Atmos. Terr. Phys.*, *57*(6), 621–629, doi: 10.1016/0021-9169(94)00102-T.

Sipler, D. P., B. B. Luokkala, and M. A. Biondi (1982), Fabry-Perot determinations of mid-latitude F-region neutral winds and temperatures from 1975 to 1979, *Planet. Sp. Sci.*, *30*(10), 1025–1032, doi: 10.1016/0032-0633(82)90152-0.

Sivjee, G. G. (1992), Airglow hydroxyl emissions, *Planet. Sp. Sci.*, *40*(l), 235–242.

Smith, R., and G. Hernandez (1995), Vertical winds in the thermosphere within the polar cap, *J. Atmos. Terr. Phys.*, *57*(6), 611–620, doi: 10.1016/0021-9169(94)00101-S.

Smith, R. W. (1980), Neutral winds in the polar cap 'Exploration of the polar upper atmosphere', *NATO Adv. Study Institutes Ser.*, *64*(ISBN: 978-94-009-8417-2), 189–198.

Smith, R. W. (1998), Vertical winds: a tutorial, *J. Atmos. Sol. Terr. Phys.*, *60*(14), 1425–1434, doi: 10.1016/S1364-6826(98)00058-3.

Sobral, J., H. Takahashi, M. Abdu, P. Muralikrishna, Y. Sahai, and C. Zamlutti (1992), O(1S) and O(1D) quantum yields from rocket measurements of electron densities and 557.7 and 630.0 nm emissions in the nocturnal F-region, *Planet. Sp. Sci.*, *40*(5), 607–619, doi: 10.1016/0032-0633(92)90002-6.

Solomon, S. C., P. B. Hays, and V. J. Abreu (1988), The auroral 6300 Å emission: Observations and modeling, *J. Geophys. Res.*, *93*(A9), 9867, doi: 10.1029/JA093iA09p09867.

Spencer, N. W., R. F. Theis, L. E. Wharton, and G. R. Carignan (1976), Local vertical motions and kinetic temperature from AE-C as evidence for aurora-induced gravity waves, *Geophys. Res. Lett.*, *3*(6), 313–316, doi: 10.1029/GL003i006p00313.

Spencer, N. W., L. E. Wharton, G. R. Carignan, and J. C. Maurer (1982), Thermosphere zonal winds, vertical motions and temperature as measured from Dynamics Explorer, *Geophys. Res. Lett.*, *9*(9), 953–956, doi: 10.1029/GL009i009p00953.

Streit, G. E. (1976), Temperature dependence of O(1D) rate constants for reactions with O_2, N_2, CO_2, O_3, and H_2O, *J. Chem. Phys.*, *65*(11), 4761, doi: 10.1063/1.432930.

Thayer, J. P., and T. L. Killeen (1991), Vorticity and divergence in the high-latitude upper thermosphere, *Geophys. Res. Lett.*, *18*(4), 701–704, doi: 10.1029/91GL00131.

Thayer, J. P., and T. L. Killeen (1993), A kinematic analysis of the high-latitude thermospheric neutral circulation pattern, *J. Geophys. Res.*, *98*(93), 11,549–11,565, doi: 10.1029/93JA00629.

Walterscheid, R. L., L. R. Lyons, and K. E. Taylor (1985), The perturbed neutral circulation in the vicinity of a symmetric stable auroral arc, *J. Geophys. Res.*, *90*(A12), 12,235, doi: 10.1029/JA090iA12p12235.

Wang, W., T. Killeen, A. Burns, and R. Roble (1999), A high-resolution, three-dimensional, time dependent, nested grid model of the coupled thermosphere-ionosphere, *J. Atmos. Sol. Terr. Phys.*, *61*(5), 385–397, doi: 10.1016/S1364-6826(98)00079-0.

Wardill, P., and F. Jacka (1986), Vertical motions in the thermosphere over Mawson, Antarctica, *J. Atmos. Terr. Phys.*, *48*(3), 289–292, doi: 10.1016/0021-9169(86)90104-2.

Weimer, D. R. (1999), Substorm influence on the ionospheric electric potentials and currents, *J. Geophys. Res.*, *104*(A1), 185, doi: 10.1029/1998JA900075.

Weimer, D. R. (2001), An improved model of ionospheric electric potentials including substorm perturbations and application to the Geospace Environment Modeling November 24, 1996, event, *J. Geophys. Res.*, *106*(A1), 407, doi: 10.1029/2000JA000604.

Whitten, R. C., and I. G. Poppoff (1971), *Fundamentals of Aeronomy*, John Wiley & Sons, Inc.

Wickwar, V. B., J. W. Meriwether, P. B. Hays, and A. F. Nagy (1984), The meridional thermospheric neutral wind measured by radar and optical techniques in the auroral region, *J. Geophys. Res. Sp. Phys.*, *89*(A12), 10,987–10,998, doi: 10.1029/JA089iA12p10987.

Yee, J., and P. Hays (1980), The oxygen polar corona, *J. Geophys. Res.*, *85*(A4), 1795, doi: 10.1029/JA085iA04p01795.

Yee, J.-h. (1988), Non-thermal distribution of O(1D) atoms in the night-time thermosphere, *Planet. Sp. Sci.*, *36*(1), 89–97, doi: 10.1016/0032-0633(88)90149-3.

Zhang, S. P., and G. G. Shepherd (1999), The influence of the diurnal tide on the O(1S) and OH emission rates observed by WINDII on UARS, *Geophys. Res. Lett.*, *26*(4), 529–532, doi: 10.1029/1999GL900033.

Zhang, S. P., and G. G. Shepherd (2004), Solar influence on the O(1D) dayglow emission rate: Global-scale measurements by WINDII on UARS, *Geophys. Res. Lett.*, *31*(7), 1–4, doi: 10.1029/2004GL019447.

Chapter 3

Distortion of Thermospheric Air Masses by Horizontal Neutral Winds Over Poker Flat Measured Using an All-Sky Scanning Doppler Imager[1]

Abstract

An air mass transported by a wind field will become distorted over time by any gradients present in the wind field. To study this effect in Earth's thermosphere, we examine the behavior of a simple parameter that we describe here as the "distortion gradient". It incorporates all of the wind field's departures from uniformity, and is thus capable of representing all contributions to the distortion or mixing of air masses. Distortion gradient is defined such that it is always positive, so averaging over time and/or space does not suppress small-scale features. Conventional gradients, by contrast, are signed quantities that would often average to zero. To analyze the climatological behavior of this distortion gradient in the real thermosphere, we used three years (2010, 2011, and 2012) of thermospheric F-region wind observations from a high latitude ground-based all-sky wavelength scanning Doppler Fabry-Perot interferometer located at Poker Flat, Alaska. Climatological averaging of the distortion gradient allowed us to investigate its diurnal and seasonal (annual) behavior at our observing location. Distortion was observed to be higher before local magnetic midnight and to be seasonally dependent. While maximum distortion occurred before local magnetic midnight under all geomagnetic conditions, the peak distortion occurred earlier under moderate geomagnetic conditions as compared to the quiet geomagnetic conditions, and even earlier still when geomagnetic conditions were active. Peak distortion was stronger and appeared earlier when interplanetary magnetic field (IMF) was southward compared to northward. By contrast, we could not resolve any time-shift effect due to the IMF component tangential to Earth's orbit.

[1]Dhadly, M. S. and M. Conde (2015), Distortion of thermospheric air masses by horizontal neutral winds over Poker Flat measured using an All-Sky scanning Doppler imager, J. Geophys. Res. Space Physics, doi:10.1002/2015JA021800 (submitted to Journal of Geophysical Research).

3.1 Introduction

At high latitudes, thermospheric winds are driven primarily by the net effect of several momentum forces [*Kwak and Richmond*, 2007]: 1) momentum exchange between convecting ions and the neutral gas (ion drag); 2) pressure gradients produced by dayside solar heating, joule heating, and auroral particle precipitation; and 3) inertial forces (e.g., Coriolis and centrifugal). Ionospheric plasma convection can significantly modify the pressure gradient driven neutral wind flow [*Roble et al.*, 1982; *Killeen and Roble*, 1988; *Thayer and Killeen*, 1993]. To first order, high latitude ion drag produces flow fields with significant vorticity but no divergence, whereas the pressure gradient drives divergent but irrotational flow [*Thayer and Killeen*, 1991]. Winds resulting from the combination of these drivers therefore contain gradients associated with both vorticity and divergence, and these gradients play an important role in the thermospheric wind transport.

A uniform wind field will transport air masses intact and undistorted, whereas any non-uniformity in the wind field can distort, stretch, and tear them. For upper thermospheric altitudes it is usually presumed that the thermosphere's large kinematic viscosity attenuates wind gradients, and hence smoothes out any structure present in the wind over distances smaller than synoptic scales. However, experimental observations [e.g., *Conde and Dyson*, 1995; *Conde and Smith*, 1998a,b; *Greet et al.*, 1999; *Aruliah and Griffin*, 2001; *Aruliah et al.*, 2004] actually do show substantial local-scale structure in horizontal thermospheric neutral wind fields, manifesting commonly as shears occurring over distances of $\sim$100 km or less. These local-scale features in the thermosphere obviously correspond to non-uniform flow. The key interest of this paper is to understand how these local-scale non-uniformities would redistribute neutral air masses. Another objective is to characterize any systematic behavior of these non-uniformities above our observing site in Alaska. To address these questions, we have used three years of the upper thermospheric horizontal wind measurements obtained with a ground-based Fabry-Perot Doppler spectrometer located at Poker Flat in Alaska. This instrument operates in an all-sky imaging mode, and uses a separation scanned etalon to resolve Doppler spectra; we refer to it here as a "scanning Doppler imager", which we abbreviate as "SDI".

The first order Taylor expansion of the horizontal wind about the station zenith re-

quires four velocity gradients $\frac{\partial u}{\partial x}$, $\frac{\partial u}{\partial y}$, $\frac{\partial v}{\partial x}$, $\frac{\partial v}{\partial y}$. Gradients are usually classified as either contributing to vorticity ($\frac{\partial u}{\partial y}$, $\frac{\partial v}{\partial x}$) or divergence ($\frac{\partial u}{\partial x}$, $\frac{\partial v}{\partial y}$). To understand how non-uniformities present in the thermospheric wind fields might redistribute the neutral air masses, we have defined a single parameter, called the "distortion gradient" (abbreviated as *Dg* and discussed later) that would indicate the likelihood of the flow to distort neutral air masses taking into account the possible contributions from all four gradient terms.

Because the thermosphere's strong convective stability, it is typically easier for the thermospheric winds to sustain strong local shear, rather than divergence. This consideration, coupled with many years of observational experience with SDI data, lead us to pose a hypothesis that shears are the major sources of distortion for upper thermospheric air masses. The horizontal shears, vertical shears, vorticity, and divergence of the thermosphere have all been examined in the past [e.g., *Thayer and Killeen*, 1991; *Forster et al.*, 2011; *Kwak and Richmond*, 2014], but to our knowledge the resulting distortion of thermospheric air masses introduced by such gradients has not been studied previously. Here we studied the climatology of the distortion in upper thermospheric winds above Alaska for three years (2010, 2011, and 2012) using *Dg* to find any persistent features in the distortion. The long term statistical studies of Fabry-Perot observations, radar studies, and modeling studies of F-region thermosphere have shown a marked dependence of the thermospheric winds on the seasons [e.g., *Roble et al.*, 1977a,b; *Biondi et al.*, 1990; *Aruliah et al.*, 1991a, 1996; *Emmert et al.*, 2006a]. In order to determine if the distortion has any similar seasonal dependencies, we inspected the seasonal behavior of *Dg* for 2010, 2011, and 2012.

Poker Flat is located at auroral latitudes, which can be thought of as a transition zone between mid-latitudes and the polar cap. The equatorward edge of the auroral oval stays poleward of Poker Flat at all times under very quiet conditions. But under moderate levels of geomagnetic activity the auroral oval passes over Poker Flat and, at high activity, the oval lies equatorward of Poker Flat. High latitude thermospheric winds are strongly driven by ionospheric "convective" flow via ion drag. Thus, as geomagnetic conditions change, there is a resulting complex time-dependent modification of the thermospheric wind field [e.g., *Wickwar et al.*, 1984; *Sica et al.*, 1986; *McCormac et al.*, 1987; *Aruliah et al.*,

1991b; *Niciejewski et al.*, 1996; *Emmert et al.*, 2008]. Since the Poker SDI's field of view passes through both the dusk and dawn cell of the ionospheric convection over the course of all but the quietest nights, the SDI wind measurements are always influenced by changes in geomagnetic activity - and wind gradients are inevitably associated with such changes. Even when activity levels are not changing, the ion convection pattern itself contains substantial spatial gradients. Hence, overall, we would expect winds and wind-driven distortion of air masses to depend strongly on ion convection, which itself depends on geomagnetic activity and on the IMF [e.g., *McCormac and Smith*, 1984; *Killeen et al.*, 1985; *McCormac et al.*, 1985; *Rees et al.*, 1986; *Meriwether and Shih*, 1987; *Sica et al.*, 1989; *Mccormac et al.*, 1991; *Niciejewski et al.*, 1992; *Emmert et al.*, 2006b]. Thus, in this study, we were also particularly interested in how the air mass distortion depends on geomagnetic activity and on the IMF.

3.2 Instrumentation and Wind Vector Analysis

An all-sky wavelength scanning Doppler Fabry-Perot of the type first described by *Conde and Smith* [1995, 1998b] and recently by *Conde and Nicolls* [2010] and *Anderson et al.* [2012], was used here for mapping upper thermospheric horizontal winds at auroral latitudes. A short description and principle of operation of an SDI is given below.

The instrument simultaneously records Doppler spectral profiles of optical emissions from many tens of look directions (typically 115) across the sky. The sky is viewed through a fish-eye lens. The beam then passes through a narrowband interference filter of typically 0.5 nm bandwidth before being collimated and entering the separation scanned etalon. A typical full angle field of view of our all-sky lens is $\sim 140^{\circ}$, which corresponds to a radial distance of $\sim$650 km from station zenith if projected at an altitude of 240 km. The scan range of the etalon plate spacing was configured to span exactly one order of interference in 128 discrete steps. When monochromatic skylight passes through the etalon, the transmission is modulated according to incidence angle. A 300 mm $f/2.8$ telephoto lens focuses this angular modulation, thus forming concentric rings on a 512 x 512 pixel high efficiency thermoelectrically cooled electron multiplying CCD detector (EMCCD). Each individual EMCCD pixel acts a separate independent detector, but the

entire 512 x 512-pixel resolution is far higher than needed to describe the angular variation of Doppler shift across the sky. We therefore trade angular resolution for improved spectral signal to noise ratio by summing the contributions from all pixels within each of 115 (typically) software-defined "zones". Because interference order changes with radial distance within a zone, we must compensate for this dependence before we can sum the spectra from all pixels in the zone. We do so using the etalon scanning and phase mapping technique first described by *Conde and Smith* [1997]. An overall "exposure" was obtained by repeating multiple relatively rapid scans (typical scan time ~23 sec) of the etalon, and co-adding the spectra obtained from each of these scans. Control software monitored the accumulating spectra during the exposure, and continued signal integration until adequate signal to noise ratio was reached (on the average) across all zones. During times of weak emission and low signal, the software enforced a maximum integration time of 10 min per exposure. The zone pattern used here was our "standard" observing mode. It was configured such that the circular field of view was divided into eight concentric annular rings centered about the station zenith, with one, six, eight, twelve, sixteen, twenty, twenty-four, and twenty-eight sectors respectively in each ring. The central zone was circular, and the total number of zones thus defined was 115. The zone allocation occurred entirely in software, and could easily be changed as desired. The acquired spectra were then analyzed numerically to determine their spectral width and Doppler shift.

A single station can only measure single line-of-sight (LOS) wind component of what is in reality a three-component wind vector. It is not possible to infer all the three wind components unambiguously from these data. However, it is possible to fit a two-dimensional horizontal vector wind field to a set of azimuthal LOS wind samples under some assumptions. This procedure of wind fitting was first used by *Burnside et al.* [1981]. A detailed discussion of deriving vector winds using this technique is given in *Conde and Smith* [1998b].

3.3 Distortion Gradient

Suppose u_i and v_i are the zonal and meridional components of the horizontal wind vector measured at the i^{th} location in the SDI field of view; u_{ave} and v_{ave} are the uniform background bulk zonal and meridional flows. Then $u_i - u_{ave}$ and $v_i - v_{ave}$ represent the

time rate of distortion in the zonal and meridional directions at that location. We defined distortion gradient (Dg) at that location by the expression:

$$Distortion\ gradient_i = \frac{\sqrt{(u_i - u_{ave})^2 + (v_i - v_{ave})^2}}{r_i} \tag{3.1}$$

where r_i is the horizontal distance of that location from the station zenith. Dg has units of sec^{-1}. Here, Dg was calculated simultaneously at 115 locations (zones) and then averaged, to give one final value per exposure.

Dg was introduced as a simple parameter to describe the overall "severity" of the gradients present in the thermospheric wind field over the instrument's field of view. It basically sums contributions from all wind non-uniformities, including both simple first-order gradients and any higher order perturbations. Dg can be crudely interpreted as indicating the average rate of change of displacement between two tracers moving with the flow and initially separated from each other by a distance d; their rate of change of displacement is simply $d \times Dg$. Of course this interpretation is a gross oversimplification for any two particular tracers at any particular moment of time - the displacement change may occur in any direction, and their actual rate of separation would depend on precisely where they are located within the non-uniform flow. Nevertheless, we contend that the climatological average behavior of the Dg parameter does provide a useful indicator of how distortion and mixing of thermospheric air parcels would depend on factors such as season, local time, and geomagnetic conditions.

Indeed, Dg was originally defined with this averaging application in mind, so one of its properties is that it is always greater than or equal to zero. This is in contrast to conventional gradients (or linear combinations thereof, such as vorticity and divergence) which can be either negative or positive. Averaging of these conventional (signed) gradients over time and/or space can thus produce small values, even if strong gradients were originally present in the contributing individual measurements. Climatological averaging of gradients would therefore often underestimate (possibly grossly) the distortion effects. This is because there are many ways for negative and positive wind gradients to cancel during the averaging process, whereas it is statistically very improbable that their distorting effects on the air masses would cancel similarly. Because Dg is always greater

than or equal to zero, it can safely be used for climatological studies without this concern.

3.4 Observational Data

For this study, we analyzed the data gathered by a 100 mm aperture, high resolution ground-based all-sky SDI observing 630 nm nightglow from the atomic oxygen occurring naturally in the upper thermosphere with centroid emission height of ~240 km. Our data were obtained from Poker Flat (local time = UT - 9, magnetic local time ≈UT + 12.8). Three years of data (2010, 2011, and 2012) were investigated. Totals of 208, 224, and 231 nights of data were recorded in 2010, 2011, and 2012 respectively, including cloudy nights. On a cloudy night, the LOS wind information cannot be used to infer thermospheric winds because the emissions that come from the sky are scattered by clouds. This scattering (Mie scattering) does not change the wavelength of the signal; however angular information regarding the LOS is lost. We eliminated the periods of substantial cloud cover from data by assessing Poker Flat sky conditions using daily Keograms from broadband all-sky imagers (located at Poker Flat), and SDI data themselves - specifically from all-sky wind plots, all-sky temperature and brightness data. Our group has many years of experience with these data sets, and we are very confident that we have correctly eliminated all days for which cloud was significant factor. Hourly auroral electrojet index (AE) and IMF data were taken from the OMNIweb NASA website.

3.5 Results

First we investigated the behavior of the thermospheric Dg, vorticity, and divergence on two individual days of 2012 (07 January and 13 November). These particular days were chosen because they represent wind patterns that we see very commonly in our data from Alaska. The summary wind dial plots as shown in Figure 3.1 and Figure 3.2 were also generated for these two days to show an overview of the evolution of the actual two-dimensional horizontal wind field with time above the observing station (as would be seen by a space-based observer located some distance above the geomagnetic north pole). In these summary wind dial plots, the Sun is always at the top of the figure and the observatory moves anticlockwise around geomagnetic north pole in a circular arc.

Background colors in these plots denote the 630 nm emission intensity derived from

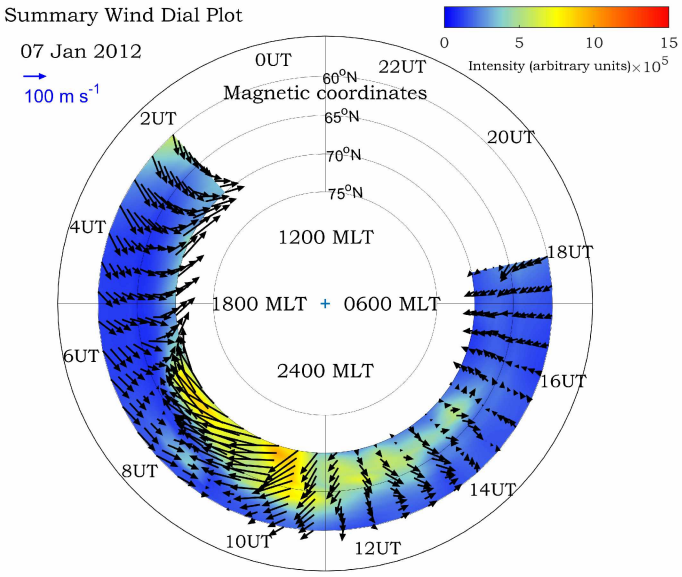

Figure 3.1: Evolution of the F-region thermospheric horizontal neutral winds above Poker Flat on 07 January 2012. In this summary wind dial plot, the sun is always at the top of the plot and the observatory moves anticlockwise around the magnetic north pole in a circular arc (for a space-based observer). Background colors indicate optical emission brightness, in arbitrary units.

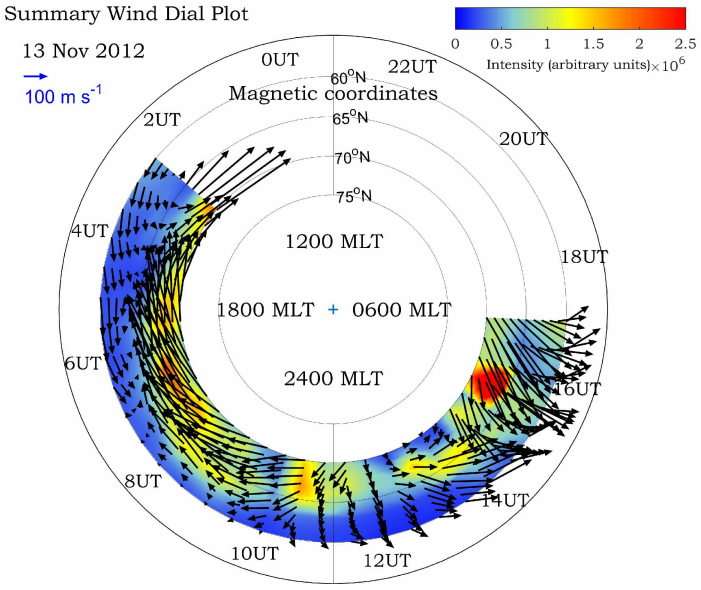

Figure 3.2: Same as for Figure 3.1, but in this case showing data for 13 November 2012.

the SDI spectra. These summary wind dial plots illustrate how the thermospheric wind field above Poker Flat expresses the time varying interplay between two primary drivers: ion drag and the heating induced pressure gradient force. In addition, vorticity and divergence were scaled by a factor of 0.5 to facilitate easy visual comparison with *Dg*, as depicted in Figure 3.3 and Figure 3.4.

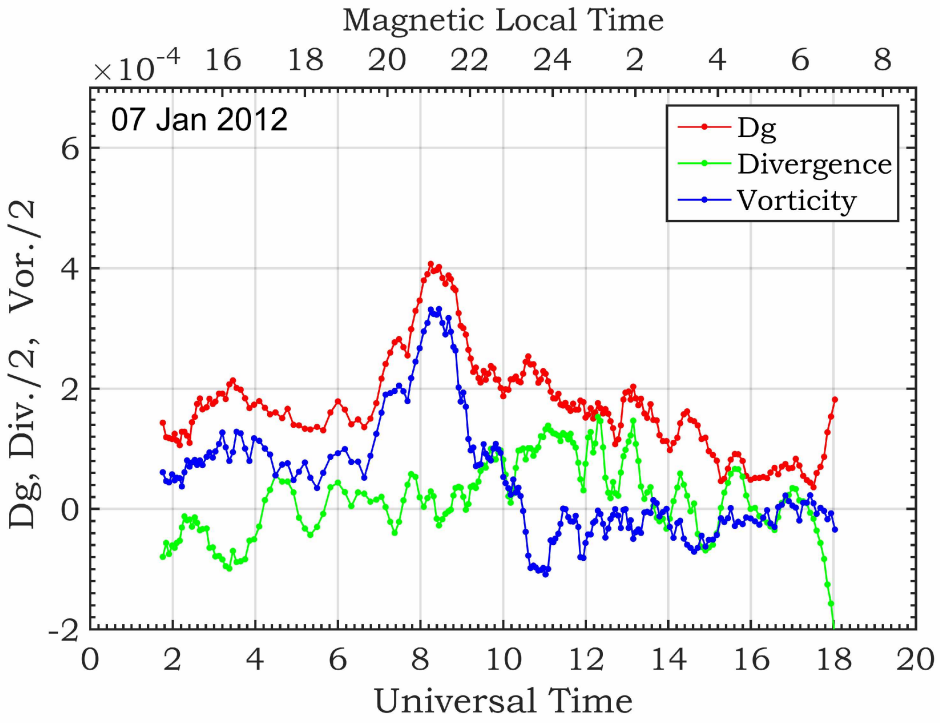

Figure 3.3: *Dg*, divergence, and vorticity on 07 January 2012 using F-region thermospheric wind measurements from Poker Flat SDI.

Inspection of the wind summary plots revealed the presence of many similar wind features on both days. In the beginning of the observation cycle, the winds equatorward of the observatory were antisunward. These flows were presumably associated with the global pressure gradient force established by dayside solar heating. The strong magnetic westward winds poleward of the observatory are commonly observed and are known to be associated with ion-drag resulting from the duskside vortex of the ionospheric convection. The investigations of *Deng and Ridley* [2006] have shown that the coupling between neutrals and ions is stronger in the presence of auroral particle precipitation due to enhancement of the local ion density. On both of the days discussed here, strong neu-

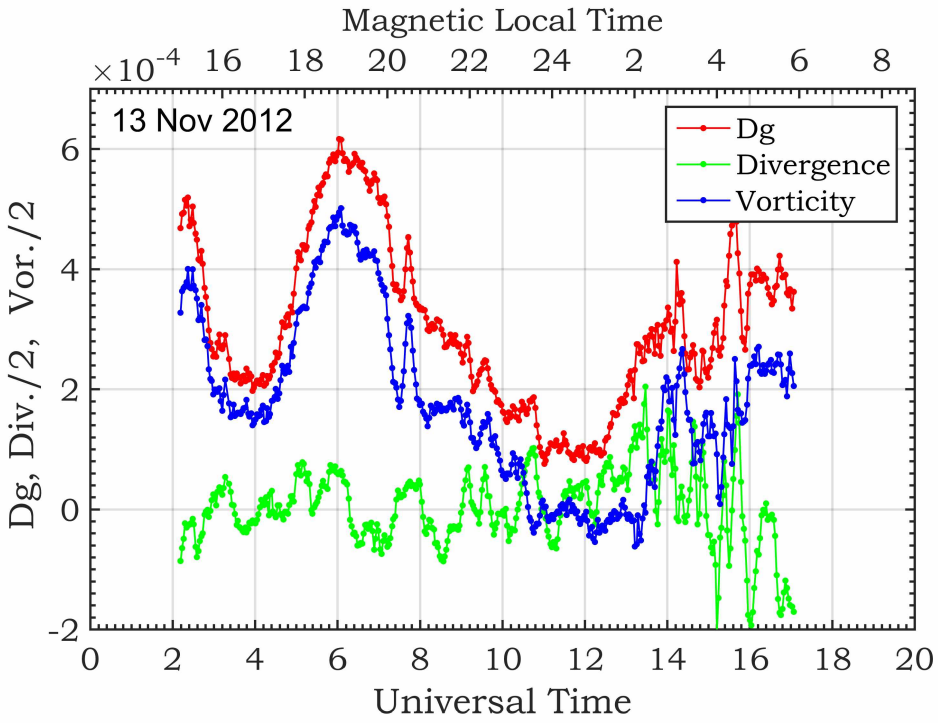

Figure 3.4: Same as for Figure 3.3, but in this case showing data for 13 November 2012.

tral winds were observed in the regions of auroral particle precipitation. A predominant feature in the wind summary plots was the development of a reversal boundary along magnetic east-west due the opposite flows on the poleward and equatorward of the observatory. It produced strong latitudinal shears around the regions of the reversal boundary, and on both days these high sheared flows occurred between 0500 UT and 1000 UT. The reversal boundary located initially poleward of the observatory slowly moved equatorward with the passage of time. These latitudinal shears on the duskside created the largest values of vorticity observed in the thermosphere above Alaska on each of these two days. It is well known that the dawn vortex of thermospheric neutral circulation is normally much weaker than the dusk vortex, and this expectation is strongly confirmed by our own extensive database of wind measurements from Poker Flat. Similar flow characteristics as depicted in Figure 3.1 and Figure 3.2 have been previously reported in many publications [e.g., *Conde and Smith*, 1998b; *Conde et al.*, 2001; *Anderson et al.*, 2012].

On both days, the most prominent feature in Figure 3.3 and Figure 3.4 is the sharp increase in the *Dg* and vorticity in the pre-magnetic midnight sector. *Dg* was obviously

strongly correlated with vorticity. Vorticity is comprised of shear gradients, which implies that shear processes were the major contribution to Dg. In the observed neutral wind field, strong latitudinal shears were present between 0500 UT and 1000 UT and their dominance on Dg can be witnessed in Dg plot (Figure 3.3 and Figure 3.4) on both days. Divergence in the winds was weaker than the vorticity, so its contribution in Dg is not as obvious. Relatively small divergences or convergences are usually observed in the thermosphere, which is not surprising because mass conservation means that large three-dimensional divergences are associated with density and ultimately pressure changes, and the latter strongly oppose the original divergence/convergence that produced them. Purely horizontal divergence can instead be balanced by vertical flow, but even this is difficult because the thermosphere's strongly positive temperature gradient greatly opposes any such vertical motion. Many years of prior SDI data confirm these expectations for local-scale flows. At larger scales, studies by *Thayer and Killeen* [1991] and *Kwak and Richmond* [2014] reached the similar conclusion that vorticity is more important than divergence for typical thermospheric winds. One exception to these arguments does occur relatively easily and frequently in the thermosphere, i.e., during periods of strong acoustic-gravity wave activity. Divergence is in fact required by such waves, at least in brief bursts, to provide the restoring force that allows them to propagate. It is thus not surprising that some contributions to Dg from divergence are recognizable, especially at times when vorticity is small. For example, in Figure 3.3, after 1000UT, divergence was stronger than vorticity, and many short duration features (e.g., spikes) in divergence are also recognizable in the Dg curve at the corresponding times.

To exclude any possibility of error in the analysis code, we performed a two-step validation of the dependence of the Dg on pure vorticity and pure divergence. In a first-order horizontal wind field, only four gradients ($\frac{\partial u}{\partial x}$, $\frac{\partial u}{\partial y}$, $\frac{\partial v}{\partial x}$, and $\frac{\partial v}{\partial y}$) are responsible for producing non-uniform wind flows. In the first step, Dg was calculated using our routine analysis code applied to a numerically simulated uniform horizontal wind field plus divergence, generated using the gradient terms $\frac{\partial u}{\partial x}$ and $\frac{\partial v}{\partial y}$. In the second step, Dg was calculated for a horizontal wind field including vorticity, generated by incorporating $\frac{\partial v}{\partial x}$, and $\frac{\partial u}{\partial y}$ gradient terms. The value of Dg calculated by our code from the first step exactly matched

with the *Dg* from the second step as expected. This procedure demonstrated that our *Dg* calculation is equally sensitive to both vorticity and divergence. Further, to examine the effect of an individual gradient on the *Dg*, it was calculated by keeping only one gradient term and switching off all other three terms. The *Dg* outcome of all four possible cases was identical, which means all the four gradient terms were contributing equally to *Dg*. This calibration exercise thus allows us to confirm that the stronger correlation between *Dg* and vorticity does indeed imply that distortion is more typically driven by shear.

To find the general diurnal behavior of the *Dg*, we analyzed all three years of SDI thermospheric wind measurements. *Dg* was calculated for each exposure available in the three years of wind data. Our data were rich enough to allow hourly binning of the *Dg* for each year. The median of each hourly bin was calculated to produce Figure 3.5. The error

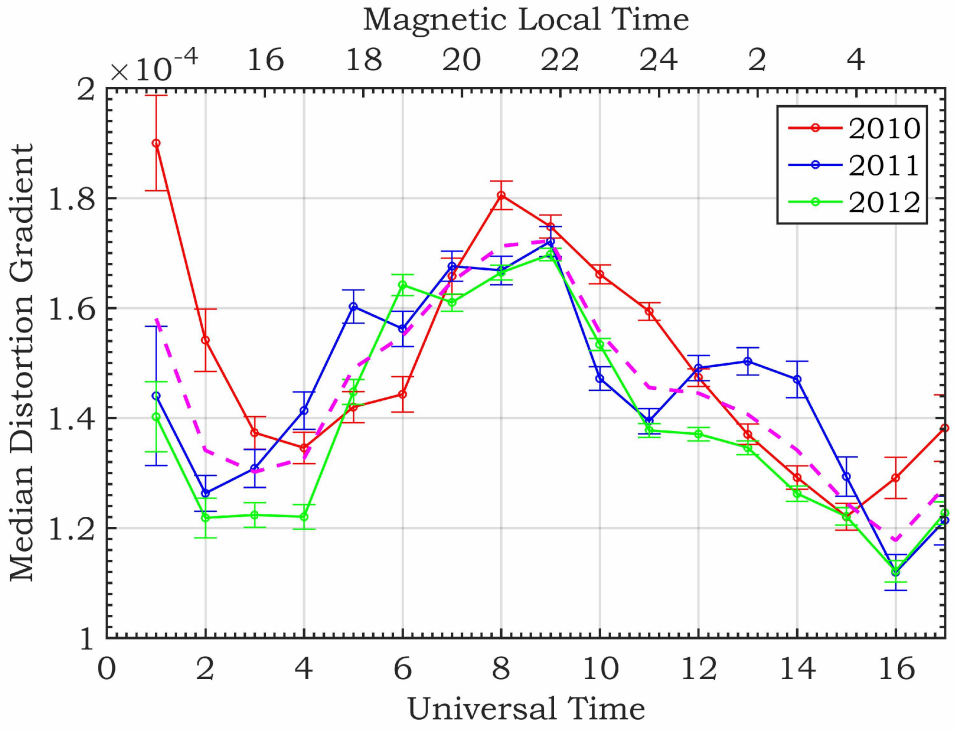

Figure 3.5: Diurnal behavior of *Dg* for 2010, 2011, and 2012. The dashed magenta line represents the average of all the three years. 'Error-bars' indicate the standard deviation of the mean.

bars represents standard deviation around the mean from the data points within each bin. All the three years displayed similar features in the diurnal behavior of the *Dg*. *Dg* was

observed to be small in the evening and morning, but high between 0600 UT and 1000 UT. This feature was consistent in all the three *Dg* curves. Observations on individual days (for example Figure 3.2 - 3.3) showed that highly sheared flows existed in pre-magnetic midnight sector between 0500 UT and 1000 UT along the wind reversal boundary. Shears cause air masses to distort. Figure 3.2 - 3.3 suggests that maximum air mass distortion on the average occurred between 0500 UT and 1000 UT and air mass distortion was higher in the pre-magnetic midnight sector than the post-magnetic midnight sector. The high value of *Dg* in the very beginning (0000 UT to 0200 UT) and at the very end (~1700 UT) of the SDI observation cycle, we believe, was largely due to artifacts in the winds that we frequently encounter as bright twilight contaminates the Doppler spectra. There are also fewer observations at the extreme ends of the observing cycle, and an associated possibility that high *Dg* at these times may partly reflect contributions from few atypical days with strong magnetic westward winds in the beginning of observation cycle.

To make dark sky observations, the Poker Flat SDI was configured to start recording sky exposures when the Sun was more than eight degree below the geometric horizon. Due to the high elevation angle of the Sun in the summer time, Poker Flat SDI usually stops taking measurements by the end of April and it starts the observation cycle again in the fall season around September. The length of night time at Poker Flat has a large seasonal variation. As a result, in peak winter, typical SDI observation cycle spans 0140 UT to 1800 UT and this time coverage gradually decreases to 0800UT - 1200UT (typically) in April. To study the seasonal behavior of *Dg*, we used the SDI measurements recorded only between 0800 UT and 1200 UT. This is because 0800 UT to 1200 UT was the only time interval in which SDI measurements was available in all the seasons (except summer). Inclusion of all the longer time intervals present deeper into the winter season would lead to inaccurate results. This is because *Dg* has a diurnal trend (small in local evening and morning; maximum around local midnight) and all of the wind measurements in local evenings and mornings were recorded only in the winter season. As a result, the inclusion of all the time intervals present in the SDI wind data would lead to underestimation of *Dg* after averaging the data for the winter seasons.

For the seasonal analysis, despite limiting our data choice to the time interval 0800 UT

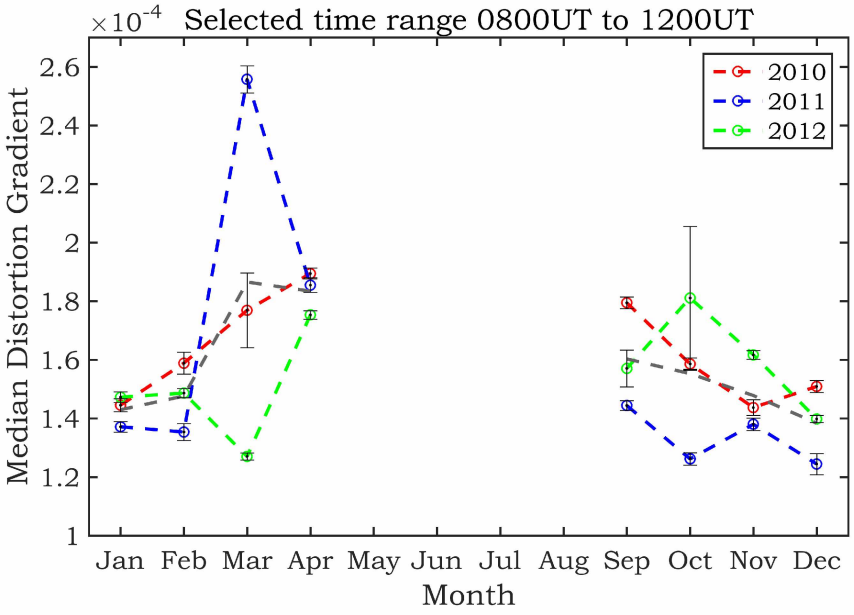

Figure 3.6: Seasonal behavior of *Dg* for 2010, 2011, and 2012. The grey line represents the average *Dg* of all the three years. 'Error-bars' indicates the standard deviation of the mean.

to 1200 UT, enough data volume was available to allow a statistically meaningful investigation of the seasonal behavior of *Dg*. We sorted data into monthly bins for each calendar year and calculated the median *Dg* for each bin. Figure 3.6 depicts the obtained seasonal behavior of *Dg* for three years selected for this analysis. A large and statistically significant variability was observed in the seasonal behavior. Despite this variability, seasonal behavior of the *Dg* indicates that on the average *Dg* was smaller in the winter season and attained higher values in pre and post summer. This was a persistent feature present in all the three years of analysis. This seasonal behavior of *Dg* was probably related to the seasonal dependence of the high latitude winds [e.g., *Aruliah et al.*, 1991a; *Emmert et al.*, 2006a]. It also suggests the dependence of the distortion in thermospheric air masses on seasons: larger in pre and post summer, and comparatively smaller in winter.

At high latitudes, geomagnetic conditions can strongly influence the behavior of thermospheric neutral winds. To investigate the response of the distortion to the change in the geomagnetic activity, we inspected the diurnal behavior of *Dg* under different levels of the geomagnetic activities. Each year *Dg* data were sorted according to the hourly Au-

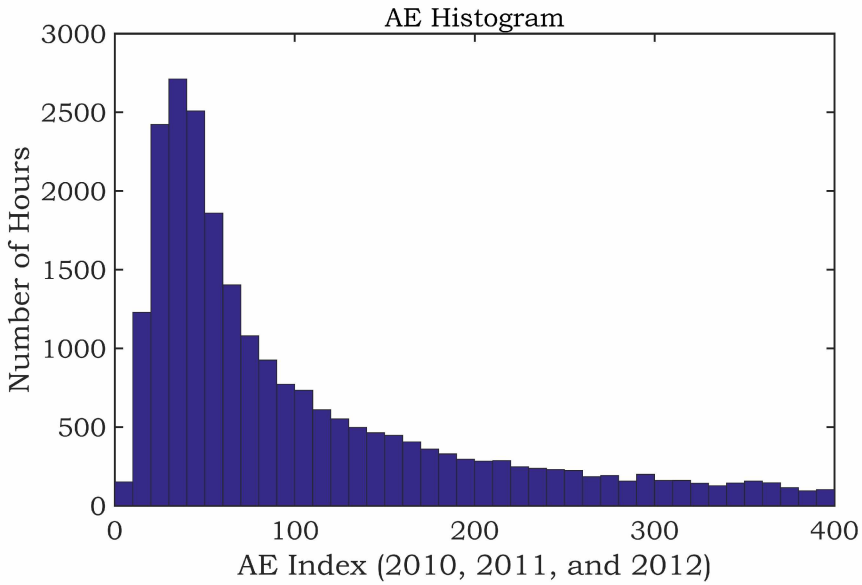

Figure 3.7: Auroral Electrojet (*AE*) indices histogram collectively for 2010, 2011 and 2012. The x-axis is shown only up to *AE* index value 400. Although larger *AE* values were also observed, they were small in number.

roral Electrojet (AE) data taken from NASA ONMIWeb. Combining the three years of AE data, a histogram was generated as shown in Figure 3.7. An hour with $AE < 50$ was considered quiet, interval $50 \leq AE \leq 150$ modest, and $AE > 150$ as active. Statistically significant numbers of *Dg* measurements were present in all the nine resulting groups based on the geomagnetic activity for each year. Diurnal behavior of the *Dg* under various geomagnetic activities is shown in Figure 3.8 - 3.10.

When geomagnetic activity was quiet (as shown in Figure 3.8), *Dg* was small in the local evening and morning time. Maximum *Dg* occurred between 0800 UT and 1000 UT. This peak was associated with the sheared flows along the wind reversal boundary. Such flow configuration occurs as Earth's rotation brings the duskside convection cell and associated wind reversals into the region poleward of Poker Flat. Under modest geomagnetic conditions, maxima of the *Dg* occurred in 0700 UT to 0830 UT time interval (Figure 3.9), which was earlier than the quiet geomagnetic conditions. Under active geomagnetic conditions (Figure 3.10), maxima of the *Dg* occurred between 0300 UT and 0700 UT except 2012 (discussed later), which was even earlier than quiet and modest geomagnetic

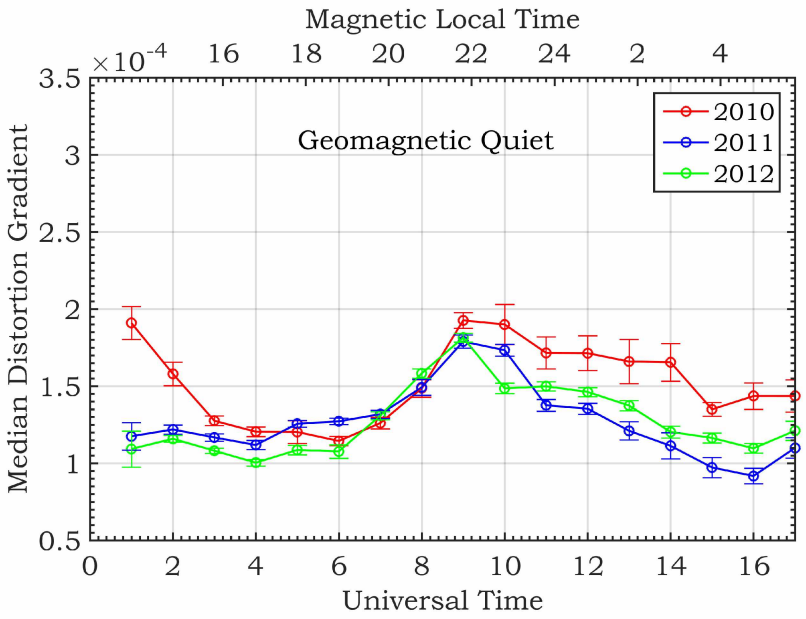

Figure 3.8: Diurnal behavior of *Dg* under quiet geomagnetic conditions ($AE < 50$) for 2010, 2011, and 2012. 'Error-bars' indicates the standard deviation of the mean.

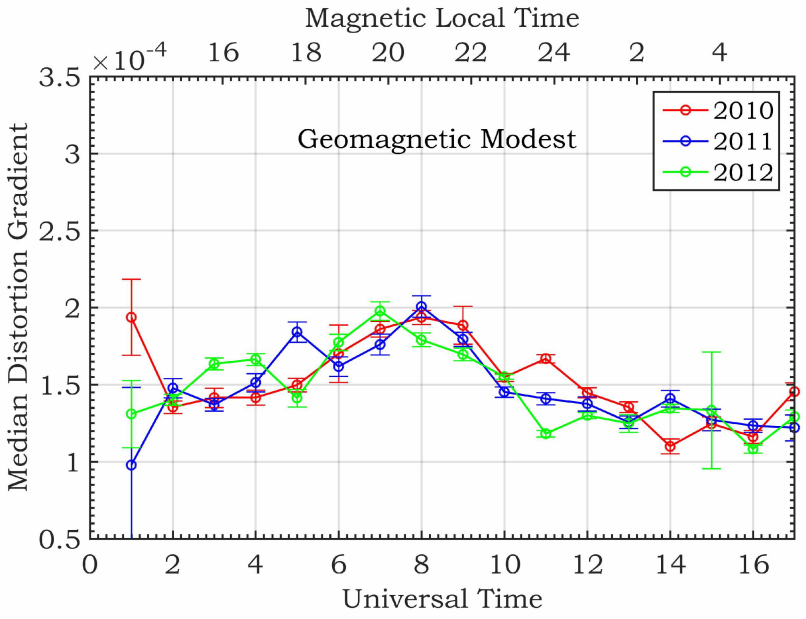

Figure 3.9: Same as for Figure 3.8, but in this case showing diurnal behavior of *Dg* for modest geomagnetic conditions ($50 \leq AE \leq 150$).

conditions. *Akasofu* [1968] showed that the auroral oval expands to lower latitudes with the increase in geomagnetic activity and auroral activity occurs earlier in local magnetic

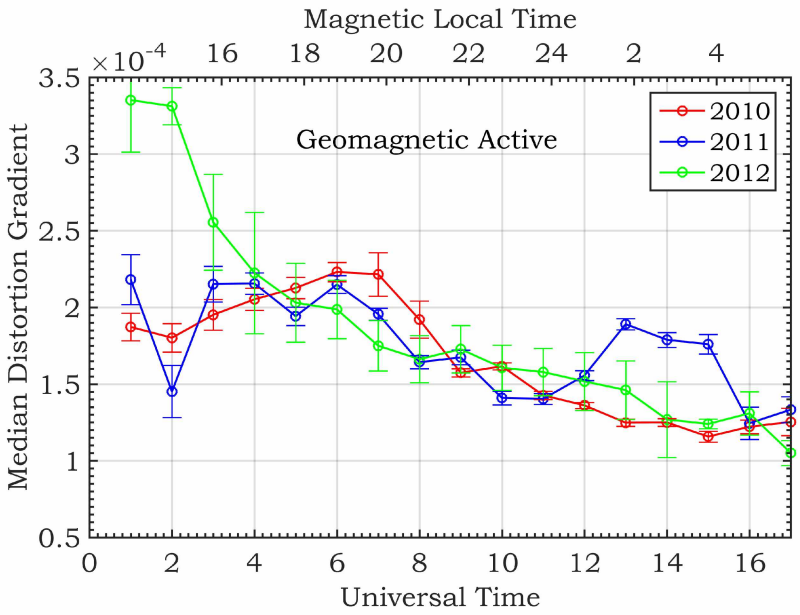

Figure 3.10: Same as for Figure 3.8, but in this case showing diurnal behavior of *Dg* for active geomagnetic conditions ($AE > 150$).

time. Investigations of the high latitude average circulation of the neutral thermosphere by *McCormac et al.* [1987] have shown that thermospheric circulation expands to lower latitudes with the increase in geomagnetic activity. As a result the wind reversal boundary also shifts to the lower latitudes. The location of Alaska is such that during moderate geomagnetic activities, it encounters high magnetic westward winds associated with ion drag earlier than the quiet geomagnetic case, and even earlier in active geomagnetic conditions. As a result sheared flows appear earlier in SDI field of view under moderate conditions than quiet and even earlier in active conditions. This suggests that the behavior of *Dg* under different levels of geomagnetic activity (Figure 3.8 - 3.10) was linked to the location of the observatory relative to the auroral oval. In all the three cases, *Dg* attained maximum value before local magnetic midnight, consistent with years of data from Poker Flat showing that sheared flow is most common at this time.

Exceptionally high *Dg* was observed in 2012 under active geomagnetic conditions between 0100 UT and 0300 UT. The number of observations present in this time bin was small. This is because the SDI requires a solar depression angle of 8 degrees or more to observe, and there are relatively few days (all around mid-winter) for which this require-

ment is satisfied during the period 0100 UT and 0300 UT. Indeed, manual inspection of the day-to-day wind dial and *Dg* plots confirmed that this exceptionally high *Dg* in 2012 was the result of few atypical days with high AE, for example 21 November 2012 and 24 November 2012. On these days, strong latitudinal shears were already present in the starting of the diurnal observation cycle which resulted in the high *Dg*.

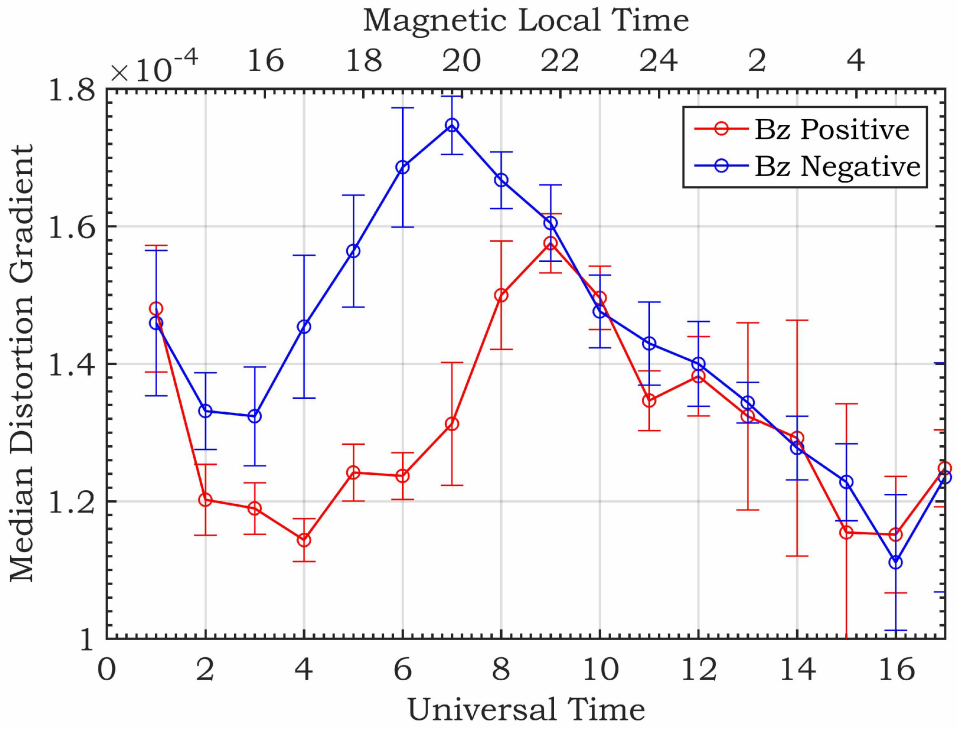

Figure 3.11: Dependence of the diurnal behavior of *Dg* on the north-south component (B_z) of the interplanetary magnetic field. 'Error-bars' indicates the standard deviation of the mean.

The configuration of IMF can considerably influence the neutral circulation pattern [e.g., *McCormac and Smith*, 1984; *Killeen et al.*, 1985, 1995; *Rees et al.*, 1986; *Meriwether and Shih*, 1987; *Sica et al.*, 1989; *Hernandez et al.*, 1991; *Mccormac et al.*, 1991; *Niciejewski et al.*, 1992; *Richmond et al.*, 2003; *Emmert et al.*, 2006b]. In order to determine if any relationship exist between *Dg* and the north-south component (B_z) of the IMF, three years of *Dg* data were first sorted according to the B_z component of IMF and the median of each hourly bin was taken. The resultant *Dg* for positive and negative B_z is presented in Figure 3.11 . As shown in Figure 3.11, before 0900 UT, *Dg* was observed to be stronger for negative B_z than

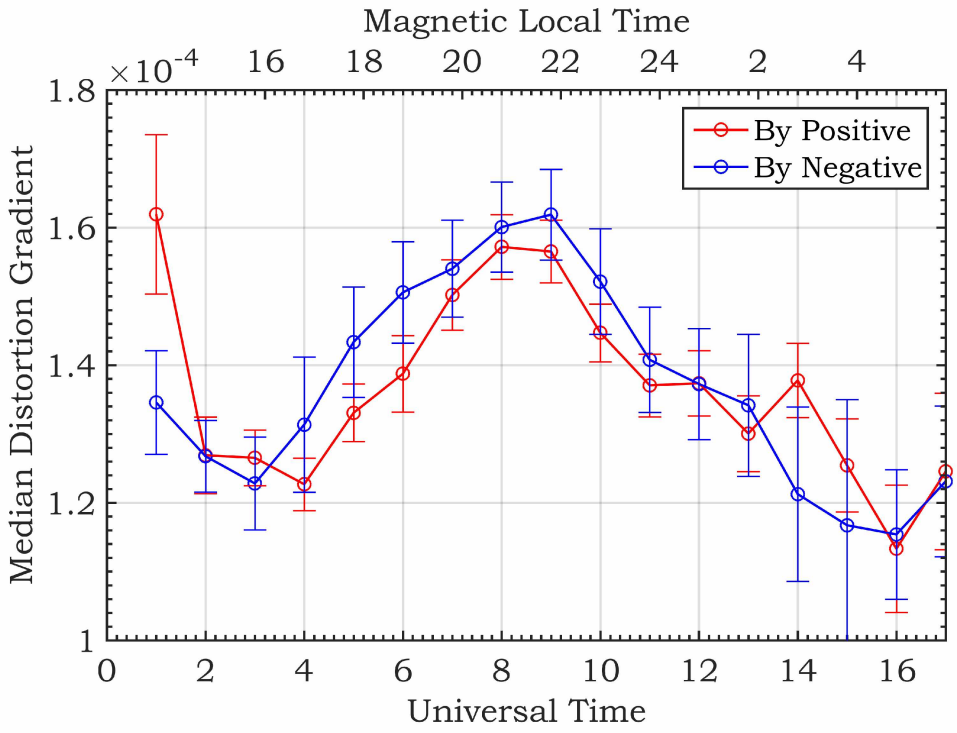

Figure 3.12: Dependence of the diurnal behavior of Dg on the dawn-dusk component (B_y) of the interplanetary magnetic field. 'Error-bars' indicates the standard deviation of the mean.

positive B_z. But, after 0900 UT, Dg behavior was similar for both cases. Peak distortion occurred earlier for negative B_z than positive B_z. In a similar way as discussed for B_z, we also investigated the influence of dawn-dusk component (B_y) of IMF on Dg a shown in Figure 3.12. There was no statistically discernible difference between the diurnal behavior of the Dg for negative and positive B_y. Because neutrals need a sufficient amount of time to be accelerated by the ions, so the next logical step could be to look at the effect of B_y and B_z on Dg using longer time scales.

3.6 Conclusions

A new parameter called the distortion gradient (Dg) was defined for use in studying the climatological behavior of how thermospheric winds distort air masses transported over Alaska. Dg includes all contributions to non-uniform horizontal flow, including all first order gradients and any higher-order perturbations. Dg is always positive, whereas

conventional gradients (or linear combinations of gradients) can be negative or positive. Climatological averaging of conventional gradients will therefore likely underestimate distortion effects, whereas *Dg* is not subject to this problem.

Climatological behavior of *Dg* was studied using three years of all-sky Fabry-Perot measurements of thermospheric winds above Alaska. The principal finding of this research work is that the distortion in the F-region thermospheric air masses above Alaska has a diurnal, seasonal, geomagnetic activity, and IMF dependence. In all the cases maximum distortion occurred before local magnetic midnight.

The diurnal behavior of *Dg* was similar for each of the years studied: 2010, 2011, and 2012. *Dg* was smaller in the climatological averages in the evening and morning, and it maximized between 0600 UT and 1000 UT. If this behavior was not a persistent feature, it would have been suppressed by averaging over a year. Despite the presence of large variability, a persistent feature was present in the seasonal behavior of *Dg* in all three years. *Dg* was smaller in winter compared to pre and post summer. This suggests the presence of seasonal dependence in the distortion of thermospheric air masses.

Timing of the *Dg* peak was observed to depend on geomagnetic activity. Air mass distortion was high between 0800 UT and 1000 UT under quiet geomagnetic conditions. Peak distortion appeared earlier (0700 UT to 0830 UT) in moderate geomagnetic conditions than quiet geomagnetic condition, and even earlier (0300 UT to 0700 UT) in active geomagnetic conditions. That is, the *Dg* peak shifted towards earlier in the evening with increasing geomagnetic activity. This is related to the expansion of the high latitude thermospheric circulation to the lower latitudes with the increase in geomagnetic activity. But in all the cases, maximum distortion always occurred before the local magnetic midnight.

Investigations of the relationship between *Dg* and IMF revealed that distortion in thermospheric air masses was larger and appeared earlier when IMF was southward compared to northward. There was no significant difference between the distortions for dawn and dusk orientation of the IMF.

3.7 References

Akasofu, S.-I. (1968), *Polar and Magnetospheric Substorms*, *Astrophysics and Space Science Library*, vol. 11, Springer Netherlands, Dordrecht, doi: 10.1007/978-94-010-3461-6.

Anderson, C., M. Conde, and M. G. McHarg (2012), Neutral thermospheric dynamics observed with two scanning Doppler imagers: 1. Monostatic and bistatic winds, *J. Geophys. Res. Sp. Phys.*, *117*(A3), A03,304, doi: 10.1029/2011ja017041.

Aruliah, A. L., and E. Griffin (2001), Evidence of meso-scale structure in the high-latitude thermosphere, *Ann. Geophys.*, *19*(1), 37–46, doi: 10.5194/angeo-19-37-2001.

Aruliah, A. L., D. Rees, and A. Steen (1991a), Seasonal and solar cycle variations in high- latitude thermospheric winds, *Geophys. Res. Lett.*, *18*(11), 1983–1986, doi: 10.1029/91GL02240.

Aruliah, A. L., D. Rees, and T. J. Fuller-Rowell (1991b), The combined effect of solar and geomagnetic activity on high latitude thermospheric neutral winds. Part I. Observations, *J. Atmos. Terr. Phys.*, *53*(6âĂŞ7), 467–483, doi: http://dx.doi.org/10.1016/0021-9169(91)90075-I.

Aruliah, A. L., A. D. Farmer, D. Rees, and U. Brändström (1996), The seasonal behavior of high-latitude thermospheric winds and ion velocities observed over one solar cycle, *J. Geophys. Res.*, *101*(A7), 15,701, doi: 10.1029/96JA00360.

Aruliah, A. L., E. M. Griffin, I. McWhirter, A. D. Aylward, E. A. K. Ford, A. Charalambous, M. J. Kosch, C. J. Davis, and V. S. C. Howells (2004), First tristatic studies of meso-scale ion-neutral dynamics and energetics in the high-latitude upper atmosphere using collocated FPIs and EISCAT radar, *Geophys. Res. Lett.*, *31*(3), L03,802, doi: 10.1029/2003gl018469.

Biondi, M. A., J. W. Meriwether, B. G. Fejer, and S. A. Gonzalez (1990), Seasonal variations in the equatorial thermospheric wind measured at Arequipa, Peru, *J. Geophys. Res.*, *95*(A8), 12,243, doi: 10.1029/JA095iA08p12243.

Burnside, R. G., F. A. Herrero, J. W. Meriwether, and J. C. G. Walker (1981), Optical observations of thermospheric dynamics at Arecibo, *J. Geophys. Res. Sp. Phys.*, *86*(A7), 5532–5540, doi: 10.1029/JA086iA07p05532.

Conde, M., and P. Dyson (1995), Thermospheric horizontal winds above Mawson, Antarctica, *Adv. Sp. Res.*, *16*(5), 41–52, doi: 10.1016/0273-1177(95)00171-A.

Conde, M., and R. W. Smith (1995), Mapping thermospheric winds in the auroral zone, *Geophys. Res. Lett.*, *22*(22), 3019–3022, doi: 10.1029/95GL02437.

Conde, M., and R. W. Smith (1997), Phase compensation of a separation scanned, all-sky imaging Fabry Perot spectrometer for auroral studies, *Appl. Opt.*, *36*(22), 5441–5450, doi: 10.1364/AO.36.005441.

Conde, M., and R. W. Smith (1998a), Simultaneous observations of the aurora and of non-uniform thermospheric winds, from Poker Flat, Alaska, *Proc NIPR Symp Up Atmos Phys (Nat Inst Polar Res)*, *12*, 30–38.

Conde, M., and R. W. Smith (1998b), Spatial structure in the thermospheric horizontal wind above Poker Flat, Alaska, during solar minimum, *J. Geophys. Res.*, *103*(A5), 9471–9949, doi: 10.1029/97JA03331.

Conde, M., J. D. Craven, T. Immel, E. Hoch, H. Stenbaek-Nielsen, T. Hallinan, R. W. Smith, J. Olson, W. Sun, L. A. Frank, and J. Sigwarth (2001), Assimilated observations of thermospheric winds, the aurora, and ionospheric currents over Alaska, *J. Geophys. Res. Sp. Phys.*, *106*(A6), 10,493–10,508, doi: 10.1029/2000JA000135.

Conde, M. G., and M. J. Nicolls (2010), Thermospheric temperatures above Poker Flat, Alaska, during the stratospheric warming event of January and February 2009, *J. Geophys. Res. Atmos.*, *115*(D3), D00N05, doi: 10.1029/2010jd014280.

Deng, Y., and A. J. Ridley (2006), Dependence of neutral winds on convection E-field, solar EUV, and auroral particle precipitation at high latitudes, *J. Geophys. Res. Sp. Phys.*, *111*(A9), A09,306, doi: 10.1029/2005JA011368.

Emmert, J. T., M. L. Faivre, G. Hernandez, M. J. Jarvis, J. W. Meriwether, R. J. Niciejewski, D. P. Sipler, and C. A. Tepley (2006a), Climatologies of nighttime upper thermospheric winds measured by ground-based Fabry-Perot interferometers during geomagnetically quiet conditions: 1. Local time, latitudinal, seasonal, and solar cycle dependence, *J. Geophys. Res.*, *111*(A12), A12,302, doi: 10.1029/2006JA011948.

Emmert, J. T., G. Hernandez, M. J. Jarvis, R. J. Niciejewski, D. P. Sipler, and S. Vennerstrom (2006b), Climatologies of nighttime upper thermospheric winds measured by ground-based Fabry-Perot interferometers during geomagnetically quiet conditions: 2. High-latitude circulation and interplanetary magnetic field dependence, *J. Geophys. Res.*, *111*(A12), A12,303, doi: 10.1029/2006JA011949.

Emmert, J. T., D. P. Drob, G. G. Shepherd, G. Hernandez, M. J. Jarvis, J. W. Meriwether, R. J. Niciejewski, D. P. Sipler, and C. A. Tepley (2008), DWM07 global empirical model of upper thermospheric storm-induced disturbance winds, *J. Geophys. Res.*, *113*(A11), A11,319, doi: 10.1029/2008JA013541.

Forster, M., S. E. Haaland, and E. Doornbos (2011), Thermospheric vorticity at high geomagnetic latitudes from CHAMP data and its IMF dependence, *Ann. Geophys.*, *29*(1), 181–186, doi: 10.5194/angeo-29-181-2011.

Greet, P. A., M. G. Conde, P. L. Dyson, J. L. Innis, A. M. Breed, and D. J. Murphy (1999), Thermospheric wind field over Mawson and Davis, Antarctica; simultaneous observations by two Fabry-Perot spectrometers of λ630 nm emission, *J. Atmos. Sol. Terr. Phys.*, *61*(14), 1025–1045, doi: http://dx.doi.org/10.1016/S1364-6826(99)00059-0.

Hernandez, G., F. G. McCormac, and R. W. Smith (1991), Austral thermospheric wind circulation and interplanetary magnetic field orientation, doi: 10.1029/90JA02458.

Killeen, T. L., and R. G. Roble (1988), Thermosphere dynamics: Contributions from the first 5 years of the Dynamics Explorer Program, *Rev. Geophys.*, *26*(2), 329–367, doi: 10.1029/RG026i002p00329.

Killeen, T. L., P. B. Hays, R. A. Heelis, W. B. Hanson, and N. W. Spencer (1985), Neutral motions in the polar thermosphere for northward Interplanetary Magnetic Field, *Geophys. Res. Lett.*, *12*(4), 159–162, doi: 10.1029/GL012i004p00159.

Killeen, T. L., Y.-I. Won, R. J. Niciejewski, and A. G. Burns (1995), Upper thermosphere winds and temperatures in the geomagnetic polar cap: Solar cycle, geomagnetic activity, and interplanetary magnetic field dependencies, *J. Geophys. Res.*, *100*(A11), 21,327, doi: 10.1029/95JA01208.

Kwak, Y. S., and A. D. Richmond (2007), An analysis of the momentum forcing in the high-latitude lower thermosphere, *J. Geophys. Res.*, *112*(A1), A01,306, doi: 10.1029/2006JA011910.

Kwak, Y. S., and A. D. Richmond (2014), Dependence of the high-latitude lower thermospheric wind vertical vorticity and horizontal divergence on the interplanetary magnetic field, *J. Geophys. Res. Sp. Phys.*, *119*(2), 1356–1368, doi: 10.1002/2013JA019589.

McCormac, F. G., and R. W. Smith (1984), The influence of the interplanetary magnetic field Y component on ion and neutral motions in the polar thermosphere, *Geophys. Res. Lett.*, *11*(9), 935–938, doi: 10.1029/GL011i009p00935.

McCormac, F. G., T. L. Killeen, E. Gombosi, P. B. Hays, and N. W. Spencer (1985), Configuration of the high-latitude thermosphere neutral circulation for IMF By negative and positive, *Geophys. Res. Lett.*, *12*(4), 155–158, doi: 10.1029/GL012i004p00155.

McCormac, F. G., T. L. Killeen, J. P. Thayer, G. Hernandez, C. R. Tschan, J.-J. J. Ponthieu, and N. W. Spencer (1987), Circulation of the polar thermosphere during geomagnetically quiet and active times as observed by Dynamics Explorer 2, *J. Geophys. Res. Sp. Phys.*, *92*(A9), 10,133–10,139, doi: 10.1029/JA092iA09p10133.

Mccormac, F. G., T. L. Killeen, and J. P. Thayer (1991), The influence of IMF B(y) on the high-latitude thermospheric circulation during northward IMF, *J. Geophys. Res.*, *96*(A1), 115, doi: 10.1029/90JA01996.

Meriwether, J. W., and P. Shih (1987), On the nighttime signatures of thermospheric winds observed at Sondrestrom, Greenland, as correlated with interplanetary magnetic field parameters, *URSI High Alt. Obs.*, *5*, 329–336.

Niciejewski, R., T. Killeen, R. Johnson, and J. Thayer (1992), The behavior of the high-latitude F-region neutral thermosphere in relation to IMF parameters, *Adv. Sp. Res.*, *12*(6), 215–218, doi: 10.1016/0273-1177(92)90058-6.

Niciejewski, R. J., T. L. Killeen, and S. C. Solomon (1996), Observations of thermospheric horizontal neutral winds at Watson Lake, Yukon Territory (Λ = 65N), *J. Geophys. Res. Sp. Phys.*, *101*(A1), 241–259, doi: 10.1029/95JA02683.

Rees, D., T. Fuller-Rowell, R. Gordon, M. Smith, N. Maynard, J. Heppner, N. Spencer, L. Wharton, P. Hays, and T. Killeen (1986), A theoretical and empirical study of the response of the high latitude thermosphere to the sense of the "Y" component of the interplanetary magnetic field, *Planet. Sp. Sci.*, *34*(1), 1–40, doi: 10.1016/0032-0633(86)90100-5.

Richmond, A. D., C. Lathuillere, and S. Vennerstroem (2003), Winds in the high-latitude lower thermosphere: Dependence on the interplanetary magnetic field, *J. Geophys. Res.*, *108*(A2), 1066, doi: 10.1029/2002JA009493.

Roble, R., J. Salah, and B. Emery (1977a), The seasonal variation of the diurnal thermospheric winds over Millstone Hill during solar cycle maximum, *J. Atmos. Terr. Phys.*, *39*(4), 503–511, doi: 10.1016/0021-9169(77)90159-3.

Roble, R. G., R. E. Dickinson, and E. C. Ridley (1977b), Seasonal and solar cycle variations of the zonal mean circulation in the thermosphere, *J. Geophys. Res.*, *82*(35), 5493–5504, doi: 10.1029/JA082i035p05493.

Roble, R. G., R. E. Dickinson, and E. C. Ridley (1982), Global circulation and temperature structure of thermosphere with high-latitude plasma convection, *J. Geophys. Res. Sp. Phys.*, *87*(A3), 1599–1614, doi: 10.1029/JA087iA03p01599.

Sica, R. J., M. H. Rees, R. G. Roble, G. Hernandez, and G. J. Romick (1986), The altitude region sampled by ground-based Doppler temperature measurements of the OI 15867 K emission line in aurorae, *Planet. Sp. Sci.*, *34*(5), 483–488, doi: http://dx.doi.org/10.1016/0032-0633(86)90035-8.

Sica, R. J., G. Hernandez, B. A. Emery, R. G. Roble, R. W. Smith, and M. H. Rees (1989), The control of auroral zone dynamics and thermodynamics by the interplanetary magnetic field dawn-dusk (Y) component, *J. Geophys. Res.*, *94*(A9), 11,921, doi: 10.1029/JA094iA09p11921.

Thayer, J. P., and T. L. Killeen (1991), Vorticity and divergence in the high-latitude upper thermosphere, *Geophys. Res. Lett.*, *18*(4), 701–704, doi: 10.1029/91GL00131.

Thayer, J. P., and T. L. Killeen (1993), A kinematic analysis of the high-latitude thermospheric neutral circulation pattern, *J. Geophys. Res.*, *98*(93), 11,549–11,565, doi: 10.1029/93JA00629.

Wickwar, V. B., J. W. Meriwether, P. B. Hays, and A. F. Nagy (1984), The meridional thermospheric neutral wind measured by radar and optical techniques in the auroral region, *J. Geophys. Res. Sp. Phys.*, *89*(A12), 10,987–10,998, doi: 10.1029/JA089iA12p10987.

Chapter 4

Tracing Trajectories of Air Parcels Transported Through Spatially Resolved Horizontal Neutral Wind Fields Observed in the Thermosphere Above Alaska[1]

Abstract

Transport by fluid flow is a very complex problem. Any velocity gradient will cause distortion of air parcels which, over time, can become extraordinarily severe. In the traditional picture of Earth's upper thermosphere, it is however widely presumed that its convective stability and enormous kinematic viscosity attenuate wind gradients, and hence smooth out any structure present in the wind over scale sizes of several hundreds of kilometers. As a result, air parcel trajectories predicted by current models are often relatively simple, so that transport effects only slowly disperse and mix air parcels. This means that regions of perturbed chemical composition, formed for example by intense aurora, would be expected to remain intact for many hours or even days. However, our observations show that this simple picture does not hold in practice; wind fields in the thermosphere have much more local-scale structure than predicated by models, at least in the auroral zone. These local small-scale structures complicate air parcel trajectories enormously, relative to typical expectations. In this study, we used an all-sky Scanning Doppler Imaging Fabry-Perot interferometer located at Poker Flat, Alaska. A single SDI instrument can simultaneously observe the thermospheric wind's line-of-sight (LOS) component in 115 (typically) independent look directions. From these data, it is possible to reconstruct time-resolved two-dimensional maps of the horizontal vector wind field and use these to infer forward and backward air parcel trajectories over time. Tracing parcel trajectories through a given geographic location maps where they will go from there (forward tracing in time) and where they came from previously (history of parcels or tracing back in time). Results show that transport of thermospheric neutral species in the presence of the local-scale wind gradients that are observed is far more complicated than what current

[1]Dhadly, M. S. and M. Conde (2015), Tracing trajectories of air parcels transported through spatially resolved horizontal neutral wind fields observed in the thermosphere above Alaska (prepared for submission in Journal of Geophysical Research).

models typically predict. Also, the wind driven transport is sensitive to the details of the wind field.

4.1 Introduction

Upper atmospheric neutral winds at high latitudes are forced by the combination of heating induced pressure gradients, momentum exchange between neutrals and convecting ions (ion drag), and inertial forces. A quantitative comparison of the F-region momentum terms is given by *Killeen and Roble* [1984]. Time varying interplay between these drivers leads to substantial variations in thermospheric circulation at local and synoptic scales, and complicates high latitude thermospheric wind flow patterns. Understanding transport of neutral air parcels driven by such time varying fluid flows is a challenging problem.

Magnetically driven processes (e.g. Joule heating and auroral precipitation) can deposit a significant amount of energy at high latitudes, which directly perturbs ionospheric and thermospheric compositions. Any perturbation in the neutral composition can significantly alter high latitude electrodynamical processes such as ionospheric convection via changes in ion drag. Also, modified neutral composition produced by such magnetospheric processes at high latitudes can be transported to lower latitudes by meridional winds, and hence disrupt the chemical production and loss rates in the ionosphere and thermosphere at mid and even low latitudes, which influences low latitude thermospheric phenomenon such as the equatorial spread F and scintillation. Thus, high latitude forcing (heating and convection) can lead to significant thermospheric disturbances on the global scale. *Crowley et al.* [1989a,b] presented such an example of upwelling of nitrogen rich air by Joule heating and its subsequent transportation to lower latitudes by meridional winds on the nightside which caused relative depletion of thermospheric oxygen at lower latitudes. *Fuller-Rowell et al.* [1996] demonstrated the seasonal dependence of these processes. *Strickland et al.* [1999] showed the latitudinal motion of thermospheric oxygen depleted large-scale patches using ultraviolet images acquired by Dynamic Explorer 1. *Pallamraju* [2005] discussed such traveling atmospheric disturbed compositions from higher to lower latitudes by analyzing strong variation in the 630 *nm* dayglow emis-

sions at a low latitude site (Carmen Alto, Chile) after a geomagnetic storm. It is now well established that thermospheric wind driven transport at high latitudes is a key component of the global thermospheric system, and its detailed knowledge is required to completely understand the global thermospheric wind transport.

At F-region thermospheric altitudes, the mean free path is $\sim$1 *km* and the collision frequency is $\sim$1 collision per sec. This distance and time scale are smaller than the characteristic distance and time scales of wind systems. That is why the thermospheric wind flows may be regarded as viscous fluid flows *Rishbeth* [1972]. When shears exist in the wind flows, viscous forces act to smooth any shear by diffusing the momentum. The reason is that the mean free path at thermospheric altitudes is very large. Consequently, the thermospheric species can communicate over longer distances and hence diffuse the momentum over large regions quickly. The kinematic viscosity, which is the molecular viscosity per unit mass, increases with increasing altitude *Rishbeth* [1972]. Due to the high kinematic viscosity of the upper thermosphere, it is most commonly presumed in global modeling studies that the Earth's upper thermosphere acts to smear out any gradients that might occur over scale sizes of several hundreds of kilometers or less as discussed in *Aruliah and Griffin* [2001]. Also, neutral gas is assumed to respond very slowly to magnetospheric forcing because of its large inertia as it consists 99.9% of the mass of the upper atmosphere. Taken together, these considerations lead most workers to presume that thermosphere is a background and easily predictable medium. For such a medium, air parcel trajectories would be relatively simple, and transport processes would only slowly disperse and mixes air parcels. In such cases, the regions of perturbed chemical composition formed for example by an intense aurora or any other mechanism, would be expected to remain intact for many hours or even days. *Killeen and Roble* [1986] investigated the high latitude thermospheric neutral wind transport by air parcel tracing using Thermospheric Global Circulation Model (TGCM). Their study used a time step of one hour to update trajectory of each air parcel assuming that the wind behavior does not change much during that time period. However, many previous independent systematic observational studies [e.g., *Meriwether et al.*, 1973, 1988; *Conde and Smith*, 1995, 1998a,b; *Killeen et al.*, 1995; *Greet et al.*, 1999; *Aruliah and Griffin*, 2001; *Aruliah et al.*, 2004] have shown that this simple

picture (as discussed above) does not hold in practice. The high latitude neutral wind dynamics can be quite variable and thermospheric F-region wind fields at high latitudes can have much more local spatial and temporal structures than predicted by global models like the one used by *Killeen and Roble* [1986]. Although modeling studies are reputable resources for determining global climatologies, they do not yet have enough details of the wind fields especially at auroral latitudes that can be obtained with experimental studies. That is why the air parcel trajectories predicted by models often contain trajectories that look smooth and unstructured (as in the case of *Killeen and Roble* [1986]). We are coming to understand that thermospheric models will require more realistic magnetospheric inputs and thermospheric drivers if they are to predict winds similar to those that are observed in practice.

High latitude wind driven thermospheric transport is one of the least studied components of high latitude aeronomy. Our ability to understand high latitude thermospheric transport is limited by the sparsity of observational data and inability to accurately predict thermospheric medium over smaller scales. Here, we examined neutral air parcel transport in the high latitude F-region thermosphere using actual observational data by applying the technique of tracing air parcels forward and backward in time to determine where the air parcels came from previously or where they will travel subsequently. This allowed us to visualize the motion of neutral air parcels and understand their transport through local-scale structures in the F-region neutral wind fields above Alaska. The primary motivation for backward tracing is to investigate whether behavior occurring in the vicinity of the observations may have been instigated or influenced by the prior history of the air parcels. Conversely, forward tracing would allow us to predict locations that may subsequently be affected by air parcels carried downwind from our location. In methodology, our study is similar to the air parcel tracing through model wind fields performed by *Killeen and Roble* [1986], although in our case, we use experimentally measured thermospheric winds with much higher spatial resolution but only confined to the region above Alaska. In *Killeen and Roble* [1986] study, at F-region altitude, they used a time step of one hour to update trajectory of each air parcel. Also, the average angular distance traveled by an air parcel in one hour was of the order of ten degree in latitude ($\sim$1100 *km*). Their

air parcel trajectory study was focused on understanding the large-scale behavior of the wind transport, so no attempt was made to capture any local-scale details in air parcel trajectories. On the other hand, our study is focused on understanding behavior of air parcel transport on local-scale in the presence of actually observed non-uniformities in the wind fields.

For a uniform wind field, transport of neutral air parcels is easily straightforward and almost trivially predictable. However, observations show that thermospheric wind fields are not uniform; wind gradients (most prominently in the form of shears) occur on the local and synoptic scale, as a result of the time varying interplay between various spatially varying drivers. As we will show, the resulting air parcel trajectories become far more complicated. Calculating these trajectories requires wind fields measurements with high enough spatial resolution to resolve all the gradients present, coupled with wide enough geographic coverage to allow the air parcels to be followed throughout the region of interest. Obtaining suitable data requires sophisticated instrumentation and a very large experimental undertaking. Although a number of instruments and instrument types exist for sampling the thermospheric winds, very few have the required high spatial and temporal resolution coupled with the ability to observe over a large geographic area [e.g., *Conde and Smith*, 1995, 1998b; *Aruliah et al.*, 2010; *Anderson et al.*, 2012]. Here, we have used spatially resolved observations of the 630 *nm* optical emissions occurring naturally in the F-region thermosphere recorded by an all-sky wavelength scanning Doppler imaging Fabry-Perot spectrometer (SDI) located at Poker Flat, Alaska (65.12N, 147.47W). Poker Flat is located in the auroral zone, which is a transition region between mid-latitudes and the polar cap, in which the relative magnitudes of the various source terms appearing in the thermosphere's energy and momentum equations vary rapidly both spatially and temporally. Thus, its data provides a sensitive test for the terms and drivers used in thermospheric wind circulation models.

4.2 Tracing Analysis

The all-sky SDI located at Poker Flat, Alaska (local time = UT - 9, magnetic local time $\approx$ UT + 12.8) is capable of collecting emission spectra simultaneously from many tens of

locations across the sky. A detailed description of the basic principles and operations of an all-sky SDI is discussed by *Conde and Smith* [1995, 1997, 1998a,b] and more recently by *Conde and Nicolls* [2010] and *Anderson et al.* [2012]. In brief, optical emissions from thermosphere are collected by a fish-eye lens in the fore-optics, passed through a narrow-band interference filter to select a single emission feature of interest. The resulting monochromatic beam is expanded, re-collimated, and passed through an etalon configured to scan its gap over one order of interference in discrete 128 steps every $\sim$20 *sec*. The etalon introduces angular modulation, which is then focused to form a ring pattern on a 512×512 pixel thermoelectrically cooled electron multiplying charge coupled device (EMCCD) detector using a Nikkor 300 $mm\, f/2.8$ telephoto lens. The detector is optically conjugate with a "plane" at infinite object distance, so the image it receives at any instant is that of the distant sky, modulated by the Fabry-Perot fringe pattern for the wavelength of the selected emission line. Each EMCCD pixel acts a single detector, albeit one that only receives very small photon flux. To increase signal/noise (at the expense of angular resolution) the digital image is binned in software into a configurable pattern of zones (numbering 115 in this study) and the spectrum recorded derived from each individual pixel is co-added within its corresponding zone using the phase mapping technique described by *Conde and Smith* [1997]. Multiple $\sim$20 *sec* scans are co-added to produce a single exposure, with the spectral integration continuing until an adequate signal to noise ratio is reached on average across all zones.

The full field of view (FOV) of the Poker Flat SDI used here was 146 degrees which covered a wide geographic region above Alaska with a radial extent of $\sim$785 *km* when projected onto a planar 630 *nm* emission layer at a centroid altitude of 240 *km*. The division of the field of view into zones is entirely configurable; the zones can be of any shape and any total number. Experience has shown that for our instrument under typical observing conditions, a good balance between the spatial and temporal resolution is achieved by dividing the FOV into 115 zones. Doppler shift and Doppler broadening of the resulting spectra were inferred by numerical fitting of a suitable model spectrum (allowing for instrumental broadening). These quantities were used to estimate LOS wind speeds and temperatures respectively. Two-dimensionally resolved horizontal wind fields were then

derived from the LOS wind components using a "monostatic" wind fitting technique based on *Burnside et al.* [1981] and discussed in more detail by *Conde and Smith* [1998b] and *Anderson et al.* [2012].

We used only the horizontal displacement of air parcels to trace their trajectories, and made no attempt to follow their vertical displacement. This approach is reasonable, because the high latitude neutral wind flows are convection dominated and vertical winds are usually (but admittedly not always) far smaller than their corresponding horizontal speeds. For forward air parcel tracing, the wind measurements from 07 January 2012 and 15 December 2012 were used as they are representative of thermospheric wind evolution above Alaska that we commonly observe on many nights. The average temporal resolution of horizontal wind data from 07 January and 15 December was 4.8 *min* and 2.5 *min* respectively. Constructing the trajectory of an air parcel requires the ability to "lookup" a value for the wind at the particular location of the air parcel at each time step. However, while the air parcel location could be anywhere, the underlying data are only measured on a spatial grid that is determined by the zone map in use. Furthermore, the trajectory calculation uses fixed time steps, whereas the sampling times of the original data are not fixed, as a result of the varying integration times used by the instrument in response to changing emission brightness. Thus, the trajectory calculation requires that the wind data be interpolated to a fixed temporal cadence and to the constantly evolving air parcel locations. Once the wind is interpolated to an air parcel location, it is trivial to project its displacement forward over a small time step by multiplying the estimated wind by the time step. This interpolation and calculation of the displacement steps were repeated every 30 *sec* for finding the new location of the air parcel. To visualize the horizontal wind driven transport of air parcels, twenty-three "virtual balloon guns" were placed in the upper thermosphere at different locations above Alaska. A new virtual balloon was released by each gun every 10 *min*. We considered a balloon as a visual representation of an air parcel. Two virtual balloons produced from a same balloon gun were attached with a stretchable virtual string. To distinguish between the balloons from different balloon guns, they were presented in different colors. Balloons were tracked as long as they remained within the SDI FOV.

For finding the history of air parcels, thirteen air parcels located above Alaska at different locations were selected and traced backward in time. Using the wind measurements from 07 January 2012, the backward displacements were calculated as before, but starting with the last exposure of the night and reversing the sign of the wind, so that the displacements were directed "upwind". The different colors were used to distinguish between the trajectories of different air parcels.

4.3 Discussion

Summary wind plots (as shown in Figure 4.1) were produced for both 07 Jan 2012 and 15 Dec 2012 to depict an overview of the spatial and temporal evolution of horizontal neutral winds that were used for air parcel tracing analysis above Alaska. They include both large-scale and local-scale horizontal wind features. In the wind summary plots, the Sun is always at the top of the figure and the observatory moves anticlockwise around the geomagnetic north pole in a circular arc as seen by a space-based observer located at some distance above the geomagnetic north pole. Due to the latitudinal spread of SDI FOV, they trace out an annular ring around the geomagnetic north pole. The background colors in these plots denote the 630 nm emission intensity derived also from SDI spectra. Horizontal wind features observed on 07 Jan 2012 and 15 Dec 2012 represents the most common features in the winds observed above Alaska. At the beginning of the observation cycle, antisunward winds equatorward of the observatory were associated with the diurnal tide due to the pressure gradient induced by solar heating, whereas the magnetic westward component in the winds poleward of the observatory were presumably associated with the ion drag due to the duskside ionospheric convection. Early in the evening, most of the wind flow was dominated by the solar diurnal tide. With the passage of time, due to Earth's rotation, the duskside ionospheric convection started dominating the wind flow poleward of the observatory. It produced a wind reversal region along the magnetic east-west direction before magnetic midnight - for example at times around 0700 UT. Large latitudinal sheared flows were present along this wind reversal boundary. With the passage of time, the wind reversal boundary slowly moved equatorward of the observatory. It is well known that coupling between ions and neutrals is stronger in the presence

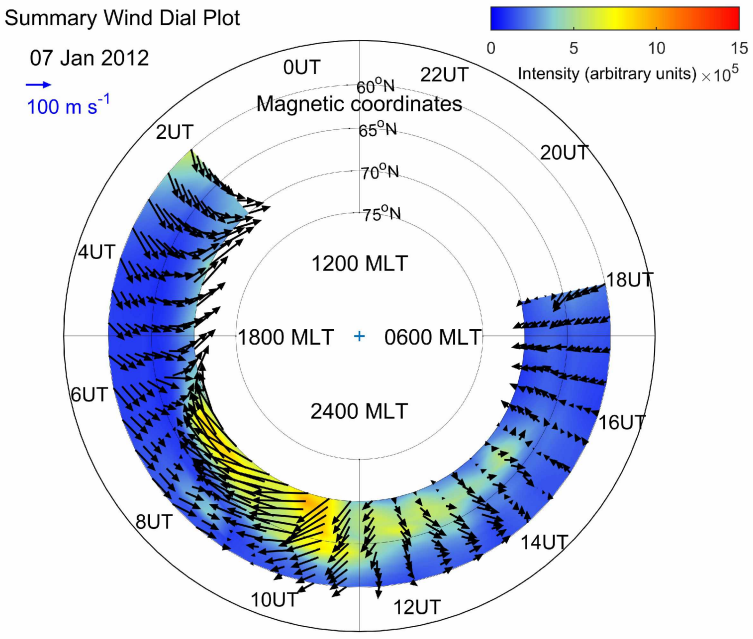

(a)

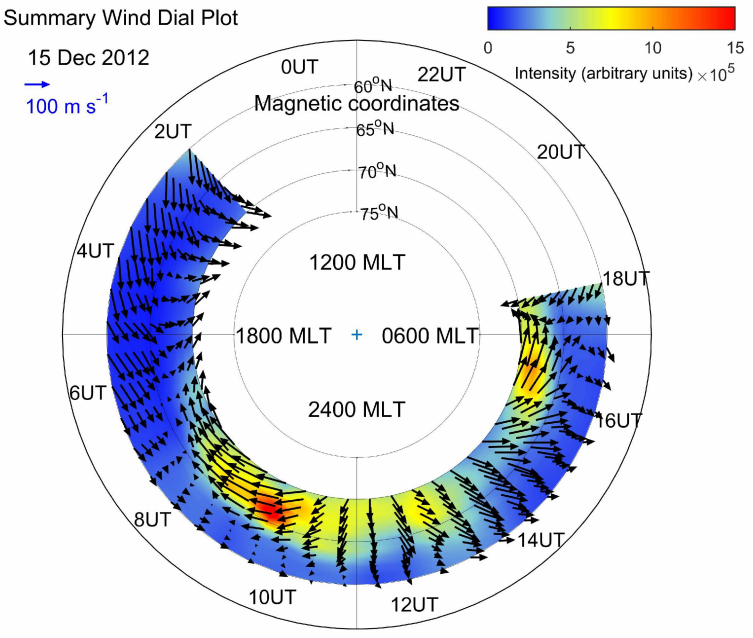

(b)

Figure 4.1: Evolution of the F-region thermospheric horizontal neutral winds above Poker Flat on a) 07 January 2012 (top panel) and b) 15 December 2012 (bottom panel). In these summary wind dial plots, the sun is always at the top of the plot, and the observatory moves anticlockwise around the geomagnetic north pole in a circular arc (for a space-based observer located at some distance above the geomagnetic north pole). Background colors indicate 630 *nm* optical emission brightness, in arbitrary units.

of auroral activity [*Deng and Ridley*, 2006]. The strong magnetic westward winds on the poleside of the observatory between 0600 UT to 1000 UT were almost certainly associated with strong ion-neutral coupling in the collocated region of auroral activity occurring at this time. The equatorward winds around 1200 UT are a common feature of winds over Alaska at this local time; they are associated with the nightside emergence of the antisunward cross polar cap jet. After 1200 UT, development of a magnetic eastward component in the wind flows was the signature of dawnside plasma convection cell. Development of the dawnside neutral circulation vortex is visible in Figure 4.1b, due to strong ion-neutral coupling in the aurorally active region between 1500 UT and 1800 UT. Day-to-day observations of the wind behaviors from Poker Flat have shown that variability in the dawn neutral circulation cell is much stronger than the duskside circulation cell. The antisunward polar cap flows and return flows via dawn and dusk wings of the thermospheric circulation are clearly visible in the summary wind dial plot (Figure 4.1b). These flow characteristics have been previously reported in many publications [e.g., *Conde and Smith*, 1998b; *Conde et al.*, 2001; *Anderson et al.*, 2012].

Balloon trajectories for 07 Jan and 15 Dec (which represent the paths traveled by air parcels) are shown in Figure 4.2-4.5 and Figure 4.6-4.9 respectively. The background colors in each frame of Figure 4.2-4.5 and Figure 4.6-4.9 indicate the 630 *nm* emission intensity, which is also derived from the SDI measurements. In this analysis, the neutral air parcel locations and trajectories were updated every 30 *sec*. Although this short time step was necessary for accurate computations, it is adequate to display the end results at much lower cadence and, in so doing, a far more compact summary of the key features is possible. Thus, Figure 4.2-4.5 and Figure 4.6-4.9 only show the calculated trajectories every 10 *min*.

To make dark sky observations, the Poker Flat SDI was configured to start observing when the Sun descended to more than eight degrees below the geometric horizon. However, the sky was still quite bright during the first few exposures thus obtained, and were contaminated with twilight on the sunward side of the SDI FOV. The result was an artificial gradient in the inferred 630 nm intensity, directed toward the magnetic south. This erroneous intensity gradient disappeared quickly as Poker Flat advanced deeper into the

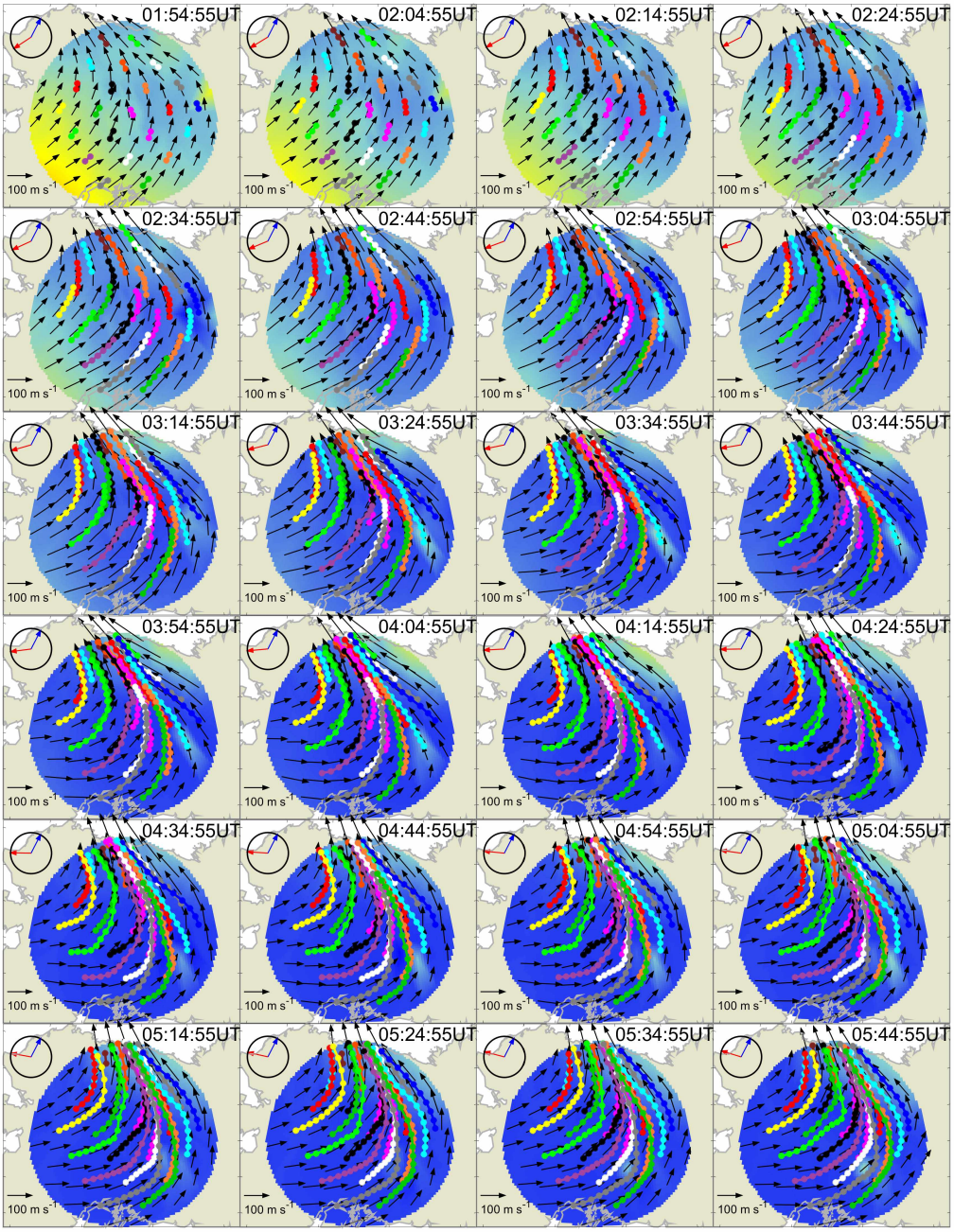

Figure 4.2: Temporal and spatial evolution of air parcel trajectories forward in time on 07 January 2012. Red and blue arrows in the circle on the top left corner of each subset point toward the azimuthal location of the sun and geomagnetic north from Poker Flat respectively. The background colors indicate 630 nm optical emission brightness in arbitrary units.

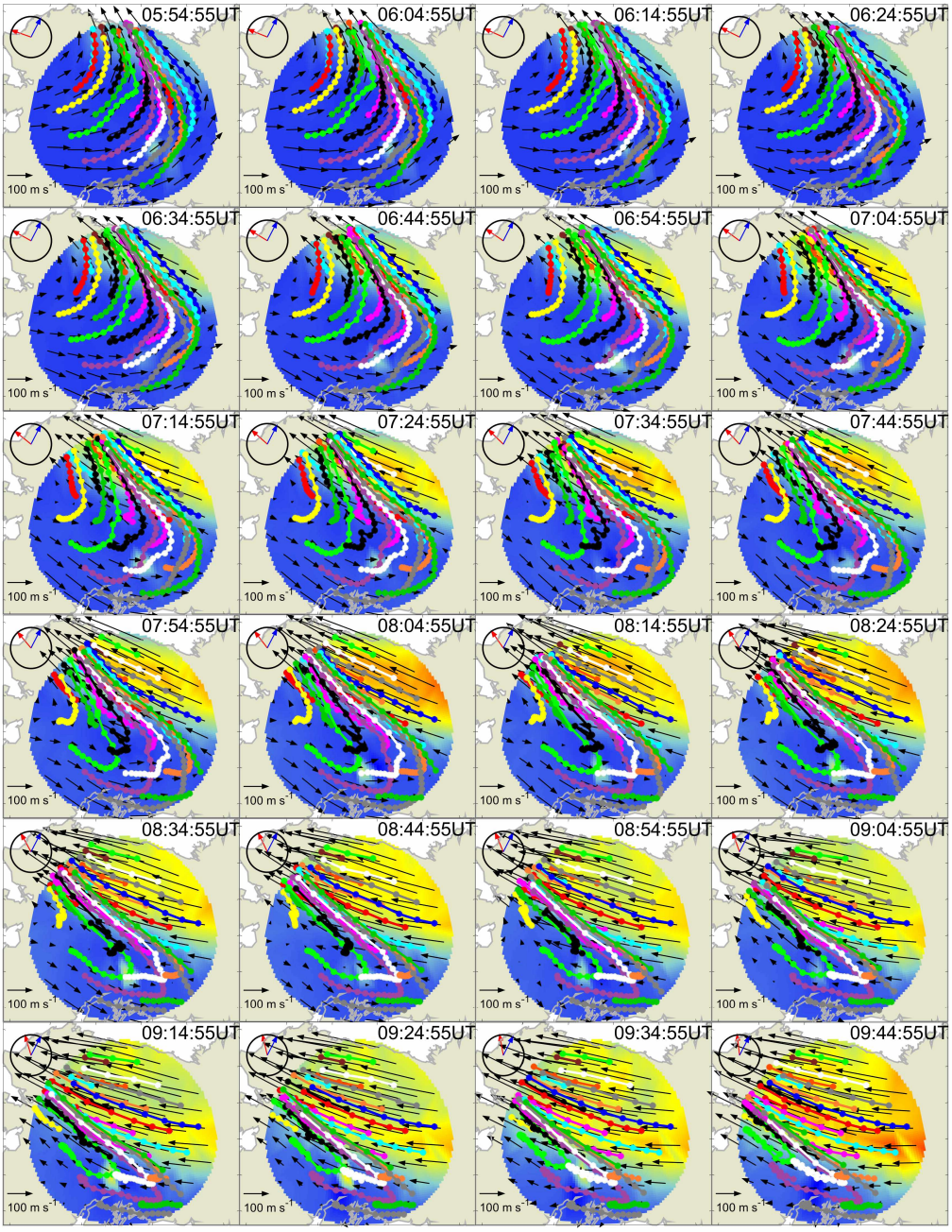

Figure 4.3: Same as for Figure 4.2, but in this case showing times from 0554 UT until 0944 UT.

nighttime darkness. In Figure 4.2-4.5, a light colorful patch on the equatorward of the observatory that moves from east to west with time was due to contamination associated with the instrument looking directly at the moon during the night of 07 Jan 2012.

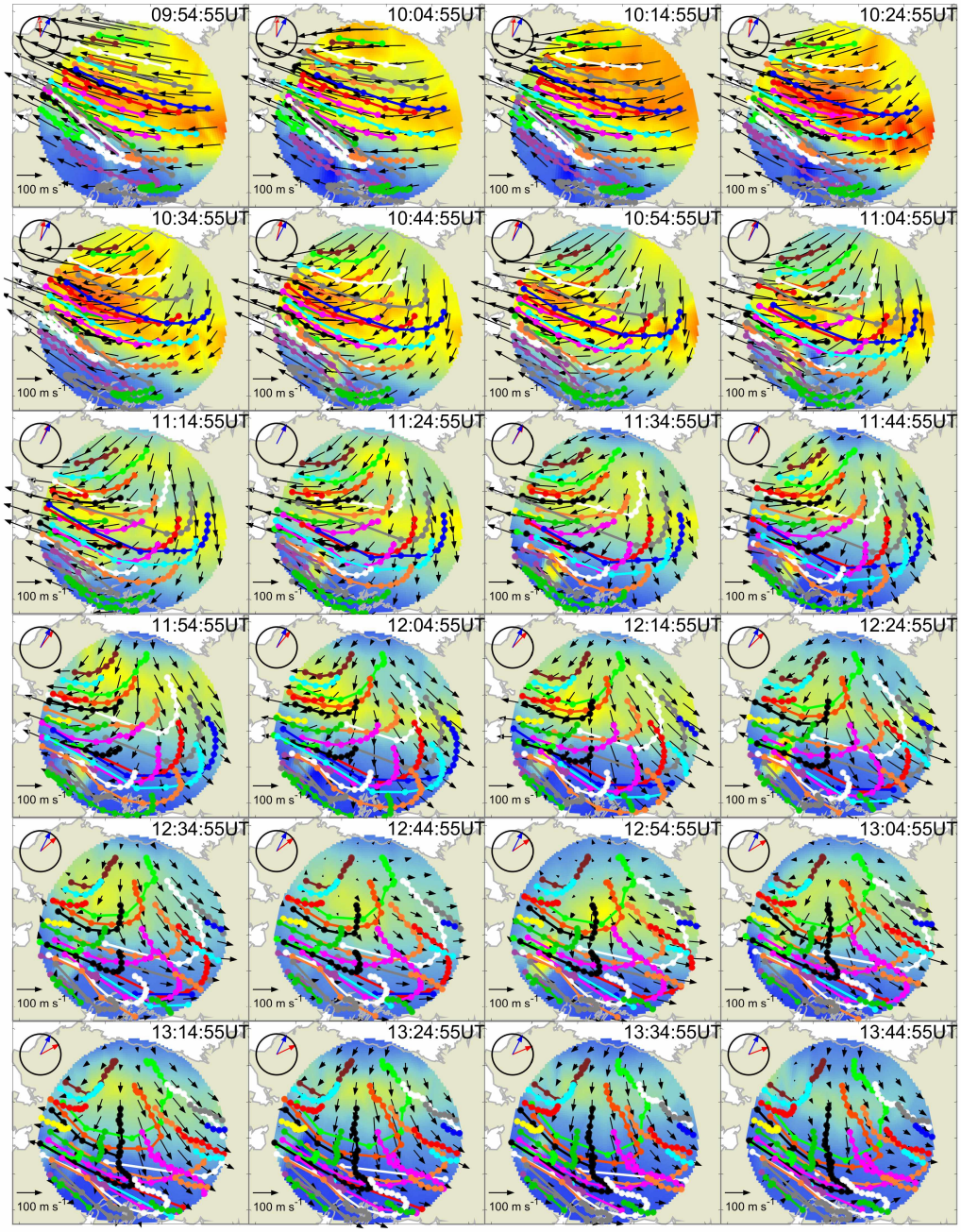

Figure 4.4: Same as for Figure 4.2, but in this case showing times from 0954 UT until 1344 UT.

As shown in Figure 4.2-4.5 and Figure 4.6-4.9, the wind field equatorward of the observatory was uniform and antisunward at the beginning of both nights, so that the neutral air parcels slowly drifted poleward. The wind flow poleward of the observatory

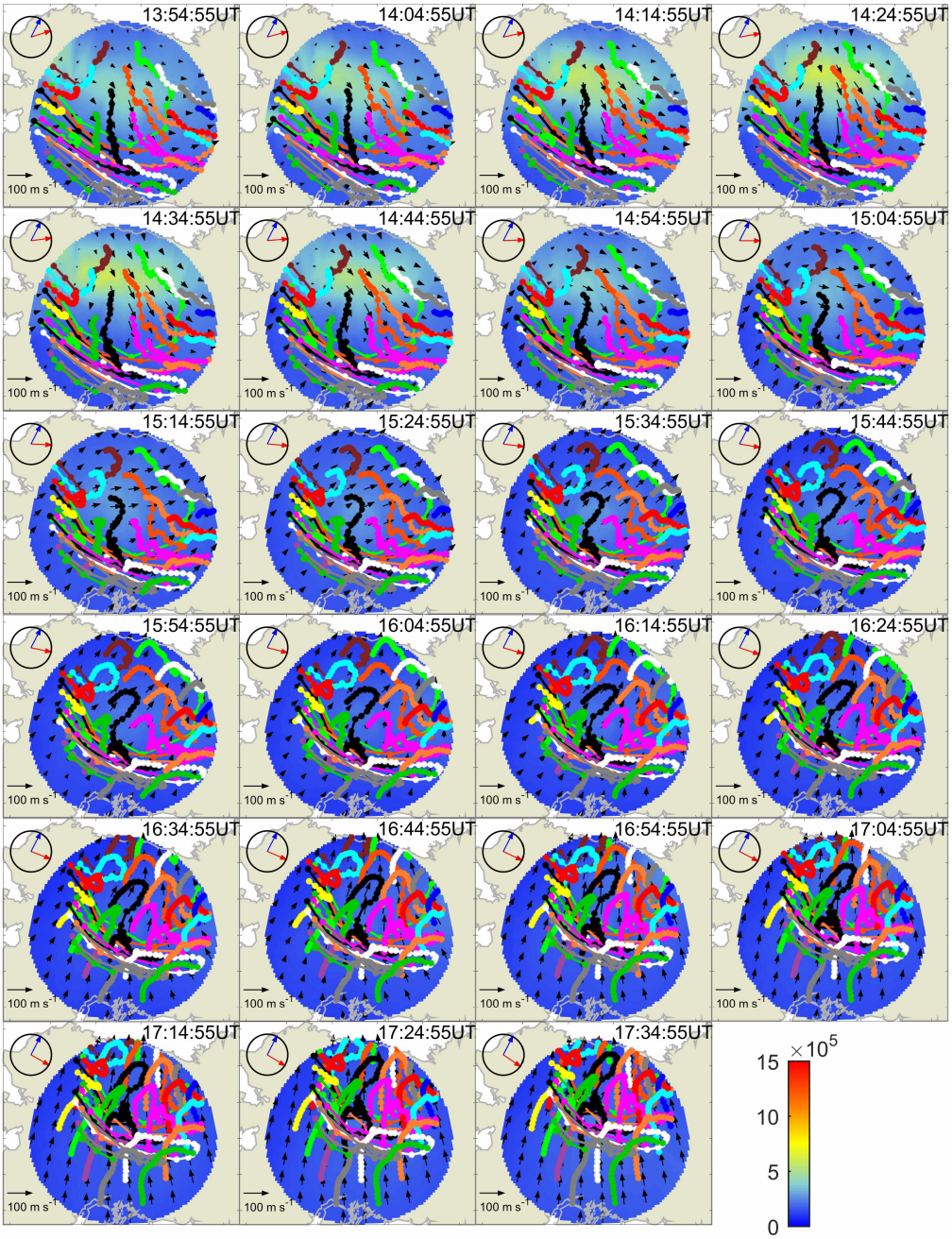

Figure 4.5: Same as for Figure 4.2, but in this case showing times from 1354 UT until 1734 UT.

was magnetic westward (probably associated with ionospheric convection). This wind flow configuration imposed curvature into the wind field. The air parcel trajectories from magnetically eastward and equatorward of the observatory started converging as a flow

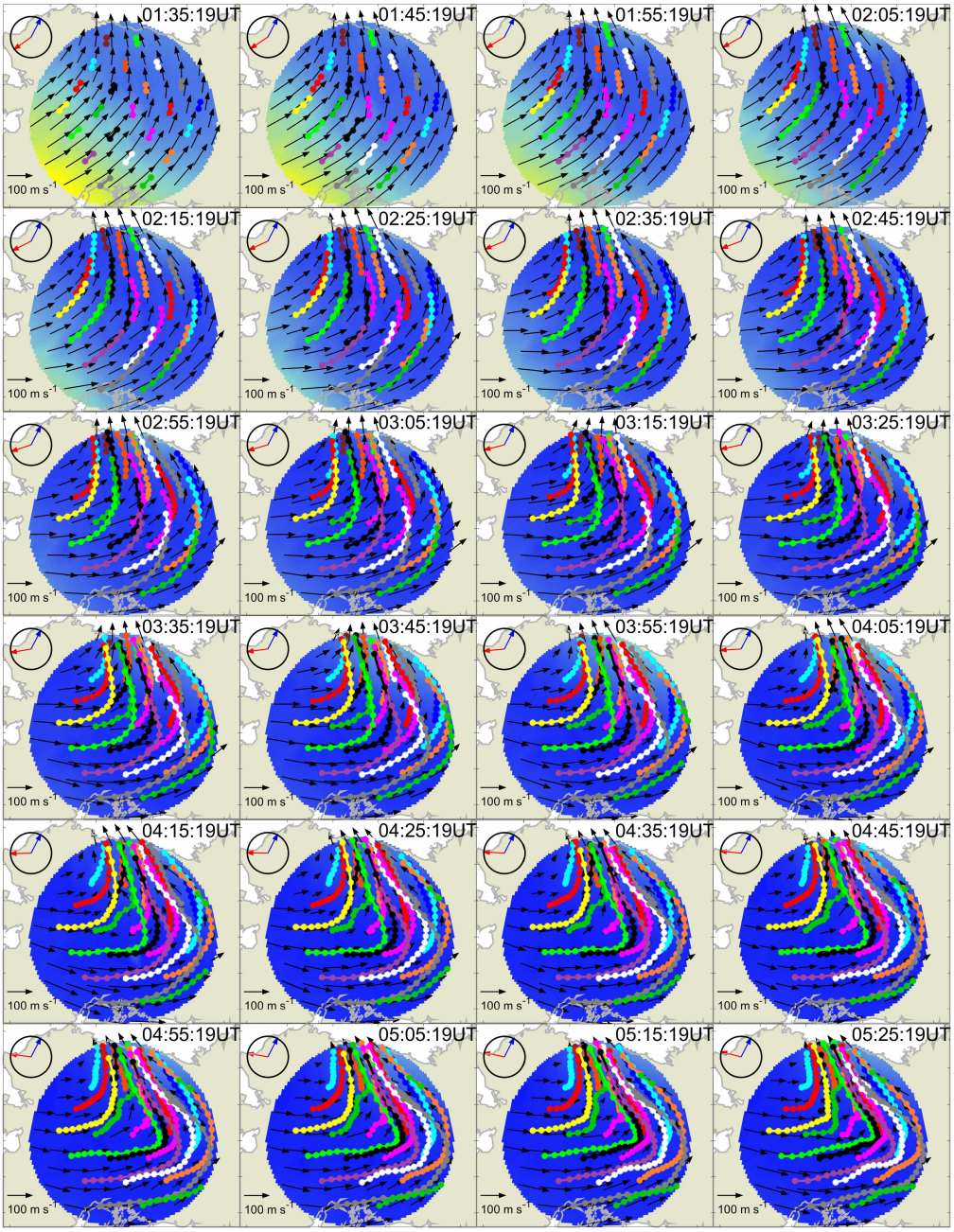

Figure 4.6: Same as for Figure 4.2, but in this case showing data for 15 December 2012 from 0135 UT until 0525 UT.

channel developed along the auroral forms. At 0334 UT, most of the air parcels above Alaska were flowing on trajectories that eventually brought them into this channel. An important consequence is that the air parcels with different geographical histories would

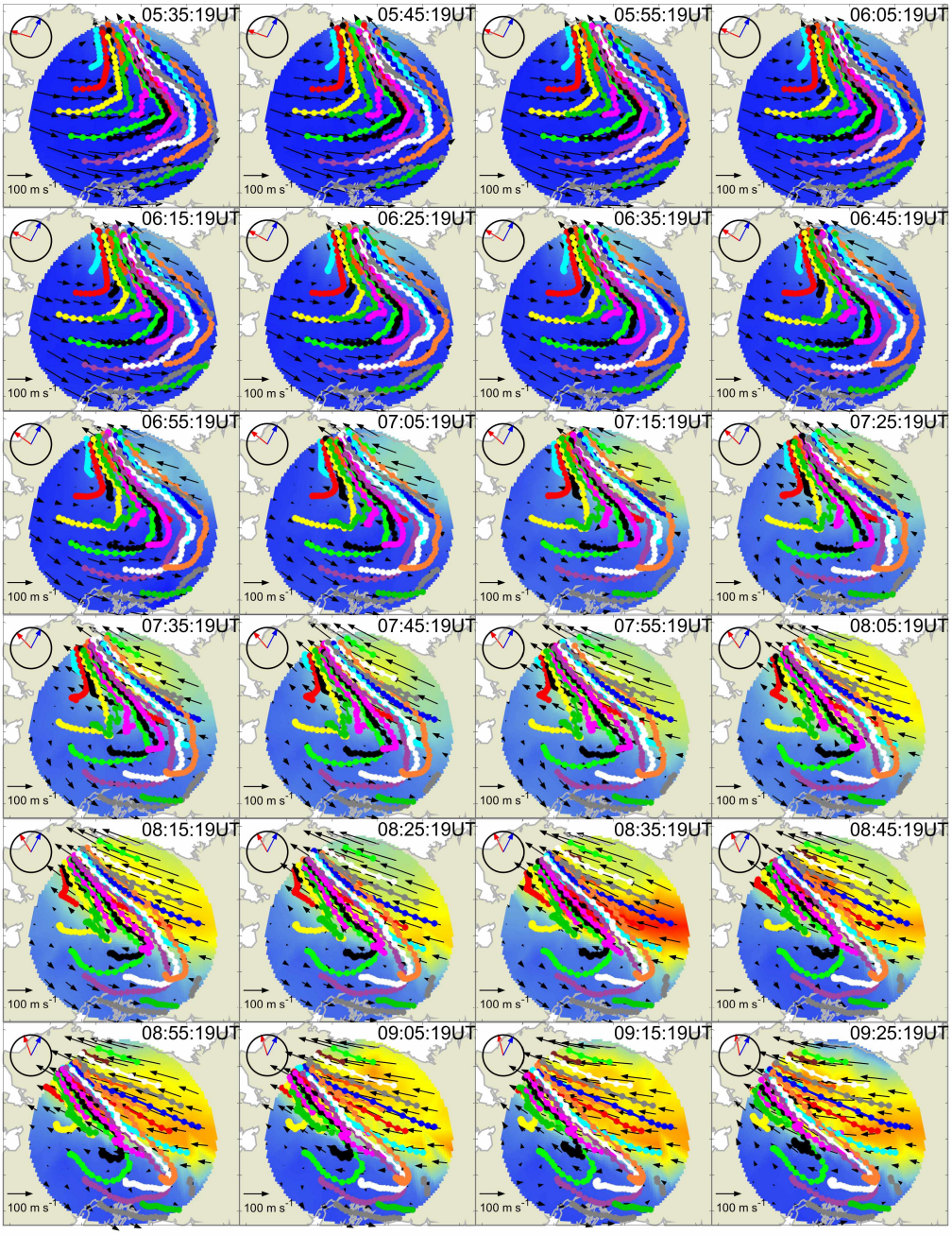

Figure 4.7: Same as for Figure 4.6, but in this case showing times from 0535 UT until 0925 UT.

have been mixed together in the channel. After 0600 UT, with the appearance of aurora on the poleward of the observatory, the winds got stronger - which we know from experience with many years of data spanning multiple data sets occurs as a result of enhanced

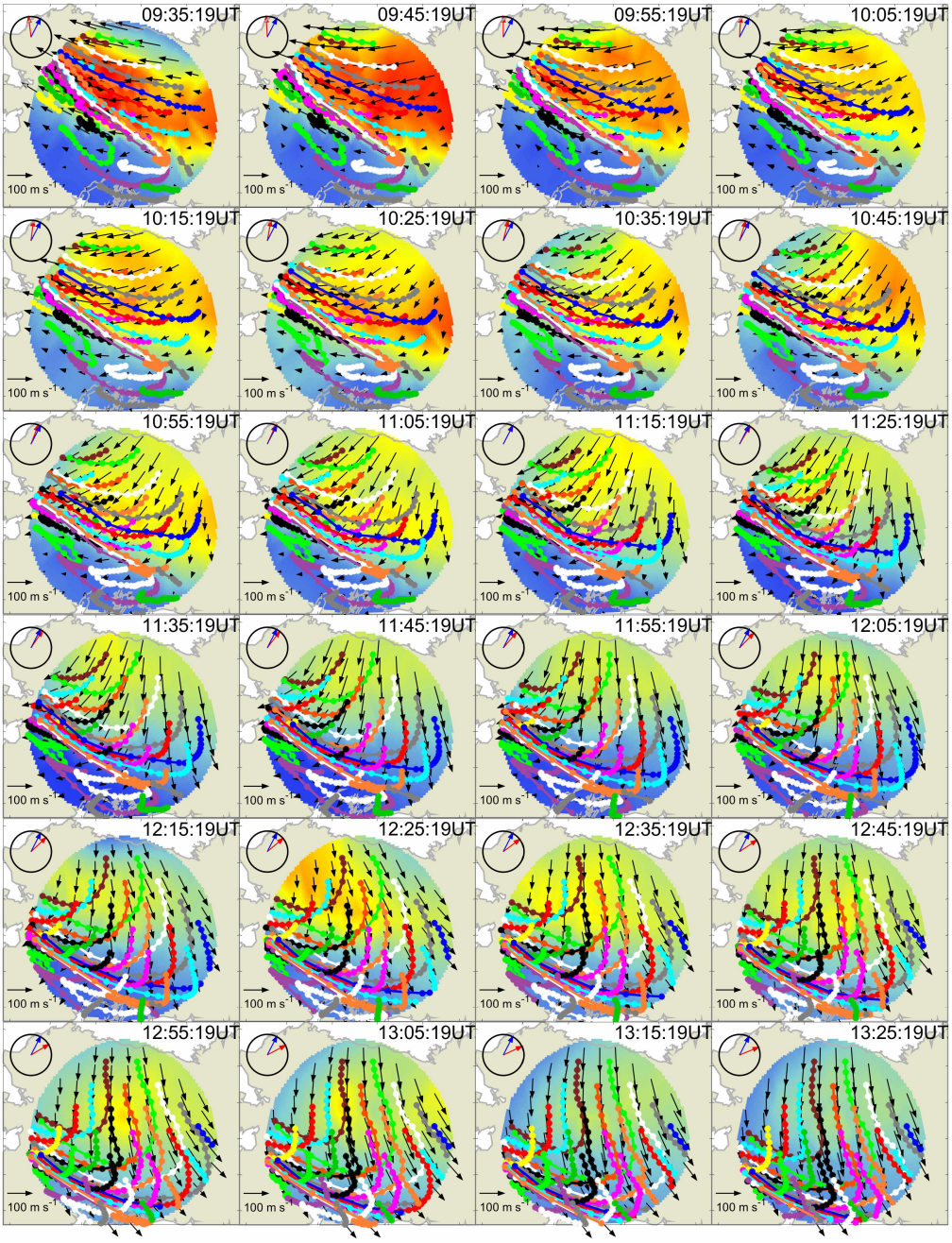

Figure 4.8: Same as for Figure 4.6, but in this case showing times from 0935 UT until 1325 UT.

ion-neutral coupling in that region. After 0630 UT, the air parcels equatorward of the observatory continue to drift antisunward, while the air parcels poleward of the observatory were entrained in the strong magnetic westward winds. As local time advances,

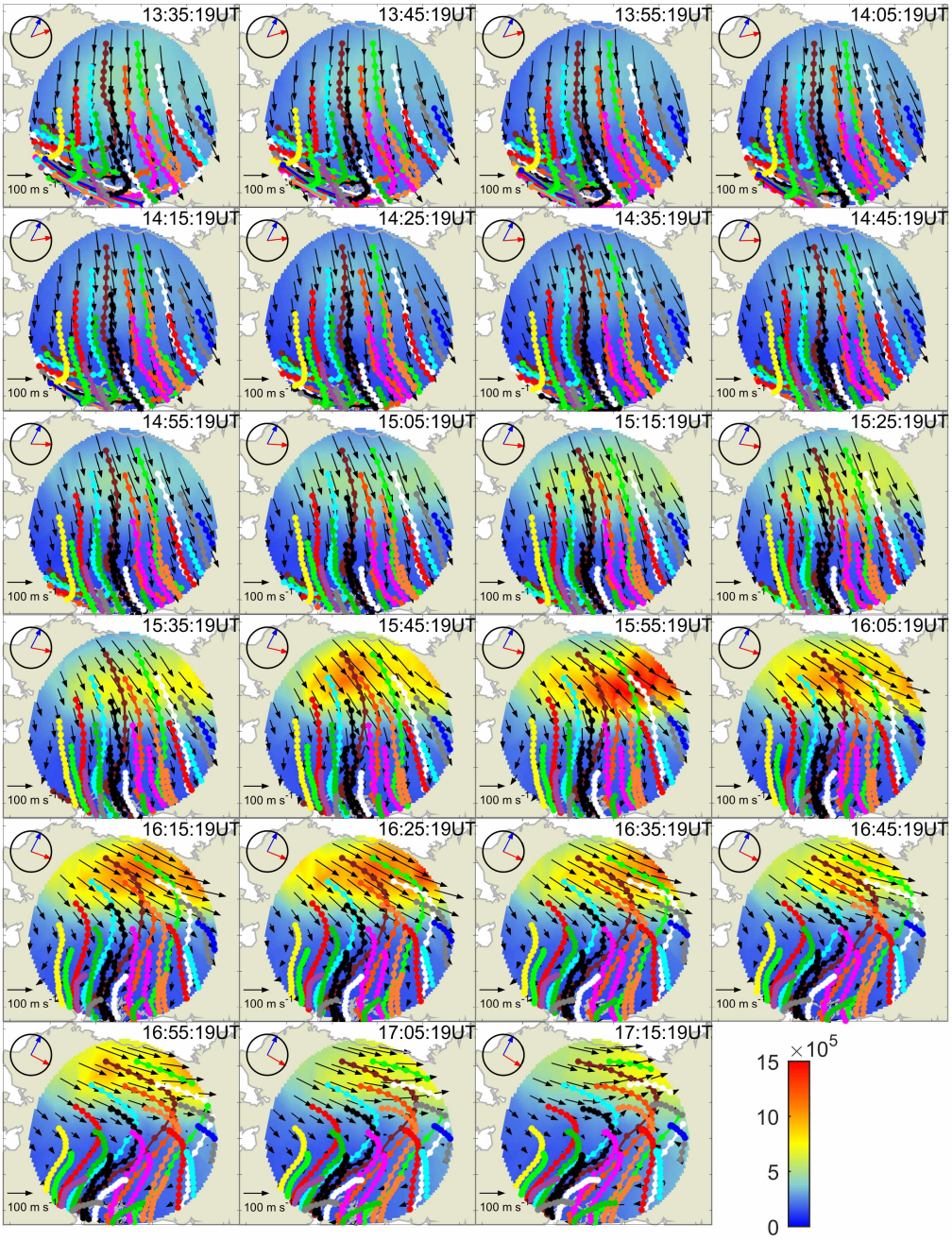

Figure 4.9: Same as for Figure 4.6, but in this case showing times from 1335 UT until 1715 UT.

antisunward flows rotate towards the magnetic east. Thus, by 0700 UT a strong line of shear had formed, with oppositely directed flows occurring poleward and equatorward of the observatory. As expected, this shear started distorting and complicating the paths

traveled by air parcels that encountered the shear. Air parcels that were initially nearby, but displaced slightly poleward and equatorward of the shear line quickly moved hundreds of kilometers apart. This clearly illustrates the role of wind shears in dispersing air parcels with previously similar geographical histories by separating the paths traveled by them. With the passage of time, the magnetic westward flow dominated the entire wind field by about 0930 UT and the magnetic east-to-west air parcel flow channel moved to the lower latitudes.

The air parcel trajectories were smooth and straight within the ion convection dominated region. After magnetic midnight (1120 UT), winds turned antisunward, and bifurcation appeared in the wind field (which is most likely associated with the antisunward jet of the Dungey cycle) which drifted the air parcels in opposite directions. It led to stretching of the virtual strings between the air parcels produced from the same location (same balloon gun) that traversed the shear and ended up moving in opposite directions. Furthermore, it also mixed air parcels with different time histories. After this time, forward air parcel trajectories started to become entangled across the SDI FOV.

The wind behaviors were broadly similar on both days before 1300UT. After 1300 UT, the horizontal air parcel transport on 07 Jan was different than 15 Dec. On 07 Dec, the wind flow was almost stagnant after 1300 UT and majority of the air parcels stayed in the SDI FOV until the end of observation cycle. After 1400 UT, the wind flows equatorward of the observatory turned magnetic northward and produced a region of densely packed air parcels of different geographical histories. A large region of air parcel mixing and complicated air parcel trajectories existed during this time interval in the SDI FOV.

On 15 Dec, after 1300 UT, the equatorward winds were strong and produced almost uniform wind flow. As a result, the entangled trajectories produced earlier by the bifurcation began to drift out of the SDI FOV. Near the end of this observation cycle, with the appearance of auroral activity poleward of the observatory around 1545 UT, stronger ion-neutral coupling drifted the neutral air parcels magnetic eastward as expected. On the equatorward side of the observatory, the wind flow was drifting air parcels equatorward. This led to the formation of latitudinal shears and skewing of the trajectories of the air parcels that started from the poleward of the observatory. Comparing this case with the

07 Jan case suggests that air parcel trajectories can become surprisingly complicated, depending on the structures in the wind fields. The data presented here are of course purely local to Alaska. Seeing this, it is not hard to imagine how complicated the trajectories of air parcels can be over the whole globe.

Our understanding of the thermospheric transport is still limited by current observational capabilities. Suppose there is a strong antisunward jet passing across the polar cap. With current observational facilities, we would be unable to find (as in the case of 15 Dec) where the air parcels emerging from the polar cap would subsequently travel to, as we have insufficient thermospheric coverage. They may be recycled by the dusk or possibly dawn circulation cells or, alternatively, they may "leak" down to equatorial latitudes and perhaps even end up in a different hemisphere. In the case of auroral sub-storms, composition perturbations (as discussed in *Crowley et al.* [1989a,b]; *Strickland et al.* [1999]; *Pallamraju* [2005]) may leak to middle and lower latitudes where they could further disturb the chemistry and dynamics of lower latitude thermosphere and ionosphere.

Having shown that we can trace air parcel trajectories forward in time, we now consider the corresponding problem of using the SDI data to find the location history of air parcels prior to some observation time. For this, we use the technique of tracing air parcels backward in time as discussed in the tracing analysis section. The motivation for this is twofold. First, if we observe some unusual activity in the thermosphere, then backward tracing can be applied to assess the likelihood that it may be related to the prior history of the observed air parcel. Secondly, it can be used to visualize how local wind gradients may have complicated the air parcel trajectories and caused air parcels with different geographical histories to mix together.

Unlike forward tracing, here only thirteen neighboring air parcels were traced backward. Here, we have used the SDI wind data to find where these air parcels came from. The first frame of Figure 4.10 depicts the location of thirteen air parcels above Alaska selected for backward tracing. Two neighboring air parcels that are at different latitudes are $\sim$56 *km* apart; two neighboring air parcels that are at different longitudes are $\sim$90 *km* apart. Full backward tracing paths of thirteen air parcels are presented in 24 frames, at the temporal resolution of 27 *min* as shown in Figure 4.10. Note that in this figure, time is

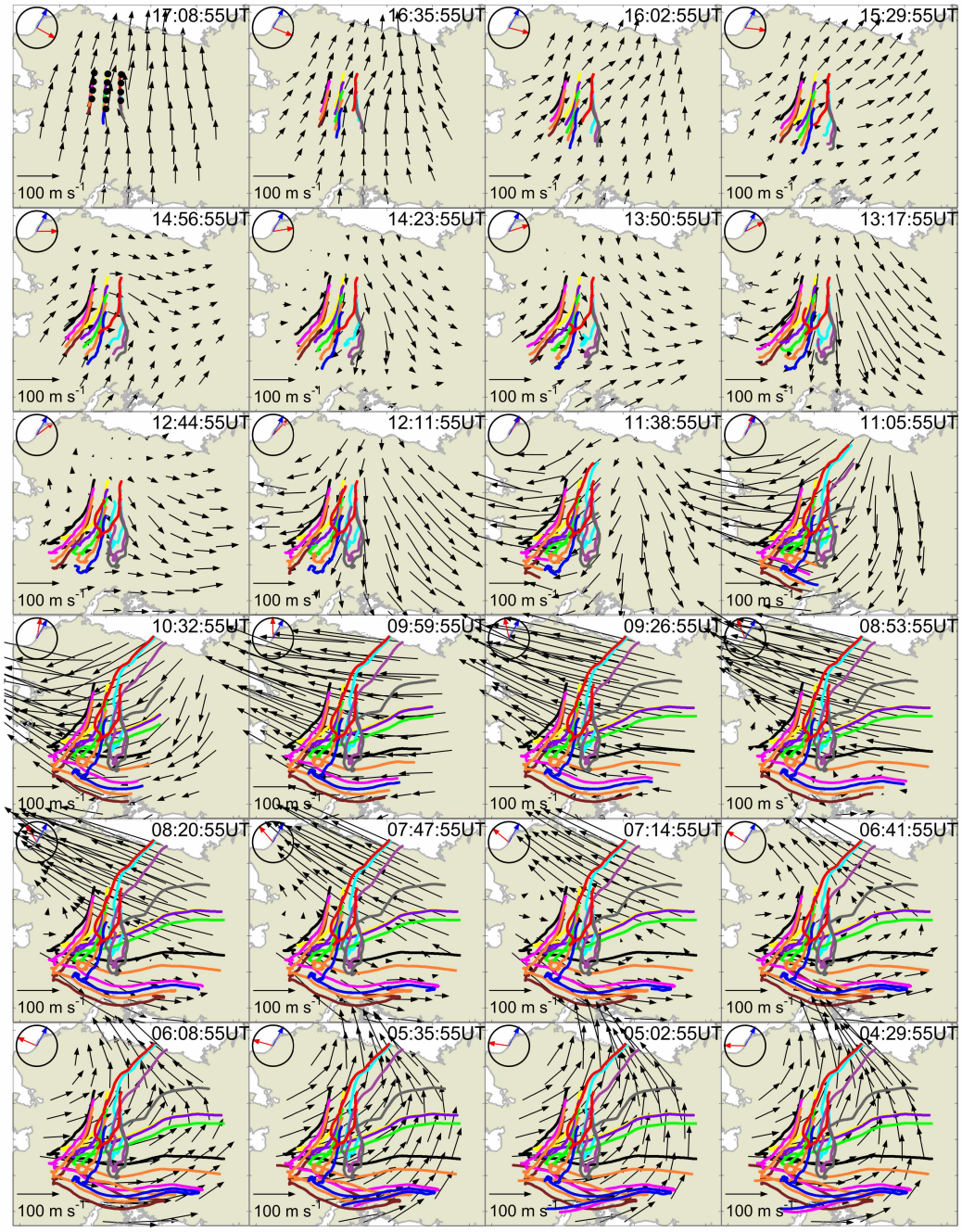

Figure 4.10: Backward tracing of 13 air parcels on 07 January 2012 to find where they came from. The first subset shows the location of all 13 air parcels selected for back tracing. Each color line represents the location history of an individual air parcel. Time is running backward in these frames.

running backward and the time corresponding to each measurement is shown at the top right of the frame. This time-reversal is necessary to follow the air parcel's prior history. It should be noted that one consequence of it may be to give the impression that air parcels are actually moving in the opposite direction to the wind, which is of course not actually the case, because time is also running backward. Finally, we were only able to trace air parcels backward until 0429 UT because before this time, all the selected air parcels were outside the SDI FOV.

Inspection of backward tracing paths revealed that nearby air parcels in the thermosphere above Alaska can have arrived there via entirely different geographical histories. Conversely, widely separated air parcels can have been in close geographic proximity at some earlier time. For example, air parcels presented in red and cyan colors were transported to their final location from poleward of the Alaska by equatorward winds. On the other hand, their neighboring yellow and pale-blue air parcels were transported to their final location from a location far to the east by the magnetic westward winds. If we consider the longest traced air parcels, presented in pink, orange, brown (all in the column on the left), and blue (from middle column), they were transported to their final locations from locations far to the west by the heating induced wind flows. Since we cannot trace air parcels to long distances due to limited geographical coverage of our instrument, there is a possibility that the orange (middle column), black, green, pale-blue, yellow, and even gray air parcels were also transported from a location far to the west. However, the wind field structure afterward 0926 UT suggests that the green, pale-blue, yellow, and gray parcel were most likely transported from eastward of Alaska by the strong magnetic westward winds. Suppose if both, for example, green and pink air parcels, were transported from locations far to the west, based on the wind fields and their current trajectories, they most likely originated from the locations hundreds of kilometers (or even more) apart. This back tracing example clearly demonstrates how various wind structures above Alaska mixed air parcels with different geographical origins. Based on the results shown above, we can definitely imagine that two nearby air parcels could originate from regions that could ultimately be separated by a whole hemisphere.

Although we have based our results on the wind data derived from a single SDI sta-

tion which is based on few assumptions (as discussed in *Conde and Smith* [1995, 1997, 1998a,b]; *Anderson et al.* [2012]), our recent study of the cross-comparison of an all-sky SDI wind measurements with a narrow field Fabry-Perot interferometer has shown that these wind measurements are most likely close to the actual wind field that prevailed during the observations. It is evident from Figure 4.2 to Figure 4.10 that the paths traveled by air parcels are quite complicated, and not smooth. Now, imagine how complex the air parcels trajectories can be over the global scale. Due to the demonstrated presence of local-scale structures in high latitude thermospheric wind fields, an extended network of observatories is needed to provide the combination high spatial resolution and wide geographic coverage that is needed to completely understand the wind driven transport in the thermosphere. Currently, no other known technique could provide the wind data required for air parcel trajectory mapping. Tracing air parcel trajectories over the global or even hemispheric scale is certainly far beyond what is currently possible either do with observations or models.

4.4 Summary and Conclusions

In methodology, our study is similar to the air parcel tracing through model wind fields performed by *Killeen and Roble* [1986], although in our case, we used experimentally measured thermospheric winds with much higher spatial resolution but only confined to the region above Alaska. Their air parcel trajectory study was focused on understanding the large-scale behavior of the wind transport, so no attempt was made to capture any local-scale details in air parcel trajectories. On the other hand, our study is focused on understanding behavior of air parcel transport on local-scale in the presence of actually observed non-uniformities in the wind fields.

Here we traced air parcel trajectories both forward and backward in time using the SDI wind measurements over a large geographic area above Alaska to show the complexity of the wind driven transport in the thermosphere. Forward tracing was used to find where air parcels would go with time and backward tracing to find where they came from. It is evident that the thermospheric air parcels do not travel in simple paths. In the thermosphere, wind shears change with time and space which introduces further

complexity in the air parcel transport.

Forward tracing showed the presence of a flow channel on the equatorward edge of the ion drag dominated wind flow before magnetic midnight. It mixed the air parcels from lower latitudes with the air parcels from high latitudes. Forward tracing clearly showed that composition perturbations caused by an active aurora can be transported to lower latitudes depending on the wind fields, which in turn can influence the lower latitude chemistry and dynamics. Backward tracing gives the history of air parcels, and revealed that two neighboring air parcels can originate from widely separated geographical regions depending on the structures in wind fields. The wind gradients led to mixing of air parcels from different parts of the thermosphere. It is evident from forward and backward tracing of air parcels that the wind transport is sensitive to the details of the wind field and any change in the wind field can cause a huge impact on where the air parcels would end up.

Our current understanding of the thermospheric transport is still limited by the paucity of observations. The real physical consequences of air parcel tracing would be fully exposed if we could trace air parcels over long distances. Currently, by combining all the data from existing operational instrumental facilities around the globe and models, we can study thermospheric climatology, but we cannot construct paths traveled by air parcels over global or even hemispheric scale with any useful accuracy. Achieving a reliable and accurate way to find paths traveled by air parcels will require an extensive network of wind measurements with instruments capable of mapping winds over wide geographic regions with high spatial resolution. If we consider air parcel tracing even over a hemisphere, the observation challenge is enormous.

4.5 References

Anderson, C., M. Conde, and M. G. McHarg (2012), Neutral thermospheric dynamics observed with two scanning Doppler imagers: 1. Monostatic and bistatic winds, *J. Geophys. Res. Sp. Phys.*, *117*(A3), A03,304, doi: 10.1029/2011ja017041.

Aruliah, A. L., and E. Griffin (2001), Evidence of meso-scale structure in the high-latitude thermosphere, *Ann. Geophys.*, *19*(1), 37–46, doi: 10.5194/angeo-19-37-2001.

Aruliah, A. L., E. M. Griffin, I. McWhirter, A. D. Aylward, E. A. K. Ford, A. Charalambous, M. J. Kosch, C. J. Davis, and V. S. C. Howells (2004), First tristatic studies of meso-scale ion-neutral dynamics and energetics in the high-latitude upper atmosphere using collocated FPIs and EISCAT radar, *Geophys. Res. Lett.*, *31*(3), L03,802, doi: 10.1029/2003gl018469.

Aruliah, A. L., E. M. Griffin, H.-C. I. Yiu, I. McWhirter, and A. Charalambous (2010), SCANDI - an all-sky Doppler imager for studies of thermospheric spatial structure, *Ann. Geophys.*, *28*(2), 549–567, doi: 10.5194/angeo-28-549-2010.

Burnside, R. G., F. A. Herrero, J. W. Meriwether, and J. C. G. Walker (1981), Optical observations of thermospheric dynamics at Arecibo, *J. Geophys. Res. Sp. Phys.*, *86*(A7), 5532–5540, doi: 10.1029/JA086iA07p05532.

Conde, M., and R. W. Smith (1995), Mapping thermospheric winds in the auroral zone, *Geophys. Res. Lett.*, *22*(22), 3019–3022, doi: 10.1029/95GL02437.

Conde, M., and R. W. Smith (1997), Phase compensation of a separation scanned, all-sky imaging Fabry Perot spectrometer for auroral studies, *Appl. Opt.*, *36*(22), 5441–5450, doi: 10.1364/AO.36.005441.

Conde, M., and R. W. Smith (1998a), Simultaneous observations of the aurora and of non-uniform thermospheric winds, from Poker Flat, Alaska, *Proc NIPR Symp Up Atmos Phys (Nat Inst Polar Res)*, *12*, 30–38.

Conde, M., and R. W. Smith (1998b), Spatial structure in the thermospheric horizontal wind above Poker Flat, Alaska, during solar minimum, *J. Geophys. Res.*, *103*(A5), 9471–9949, doi: 10.1029/97JA03331.

Conde, M., J. D. Craven, T. Immel, E. Hoch, H. Stenbaek-Nielsen, T. Hallinan, R. W. Smith, J. Olson, W. Sun, L. A. Frank, and J. Sigwarth (2001), Assimilated observations of thermospheric winds, the aurora, and ionospheric currents over Alaska, *J. Geophys. Res. Sp. Phys.*, *106*(A6), 10,493–10,508, doi: 10.1029/2000JA000135.

Conde, M. G., and M. J. Nicolls (2010), Thermospheric temperatures above Poker Flat, Alaska, during the stratospheric warming event of January and February 2009, *J. Geophys. Res. Atmos.*, *115*(D3), D00N05, doi: 10.1029/2010jd014280.

Crowley, G., B. A. Emery, R. G. Roble, H. C. Carlson, and D. J. Knipp (1989a), Thermospheric dynamics during September 18-19, 1984: 1. Model simulations, *J. Geophys. Res.*, *94*(A12), 16,925, doi: 10.1029/JA094iA12p16925.

Crowley, G., B. A. Emery, R. G. Roble, H. C. Carlson, J. E. Salah, V. B. Wickwar, K. L. Miller, W. L. Oliver, R. G. Burnside, and F. A. Marcos (1989b), Thermospheric dynamics during September 18-19, 1984: 2. Validation of the NCAR Thermospheric General Circulation Model, *J. Geophys. Res.*, *94*(A12), 16,945, doi: 10.1029/JA094iA12p16945.

Deng, Y., and A. J. Ridley (2006), Dependence of neutral winds on convection E-field, solar EUV, and auroral particle precipitation at high latitudes, *J. Geophys. Res. Sp. Phys.*, *111*(A9), A09,306, doi: 10.1029/2005JA011368.

Fuller-Rowell, T. J., M. V. Codrescu, H. Rishbeth, R. J. Moffett, and S. Quegan (1996), On the seasonal response of the thermosphere and ionosphere to geomagnetic storms, *J. Geophys. Res.*, *101*(A2), 2343, doi: 10.1029/95JA01614.

Greet, P. A., M. G. Conde, P. L. Dyson, J. L. Innis, A. M. Breed, and D. J. Murphy (1999), Thermospheric wind field over Mawson and Davis, Antarctica; simultaneous observations by two Fabry-Perot spectrometers of λ630 nm emission, *J. Atmos. Sol. Terr. Phys.*, *61*(14), 1025–1045, doi: http://dx.doi.org/10.1016/S1364-6826(99)00059-0.

Killeen, T. L., and R. G. Roble (1984), An analysis of the high-latitude thermospheric wind pattern calculated by a thermospheric general circulation model: 1. Momentum forcing, *J. Geophys. Res.*, *89*(A9), 7509–7522.

Killeen, T. L., and R. G. Roble (1986), An analysis of the high-latitude thermospheric wind pattern calculated by a thermospheric general circulation model: 2. Neutral parcel transport, *J. Geophys. Res.*, *91*(A10), 11,291, doi: 10.1029/JA091iA10p11291.

Killeen, T. L., Y.-I. Won, R. J. Niciejewski, and A. G. Burns (1995), Upper thermosphere winds and temperatures in the geomagnetic polar cap: Solar cycle, geomagnetic activity, and interplanetary magnetic field dependencies, *J. Geophys. Res.*, *100*(A11), 21,327, doi: 10.1029/95JA01208.

Meriwether, J. W., J. P. Heppner, J. D. Stolarik, and E. M. Wescott (1973), Neutral winds above 200 km at high latitudes, *J. Geophys. Res.*, *78*(28), 6643–6661, doi: 10.1029/JA078i028p06643.

Meriwether, J. W., T. L. Killeen, F. G. McCormac, A. G. Burns, and R. G. Roble (1988), Thermospheric winds in the geomagnetic polar cap for solar minimum conditions, *J. Geophys. Res.*, *93*(A7), 7478, doi: 10.1029/JA093iA07p07478.

Pallamraju, D. (2005), First ground-based measurements of OI 6300 Å daytime aurora over Boston in response to the 30 October 2003 geomagnetic storm, *Geophys. Res. Lett.*, *32*(3), L03S10, doi: 10.1029/2004GL021417.

Rishbeth, H. (1972), Thermospheric winds and the F-region: A review, *J. Atmos. Terr. Phys.*, *34*(1), 1–47, doi: 10.1016/0021-9169(72)90003-7.

Strickland, D. J., R. J. Cox, R. R. Meier, and D. P. Drob (1999), Global O/N_2 derived from DE 1 FUV dayglow data: Technique and examples from two storm periods, *J. Geophys. Res.*, *104*(A3), 4251, doi: 10.1029/98JA02817.

Chapter 5

First Ever Cross-Comparison of Thermospheric Wind Measured by Narrow and Wide Field Optical Doppler Spectroscopy[1]

Abstract

We present the first ever cross-comparisons of F-region horizontal neutral wind measurements taken using two different types of optical Doppler spectrometer: all-sky scanning Doppler imagers (SDI) and narrow-field Fabry-Perot Interferometers (NFPI). Horizontal neutral winds were inferred using bistatic observations from three NFPIs, together with monostatic and bistatic observations from two SDIs. All instruments were located in Alaska. Cross-comparisons were made for a total of 7 nights in January and February of 2010. The results show a high degree of correlation between the diurnal behaviors of the line-of-sight (LOS) winds measured by both instruments. The SDI and NFPI LOS wind time series also often contained high frequency fluctuations with similar overall characteristics, strongly suggesting that these fluctuations were geophysical in origin. However, the amplitude of the high-frequency component was stronger in the NFPI LOS wind than SDI data. Even the smallest SDI angular resolution element is much larger than the NFPI field of view, suggesting that its relative insensitivity to high frequencies is because these fluctuations are associated with local-scale structures whose spatial extent is smaller than the $\sim$40 *km* spanned by the smallest SDI viewing field. Upon fitting vectors to the LOS wind data, close agreement was found between the wind components estimated by the two types of instrument. Discrepancies that did arise occurred most often when the neutral wind speed was weak, suggesting that conditions capable of driving higher neutral wind speeds also suppressed the development of small-scale structures in the thermospheric neutral wind fields.

[1]Dhadly, M. S., J. Meriwether, M. Conde, and D. Hampton (2015), First ever cross-comparison of thermospheric wind measured by narrow and wide field optical Doppler spectroscopy, J. Geophys. Res. Space Physics, doi:10.1002/2015JA021316.

5.1 Introduction

Although thermospheric dynamics have been studied for many decades, we still know relatively little about how the spatial and temporal spectra of wind motion behave at the smallest observable scales. At auroral latitudes, thermospheric winds are driven by two dominant processes, namely, the global pressure gradient established by solar heating, and momentum deposition due to collisions with ions moving in response to the magnetospheric "convection" electric field. Time varying interplay between these two drivers leads to substantial variations in thermospheric circulations at local, synoptic, and even global scales. Characterization of this complex behavior presents a formidable observational challenge.

Since the 1950s, many techniques have been developed to observe Earth's thermospheric winds. Of these, optical remote sensing has produced the most data to date. In recent decades, Fabry-Perot interferometers (FPI) have become popular for measuring wind speed and temperature in the neutral thermosphere using Doppler shift and Doppler broadening (width) of natural optical line emissions.

Several variants of ground-based FPIs are in current use. Because they employ different techniques that are somewhat indirect, it is important for the various "flavors" of these instruments to be cross-validated. Because the global Fabry-Perot interferometer network is sparse [*Meriwether*, 2006], opportunities for such cross-validation are rare.

Fortunately, in Alaska, two different variants of ground-based optical Doppler spectroscopic instruments are operating and mapping neutral winds independently. Both are Fabry-Perot Doppler spectrometers. One type, which we refer to here as a "narrow-field FPI" (NFPI), uses a narrow field of view (FOV) with a fixed gap etalon. The other is an all-sky scanning interferometer with a separation-scanning etalon. We refer to it as a "Scanning Doppler Imager" (SDI). Although both are based on Doppler spectroscopy of naturally occurring optical emissions from the thermosphere and use Fabry-Perot etalons to obtain the required spectral resolution, they are entirely different in their modes of operation, data collection, and data analysis. *Ishii et al.* [2001] compared the vertical winds inferred by SDI and NFPI techniques, but horizontal winds inferred by NFPI and SDI instruments have never been cross-compared. In the present research, we focus on com-

paring horizontal thermospheric winds measured by these two related but nonetheless very different instruments from Alaska using the 630 *nm* atomic oxygen emission, which occurs naturally in a broad layer centered around 240 *km* altitude and spanning many tens of km in height. The major goal of the present study is to compare geophysical results derived using these two very different sampling strategies.

The value of Fabry-Perot etalons for airglow and auroral studies was first demonstrated by *Babcock* [1923] in a study of the spectral profile of the 558 *nm* auroral green line. Since then, the Fabry-Perot technique has improved extensively, especially in the past two decades. This has largely been due to the availability of new imaging detectors with high sensitivity, low noise, and wide dynamic range. Traditional Fabry-Perot spectrometers only view a small region of sky at one time (typically spanning only a degree or so); this small FOV must be re-pointed between exposures in order to map how the medium's bulk flow speed (derived from the Doppler spectrum) depends on the look direction toward the source region. The NFPI instrument types discussed here operate this way, whereas the SDI is able to resolve spectra for numerous look directions across almost the entire sky at once.

To derive a high-resolution spectral profile of a single emission line, the transmission pass bands of an etalon can be tuned or "scanned" in wavelength by varying any one of three parameters: the etalon gap, the optical incidence angle, or the refractive index of the gas within the etalon gap. A few researchers [*Rees et al.*, 1984; *Biondi et al.*, 1995; *Nakajima et al.*, 1995] have utilized all sky fore-optics coupled to a fixed gap etalon to achieve multiple simultaneous measurements over an extended spatial FOV. The problem with this approach is that the angular and spectral information are encoded together because the incidence angle at the etalon also maps to the look angle in the sky. A more elaborate instrumental technique, namely the all-sky scanning Doppler imager (SDI) reported here, uses a combination of the first two of these three possible scanning methods. All-sky scanning Doppler Fabry-Perot interferometers with scanning etalons have been operating in auroral regions since the mid 1990's [*Conde and Smith*, 1997, 1998a; *Griffin et al.*, 2008; *Anderson et al.*, 2009; *Aruliah et al.*, 2010].

SDI instruments map the two-dimensional horizontal neutral wind and temperature

field over a wide zenith-centered (typically) geographic region that extends down to about 70 degrees zenith angle. This wide field is divided (in software) into multiple sub-fields (zones), allowing independent spectra to be sampled from many directions simultaneously. For the work presented here, the SDI was configured to use 115 zones. Regardless of how many look directions are used, a single station can only measure the line-of-sight (LOS) component (in each direction) of what is in reality a three-component wind vector. Geophysical information is extracted from a single site by applying a "mono-static" wind fit algorithm, which will inevitably require substantial assumptions. Bistatic wind fitting has been demonstrated previously by *Sipler et al.* [1995]; *Ford et al.* [2006]; *Anderson et al.* [2011, 2012]; *Chapagain et al.* [2012, 2013]; *Nicolls et al.* [2012].

The studies of *Anderson et al.* [2012] combined the measurements of two independent SDIs (Poker Flat and Gakona) in their overlapping all-sky fields of view to infer horizontal vector wind field. With three stations, three independent LOS wind components can be measured, allowing a fully unambiguous reconstruction of the three-component wind vector without assumptions. This approach was demonstrated by *Aruliah et al.* [2004, 2005] and *Ford et al.* [2006]. The work described by *Chapagain et al.* [2012, 2013] reported on the study of the ion-neutral coupling found for the equatorial thermosphere derived from the comparison of the horizontal neutral wind vector determined with common volume bistatic NFPI observations for a region that was also observed by an imaging all-sky system. The plasma ion drift motion was derived from the all-sky image analysis of the motions of airglow depletion region. Comparison of the horizontal ion drift vector derived from the imaging analysis with the horizontal neutral wind vector derived from the bistatic FPI analysis found that the F-region dynamo was not fully activated in the early evening period. The FPI instruments used in these two Chapagain studies were similar in sensitivity and design (fixed gap) to the two NFPI Alaskan instruments.

Thermospheric wind measurements reported in the present study were obtained with five ground-based optical Doppler spectrometers. Out of these five Doppler spectrometers, two are wide FOV SDIs, located in Alaska at Poker Flat (65.12N, 147.43W) and Gakona (62.39N, 145.15W). Two others are NFPIs located at Poker Flat (65.12N, 147.43W) and Fort Yukon (66.56N, 145.25W). The fifth instrument is also a NFPI located at Poker

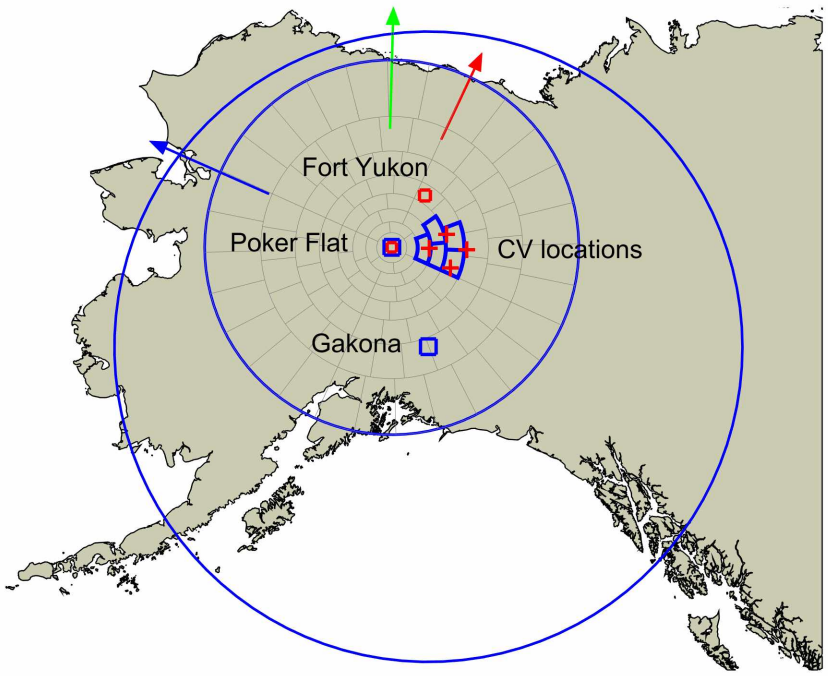

Figure 5.1: Location of the SDI (blue squares) and NFPI observatories (red squares) along with the common volume locations indicated as red crosses. CV1, CV2, CV3, and CV4 are in clockwise sequence with CV1 as westernmost vertex of CV polygon and closest to Poker Flat. Shown in blue are the nearby Poker Flat SDI observing zones that were used in this study for zonal and meridional winds. Large blue circles represent the outer extents of the FOVs of the SDIs located at Poker Flat and Gakona, when projected at 240 altitude. The red, blue, and green arrows point towards the magnetic north (direction perpendicular to auroral oval), magnetic west, and geographic north respectively.

Flat, but it was only viewing in the zenith direction, and thus measuring vertical winds and temperatures directly overhead. The SDI and NFPI instruments are operated by the Geophysical Institute (University of Alaska Fairbanks) and Clemson University respectively. Figure 5.1 shows the geographic locations of these instruments and also describe the viewing geometry used by these instruments.

The NFPIs were viewing in four look directions that intersected the 630 *nm* emission layer within the overlap region of the Gakona and Poker Flat SDIs. These instruments also

obtained vertical wind measurements required to determine for each NFPI instrument the Doppler zero-wind reference. Look directions were selected in such a way that the LOS from the Poker Flat NFPI intersects the LOS from the Fort Yukon NFPI, at an altitude of the 630 *nm* emission layer. These locations of intersection of LOSs are referred to here as "common volume (CV) locations". Bistatic wind fit analysis of the data from these two NFPI sites was performed following the analysis described by *Chapagain et al.* [2012, 2013]. Horizontal neutral wind fit data, raw LOS wind Doppler shift data, and temperature data were made available for the cross-comparisons presented here.

5.2 Instrument Description and Data Analysis

5.2.1 Narrow-Field Fabry-Perot Interferometer

The two NFPI instruments used a full-angle FOV of typically 1 degree, which maps to a spatial extent of 4-5 *km* at zenith when projected at an altitude of 240-250 *km*. Observation in any direction with a pointing accuracy of $\sim$0.1 degree is obtained by using a steerable double-axis mirror system. Basic principles, description of the operational technique, and details regarding analysis are described by *Makela et al.* [2011]; *Meriwether et al.* [2011]; *Nicolls et al.* [2012]; *Shiokawa et al.* [2012]. A brief summary is presented here.

Light collected by sky scanner fore-optics passes through a fixed gap etalon, which produces angular modulation of brightness. This modulation is imaged to form a two-dimensional ring pattern (fringes) on a high efficiency back-thinned CCD detector. The number of rings varied from one NFPI instrument to another with 3 and 1 for the Fort Yukon and Poker Flat, respectively. These ring patterns were transformed into one-dimensional interferograms (or sky spectrum) by the application of annular summing around the ring center [*Coakley et al.*, 1996].

Derivation of data products from NFPI sky spectra is described in *Meriwether et al.* [2008, 2011]; *Makela et al.* [2011]; *Shiokawa et al.* [2012]. Data analysis was carried out by determining the instrument function independently for each order of the recorded laser spectra. The analysis procedures uses a non-linear least square fit algorithm to estimate the Doppler line center, Doppler width (temperature), 630 *nm* intensity, and the contin-

uum background intensity for each of the interference orders analyzed. The error bars for these estimates are determined by the analysis routine and represent the statistical uncertainty in the fit of the observed data [*Makela et al.*, 2011; *Chapagain et al.*, 2012]. The Doppler line center is the centroid position of the peak of the 630 *nm* spectral profile. Except for the Doppler line centers, these data products were then averaged using the estimated error bars to produce a weighted average of each of these.

The sky spectrum derived from the annular-summed interferogram of each order in a fringe image is in reality a convolution of the actual sky spectrum and the instrumental response to a spectrally narrow input signal. This response is conventionally called the "instrument function". It must be measured experimentally, which is done by observing a diffuse target illuminated by a frequency stabilized He-Ne laser. It is de-convolved from the recorded spectra when fitting model emission spectra to them. The method of Fourier coefficients described by *Hays and Roble* [1971] and *Makela et al.* [2011] was used for this purpose of deconvolution. The sky emission spectrum is analyzed for each order yielding data products of background, 630 *nm* intensity, Doppler line center, and Doppler temperature that are then averaged using the measured errors for each sky spectrum in a weighted average.

In the analysis of the Doppler line center determination for each order to infer the Doppler shift for the look direction chosen, a Doppler zero wind reference must be determined before the Doppler shift can be determined. Frequent observations during the data taking period of the laser Doppler line center are used to determine the temporal variation of this Doppler zero-wind reference caused by ambient temperature variation. To get the Doppler zero-wind reference, an offset of the laser reference curve must be determined that would be added to the laser reference curve to get the zero wind reference. To determine the value of this offset, the assumption is made that any existing vertical wind variation when averaged over a night of data collection would be zero. The offset value is calculated by averaging all of the differences of the Doppler line centers observed for the zenith direction relative to the laser reference curve. This step in the analysis using this assumption is the same as what was done in previous work described by *Aruliah and Rees* [1995]; *Faivre et al.* [2006]; *Meriwether et al.* [2008, 2011]; *Makela et al.* [2012] showed that

the assumption of zero-average vertical wind over one night is valid when observation periods are long and geomagnetic activity is low.

In the observations described here, the two NFPI instruments were pointed in sequence toward each one of four common volumes (CV) used for LOS wind measurement. The cycle progressed repeatedly through the four selected CV locations in a succession of CV1 (65.11N, 145.02W), CV2 (65.48N, 143.84W), CV3 (65.03N, 142.55W), and CV4 (64.54N, 143.66W) positions in a clockwise direction from CV1 to CV4 where CV1, CV2, CV3, and CV4 were the westernmost, northernmost, easternmost, and southernmost vertex of the CV polygon respectively. These observations were then augmented by a local zenith observation needed for the zero reference determination. These observations were not synchronized in time but each set of observations was fitted with a spline fit against time so that simultaneous values were determined. Two independent Doppler shifts along the two lines of sight were therefore determined at each CV location. This set of eight independent measurements at four CV locations allowed the NFPI network to measure mean horizontal winds and meridional/zonal gradients as well as vorticity and divergence. Each complete set of CV, zenith, and laser measurements took ~7.5 minutes. The meridional and zonal wind components of the neutral wind vector in each CV location were calculated using the bistatic analysis algorithm described by *Nicolls et al.* [2012].

Systematic error in the zero Doppler baseline can be as much as 10 to 20 $m.sec^{-1}$ under active geomagnetic conditions, although such errors would be rare. Typical bias in wind estimates is more likely to be less than 5 $m.sec^{-1}$. A complete discussion of bias introduced by the vertical winds in wind estimates is given in *Aruliah and Rees* [1995].

Another NFPI at Poker Flat was monitoring only vertical winds by looking solely in the station zenith with a temporal resolution of 90 sec. The vertical wind component derived from these observations was spatially extended to the four CV polygon vertices under the assumption that vertical wind was constant at all locations. Although this assumption was not tested here, experience from the other campaigns suggests that although the assumption may often be violated, the consequent errors will not be large.

Table 5.1: SDI and NFPI instrument parameters

Instrument	Full FOV	Etalon	Etalon size	Max etalon gap
SDI Poker Flat	136 deg	Scanning	100 mm	18.6 mm
SDI Gakona	160 deg	Scanning	150 mm	18.6 mm
NFPI Poker Flat	~1 deg	Fixed	100 mm	10 mm
NFPI Fort Yukon	~1 deg	Fixed	100 mm	15 mm
NFPI Poker Flat (vertical)	~1 deg	Fixed	70 mm	15 mm

5.2.2 Scanning Doppler Imager

Our scanning Doppler Imagers are Fabry-Perot interferometers capable of collecting optical emission profiles simultaneously from many tens of locations (typically 115) across the sky. They do so using all sky fore-optics coupled to a separation scanned etalon. A detailed description of the operation of an SDI was presented by *Conde and Dyson* [1995]; *Conde and Smith* [1997, 1998b,a] and most recently in *Conde and Nicolls* [2010]. A short description of the principle of operation of an SDI is given below.

Optical emissions from the thermosphere are collected by all-sky fore-optics. A motor driven filter wheel carrying various narrow band interference filters is incorporated in the fore-optics and selects the wavelength of interest. Filtered light is then modulated by a separation scanned etalon. The working aperture diameters of the etalons at Poker Flat and Gakona SDI were 100 mm and 150 mm respectively. The etalons separation scans were configured to span one order of interference at 630 *nm* wavelength and were typically conducted in 128 discrete steps. The basic comparison between SDI and NFPI parameters is presnted in Table 5.1.

The angularly modulated signal emerging from the etalon was then focused onto a high efficiency thermoelectrically cooled electron multiplying CCD detector. The recorded image was divided (in software) into zones (sets of contiguous pixels), which allowed us to map the Doppler parameters across the sky. The interference order varied with angle of incidence at the etalon, resulting in a range of interference orders occurring in the radial direction across a zone. This was compensated by phase mapping as discussed in

Conde and Smith [1997]. Each exposure was produced by co-adding spectra from multiple rapid scans (single scan time $\approx$ 23 sec). This process of co-adding spectra was performed until an appropriate signal to noise was reached on average across all zones. The instrument functions and instrument drift were measured routinely by introducing a diffuse frequency-stabilized He-Ne laser source into the SDI using an integration sphere. Independent instrument functions were derived for each of the 115 viewing zones. The SDI etalon is separation-scanned which, as described by *Conde and Smith* [1998a], means that auroral intensity gradients across the field of view do not normally distort the spectra. In the case of NFPI, the spatial auroral intensity gradients do not matter due to its narrow field of view and because all spectral elements in the spectral profile are observed simultaneously so temporal changes would not produce any modification of the spectral profile shape.

In this study, we consider SDI winds derived monostatically and bistatically. Our monostatic analysis models the two-component horizontal vector wind field using a first order Taylor expansion about the station zenith. To obtain a unique fit, two typical substantial assumptions used regarding the meridional and vertical wind are: zonal gradient of meridional wind is negligible and vertical wind speed is small compared to horizontal wind speed. Details of monostatic wind analysis are described in *Conde and Smith* [1998a]; *Anderson et al.* [2012] which is in turn based on *Burnside et al.* [1981].

There was considerable overlap between the FOVs of SDIs at Poker Flat and Gakona as shown in Figure 5.1. It was therefore also possible to perform a bistatic analysis of the SDI data on nights with clear skies and good instrument operation at both Gakona and Poker Flat. The NFPI CV polygon was also located inside this common. To compare the results from the SDI and NFPI bistatic analysis, a location that was at the center of the CV polygon (at 65.075N, 143.75W) was selected for SDI bistatic wind fitting. Vertical winds were considered negligible. This was the only assumption used in bistatic wind analysis. Details of the bistatic wind fit analysis is discussed in *Anderson et al.* [2012].

The full-angle FOV of the Poker Flat and Gakona SDIs were 136 degree and 160 degree respectively. These fields of view were calibrated by observing the moon location in accumulated sky images at several different times, each separated by a few hours.

The errors in the LOS wind speed that represent statistical uncertainty were calculated by the analysis routines. The typical uncertainty in the LOS wind speed for both instruments was ~5-10 $m.sec^{-1}$. The uncertainty in the fitted wind components (zonal and meridional winds) totally depends on how well the assumptions used in wind fit analysis hold. There is no mathematical way to quantify the uncertainties introduced by these assumptions in the fitted wind components. Based on our experience and other comparison studies [e.g., *Anderson et al.*, 2012], uncertainties are unlikely to be more than 15-20 $m.sec^{-1}$ in the fitted wind components.

Both SDIs and NFPIs record frequent 632.8 *nm* spectra of frequency-stabilized He-Ne lasers, that are used for monitoring wavelength drift and to determine the zero velocity baselines. However, the routine method for drift correction at Poker Flat and Gakona SDIs is simply to use low-pass filtered vertical winds (derived from the central zone) as a time-resolved zero velocity reference. Experience shows that this works well, because etalon drift in the SDI instruments is normally slow and smooth (on time scales of hours). Laser spectra are only used on the very rare occasions, when the instrumental drift is less smooth. The process of correcting for any SDI drift is discussed in *Anderson et al.* [2012]. By contrast, the NFPIs at Poker Flat and Fort Yukon routinely use a combination of vertical wind measurements and laser spectra to derive the time-resolved zero velocity reference. For these instruments He-Ne laser spectra are used to characterize time varying etalon drift, whereas the "DC" level of the zero velocity reference is derived by requiring that the vertical wind is averaged to zero over the entire night. The etalon drift for NFPIs at Poker and Fort Yukon was 100-150 $m.sec^{-1}$ over 10-15 hours [*Nicolls et al.*, 2012]. The drift for the vertical pointing NFPI at Poker Flat was ~10-20 $m.sec^{-1}$ over 15 hours. For SDIs, this drift rarely exceeds 15 $m.sec^{-1}$ during the night. For both SDIs and NFPIs, the measurement errors in the LOS wind vary between 5-10 $m.sec^{-1}$ depending on the activity of 630 *nm* emissions.

5.3 Observational Data

Comparison data sets generated by SDI and NFPI were available for a total of seven nights during early 2010: three in January (10, 11, and 24) and four in February (03, 11,

12, and 16). NFPI data sets reported here were taken from Poker Flat and Fort Yukon. Vertical wind data was obtained from a second NFPI at Poker Flat. NFPI bistatic analysis was performed both with and without vertical wind correction.

Monostatic vector wind fields were derived using LOS wind data obtained with the Poker Flat SDI. SDI bistatic wind vectors derived using LOS winds from Poker Flat and Gakona SDI were produced at a temporal resolution of 6 min. The zonal and meridional wind components obtained from the SDI monostatic and SDI bistatic wind fitting algorithms were aligned such that the magnetic east-west direction of the coordinate system was parallel to the local auroral oval. The direction of the magnetic north is the direction perpendicular to the auroral oval. In terms of magnetic coordinates, the magnetic westward is the direction in which magnetic longitude increases most rapidly. The effect of curvature of Earth's surface on the geometry for wind analysis was small, and so neglected in both SDI and NFPI analysis.

Poker Flat and Fort Yukon sky conditions were assessed using Keograms from broadband all-sky imagers. Sky conditions at these observatories were clear on all the nights presented here. Gakona sky conditions assessed solely from the SDI data themselves - specifically from all-sky wind dial plots, all-sky SDI temperature and brightness data. While not quite as definitive as the Keogram method, we have many years of experience showing that reliable cloud assessment can be made solely from SDI data. Based on this we determined that Gakona was cloudy on 03 February 2010. Moreover, data from Gakona were not available on 11 January 2010.

5.4 Results

While both SDI and NFPI techniques do generate wind vectors, we focus first on the raw LOS wind measurements, to make the most direct comparison possible between SDI and NFPI, without imposing assumptions or significant smoothing. Only the SDI and NFPI instruments at Poker Flat were suitable for this comparison, since it requires a common LOS direction and hence collocated instruments. Nevertheless, none of the SDI's 115 look directions exactly matched those of the NFPI, so the SDI data were spatially interpolated to provide the best possible estimates of the LOS wind speed that SDI would have ob-

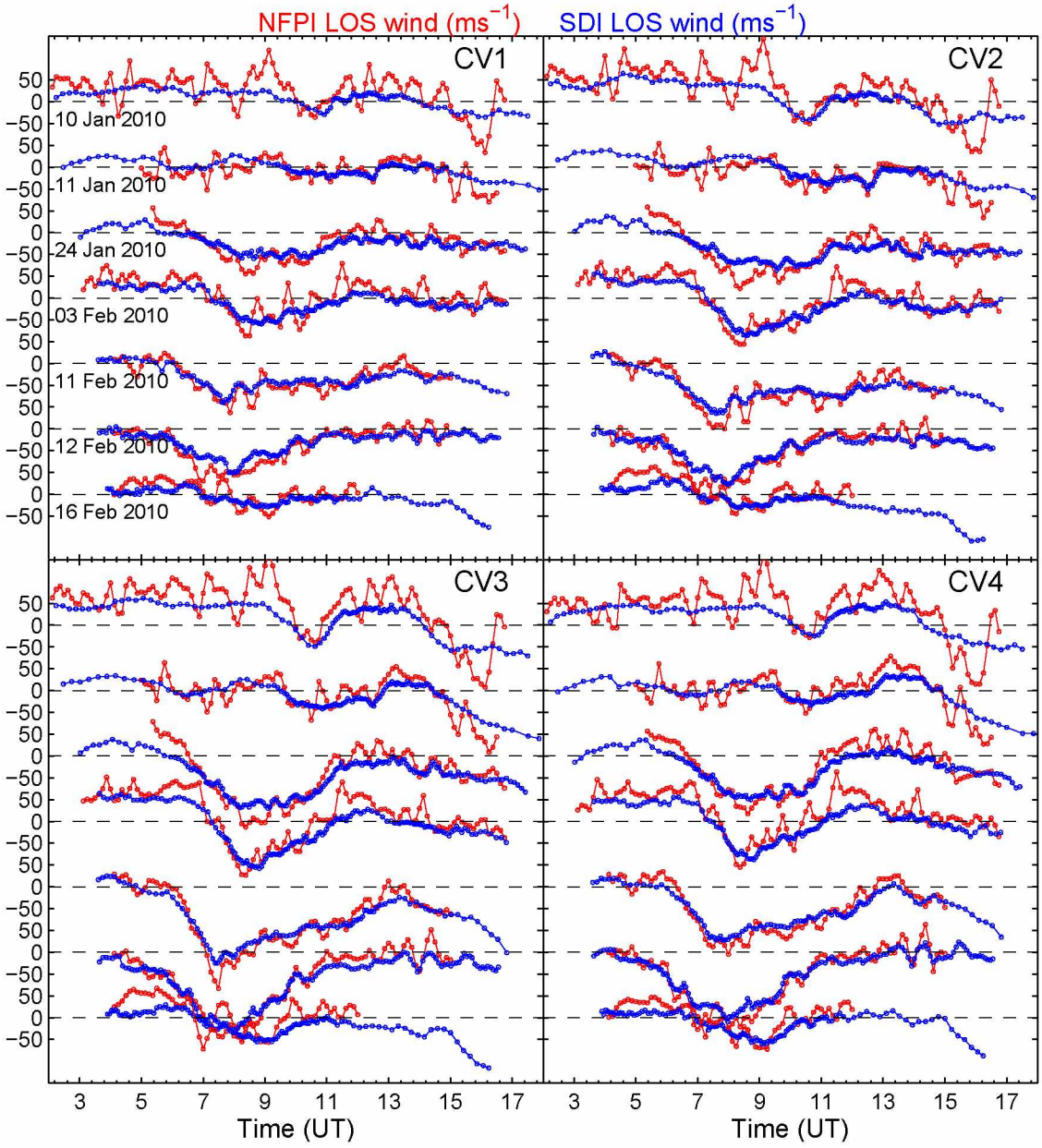

Figure 5.2: LOS wind speed ($m.sec^{-1}$) measured by SDI and NFPI observatories from CV1 (top left), CV2 (top right), CV3 (bottom left), and CV4 (bottom right) locations. Data were obtained from SDI and NFPI located at Poker Flat. The uncertainties in the SDI and NFPI LOS winds were ~5-10 $m.sec^{-1}$

served at the four CV locations. The resulting LOS wind comparisons for seven nights are presented in Figure 5.2. A zoomed-in view of the 11 February LOS wind data is presented in Figure 5.3. These figure were produced at the original temporal resolution of the data. LOS wind signs are chosen to be positive when wind is blowing away from

observatory, which ensures that a positive LOS wind observed in the zenith is consistent with the usual convention that upward vertical winds are positive.

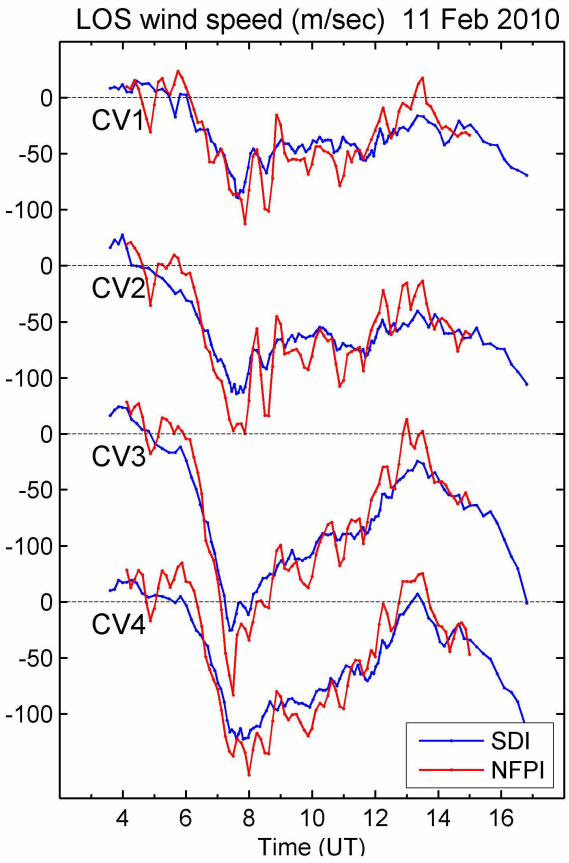

Figure 5.3: A more detailed view of the LOS wind speed measured by SDI (blue) and NFPI (red) observatories at Poker Flat in CV regions on the night 11 February 2010.

Figure 5.4 shows the temperature comparison of Poker Flat SDI and Poker Flat NFPI data. Four panels of this figures correspond to the measurements from four CV locations. A zoomed-in view of the 11 February LOS wind data is presented in Figure 5.5. Four subsets in this figure correspond to the measurements from four CV locations. Both temperatures comparison figures were produced at the original temporal resolution of the temperature data from two instruments. The standard deviations in their data were indicated by the error bars.

Figure 5.6 to Figure 5.12 show the geographically resolved horizontal vector wind fields derived from monostatic wind fits to the observations from SDI at Poker Flat. The SDI and NFPI instruments operate independently, so data sets generated by them are

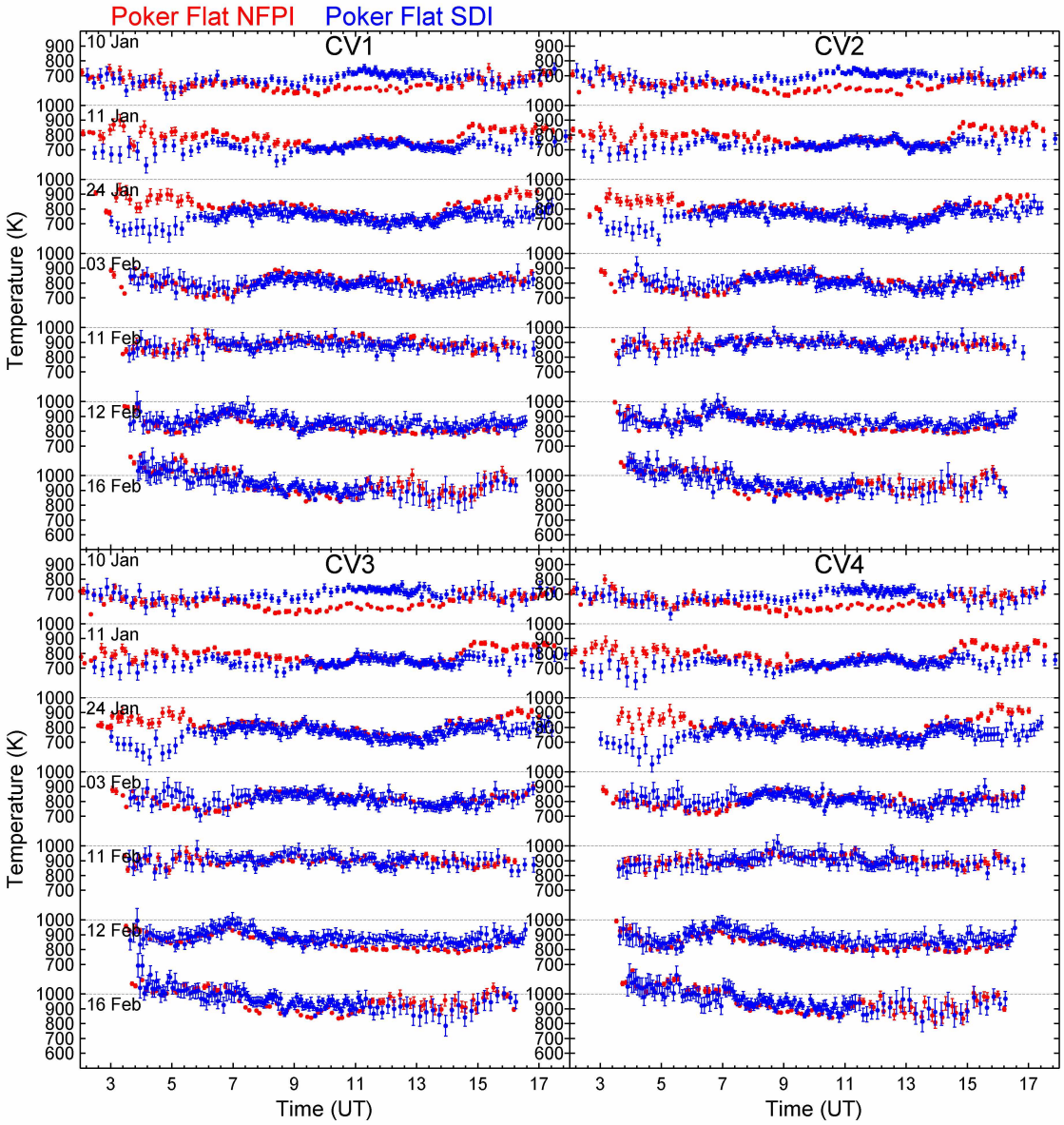

Figure 5.4: Temperature measured by SDI and NFPI observatories from CV1 (top left), CV2 (top right), CV3 (bottom left), and CV4 (bottom right) locations. Data were obtained from SDI and NFPI located at Poker Flat. The error bars represent standard deviation in the data.

entirely independent. They also have different sampling rates rates. For the data sets presented in here, the average sequence cycle time for NFPI was ∼7.5 min. This means that the observations at each NFPI CV location were 7.5 min apart, which is greater than the average exposure time of SDI (∼4.2 min) on any of the selected days for this cross-

comparison. To produce Figures 5.6 - 5.12, SDI data were downsampled in time to match with the NFPI cadence. These figures illustrate one substantial benefit of having the full SDI FOV: with a set of single-point comparisons it may not be apparent whether a small spatial displacement would correct any mismatches in the winds measured by two instruments. However, no such mismatches were observed that could be corrected by any spatial displacement. Another benefit of showing full SDI FOV is to provide a sense to the readers of the spatial variation in the wind vector fields with time over a wide geographic area and with high spatial resolution.

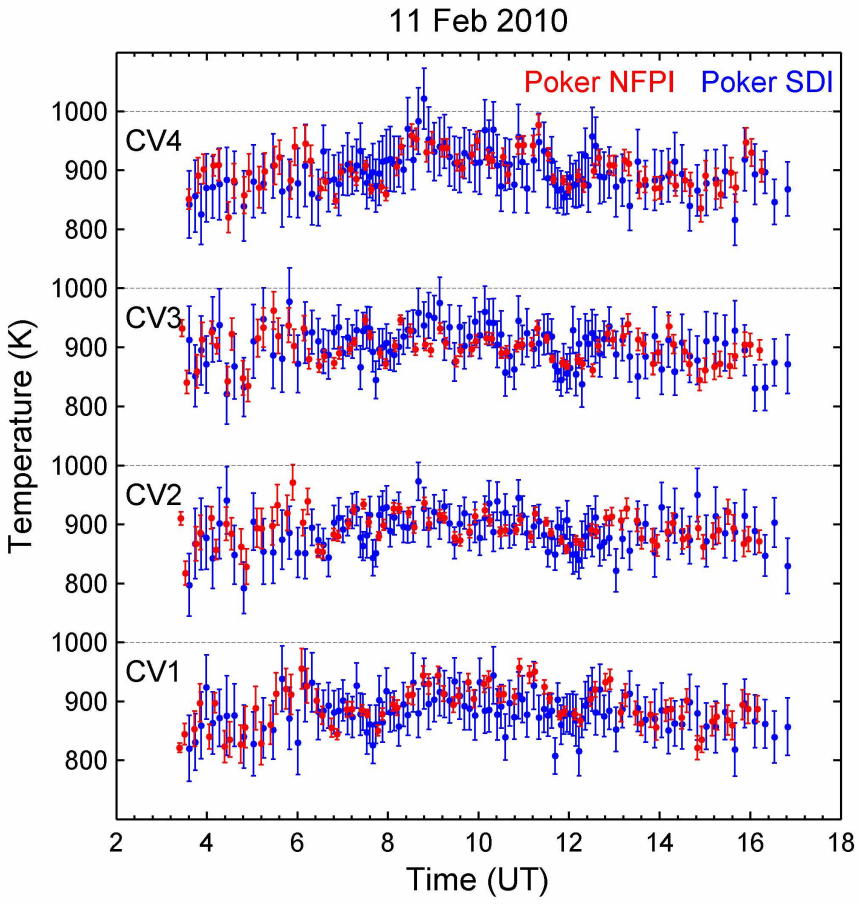

Figure 5.5: Temperature measured at CV locations from Poker Flat SDI (blue) and NFPI (red). The error bars represent standard deviation in the data.

Horizontal bistatic wind fields derived from the NFPIs at Poker Flat and Fort Yukon both with and without vertical wind corrections are shown at their respective CV locations, superposed on SDI monostatic wind fields (Figures 5.6 - 5.12). Figure 5.6 and 5.9

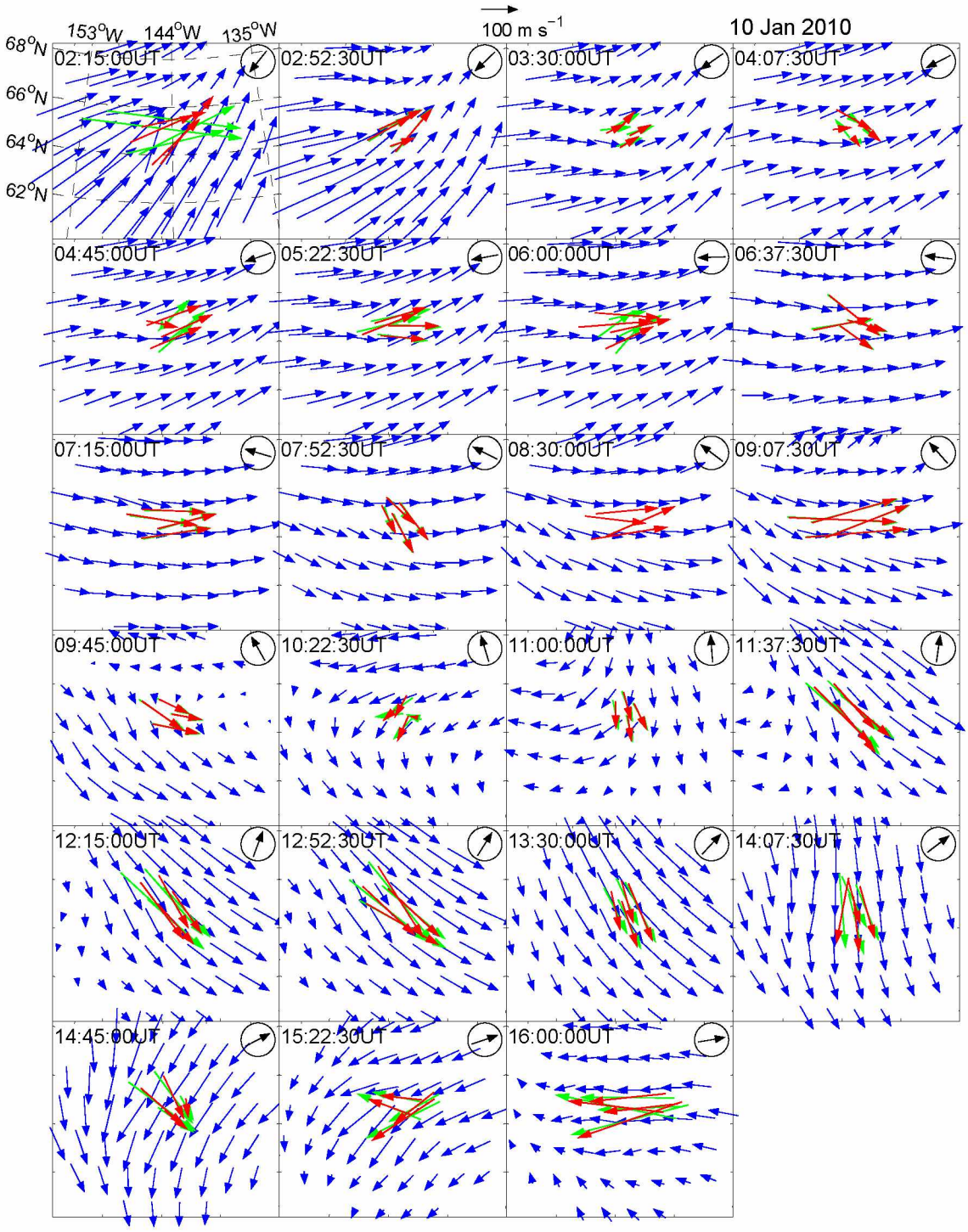

Figure 5.6: Temporal and spatial evolution of horizontal neutral wind field on 10 January 2010 estimated by SDI (monostatic (blue)) and NFPI bistatic (without vertical wind correction (red) and with vertical wind correction (green)). Universal times are indicated. An arrow in a circle represents the azimuthal direction towards the sun from Poker Flat. Arrows point in the direction of the flow and are centered over their respective observing locations.

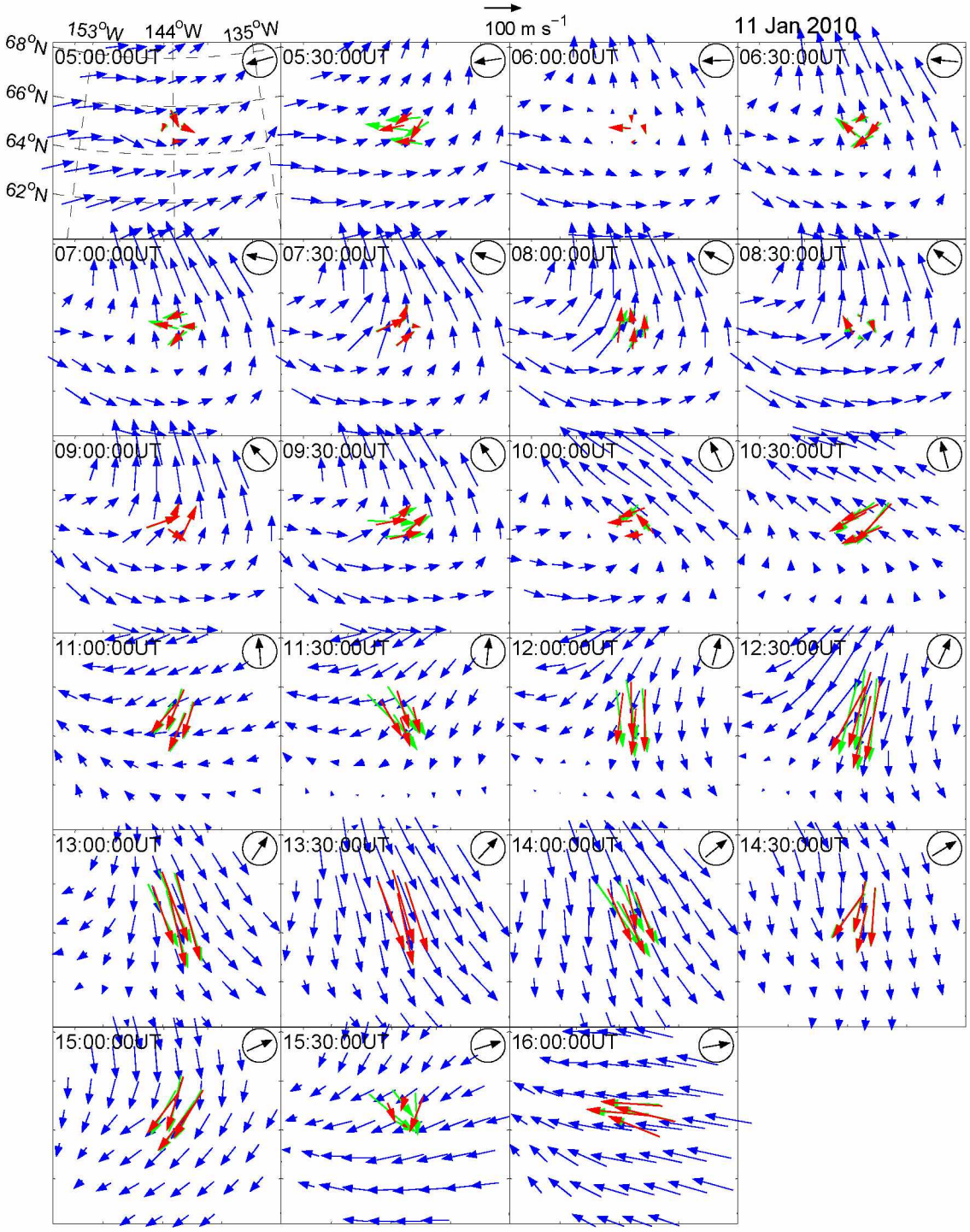

Figure 5.7: Same as for Figure 5.6, but in this case showing data for 11 January 2010.

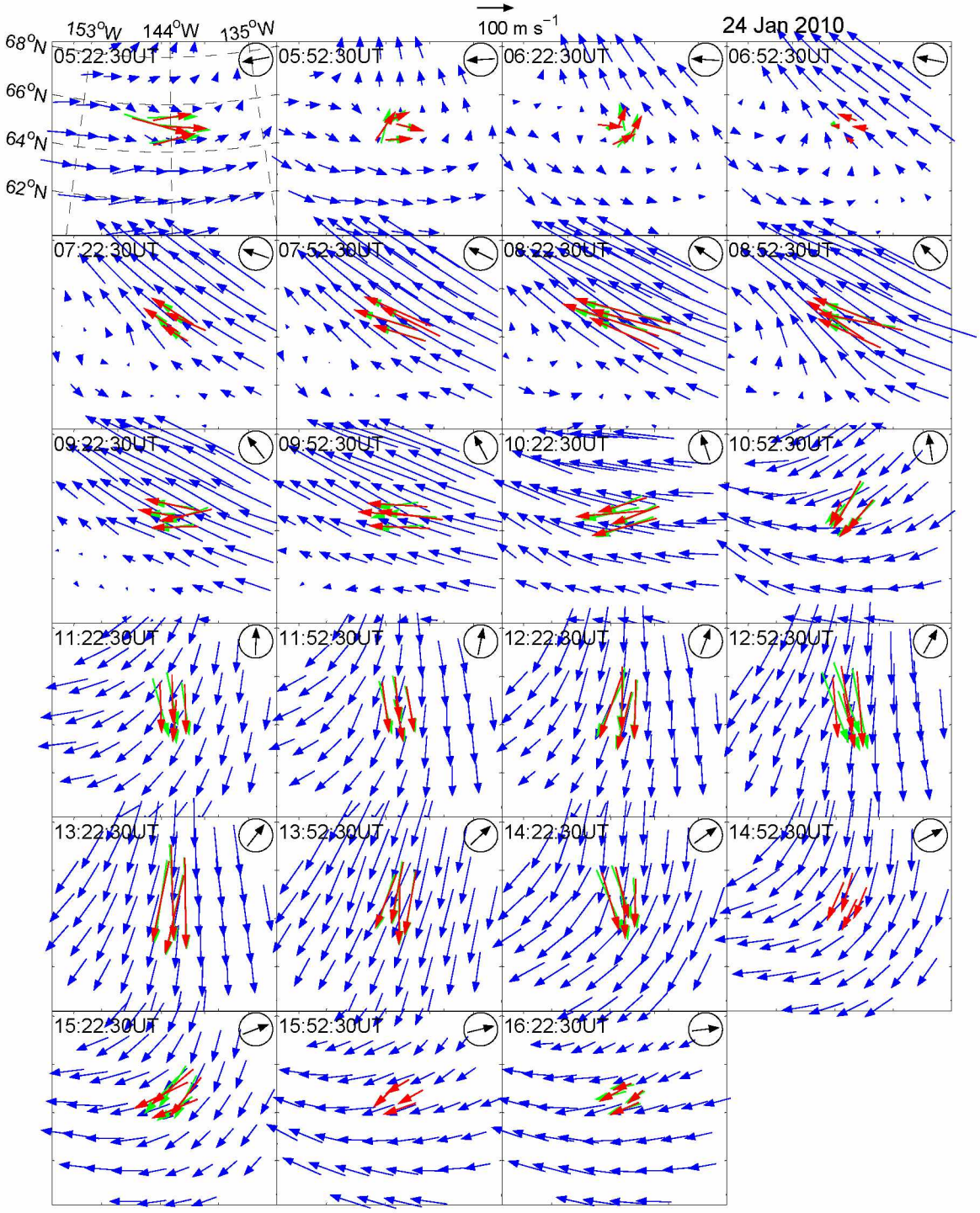

Figure 5.8: Same as for Figure 5.6, but in this case showing data for 24 January 2010

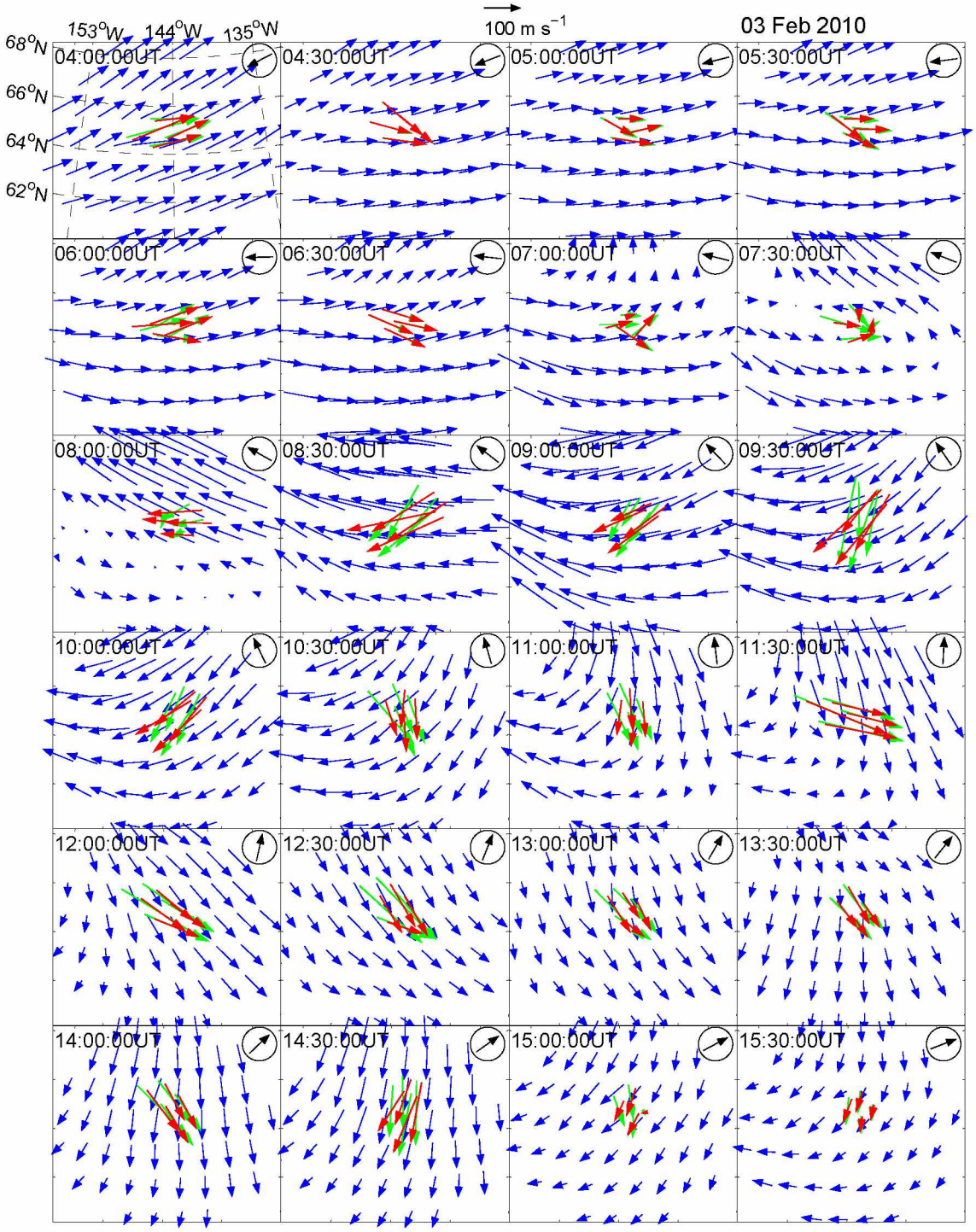

Figure 5.9: Same as for Figure 5.6, but in this case showing data for 03 February 2010.

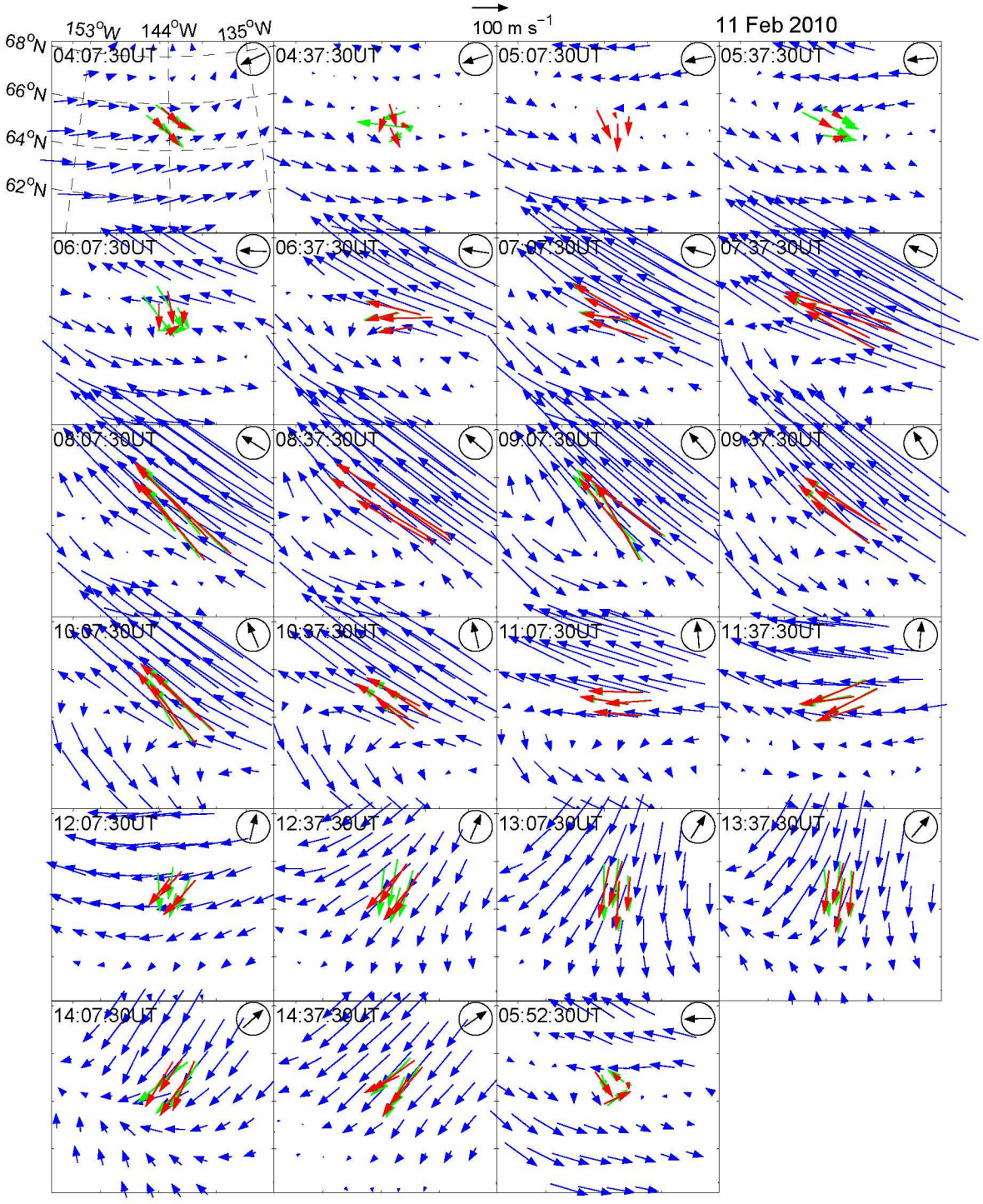

Figure 5.10: Same as for Figure 5.6, but in this case showing data for 11 February 2010.

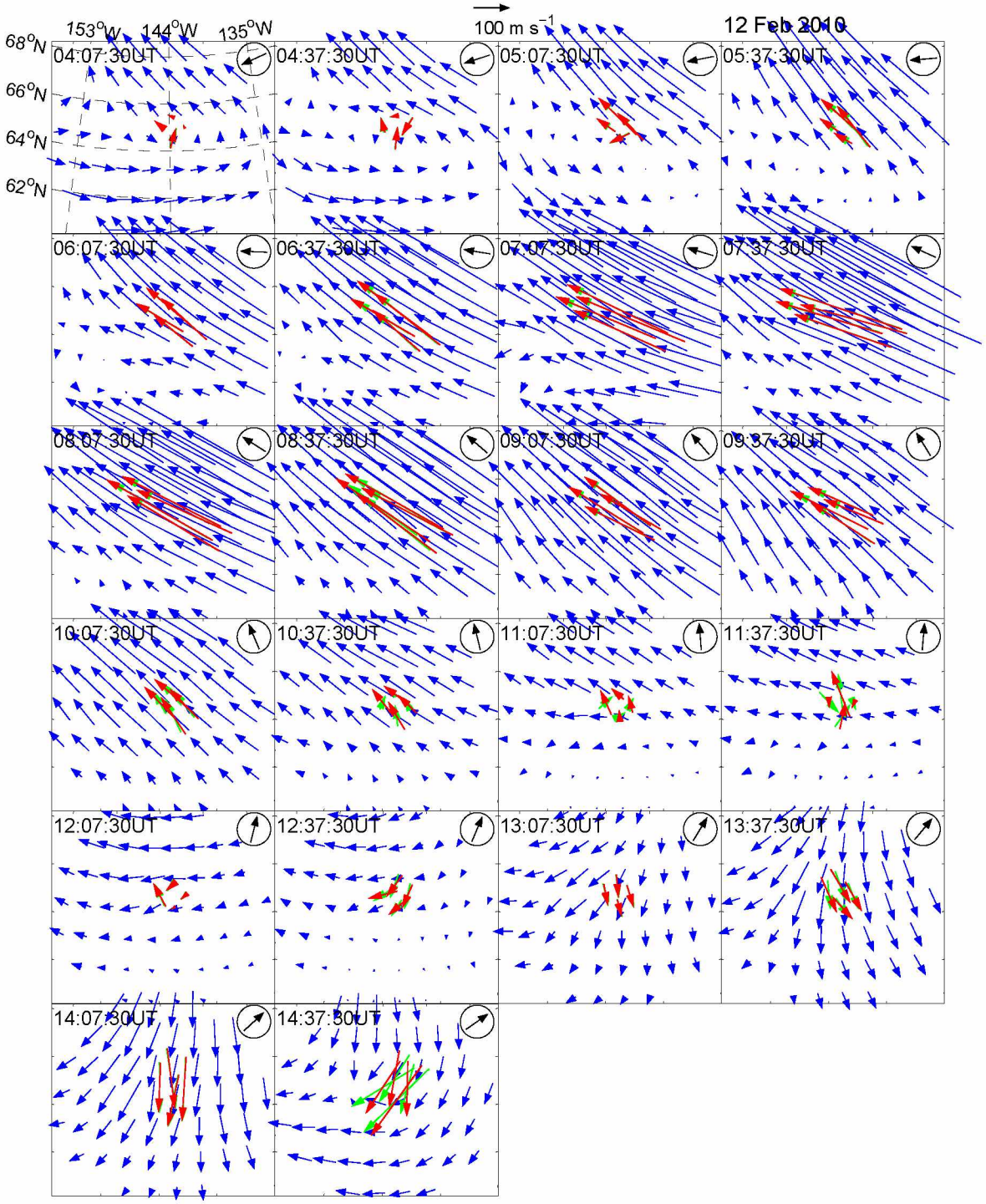

Figure 5.11: Same as for Figure 5.6, but in this case showing data for 12 February 2010.

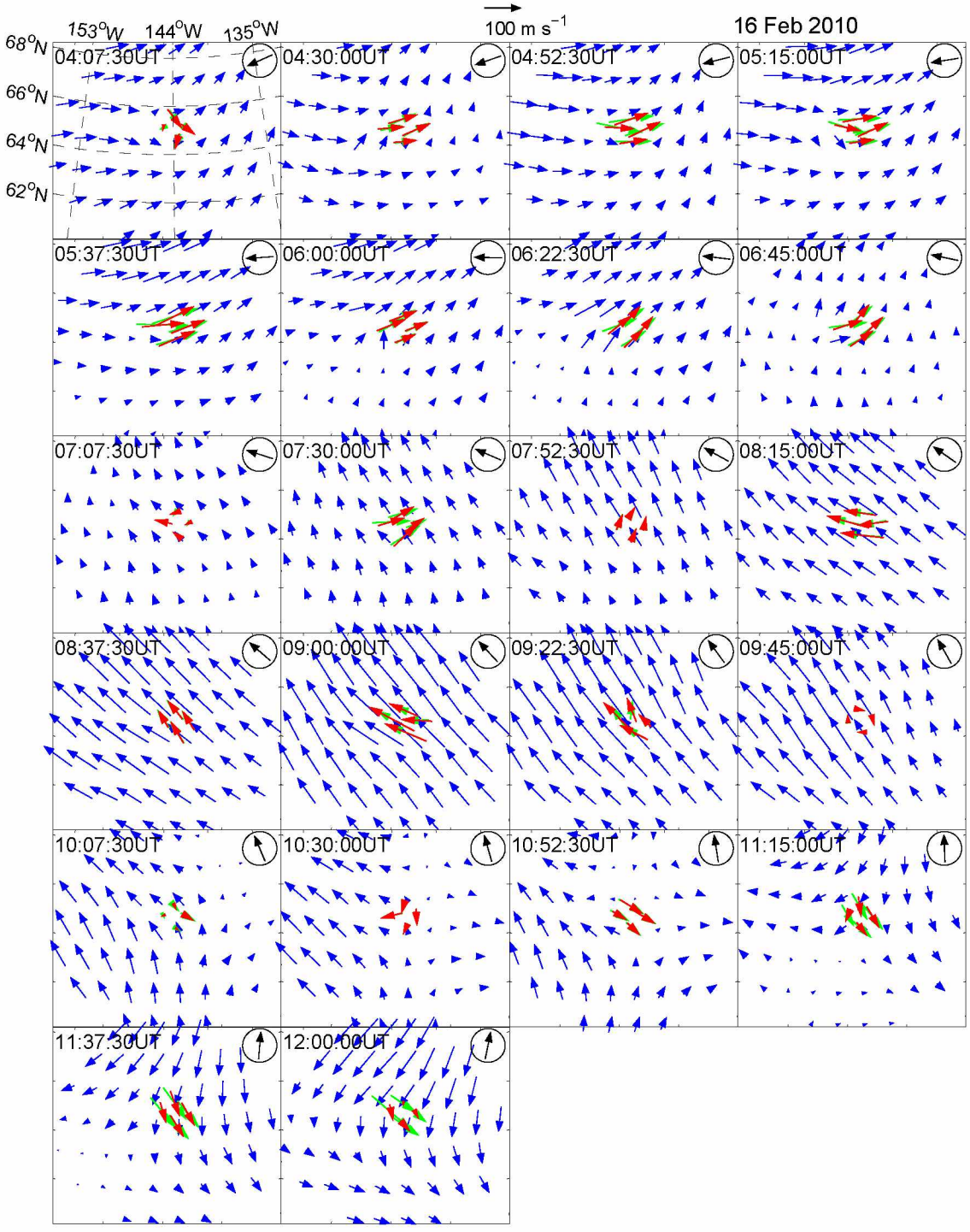

Figure 5.12: Same as for Figure 5.6, but in this case showing data for 16 February 2010.

were produced at temporal resolution of 37.5 min; Figure 5.7, 5.8, 5.10, and 5.11 at 30 min; and Figure 5.12 at 22.5 min. These cadences were chosen simply to allow exposures taken over a single night to fit on a single page. Nevertheless the plots cadence is in all cases adequate to resolve the complete space and time evolution of the wind fields (that is, no higher level of detail can be seen in the full resolution data). Azimuthal direction to the Sun is represented by a black arrow in the circle placed on the top right corner of each the exposure frame.

To better check the agreement between the SDI monostatic and NFPI bistatic wind fits, Figure 5.13 shows the inferred SDI and NFPI azimuthal wind directions. Positive (negative) angles from 0 to 180 (0 to -180) degree represent wind directions clockwise (anticlockwise) from geographic north to geographic south.

The zonal wind components computed from NFPI bistatic fits mimic closely the original LOS winds directly observed by Poker Flat NFPI. This is because all four CV look directions lie eastward of Poker Flat. Similarly, the meridional wind computed from NFPI bistatic fit anti-correlate with LOS wind measured by the NFPI at Fort Yukon (not shown). This is because all four CV locations lie southward of Fort Yukon. The overall wind behavior was similar on each of the available nights of observations. So, instead of repeating the results for every night, cross-comparison results derived on 11 February 2010 were selected out of the seven nights for a more detailed discussion. Spatial and temporal features observed on 11 February 2010 were representative of the features of the thermospheric winds as obtained on other nights. Differences between results obtained on other nights compared to 11 February are discussed where relevant.

The LOS winds from 11 February are presented in the fifth panel of each subset of Figures 5.2. A zoomed-in view of the 11 February data is presented in Figure 5.3. At the beginning of the observations, both instruments observed LOS wind close to zero. After 0600 UT, LOS wind turned towards the observatory, and stayed towards the observatory until the end of observations. Compared to LOS wind measured by the SDI, significant variability was present in NFPI LOS wind. Short period low amplitude oscillations were also present in the SDI LOS wind. On the other hand, NFPI recorded short period oscillations with larger amplitude compared to SDI LOS wind. The overall âĂIJbackgroundâĂİ

diurnal behavior of LOS wind observed by two instruments was in good agreement.

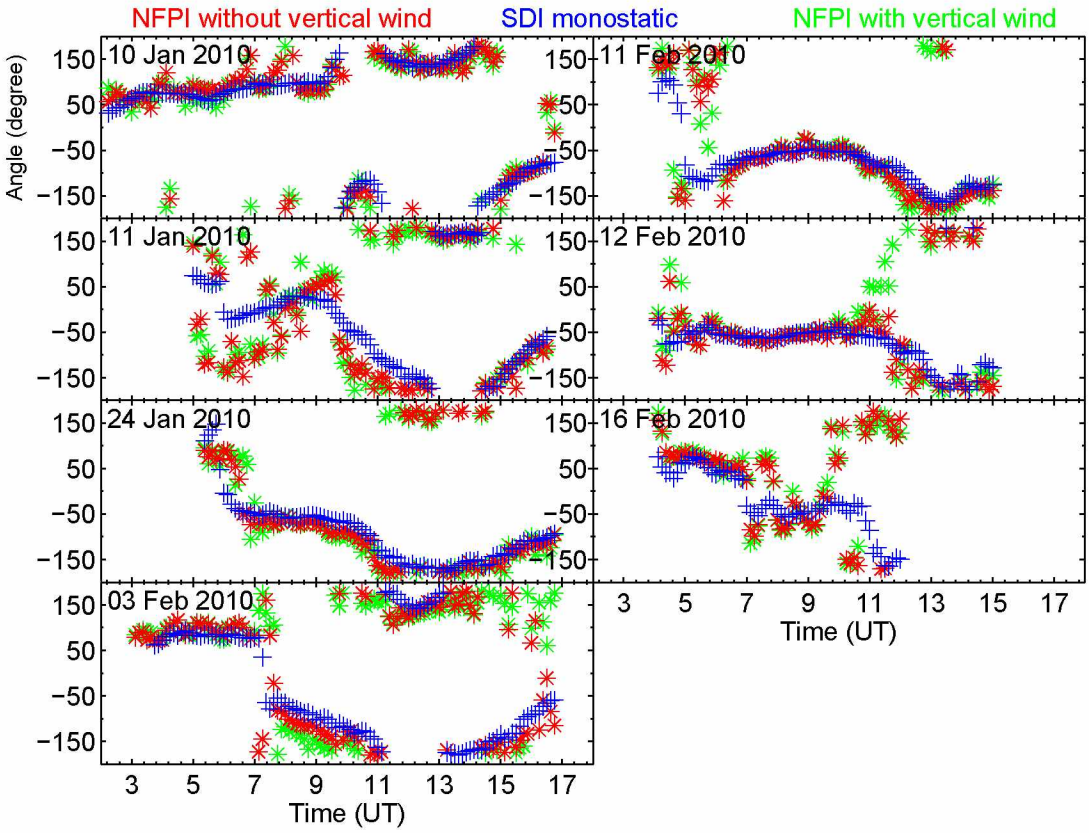

Figure 5.13: Comparison between geographic azimuthal wind directions inferred by SDI monostatic and NFPI bistatic fits. Blue, red, and green represent the wind directions computed by SDI monostatic fit, NFPI bistatic fit without vertical wind correction, and NFPI bistatic fit with vertical wind correction respectively. Positive angle from 0 to 180 degree represents directions clockwise from geographic north to geographic south. Negative angles from 0 to -180 degree represents directions anticlockwise from geographic north to geographic south.

To check whether the measured LOS winds by two instruments were related, correlation coefficients were calculated as shown in Table 5.2. R_i represents the correlation between the LOS wind observed at CV_i by NFPI and SDI. The significance of correlation (probability of getting observed correlation by random chance, when the true correlation is zero (p-value)) was also checked. P-values were so small that the likelihood that time series were uncorrelated is utterly insignificant. High correlation and low p-values on

available nights establish that both instruments were indeed seeing the same events occurring in the region of their overlapping FOV. The root mean square difference (RMSD) was also calculated between the SDI and NFPI measurements. This comparison is shown in Table 5.3. The RMSD provides a meaningful measure of the difference between the LOS winds measured by two instruments. The larger the RMSD, the larger the difference between measurements.

Table 5.2: Correlation (R_i) between the SDI and NFPI LOS winds at CV locations

Day	R_1	R_2	R_3	R_4
10 Jan 2010	0.6703	0.7701	0.8142	0.7543
11 Jan 2010	0.5673	0.7323	0.8188	0.8356
24 Jan 2010	0.8542	0.8815	0.9608	0.9522
03 Feb 2010	0.8045	0.8986	0.9340	0.9028
11 Feb 2010	0.8540	0.9144	0.9723	0.9657
12 Feb 2010	0.9304	0.9366	0.9740	0.9746
16 Feb 2010	0.7863	0.8158	0.8664	0.8445

Table 5.3: Root mean square difference between the SDI and NFPI LOS winds at CV locations

Day	$CV1$ (m/sec)	$CV2$ (m/sec)	$CV3$ (m/sec)	$CV4$ (m/sec)
10 Jan 2010	35.29	36.83	44.15	43.29
11 Jan 2010	22.49	23.47	25.60	25.85
24 Jan 2010	20.21	24.50	26.08	23.75
03 Feb 2010	25.79	23.30	27.26	29.59
11 Feb 2010	16.90	19.95	19.88	18.34
12 Feb 2010	18.39	19.74	22.09	20.12
16 Feb 2010	18.71	23.92	30.90	23.83

Similar diurnal trends in LOS winds were observed on all other available nights apart from some minor differences on 10 January. Also, similar characteristics of high frequency

fluctuations in SDI (with low amplitude) and NFPI (with higher amplitude) as observed on 11 February were observed on all other nights except 10 January. The NFPI LOS wind oscillations on 10 January were stronger than on any other available night. This was probably associated with the strong monochromatic wave activity as discussed in *Nicolls et al.* [2012]. Curiously, SDI LOS winds were smoother on 10 January than on any other night studied here.

The temperature measurements from Poker Flat SDI and NFPI at CV locations on 11 February as depicted in Figure 5.5 shows that uncertainties (as indicated by the error bars) were stronger in the SDI temperatures than NFPI. Despite the difference in uncertainties, both instruments tracked the diurnal variation in temperatures very closely. A study by *Conde and Nicolls* [2010] compared Poker Flat SDI neutral temperatures with ion temperatures from the PFISR incoherent scatter radar, also located at Poker Flat. They found that F-region neutral and ion temperatures showed similar overall seasonal and short term day-to-day fluctuations.

The wind field maps for our focused study day, 11 February, can be seen in Figure 5.10. At the beginning of observations, wind flow was mostly antisunward. Winds poleward of Poker Flat manifested a small poleward component and, with the passage of time, they started turning magnetic westward and developed a wind reversal boundary along magnetic east-west direction. Wind shear was present along this wind reversal boundary. With time, this wind reversal boundary started traveling magnetic equatorward slowly, and by 0600 UT it was at the Poker Flat zenith. Wind speeds in the regions magnetic equatorward and magnetic poleward of the Poker Flat were of the same order, but were oppositely directed. Wind flow poleward (magnetic) of the Poker Flat was magnetic westward whereas equatorward of Poker Flat the wind flow was still magnetic eastward. Magnetic eastward flow was presumably associated with the solar diurnal tide. An auroral arc appeared poleward of Poker Flat around 0538 UT and started moving slowly equatorward. Coupling between neutral and ion flow is usually stronger in the presence of auroral particle precipitation [*Deng and Ridley*, 2006] due to the enhancement in ion density. After 0615 UT, strong magnetic westward wind flows were observed poleward of Poker Flat, which were presumably associated with the strong coupling between neutrals and ions

(duskside of the ionospheric convection cell). Wind flow equatorward of the observatory was presumably driven by solar tide. Strong gradients in the ion and neutral momentum deposition produced strong latitudinal shear in wind flow. This latitudinal shear contributed to the vorticity in the wind field. Highly sheared flow passed overhead at Poker Flat. After 1100 UT, the entire wind flow started turning antisunward and, by 1237 UT, it was antisunward with a small tendency to bifurcate. This bifurcated antisunward flow was most likely associated with the antisunward jet of the Dungey cycle. The last exposure (05:53:30 UT) shown in Figure 5.10 was added to show the presence of small vortex in the wind field at wind reversal boundary. Both instruments typically observed similar changes in the wind flows in their overlapping FOV, including this interesting vortex. The vortex may easily have been dismissed as an instrumental or analysis artifact, had it not been seen simultaneously by two independent instruments.

Horizontal wind fields with similar characteristics as discussed above have been reported in the past by *Conde and Smith* [1998a]; *Conde et al.* [2001]; *Anderson et al.* [2012]. The SDI observes wind flow on a large-scale and over a wide geographic region as compared to the NFPI. Many wind flow structures were present in the SDI derived wind field that were not possible for the NFPI to resolve, because of its narrow FOV and limited spatial sampling. Overall, the horizontal flow configuration captured by both instruments in their overlapping FOV was in good agreement. Most of the discrepancies between the SDI and NFPI observations occurred when either the wind speed was small or there were strong shears in their overlapping FOVs. Visual inspection of Figure 5.10 shows that SDI winds were changing gradually from exposure to exposure. On the other hand, horizontal thermospheric winds inferred by the NFPI displayed more variability in time compared to SDI (and, to the extent resolved, also in space). Although SDI winds were typically less variable from exposure to exposure, they sometimes display the same temporal and spatial fluctuations as inferred by NFPI. Time series of computed wind direction (Figure 5.13, top right panel) show a good agreement between the wind directions estimated by two instruments throughout the entire night after 0630 UT.

The diurnal behavior of the horizontal vector wind components (zonal and meridional) derived from SDI wind fits (monostatic and bistatic) and NFPI wind fits (bistatic

both with and without vertical wind correction) is presented in Figure 5.14. NFPI zonal (meridional) wind time series for comparison with SDI were produced by averaging the zonal (meridional) wind from all the four CV locations at each exposure. SDI zonal (meridional) wind time series as shown in Figure 5.14 were produced by averaging the zonal (meridional) wind at each exposure from zones lying nearby the CV locations. SDI

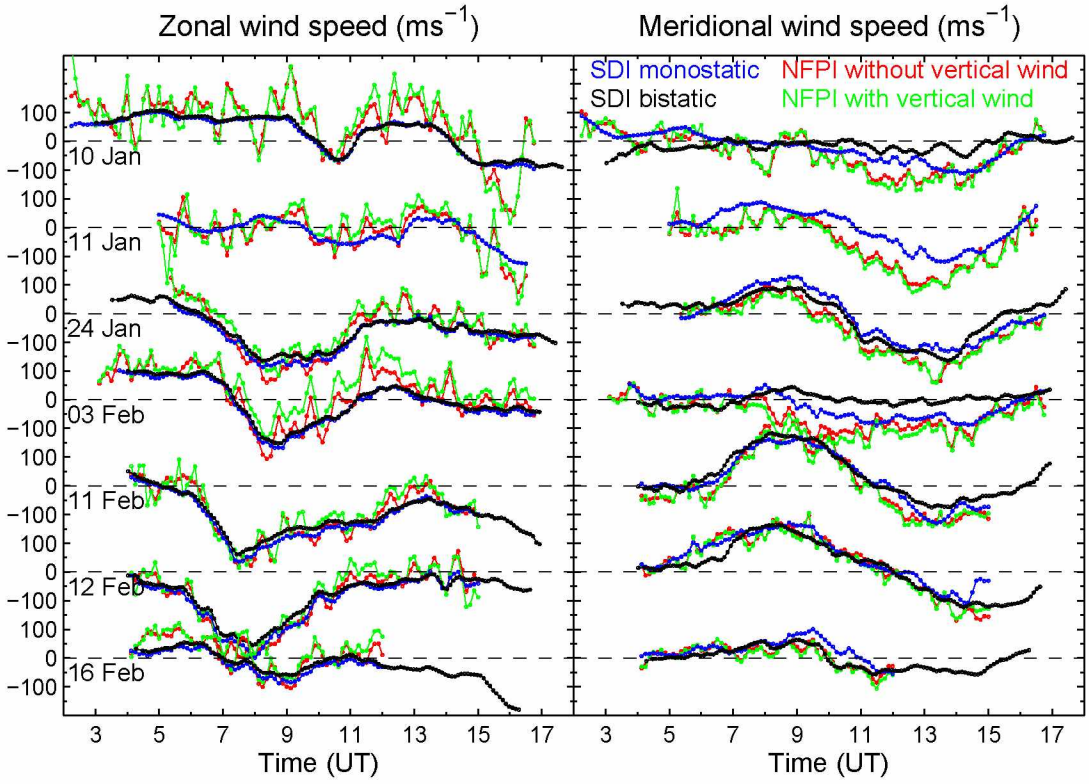

Figure 5.14: Zonal (left column) and meridional wind (right column) inferred from SDI and NFPI instruments. Blue, black, red, and green represent respectively the zonal and meridional winds estimated by SDI monostatic fits, SDI bistatic fits, NFPI bistatic fits without vertical wind correction, and NFPI bistatic fits with vertical wind correction. SDI data from Gakona were unavailable on January 11, 2010.

zonal and meridional winds were smoother than NFPI zonal and meridional winds. High frequency large amplitude oscillations were present in the NFPI time series of zonal and meridional wind. On the other hand, the SDI did observe at least small amplitude oscillatory behavior in zonal and meridional winds. Regardless of this variability, the diurnal trend in the zonal and meridional wind observed by both instruments was in good agree-

ment. Maxima of the zonal wind speeds occurred before magnetic midnight between 0600 UT and 1000 UT. SDI data from Gakona were not available on 11 January 2010; therefore SDI bistatic wind fits were not produced for that night. The SDI meridional bistatic wind estimates were flatter on 03 February 2010 compared to other selected nights, which may suggest clouds at Gakona. However, this is considered unlikely, since zonal winds on 03 February as measured by both instruments were not flat. On 10 January 2010, NFPI observed very strong fluctuations in zonal wind. Meridional wind fluctuations were similar to the other night's fluctuations.

Geomagnetic conditions were roughly similar on all our study nights. As a result, similar wind features were observed on most of the nights, such as eastward flow in evening; strong magnetic westward flow before magnetic midnight; antisunward flow with bifurcation equatorward of the Poker Flat. Observations of the zonal and meridional wind components typically showed a similar diurnal behavior; 11 February 2010 has been presented as a representative example. The NFPI often observed short period large amplitude oscillations compared to the SDI data, although both instruments saw similar long period structures in wind components.

In most cases, the NFPI bistatic winds with and without vertical wind correction were in agreement. The small differences that did occur between the NFPI bistatic wind with and without vertical wind correction are presumably indicative of the contribution from vertical winds. Nevertheless, results presented in Figure 5.6 to 5.12 show that the monostatic SDI winds agree more with the bistatic NFPI winds without vertical wind correction than with the bistatic NFPI winds with vertical wind correction. This may be because the SDI monostatic wind fit was itself produced assuming negligible vertical wind (one of the assumption used in SDI monostatic wind fit). This choice is based on many years of experience with the SDI bistatic and monostatic wind fits, which are almost always more stable and in better agreement without including any attempt at vertical wind correction. The implication is that extrapolating vertical winds over a wide geographic area is problematic, so it is not surprising that the NFPI fits would also be slightly better behaved without any attempted correction.

High frequency oscillations on top of diurnal structure of LOS wind (as well as wind

vector components) were observed by both instruments and likely imply the occurrence of small-scale dynamical structures. There were many cases when both independent instruments observed similar oscillation simultaneously. For example, on 11 February 2010 (Figure 5.3), oscillations in CV1 and CV2 region between 0700 UT and 0900 UT, 1000 UT and 1100 UT, 1130 UT and 1230 UT were observed by both instruments, and they were in agreement except for their amplitude. Similarly, oscillations observed by both instrument in CV3 between 0700 UT and 0815 UT, 1200 UT and 1230 UT were in agreement. Also, in CV4 region, there were many times for example between 1000 UT and 1500 UT when oscillations in LOS wind observed by two instruments were in good agreement. Simultaneous observations of similar oscillations by two independent instruments suggest that these high frequency oscillations have thermospheric origin rather than measurement noise. We cannot determine what caused these short period fluctuations. However, since all the instruments reported here were located in the auroral zone, aurorally forced gravity waves are a likely candidate [e.g., *Ford et al.*, 2006; *Nicolls et al.*, 2012].

There are several possible reasons for high-frequency discrepancies between the SDI and NFPI LOS wind. One possible cause is the larger sampling volumes observed by the SDI zones compared to the NFPI. The radial and azimuthal coverage at 240 *km* altitude of the biggest SDI zone considered here were 56 *km* and 87 *km* respectively. The LOS wind recovered from each SDI zone is the spatial intensity-weighted average of the LOS wind over the thermospheric volume in which the look angles intersect the emission layer. Thus, if there were small-scale structures in the thermosphere with scale size much smaller than zone sampling volume, the LOS wind averaged over a large volume would smooth out any variation present in the LOS wind due to the small-scale structures. On the other hand, NFPI is a narrow FOV instrument with spatial extent of each CV around 4 *km* to 5 *km* horizontally - i.e., roughly an order of magnitude less that the SDI in each direction. This means there is far less spatial averaging of the LOS wind inferred from the NFPI instruments [*Nicolls et al.*, 2012]. In addition, SDI uses a small amount of smoothing (adjacent measurements contributed < 10%) both temporally and spatially, even for LOS wind data. This smoothing algorithm is required to identify and remove any conspicuous outliers in the peak position data that arise, for example, when a near full or full

moon appears in one of SDI's viewing zones. The presence of smoothing in the SDI measurements and data analysis compared to NFPI measurements strongly suggests that the different high-frequency behaviors between the two instruments is a result of small-scale structures in the upper thermosphere, with expected scale sizes smaller than the size of SDI zones used here.

All the observatories considered in the current research lie well within the auroral zone (fixed region). The actual location of the auroral oval at any given time itself depends on geomagnetic activity. The presence of the auroral precipitation can significantly complicate the neutral wind dynamics at these high latitudes. In the presence of soft auroral precipitation, the 630 *nm* airglow layer peaks around 240 *km* to 250 *km*. With very soft or no auroral precipitation the layer can peak higher than this, whereas very hard precipitation can move the layer peak down in altitude many tens of kilometers lower [*Sica et al.*, 1986]. However, although there are variations in emission altitude, many years of in-situ height-resolved wind measurements by rockets show that height variations in the thermospheric winds themselves are weak at altitudes above 200 *km*. Given this, it is considered highly unlikely that the short period fluctuations in observed LOS winds or fitted wind components could be caused by height variations in the emission layer. A study by *Nicolls et al.* [2012] used 9-10 Jan 2010 data from all the three NFPIs and Poker Flat SDI to study the fluctuations observed between the time period 1130 UT to 1300 UT. They also compared the NFPI data with the co-located PFISR radar and verified that those high frequency fluctuations in NFPI data are real and generated by upward propagating monochromatic gravity waves (~32 min period). These findings strongly support our interpretation that the fluctuations observed in our data and presented in the manuscript are not due to the variation in altitude of emission layer. Their origin lies in the thermosphere.

Inspection of Figures 5.6 to 5.12 shows that most discrepancies between the SDI and NFPI winds occurred when the LOS wind speed was small or the wind reversal boundary was closer or above CV locations. Neither of these behaviors was surprising. The best agreement occurred when wind speeds were high (high wind speed was mostly magnetic westward).

We note that although the monostatic SDI wind fit involved substantial assumptions, monostatic and bistatic SDI zonal and meridional winds were in close agreement with each other (as shown in Figure 5.14). This gives confidence that the simpler monostatic SDI observations will be satisfactory in most situations.

SDI bistatic fits used the LOS wind data from Poker Flat and Gakona, while NFPI bistatic wind fits used the LOS wind data from Fort Yukon and Poker Flat. Due to the variation in emission layer altitude, the observatories situated at different latitudes could potentially be monitoring different regions of the thermosphere which, combined with different observing volumes and look directions, could contribute to the small discrepancies that we saw between SDI and NFPI derived winds. Also, another important point is that NFPI CV locations won't be common anymore, if the emission height changes. Nevertheless, these scenarios probably do not occur frequently enough to substantially impact our overall conclusions here.

Figure 5.13 shows good agreement between the azimuthal wind directions computed by SDI and NFPI, but this agreement was not consistent. Figures 5.6 to 11 show that with the increasing wind speed, differences between wind directions derived from SDI and NFPI also decrease. To visualize this behavior of wind direction with wind speed, differences between the wind directions computed by both instruments were calculated and scatter-plotted against the wind speed computed from the respective instruments as shown in Figure 5.15. It shows that the consistency between wind directions computed by two instruments improves with increasing wind speed.

Note that SDI and NFPI are two different instruments working independently of each other. Their optics, FOVs, data collection methodology, and spectral analysis schemes are very different. Nevertheless, there is strong correlation between the geophysical data they produce. Diurnal behavior of the geophysical parameters (LOS winds, zonal and meridional winds, and temperatures) derived by both instruments matched closely regardless of the fact that strong variability was present in the NFPI measurements. For most applications, either technique would give acceptable winds at a given location. In addition, the SDIs can map spatial variations over a wide field around that location.

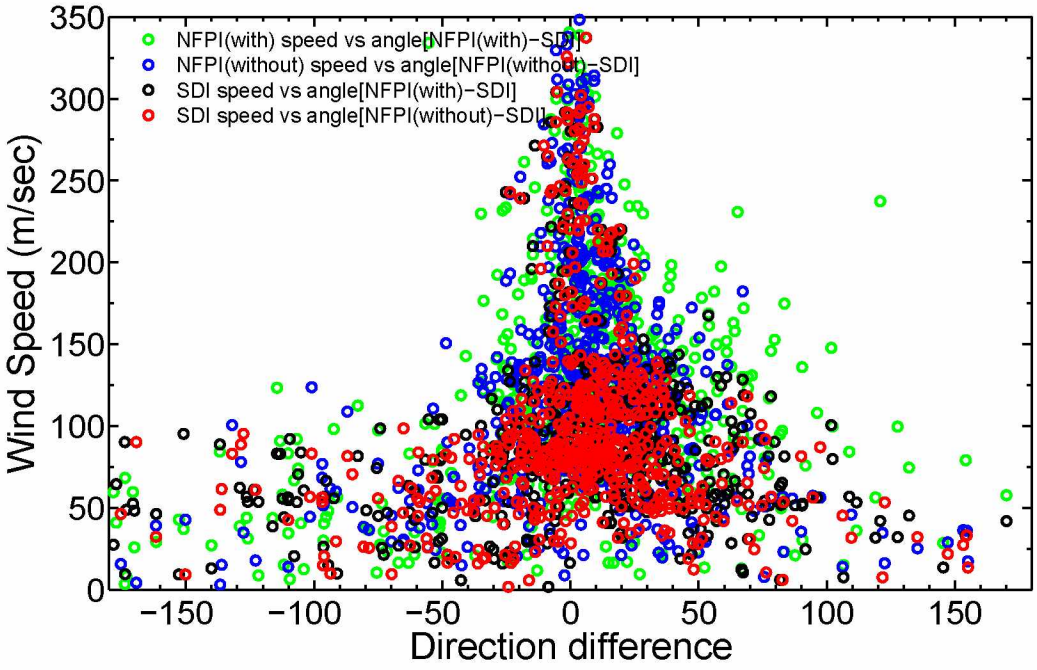

Figure 5.15: Relation between wind speed and difference in wind directions estimated by SDI and NFPI. Legends are given in top right corner. Wind speed and wind direction computed from SDI monostatic wind fits were used. "NFPI (with/without)" represents wind speeds inferred from NFPI bistatic wind with/without vertical wind correction in wind fit analysis.

5.5 Conclusions

We have presented the first ever cross-comparison of horizontal neutral wind fields at F-region heights mapped by two different types of ground based optical Doppler spectrometers (SDI and NFPI) working independently of each other at auroral latitudes. One type (SDI) is a wide FOV Fabry-Perot spectrometer with a scanning etalon. The second (NFPI) is a narrow FOV Fabry-Perot spectrometer with fixed etalon gap. Here, the 630 *nm* emission that originates from the 630 *nm* emission layer within the upper thermosphere was used by both instruments to monitor thermospheric wind fields at ~240 *km* altitude. Although, both instruments are observing the Doppler shifts and have etalons (one with fixed gap and other with scanning gap), they are very different in technical implementation, modes of operation, spectral derivation, and data analysis.

NFPI observation locations lie within the FOV of the SDIs located at Poker Flat and

Gakona. To exhibit the most direct comparison between them, raw LOS winds from SDI and NFPI at Poker Flat were compared. Our results showed that the slowly-varying "background" behavior of the LOS winds inferred by these two techniques exhibited very good agreement. Strong correlation over entire data set was observed between SDI and NFPI LOS winds. Also, despite the differences in uncertainties, the time variations in temperatures measured by NFPI and SDI located at Poker Flat were in a good agreement.

Both instruments observed additional short period fluctuations in LOS winds. There were many instances when both instruments observed similar short period fluctuation at the same time. This suggests that these fluctuations have thermospheric origin. However, the amplitude of the NFPI fluctuations was substantially higher than those observed by the SDI. These short period fluctuations are likely related to the existence of thermospheric gravity waves caused by auroral activity, or gravity waves propagating from below.

Zonal and meridional winds were inferred from the LOS winds, after somewhat indirect wind fitting. It was found that horizontal neutral wind vector fields estimated by both methods were still in good agreement, and oscillations similar to those present in LOS wind were also present in estimated wind components. The neutral wind behavior observed here was consistent both between the SDI and NFPI, and also with numerous previous studies

Monostatic SDI wind fits are based on substantial assumptions compared to the bistatic wind fits, which involved only an assumption regarding the vertical wind. Nevertheless, both monostatic and bistatic wind fits showed very good agreement on all nights available for comparison. Although the amplitude of fluctuations in NFPI estimated winds was considerably stronger than those from the SDI, oscillations were present in both data sets at the same times and spatial locations. Improvement in consistency between the winds estimated by two instruments was observed with increasing wind speed.

The temporal responses of SDI LOS winds and horizontal wind components were smoother than corresponding data from the NFPI. This was most likely related to the large geographic sampling volume of even the smallest SDI zone compared to typical NFPI sampling volumes. The SDI averages its observations over these larger volumes,

rendering the instrument insensitive to small-scale spatial structures. Smoother SDI time series compared to NFPI suggests that small-sized and previously unobserved wind features occur in the upper thermosphere, with typical length scales smaller than the lengths spanned by the SDI zones. Notwithstanding small-scale discrepancies, the overall large-scale agreement between the two instrument types would be considered excellent for most routine applications. Ultimately, to completely resolve and characterize small-scale short-lived thermospheric wind structures will require either a network of modified SDIs (with smaller FOVs), or else a very dense network of NFPIs.

5.6 References

Anderson, C., M. Conde, P. Dyson, T. Davies, and M. J. Kosch (2009), Thermospheric winds and temperatures above Mawson, Antarctica, observed with an all-sky imaging, Fabry-Perot spectrometer, *Ann. Geophys.*, *27*(5), 2225–2235, doi: 10.5194/angeo-27-2225-2009.

Anderson, C., T. Davies, M. Conde, P. Dyson, and M. J. Kosch (2011), Spatial sampling of the thermospheric vertical wind field at auroral latitudes, *J. Geophys. Res. Sp. Phys.*, *116*(A6), A06,320, doi: 10.1029/2011ja016485.

Anderson, C., M. Conde, and M. G. McHarg (2012), Neutral thermospheric dynamics observed with two scanning Doppler imagers: 1. Monostatic and bistatic winds, *J. Geophys. Res. Sp. Phys.*, *117*(A3), A03,304, doi: 10.1029/2011ja017041.

Aruliah, A. L., and D. Rees (1995), The trouble with thermospheric vertical winds: Geomagnetic, seasonal and solar cycle dependence at high latitudes, *J. Atmos. Terr. Phys.*, *57*(6), 597–609, doi: 10.1016/0021-9169(94)00100-3.

Aruliah, A. L., E. M. Griffin, I. McWhirter, A. D. Aylward, E. A. K. Ford, A. Charalambous, M. J. Kosch, C. J. Davis, and V. S. C. Howells (2004), First tristatic studies of meso-scale ion-neutral dynamics and energetics in the high-latitude upper atmosphere using collocated FPIs and EISCAT radar, *Geophys. Res. Lett.*, *31*(3), L03,802, doi: 10.1029/2003gl018469.

Aruliah, A. L., E. M. Griffin, A. D. Aylward, E. A. K. Ford, M. J. Kosch, C. J. Davis, V. S. C. Howells, S. E. Pryse, H. R. Middleton, and J. Jussila (2005), First direct evidence of meso-scale variability on ion-neutral dynamics using co-located tristatic FPIs and EISCAT radar in Northern Scandinavia, *Ann. Geophys.*, *23*(1), 147–162, doi: 10.5194/angeo-23-147-2005.

Aruliah, A. L., E. M. Griffin, H.-C. I. Yiu, I. McWhirter, and A. Charalambous (2010), SCANDI - an all-sky Doppler imager for studies of thermospheric spatial structure, *Ann. Geophys.*, *28*(2), 549–567, doi: 10.5194/angeo-28-549-2010.

Babcock, H. D. (1923), A study of the green auroral line by the interference method, *Astrophys. J.*, *57*, 209, doi: 10.1086/142747.

Biondi, M. A., D. P. Sipler, M. E. Zipf, and J. L. Baumgardner (1995), All-sky Doppler interferometer for thermospheric dynamics studies, *Appl. Opt.*, *34*(10), 1646–1654.

Burnside, R. G., F. A. Herrero, J. W. Meriwether, and J. C. G. Walker (1981), Optical observations of thermospheric dynamics at Arecibo, *J. Geophys. Res. Sp. Phys.*, *86*(A7), 5532–5540, doi: 10.1029/JA086iA07p05532.

Chapagain, N. P., J. J. Makela, J. W. Meriwether, D. J. Fisher, R. A. Buriti, and A. F. Medeiros (2012), Comparison of nighttime zonal neutral winds and equatorial plasma bubble drift velocities over Brazil, *J. Geophys. Res.*, *117*(A6), A06,309, doi: 10.1029/2012JA017620.

Chapagain, N. P., D. J. Fisher, J. W. Meriwether, J. L. Chau, and J. J. Makela (2013), Comparison of zonal neutral winds with equatorial plasma bubble and plasma drift velocities, *J. Geophys. Res. Sp. Phys.*, *118*(4), 1802–1812, doi: 10.1002/jgra.50238.

Coakley, M. M., F. L. Roesler, R. J. Reynolds, and S. Nossal (1996), Fabry-Perot CCD annular-summing spectroscopy: Study and implementation for aeronomy applications, *Appl. Opt.*, *35*(33), 6479–93, doi: 10.1364/AO.35.006479.

Conde, M., and P. Dyson (1995), Thermospheric vertical winds above Mawson, Antarctica, *J. Atmos. Terr. Phys.*, *57*(6), 589–596, doi: 10.1016/0021-9169(94)00099-A.

Conde, M., and R. W. Smith (1997), Phase compensation of a separation scanned, all-sky imaging Fabry Perot spectrometer for auroral studies, *Appl. Opt.*, *36*(22), 5441–5450, doi: 10.1364/AO.36.005441.

Conde, M., and R. W. Smith (1998a), Spatial structure in the thermospheric horizontal wind above Poker Flat, Alaska, during solar minimum, *J. Geophys. Res.*, *103*(A5), 9471–9949, doi: 10.1029/97JA03331.

Conde, M., and R. W. Smith (1998b), Simultaneous observations of the aurora and of non-uniform thermospheric winds, from Poker Flat, Alaska, *Proc NIPR Symp Up Atmos Phys (Nat Inst Polar Res)*, *12*, 30–38.

Conde, M., J. D. Craven, T. Immel, E. Hoch, H. Stenbaek-Nielsen, T. Hallinan, R. W. Smith, J. Olson, W. Sun, L. A. Frank, and J. Sigwarth (2001), Assimilated observations of thermospheric winds, the aurora, and ionospheric currents over Alaska, *J. Geophys. Res. Sp. Phys.*, *106*(A6), 10,493–10,508, doi: 10.1029/2000JA000135.

Conde, M. G., and M. J. Nicolls (2010), Thermospheric temperatures above Poker Flat, Alaska, during the stratospheric warming event of January and February 2009, *J. Geophys. Res. Atmos.*, *115*(D3), D00N05, doi: 10.1029/2010jd014280.

Deng, Y., and A. J. Ridley (2006), Dependence of neutral winds on convection E-field, solar EUV, and auroral particle precipitation at high latitudes, *J. Geophys. Res. Sp. Phys.*, *111*(A9), A09,306, doi: 10.1029/2005JA011368.

Faivre, M., J. W. Meriwether, C. G. Fesen, and M. A. Biondi (2006), Climatology of the midnight temperature maximum phenomenon at Arequipa, Peru, *J. Geophys. Res.*, *111*(A6), A06,302, doi: 10.1029/2005JA011321.

Ford, E. A. K., A. L. Aruliah, E. M. Griffin, and I. McWhirter (2006), Thermospheric gravity waves in Fabry-Perot interferometer measurements of the 630.0 nm OI line, *Ann. Geophys.*, *24*(2), 555–566, doi: 10.5194/angeo-24-555-2006.

Griffin, E. M., A. L. Aruliah, I. McWhirter, H. C. I. Yiu, A. Charalambous, and I. McCrea (2008), Upper thermospheric neutral wind and temperature measurements from an extended spatial field, *Ann. Geophys.*, *26*(9), 2649–2655, doi: 10.5194/angeo-26-2649-2008.

Hays, P. B., and R. G. Roble (1971), A technique for recovering Doppler line profiles from Fabry-Perot interferometer fringes of very low intensity., *Appl. Opt.*, *10*(1), 193–200.

Ishii, M., M. Conde, R. W. Smith, M. Krynicki, E. Sagawa, and S. Watari (2001), Vertical wind observations with two Fabry-Perot interferometers at Poker Flat, Alaska, *J. Geophys. Res. Sp. Phys.*, *106*(A6), 10,537–10,551, doi: 10.1029/2000ja900148.

Makela, J. J., J. W. Meriwether, Y. Huang, and P. J. Sherwood (2011), Simulation and analysis of a multi-order imaging Fabry-Perot interferometer for the study of thermospheric winds and temperatures, *Appl. Opt.*, *50*(22), 4403–4416, doi: 10.1364/ao.50.004403.

Makela, J. J., J. W. Meriwether, A. J. Ridley, M. Ciocca, and M. W. Castellez (2012), Large-scale measurements of thermospheric dynamics with a multisite Fabry-Perot interferometer network: Overview of plans and results from midlatitude measurements, *Int. J. Geophys.*, *2012*(3), 872,140, doi: 10.1155/2012/872140.

Meriwether, J., M. Faivre, C. Fesen, P. Sherwood, and O. Veliz (2008), New results on equatorial thermospheric winds and the midnight temperature maximum, *Ann. Geophys.*, *26*(3), 447–466, doi: 10.5194/angeo-26-447-2008.

Meriwether, J. W. (2006), Studies of thermospheric dynamics with a Fabry-Perot interferometer network: A review, *J. Atmos. Sol. Terr. Phys.*, *68*(13), 1576–1589, doi: 10.1016/j.jastp.2005.11.014.

Meriwether, J. W., J. J. Makela, Y. Huang, D. J. Fisher, R. A. Buriti, A. F. Medeiros, and H. Takahashi (2011), Climatology of the nighttime equatorial thermospheric winds and temperatures over Brazil near solar minimum, *J. Geophys. Res. Sp. Phys.*, *116*(A4), A04,322, doi: 10.1029/2011ja016477.

Nakajima, H., S. Okano, H. Fukunishi, and T. Ono (1995), Observations of thermospheric wind velocities and temperatures by the use of a Fabry-Perot Doppler imaging system at Syowa Station, Antarctica, *Appl. Opt.*, *34*(36), 8382–8395, doi: 10.1364/AO.34.008382.

Nicolls, M. J., S. L. Vadas, J. W. Meriwether, M. G. Conde, and D. Hampton (2012), The phases and amplitudes of gravity waves propagating and dissipating in the thermosphere: Application to measurements over Alaska, *J. Geophys. Res. Sp. Phys.*, *117*(A5), A05,323, doi: 10.1029/2012ja017542.

Rees, D., A. Greenaway, R. Gordon, I. McWhirter, P. Charleton, and A. Steen (1984), The Doppler imaging system: Initial observations of the auroral thermosphere, *Planet. Sp. Sci.*, *32*(3), 273–285, doi: 10.1016/0032-0633(84)90163-6.

Shiokawa, K., Y. Otsuka, S. Oyama, S. Nozawa, M. Satoh, Y. Katoh, Y. Hamaguchi, Y. Yamamoto, and J. Meriwether (2012), Development of low-cost sky-scanning Fabry-Perot interferometers for airglow and auroral studies, *Earth Planets Sp.*, *64*(11), 1033–1046, doi: 10.5047/eps.2012.05.004.

Sica, R. J., M. H. Rees, R. G. Roble, G. Hernandez, and G. J. Romick (1986), The altitude region sampled by ground-based Doppler temperature measurements of the OI 15867 K emission line in aurorae, *Planet. Sp. Sci.*, *34*(5), 483–488, doi: http://dx.doi.org/10.1016/0032-0633(86)90035-8.

Sipler, D., M. Biondi, and M. Zipf (1995), Vertical winds in the midlatitude thermosphere from Fabry-Perot interferometer measurements, *J. Atmos. Terr. Phys.*, *57*(6), 621–629, doi: 10.1016/0021-9169(94)00102-T.

Chapter 6
Conclusions

The motivation behind this dissertation was to investigate how local-scale gradients present in Earth's upper thermosphere at high latitudes would redistribute neutral air masses and influence the thermospheric wind transport. An air mass transported by a wind field will become distorted over time by any gradients present in the wind field. To achieve our objective, we used thermospheric wind fields inferred from F-region 630 *nm* optical emission spectra measured over a wide geographic area of Alaska by high latitude ground-based all-sky scanning Doppler imaging Fabry-Perot interferometers (all-sky SDI) located at Poker Flat (65.12N, 147.47W) and Gakona (62.30N, 145.27W). For one of our studies, we also used data from three narrow-field Fabry-Perot interferometers (NFPIs) operated by Clemson University. Two of them are located at Poker Flat, and the other one is at Fort Yukon (66.57N, 145.26W).

In addition to our main studies, appendix B explains how we obtained the first ever application of the all-sky SDI technique to study winds and temperatures of the mesopause heights derived from observations of the hydroxyl (OH) airglow emissions from the (6,2) Meinel band at wavelength 843 *nm*.

The major findings of our studies are following:

6.1 Distortion in Thermospheric Air Masses

A new parameter called distortion gradient (Dg) was defined for use in studying the climatological behavior of how thermospheric winds distort air masses transported over Alaska. Dg includes all contributions to non-uniform horizontal flow, including all first order gradients and any higher-order perturbations. Dg is always positive, whereas conventional gradients (or linear combinations of gradients) can be negative or positive. Climatological averaging of conventional gradients will therefore likely underestimate distortion effects, whereas Dg is not subject to this problem.

The average climatological behavior of Dg was studied using three years of all-sky Fabry-Perot measurements of thermospheric winds above Alaska. The principal finding of this research work is that the distortion in the F-region thermospheric air masses above

Alaska has a diurnal, seasonal, geomagnetic activity, and IMF dependence. In all the cases, maximum distortion occurred before local magnetic midnight.

The diurnal behavior of *Dg* was similar for each of the years studied: 2010, 2011, and 2012. *Dg* was smaller in the climatological averages in the evening and morning, and it maximized between 0600 UT and 1000 UT. If this behavior was not a persistent feature, it would have been suppressed by averaging over a year. Despite the presence of large variability, a persistent feature was present in the seasonal behavior of *Dg* in all three years. *Dg* was smaller in winter compared to pre and post summer. This suggests the presence of seasonal dependence in the distortion of thermospheric air masses.

Timing of the *Dg* peak was observed to depend on geomagnetic activity. Air mass distortion was high between 0800 UT and 1000 UT under quiet geomagnetic conditions. Peak distortion appeared earlier (0700 UT to 0830 UT) in moderate geomagnetic conditions than quiet geomagnetic condition, and even earlier (0300 UT to 0700 UT) in active geomagnetic conditions. That is, the *Dg* peak shifted towards earlier in the evening with increasing geomagnetic activity. This is related to the expansion of the high latitude thermospheric circulation to the lower latitudes with the increase in geomagnetic activity. But in all the case, maximum distortion always occurred before the local magnetic midnight.

Investigations of the relationship between *Dg* and IMF revealed that distortion in thermospheric air masses was larger and appeared earlier when IMF was southward compared to northward. There was no significant difference between the distortions for dawn and dusk orientation of the IMF.

6.2 Thermospheric Wind Transport

In this study, we traced air parcel trajectories both forward and backward in time using the SDI wind measurements over a large geographic area above Alaska to show the complexity of the wind driven transport in the thermosphere. In methodology, our study is similar to the air parcel tracing through model wind fields performed by *Killeen and Roble* [1986], although in our case, we used experimentally measured thermospheric winds with much higher spatial resolution but only confined to the region above Alaska. Forward tracing was used to find where air parcels would go with time and backward trac-

ing to find where they came from. It is evident that the thermospheric air parcels do not travel in simple paths. In the thermosphere, wind shears change with time and space which introduces further complexity in the air parcel transport.

Forward tracing showed the presence of a flow channel on the equatorward edge of the ion drag dominated wind flow before magnetic midnight. It mixed the air parcels from lower latitudes with the air parcels from high latitudes. Forward tracing clearly showed that composition perturbations caused by active aurora can be transported to lower latitudes depending on the wind fields, which in turn can influence the lower latitude chemistry and dynamics. Backward tracing gives the history of air parcels, and revealed that two neighboring air parcels can originate from widely separated geographical regions depending on the structures in wind fields. The wind gradients led to mixing of air parcels from different regions of the thermosphere. It is evident from forward and backward tracing of air parcels that the wind transport is sensitive to the details of wind field and any change in the wind field can cause a huge impact on where the air parcels would end up.

Our current understanding of the thermospheric transport is still limited by the paucity of observations. The real physical consequences of air parcel tracing would be fully exposed if we could trace air parcels over long distances. Currently, by combining all the data from existing operational instrumental facilities around the globe and models, we can study thermospheric climatology, but we cannot construct paths traveled by air parcels over global or even hemispheric scale with any useful accuracy. Achieving a reliable and accurate way to find paths traveled by air parcels will require an extensive network of wind measurements with instruments capable of mapping winds over wide geographic regions with high spatial resolution. If we consider air parcel tracing even over a hemisphere, the observation challenge is enormous.

6.3 SDI and NFPI Cross-comparison

In this study, we have presented the first ever cross-comparison of horizontal neutral wind fields at F-region heights mapped by two different types of ground-based optical Doppler spectrometers (SDI and NFPI) working independently of each other at auro-

ral latitudes. One type (SDI) is a wide FOV Fabry-Perot spectrometer with a scanning etalon. The second (NFPI) is a narrow FOV Fabry-Perot spectrometer with fixed etalon gap. Here, the 630-nm emission that originates from the 630 *nm* emission layer within the upper thermosphere was used by both instruments to monitor thermospheric wind fields at ~240km altitude. Although, both instruments are observing the Doppler shifts and have etalons (one with fixed gap and other with scanning gap), they are very different in technical implementation, modes of operation, spectral derivation, and data analysis.

NFPI observation locations lie within the FOV of the SDIs located at Poker Flat and Gakona. To exhibit the most direct comparison between them, raw LOS winds from SDI and NFPI at Poker Flat were compared. Our results showed that the slowly-varying "background" behavior of the LOS winds inferred by these two techniques exhibited very good agreement. Strong correlation over entire data set was observed between SDI and NFPI LOS winds. Also, despite the differences in uncertainties, the time variations in temperatures measured by NFPI and SDI located at Poker Flat were in a good agreement.

Both instruments observed additional short period fluctuations in LOS winds. There were many instances when both instruments observed similar short period fluctuation at the same time. This suggests that these fluctuations have thermospheric origin. However, the amplitude of the NFPI fluctuations was substantially higher than those observed by the SDI. These short period fluctuations are likely related to the existence of thermospheric gravity waves caused by auroral activity, or gravity waves propagating from below.

Zonal and meridional winds were inferred from the LOS winds, after somewhat indirect wind fitting. It was found that horizontal neutral wind vector fields estimated by both methods were still in good agreement, and oscillations similar to those present in LOS wind were also present in estimated wind components. The observed neutral wind behavior was consistent both between the SDI and NFPI, and also with numerous previous studies.

Monostatic SDI wind fits are based on substantial assumptions compared to the bistatic wind fits, which involved only an assumption regarding the vertical wind. Nevertheless, both monostatic and bistatic wind fits showed very good agreement on all nights avail-

able for comparison. Although the amplitude of fluctuations in NFPI estimated winds was considerably stronger than those from the SDI, oscillations were present in both data sets at the same times and spatial locations. Improvement in consistency between the winds estimated by two instruments was observed with increasing wind speed.

The temporal responses of SDI LOS winds and horizontal wind components were smoother than corresponding data from the NFPI. This was most likely related to the large geographic sampling volume of even the smallest SDI zone compared to typical NFPI sampling volumes. The SDI averages its observations over these larger volumes, rendering the instrument insensitive to small-scale spatial structures. Smoother SDI time series compared to NFPI suggests that small sized and previously unobserved wind features occur in the upper thermosphere, with typical length scales smaller than the lengths spanned by the SDI zones. Notwithstanding small-scale discrepancies, the overall large-scale agreement between the two instrument types would be considered excellent for most routine applications. Ultimately, to completely resolve and characterize small-scale short-lived thermospheric wind structures will require either a network of modified SDIs (with smaller FOVs), or else a very dense network of NFPIs.

6.4 Mesospheric Application of All-sky SDI

In this study (included as appendix B), we have presented the mesopause wind and temperature data recorded at auroral latitudes with an all-sky SDI using $P_1(3)$ airglow emission from (6,2) Meinel band. This was the first time ever this all-sky SDI technique was employed to study middle atmospheric dynamics. The temperatures estimated with these data were higher than the range of normally observed mesopause temperatures. The comparison of $P_1(3)$ airglow emission intensity and the 557.7 *nm* emission intensity suggested that the auroral emissions were leaking through the OH filter which contaminated the OH airglow spectra. Another possible cause of temperature overestimation could be the scaling of instrument function from the calibration to source wavelength without including effects of wavelength variation in etalon reflective finesse. Nevertheless, the overall trend in the mesopause temperature from winter to early summer season was similar to that expected (higher in winter and lower in summer). Also, the magni-

tudes of estimated wind components were within in the expected range (0-100 $m.sec^{-1}$). These results show that this could be a promising new technique for studying middle atmospheric dynamics if used at wavelengths that are not easily contaminated by other emission sources. The data presented here are preliminary and require further validation before it could be used for detailed study of mesospheric dynamics.

Appendix A
Instrumentation: All-sky Fabry-Perot Spectrometer

A.1 Introduction

Since the 1950's, many techniques have been developed to study Earth's upper atmospheric dynamics. Of these, optical remote sensing is a very powerful tool and has produced the most thermospheric wind data to date. In recent decades, Fabry-Perot spectrometers (also called Fabry-Perot interferometers) (FPS or FPI) have become a popular spectroscopic tool for high resolution remote sensing of winds and temperatures in the middle and upper atmosphere. It is because of their advantage of estimating wind speed and temperature directly from the Doppler shift and Doppler broadening (width) of natural optical line emissions. Equivalent data would be very difficult or impossible to obtain by other means. Use of FPIs in spectral imaging of the atmosphere started with the measurement of the wavelength of the atmospheric auroral green line emission in the airglow by Harold Babcock in 1923 [*Babcock*, 1923]. This study proved the existence of atomic oxygen in the upper atmosphere. Since then, FPIs have been used for a wide range of spectroscopic purposes.

In the early development phases of FPI, photographic film was used to record data [*Hernandez*, 1986]. This approach was replaced with photoelectric detectors in 1948 and required a slightly different mode of operation. FPI with photographic film produces an interferogram, whereas FPI with photoelectric detector produces a spectrum. The photoelectric detectors were then replaced with photomultiplier tubes (PMT). These days imaging charged coupled device (ICCD) and electron multiplying charged coupled device (EMCCD) are commonly used as detectors. FPI is improving day-by-day and taking on new forms. A complete discussion of the historical background and details of FPI is given in *Hernandez* [1986] and *Vaughan* [1989].

In our studies, we used an all-sky SDI (Scanning Doppler Imager) which is a variant of the traditional FPI. A brief discussion of the comparison between FPI and all-sky SDI technique is presented in the sections 5.2.1 and 5.2.2 of chapter 5. Here, general princi-

ples of optical Doppler spectroscopy, basic design, and operation of an all-sky SDI are reviewed.

A.2 General Principles

A simple Fabry-Perot etalon consists of two plane parallel transparent glass plates separated by a spacer of thickness t and refractive index μ. The commonly spacer is air, but other media for example - lithium niobate or liquid crystals are also used [*Hernandez*, 1986]. The inner surfaces of each plate are polished and coated to provide a reflectance usually somewhere in the range 0.7 to 0.9. The enclosed gap would typically be chosen to be somewhere in the range from several millimeters to several centimeters. Consider two rays of light at wavelength λ are incident on etalon at an angle θ. They undergo reflection between the etalon plates and split into a series of parallel transmitted rays. The rays are partially transmitted at each reflection from the second surface (as shown in Figure A.1). Let us consider incident rays 1 and 2 (as shown in Figure A.1). When the difference

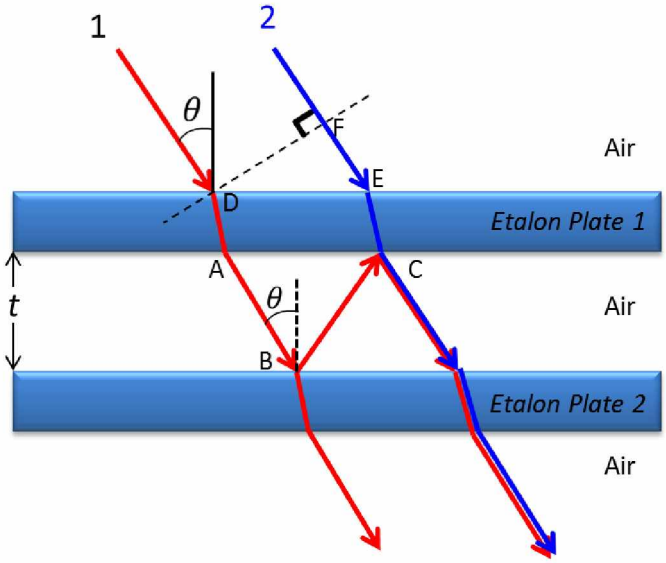

Figure A.1: Schematics of Fabry-Perot etalon plates separated by distance t and multiple reflections of a light ray of wavelength λ entering etalon at an angle θ relative to the plate normal.

in their optical path length is such that they are in the same phase, then constructive interference will occur, and the etalon will show a maximum in transmission. If rays 1

and 2 are out of phase, they will produce destructive interference, and the transmission will be relatively low.

The phase difference between rays emerging rays 1 and 2 at other end is due to the different paths traveled by them through etalon. The optical path length difference between rays 1 and 2 arises from the difference between optical paths ABC and FE (shown in Figure A.1). The optical path difference between rays 1 and 2 is given by the product of refractive index of the medium and difference in geometric paths traveled by them. The optical path difference (d) is:

$$d = \mu\,(AB + BC) - \mu\,(FE) \tag{A.1}$$

Note that AB = BC and AB = $\frac{t}{cos\theta}$, AC = 2 t $tan\theta$, and FE = 2 t $\frac{sin^2\theta}{cos\theta}$.

$$d = \mu\,(\frac{t}{cos\theta} + \frac{t}{cos\theta}) - \mu\,(2\,t\,\frac{sin^2\theta}{cos\theta}) \tag{A.2}$$

$$d = 2\mu\,t\,cos\theta \tag{A.3}$$

This shows that optical path difference is a function of refractive index of the spacer, etalon plate separation, and angle of incidence. The optical path difference maximizes ($d = 2\mu t$) at normal incidence, and decreases as θ increases.

In an actual Fabry-Perot interferometer, the basic layout is similar to as shown in Figure A.2 (all-sky lens on the top is specific to all-sky SDI). The parallel rays emerging from etalon are focused on to a detector using a focusing lens. Now, if the emerging rays arrive at the detector in phase, they produce constructive interference and hence maximum brightness; if not then destructive and low transmission. For entirely constructive interference to occur, the optical path difference must be an integral multiple of the wavelength; for fully destructive interference, the optical path difference must be an odd multiple of half wavelength.

$$Constructive : d = m\lambda$$

$$Destructive : d = (m + \frac{1}{2})\lambda$$

where m = 0, 1, 2, ... is called order of interference. For constructive interference,

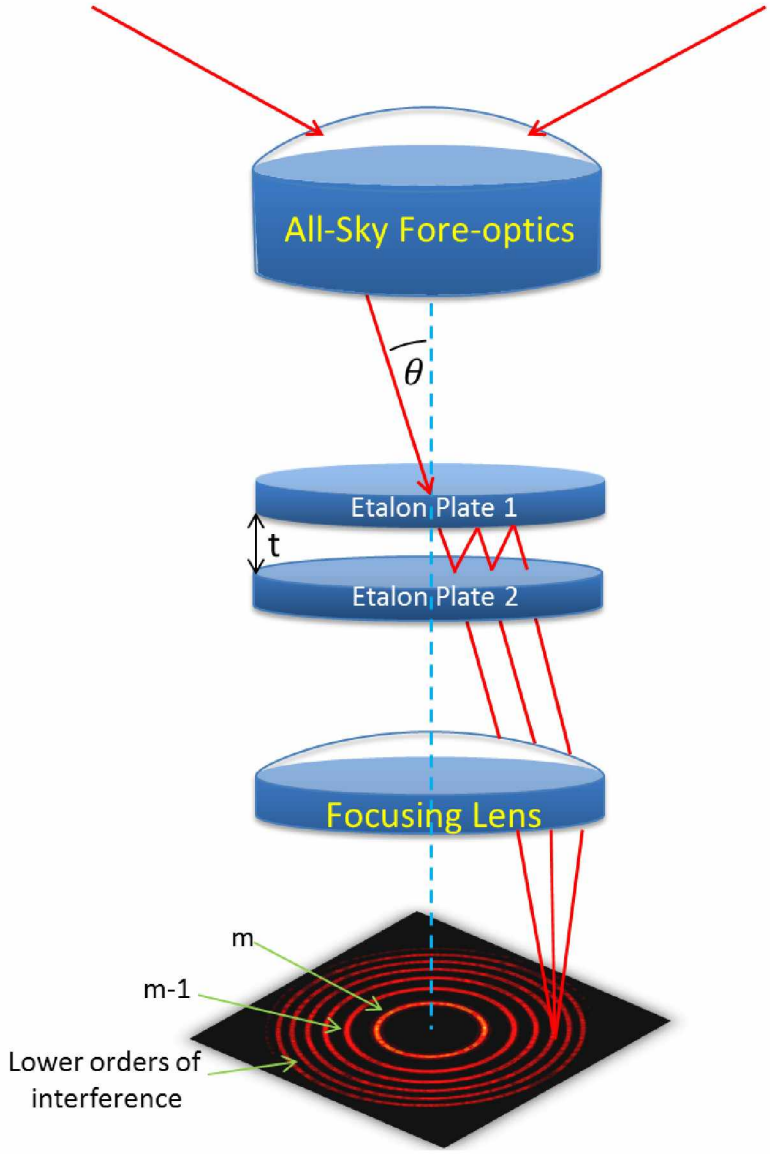

Figure A.2: Basic layout of the working of Fabry-Perot etalon plates separated by distance t. The red line shows an example of the path followed by a ray before it is collected at the detector. All-sky lens at the top is to collect light from a wide angle. The focusing is to map the angular brightness modulation emerging from the etalon onto positions on the detector surface.

equation A.3 can be written as:

$$m\,\lambda = 2\,\mu\,t\,cos\theta \tag{A.4}$$

$$m = \frac{2\,\mu\,t\,cos\theta}{\lambda} \tag{A.5}$$

For a given μ, t, and λ, the order of interference decreases with the increase in θ. For a given θ, all azimuths at this angle result in a constant order of interference at the detector. The angle θ maps to the radius on the detector. As θ changes, it also changes the order of interference, and therefore by axial symmetry transmission maxima forms a series of concentric rings at the detector (example 632.8 *nm* laser fringe pattern shown in Figure A.2).

The order of interference shows periodic behavior. So, a similar interference pattern can be obtained by changing m to $m+1$ (or $m\lambda$ to $(m+1)\lambda$). If m is kept fixed, then a similar interference pattern can be obtained by changing changing λ to $\lambda+\Delta\lambda$ (or $m\lambda$ to $m(\lambda+\Delta\lambda)$) such that the order changes from m to $m+1$ [*Hernandez*, 1986; *Shepherd*, 2002]). Thus:

$$(m+1)\lambda = m(\lambda+\Delta\lambda) \tag{A.6}$$

$$\Delta\lambda = \frac{\lambda}{m} = \frac{\lambda^2}{2\,\mu\,t\,cos\theta} \tag{A.7}$$

$\Delta\lambda$ is called the free spectral range and corresponds to the wavelength interval between successive interference orders.

The transmission of an ideal etalon can be calculated by summing the amplitudes of each of the transmitted rays (or from the reflected power as transmitted power = 1 - reflected power). The normalized transmission of an ideal etalon (also called Airy function) can be expressed in terms of etalon reflectance (R), the refractive index of the spacer medium (μ), spacing between plates (t), the angle of incidence (θ), and wavelength of incidence (λ). A complete discussion and development of the Airy function is discussed in *Hernandez* [1986] and *Vaughan* [1989]. The Airy function (also known as passband response function which is dependent solely on the etalon, is usually written as:

$$A(m) = \frac{1}{1+\frac{4R}{(1-R)^2}sin^2(m\pi)} \tag{A.8}$$

The behavior of etalon transmission with m and λ is depicted in Figure A.3. The transmission reaches its maximum value at integral values of m. Free spectral range, which corresponds to the wavelength interval between successive transmission peaks is also shown in Figure A.3.

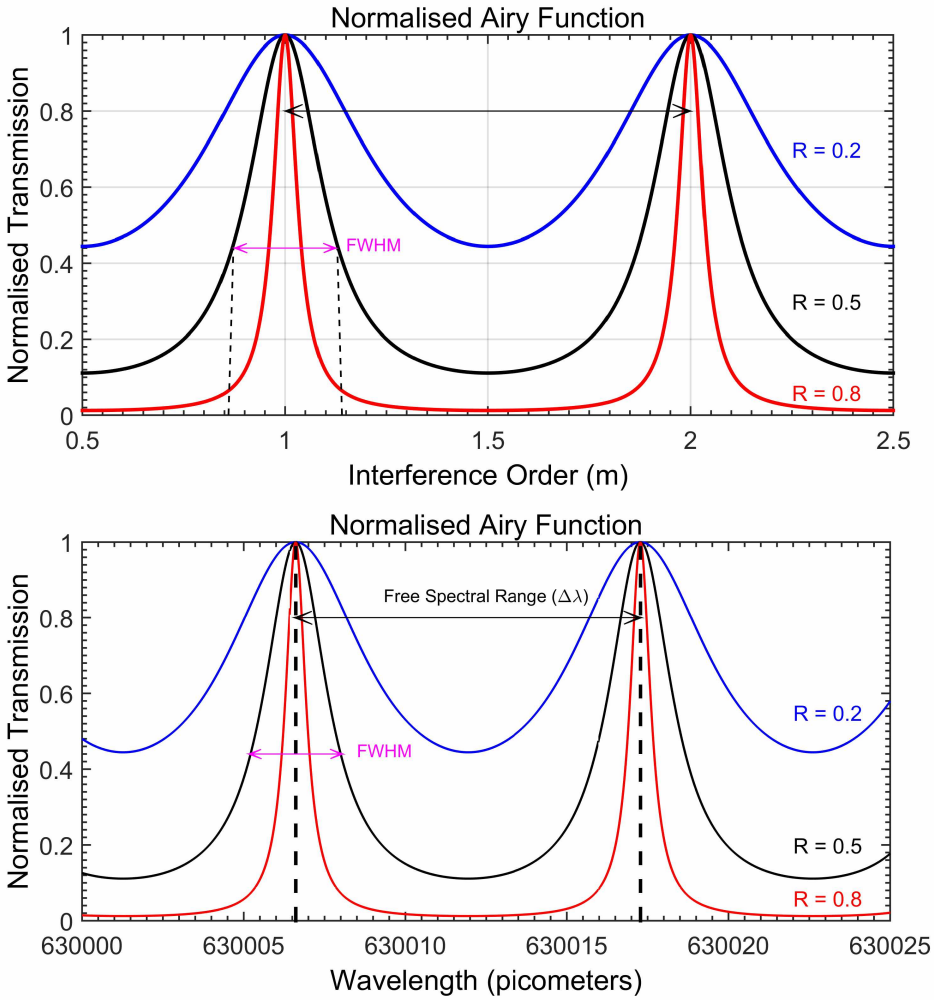

Figure A.3: Normalize transmission (Airy function) of a plane-parallel etalon as function of order of interference (top panel) and wavelength (bottom panel) for different plate reflectivities (R = 0.2, 0.5, and 0.8).

The spectral resolution of an etalon is defined by the spectral width of the passbands i.e. the broadening imposed on the emission line by the etalon. It is given in terms of full width at half maxima (*FWHM*) of the spectral width of the emission line. Mathematically it is written as:

$$FWHM = \frac{1-R}{\pi\sqrt{R}} \tag{A.9}$$

As shown in Figure A.3, the reflectivity of the etalon plate coatings affects the transmission. Each of the peaks represents one passband of the etalon. High reflectance coating produces spectrally narrow passbands, whereas lower reflectance both broaden the

passbands and raise the minimum transmission value between them. This leads to the concept of "finesse". It is a measure of the sharpness of the passbands, and the ability of the interferometer to resolve closely spaced spectral lines. The finesse (reflectivity finesse) is defined as the ratio of the free spectral range to the width of one transmission peak:

$$F = \frac{\pi\sqrt{R}}{1-R} \tag{A.10}$$

The above discussed formulation is valid for an ideal etalon. In practice, etalon plates are not perfectly smooth or flat. There are always imperfections in the surface polishing and coating which add roughness to the plate surface. These imperfections introduce a small range of gaps, and the width of this range produces the broadening of the recorded line spectrum. In real applications, the response of an FPI to a delta-function input signal (instrument function) is calculated by exposing it to a spectrally stable and very narrow source (generally frequency stabilized lasers). To obtain actual line spectrum of an emission source, the instrument function which describes the broadening effect of the etalon plates is deconvolved from the recorded source spectrum. A detailed discussion and derivation of instrument function is given in *Jacka* [1985].

A.3 Basic Design of an All-Sky SDI

An all-sky SDI is a variant of the traditional FPI. It uses all sky fore-optics coupled with a separation scanned etalon. A detailed description of its design and working was first described by *Conde and Smith* [1995, 1997, 1998] and recently by *Conde and Nicolls* [2010]; *Anderson* [2011]; *Anderson et al.* [2012]. A schematic layout of the design of an all-sky SDI is shown in Figure A.4. The following discussion of the SDI's principles of operation follows the formulation given in *Anderson* [2011].

An all-sky lens in the fore-optics collects atmospheric optical emissions from a wide field of view (FOV) in the sky (typically 140 degrees full angle). A software driven filter wheel carrying various narrow band interference filters (maximum six) is incorporated in the fore-optics and allows selection of the wavelength of interest. All the existing SDIs have 630 *nm* and 577.7 *nm* filters. They routinely observe at these two wavelengths, automatically selecting filters according to a programmed sequence. Other filters are added

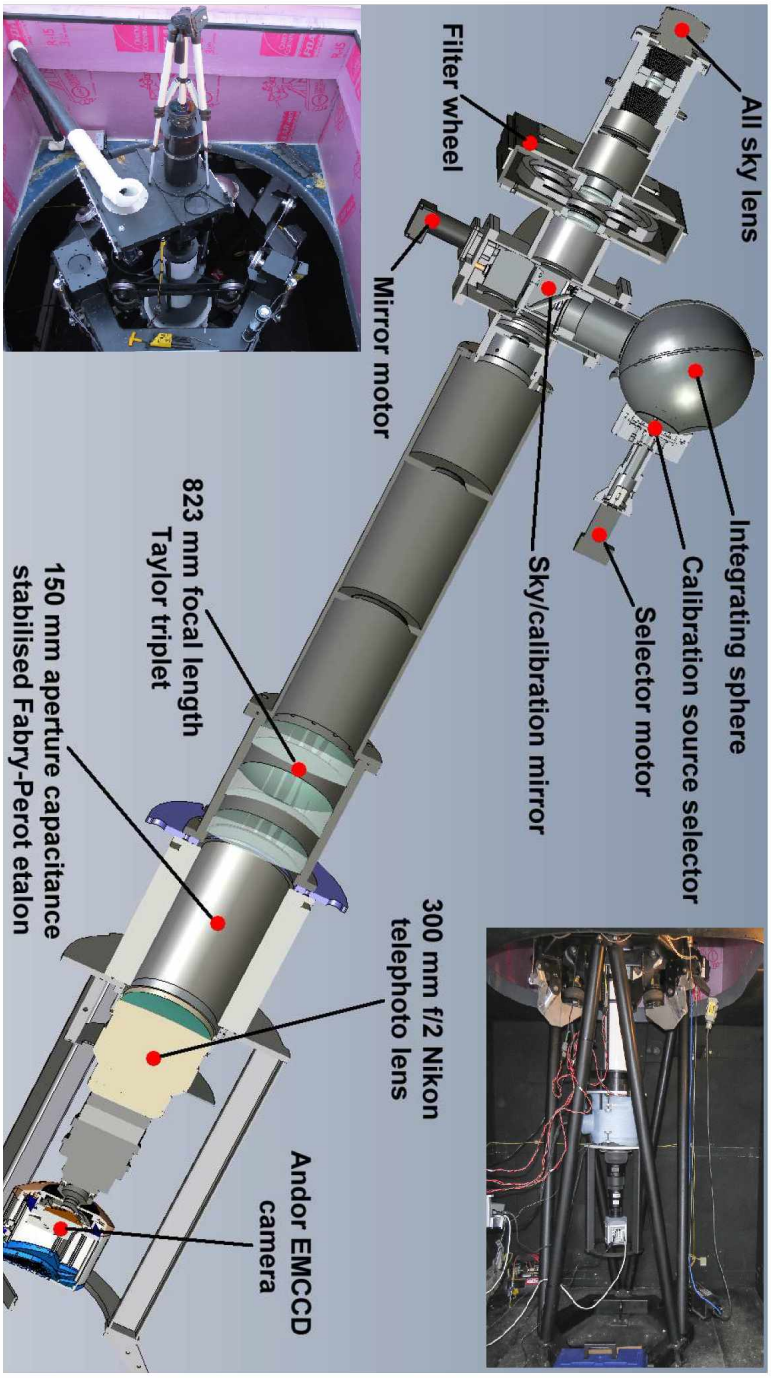

Figure A.4: Schematic layout of the design of an all-sky SDI (modified from *Anderson* [2011]). The insets in the upper left and bottom right corner of the figure are actual pictures of the all-sky SDI installed at Toolik Field station (Alaska). The top left inset shows a picture taken from the top, and bottom right inset shows a picture taken from the side.

for measurements at other wavelengths when needed. For example, an *OH* filter was added in the SDI located at Gakona for observing season 2011-2012 (as discussed in appendix B). For calibration purposes, the SDI periodically illuminated with diffused light from sources (typically frequency stabilized He-Ne laser operating at 632.8 *nm*) with the help of an integrating sphere and a view-switch mirror. This mirror is driven by a small motor controlled by software. Light from the sky/calibration source then passes through a collimating set of lenses and enters in a separation scanned Fabry-Perot etalon. The aperture and nominal gap between etalon plates for the SDIs located at Poker Flat and Gakona are listed in Table 1 of chapter 5. The gap between etalon plates is scanned piezoelectrically. The etalon plate spacing is typically configured to span exactly over one order of interference in 128 discrete steps. When monochromatic light passes through the etalon, the transmission is modulated according to the incidence angle. A 300 $mm\, f/2.8$ telephoto lens focuses this angularly modulated beam, thus forming concentric rings on light onto a 512×512 pixel high efficiency thermoelectrically cooled electron multiplying CCD camera (EMCCD). The quantum efficiency of this camera is $\sim 90\%$ for the visible spectrum and drops to $\sim 50\%$ for the infrared region.

A.4 Etalon Scanning

We need to record spectra, which mean we need to sample the sky spectra at a number of discrete wavelengths. Scanning the etalon allows us to "tune" the instrumental passband in wavelength, and hence record these spectra.

The gap between etalon plates is controlled with the help of three sets of piezoelectric ceramics and capacitive sensors placed between the etalon plates (shown in Figure A.5). They are placed at equal distances around the circumference at three places. A special property of these piezoelectric ceramics (called transducers) is that they change in size when voltage is applied across them. The etalon gap is controlled by applying a voltage across each transducer. When etalon gap changes, the capacitance of the capacitive sensor also changes. This change in capacitance is compared with a reference capacitor and hence used to sense small changes in the gap between etalon plates. Each transducer and sensor pair is referred to as a leg [*Anderson*, 2011].

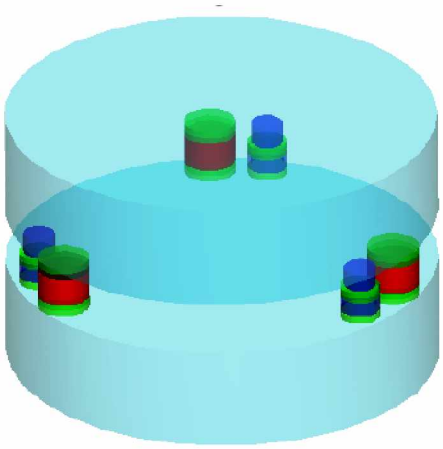

Figure A.5: Schematic layout of piezoelectric transducers (green-red-green) and sensors (blue-green-blue) between the etalon plates [*Anderson*, 2011].

Commands are sent to a dedicated etalon controller by the main control computer. For a sharp and undistorted interference fringes, the etalon plates must always remain parallel. To set the etalon plates parallel, the software applies a pre-determined "base" voltage to each etalon leg. Determination of the correct offsets is done by finding the values that produce the highest finesse laser fringes. Each leg is assigned a 12-bit digital number between 0 and 4095 representing plate spacing at the leg. The settings is also often referred to as "voltage", because the command number for a given leg maps directly to a physical voltage that is applied across the ceramic spacer for that leg. The digital voltage at a leg n is written as V_{L_n}. The voltage response of each leg's spacer and capacitive sensor may not be the same. So, the leg-to-leg variation in sensor response is accounted for by appling a unique gain to each leg during the scan, to maintain parallelism. To calculate the response of one sensor relative to the other, first the sharpest fringe image of the calibration source is obtained by individually varying the digital voltage applied to each leg at around 25% of the possible range. Let the resulting values be $V_{L_n}(0)$. Then this step is repeated but with instead using voltages of around 75% of the possible range, to produce values of $V_{L_n}(1)$. The difference in step 1 and step 2 voltage for leg 1 is $\Delta V_{L_1} = V_{L_1}(1) - V_{L_1}(0)$. The response of leg n relative to leg 1 is $R_{L_n} = \frac{\Delta V_{Ln}}{V_{L_1}}$. This means, if ΔV_{L_1} voltage increment is applied to leg 1, $R_{L_1} \times \Delta V_{L_n}$ must be applied to leg n to keep the etalon plates parallel.

As discussed above, the etalon is scanned over exactly one order of interference. The radius of interference fringes increases with the increase in plate separation. Suppose the original fringe pattern is recorded at plate separation t, then by increasing the plate separation there would be a stage when the $(m-1)^{th}$ order of interference of the original fringe pattern would exactly overlap with the m^{th} order of interference of the current pattern. At this plate new separation, the etalon would have scanned over one order of interference ($\Delta m = 1$) from its starting gap. Let us calculate how much digital voltage is to be applied to legs to scan over one order of interference. To calculate it, the etalon leg voltages are set to their initial positions $V_{L_n}(0)$ and fringe image (I_o) of a calibration source (wavelength λ_o) is recorded by 512×512 pixel EMCCD. Then a set of P "trial" voltages is applied, with the range scanned by the trial voltages chosen such that it should include the change from the base voltage that will correspond to a change in plate spacing of one order. The resulting fringe images (I_p) are recorded. The general expression for the p trial voltages is:

$$V_{L_n}(p) = V_{L_n}(p)(0) + pR_{L_n}\delta V \tag{A.11}$$

$$p = 1, 2, 3, \ldots\ldots P$$

where p is just an integer and δV is a voltage increment. At each increment, the recorded fringe image (I_p) is cross-correlated with the reference imager (I_o). The magnitude of cross-correlation is calculated by:

$$X(p) = \sum_{x=0}^{N_x-1} \sum_{y=0}^{N_y-1} [I_o(x,y) \times I_p(x,y)] \tag{A.12}$$

Where $N_x = N_y = 512$ and (x, y) denotes a pixel location on image. Note that in practice we first determine the minimum brightness in each image and subtract it from every pixel in that image before we do the cross correlation. This increases the "contrast" of the peak we are fitting. At certain value of p, I_o and I_p will appear identical and it will maximize the cross-correlation $X(p)$. That value of p (say p_{max}) will corresponds to one free spectral range. The voltage that maximizes $X(p)$ across each leg needed for etalon scanning over one order of interference is:

$$\Delta V_{L_n}^{fsr} = p_{max} R_{L_n} \delta V \tag{A.13}$$

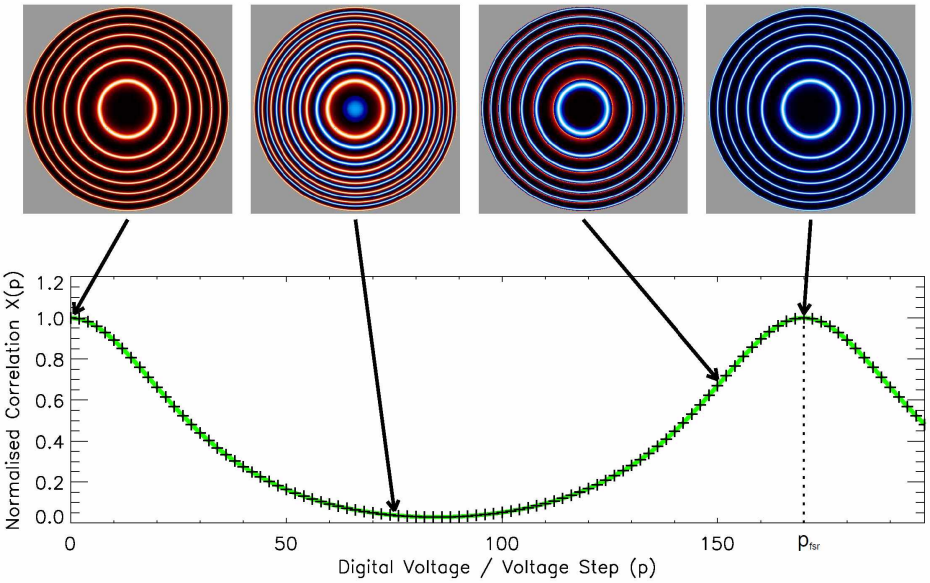

Figure A.6: An illustration of how the cross-correlation between reference fringe image (shown in red) and scanning fringe image (shown in blue) varies with digital voltage. For illustration, only four scan image steps in one free spectral range are shown [*Anderson*, 2011].

In terms of distance, the change in etalon gap for one order of interference at normal incidence is given by Equation A.5 as:

$$1 = \frac{2\mu\Delta t_o cos(0)}{\lambda_o}$$

$$\Delta t_o = \frac{\lambda_o}{2\mu} \tag{A.14}$$

This was the case for calibration source. For some other wavelengths λ_i:

$$\Delta t_i = \frac{\lambda_i}{2\mu} \tag{A.15}$$

Dividing 15 by 14:

$$\Delta t_i = \Delta t_o \frac{\lambda_i}{\lambda_o} \tag{A.16}$$

Since the applied leg voltage is proportion to the leg height, so a correction of factor $\frac{\lambda_i}{\lambda_o}$ must be applied to the digital voltage of each leg when observing at a different wavelength to that used for calibration.

Each single scan of the etalon gap is comprised of a series of small discrete steps (Q in number). Each step is called a channel; they are completely configurable in software. We typically configure the scan to be performed in Q=128 steps. For incident wavelength λ_i, the voltage applied to each leg to complete a single step is:

$$S_{L_n} = \frac{\Delta V_{L_n}^{fsr}}{Q} \frac{\lambda_i}{\lambda_o} \tag{A.17}$$

A.5 Phase Mapping

As discussed in the etalon scanning section, the order of interference m for a given wavelength changes at position (x,y) on the detector as plate separation t changes. Since the etalon transmission is an Airy function of m, the brightness at pixel (x,y) also changes. Because also m varies radially in the image, two pixels at different radii will not in general respond in phase as the etalon scans. To illustrate this effect, consider two neighboring pixels shown in red and blue in Figure A.7. This figure is just an artistic concept. The radial distance of the red pixel from the optical axis (fringe center) is larger than the blue pixel, so the order of interference is always higher at the blue pixel than the red pixel. Six panels shown in Figure A.7 depict the fringe patterns obtained at different plate separations (scan channel). The etalon plates were assumed to be scanned over one order of interference in 128 steps, and that is why the last fringe panel (6) is similar to as the first one (1). As shown in the figure, as the fringe radii increase with increasing plate separation, interference fringes cross the blue pixel before the red pixel. As a result, the blue pixel records transmission maximum at smaller plate separation (scan channel) than for the red pixel. It means the radial distance between the two pixels introduces a phase shift in the spectra recorded by them. This phase shift can be corrected for each pixel by finding the scan channel number at which the transmission recorded by the pixel maximizes. Then, the response at each pixel can be shifted by this amount along channel axis, so that the resultant spectra from all pixels are brought into phase. The process of finding the variation in spectral peak position at each pixel on the detector is known as "phase mapping". A detailed discussion of the phase mapping is given in *Conde and Smith* [1997]. A brief discussion is given below following the presentation in *Anderson* [2011].

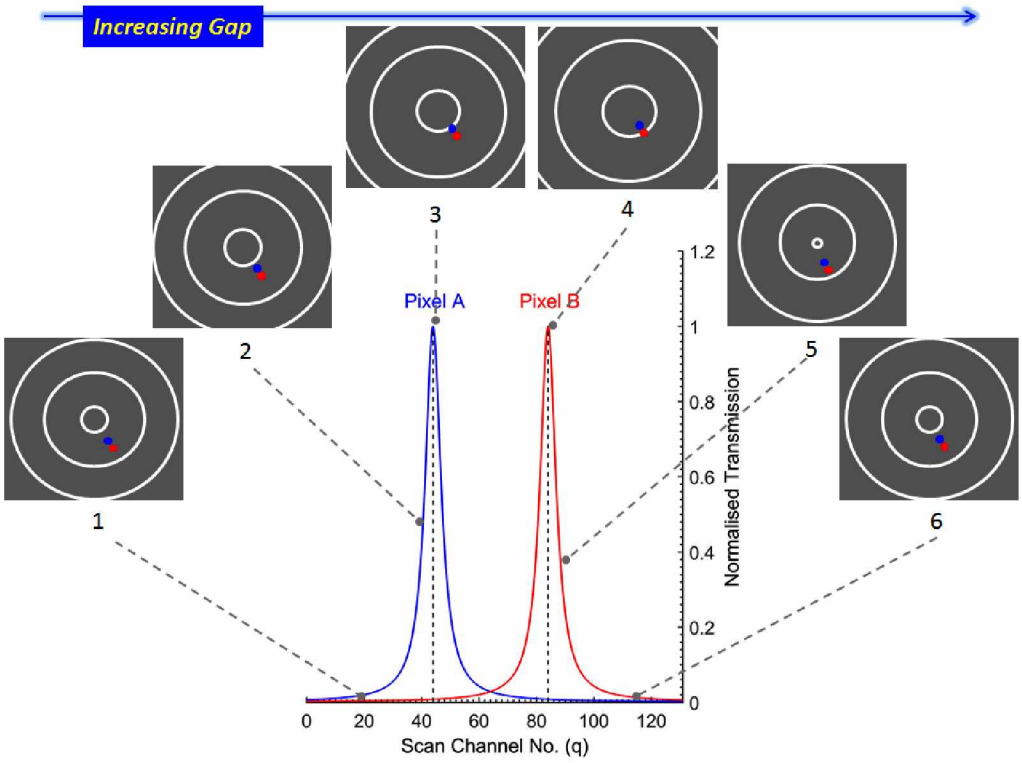

Figure A.7: The variation in recorded spectra at two pixels (blue and red) on the detector. Six modeled fringe subsets show fringes at six different plate spacing in one free spectral range. The phase shift between the spectra recorded by blue and red pixel is the result of the different radial location of these two pixels.

During scanning, a two-dimensional fringe image (say $R(x,y,q)$) is recorded at each scan step (q). A pair of phase-weighted sums is calculated for image:

$$a(x,y) = \sum_{q=0}^{Q-1} R(x,y,q) cos\left(\frac{2\pi q}{Q-1}\right) \tag{A.18}$$

$$b(x,y) = \sum_{q=0}^{Q-1} R(x,y,q) sin\left(\frac{2\pi q}{Q-1}\right) \tag{A.19}$$

Since the etalon scan is performed over one free spectral range, the intensity recorded by $R(x,y,q)$ will span at most one peak. The intensity variation at pixel (x_i,y_i) can be written as a function of phase angle ψ_q (details in *Anderson* [2011]):

$$\psi_q = \psi(x_i,y_i) = \frac{2\pi q}{Q-1} = tan^{-1}\left(\frac{b(x_i,y_i)}{a(x_i,y_i)}\right) \tag{A.20}$$

The two-dimensional array $\psi(x,y)$ is called a phase map. It describes the variation of phase angle across the detector at which a spectrum peaks. The phase angle can be written in the units of channel number (q):

$$q = \frac{\psi_q}{2\pi}(Q-1) \tag{A.21}$$

So phase map can be stored in the units of channel number. Figure A.8 shows an example of a recorded phase map. The top panel shows the variation of phase angle across the detector. Light colors correspond to higher values of phase and dark color to lower values. The phase map depends on wavelength. This means a phase map obtained with a calibration source cannot be used directly at other wavelengths. A technique discussed by *Conde and Smith* [1997] is used to solve this problem. The discontinuities are removed from the recorded phase map in a process called 'unwrapping'. The discontinuities in the recorded phase map are removed by using a radial search process to map the variations of the order of interference across the image plane as a continuous paraboloidal surface. The right panel in Figure A.8 shows such an example. This unwrapped paraboloidal phase map can then be freely scaled to a new wavelength. The result is then 'wrapped' back to the discontinuous form in order to use it to acquire spectra at new wavelength. For in-depth details, the reader is referred to *Conde and Smith* [1997] and *Anderson* [2011].

A.6 Zone Mapping

Each pixel on the detector acts as a tiny independent detector collecting a small amount of airglow photons per unit time. However, each pixel will not accumulate enough airglow photons to achieve an adequate signal to noise ratio in a reasonable amount of time. Also, the entire 512×512 pixel resolution is far higher than needed to describe the angular variation of spectra across the sky. We, therefore, trade angular resolution for improved spectral signal to noise ratio by grouping contiguous sets of pixels into software-defined regions known as "zones". This process is implemented using a "zone map" which is a two-dimensional look-up table defined in software. For each pixel on the detector, it specifies which zone that pixel belongs to. Because the etalon scanning and phase mapping technique discussed in above section shifts the response all pixels to a common phase, we

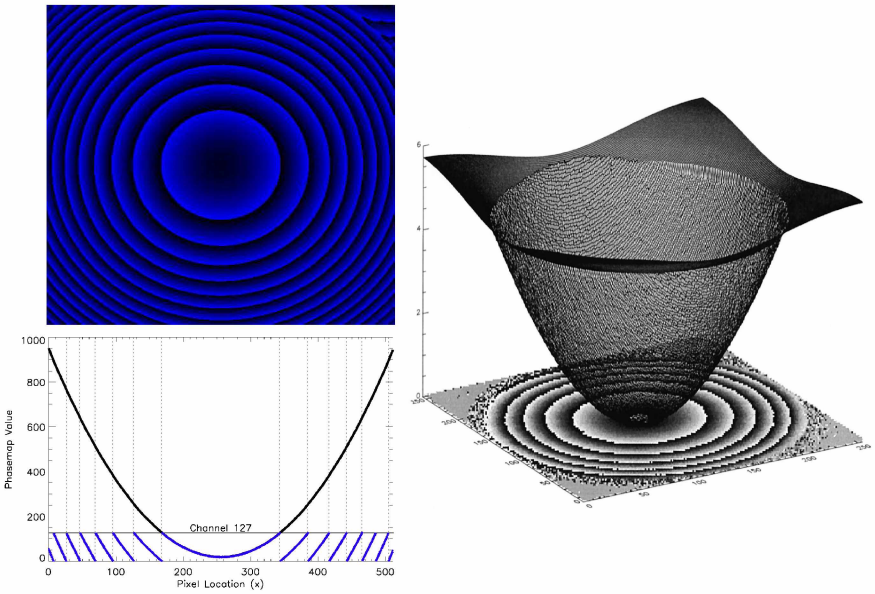

Figure A.8: Example phase map from *Anderson* [2011] (left) and *Conde and Smith* [1997] (right). The top panel of the left shows phase map recorded by instrument located at Mawson, Antarctica. Light colors correspond to higher values of phase and dark color to lower values. Bottom panel of left shows cross-section through the phase map (blue lines). The black line corresponds to the cross-section through paraboloid surface (shown in right) fitted to remove discontinuities in phase map across the image plane. In the right image, the original phase map is projected onto a horizontal plane. The horizontal axes are in the units of pixel number, and the vertical axis is the order of interference. The paraboloidal surface represents a map of the variation of the order of interference across the image plane for fixed plate spacing.

may co-add spectra from any subset of pixels (in particular, the subsets that correspond to our zones) to produce spectra with higher signal/noise ratio without introducing any loss of spectral resolution.

In our studies discussed in chapter 3 to 5, a zone map configuration as shown in Figure A.9 (left subset) was used. This zone pattern is our "standard" observing mode. It is configured such that the detector area is divided into eight concentric annular rings of equal radial width with one, six, eight, twelve, sixteen, twenty, twenty-four, and twenty-eight sectors respectively in each ring. The areas on the detector of all the zones so defined

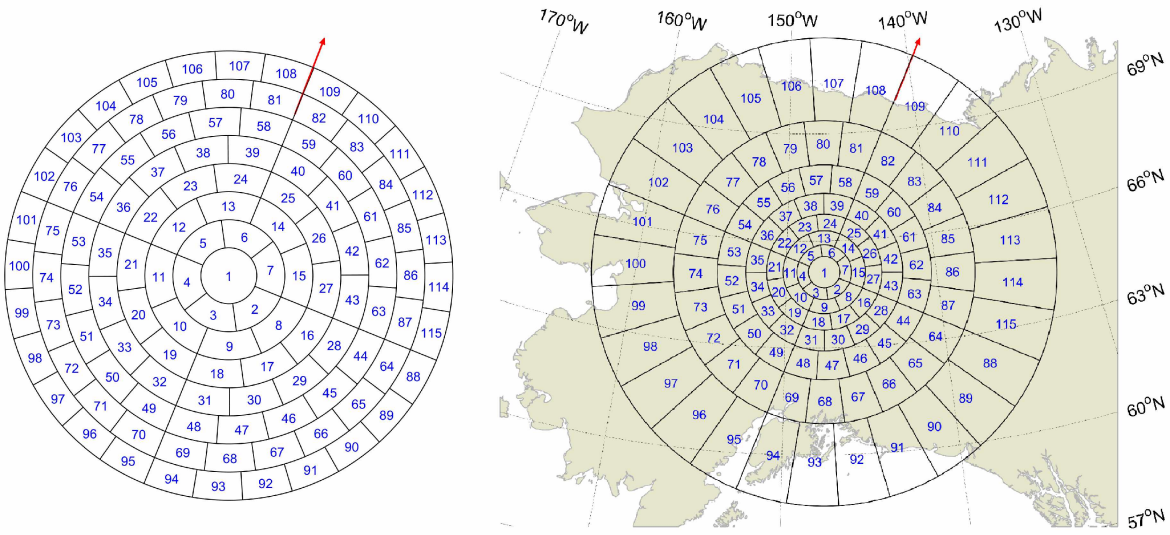

Figure A.9: Left panel shows the division of detector area into 115 zones. The right panel shows same zone map (as shown in left panel) projected onto the sky at ∼240 *km* altitude over Alaska (as viewed by a space-based observer). The center of phase map is at the zenith of Poker Flat and with the field of view of ∼72 degrees. The red arrow in both panels points toward the geomagnetic north.

are roughly (but not exactly) equal. The total number of zones is 115. The 115 final spectra recorded by the instrument are co-added spatially from all pixels within each zone.

The zone allocation occurred entirely in software, and could easily be changed as desired. The selection of number of zones is also entirely in our hands. There is always a trade-off between temporal and spatial resolution. We can increase the number of zones by reducing the number of pixels in each zone to increase the spatial resolution, but this would also decrease the amount of light intercepted by each zone per unit time. A balance between these two is maintained by choosing 115 numbers of zones; it works out to be a good trade-off in practice. The 115 zone map scheme works well for accumulating 630 *nm* and 577.7 *nm* spectra because these airglow emissions are very bright. However, for other fainter airglow emissions, zones this small may not accumulate airglow photons fast enough to achieve adequate signal to noise ratio in a reasonable amount of time. In our study discussed in appendix B, we studied very faint hydroxyl emissions (∼100 Rayleigh) from the mesopause. To obtain an adequate signal spectrum from each zone in

a reasonable time (10 *min*), a zone map divided into only 43 zones was used.

A.7 Spectral Accumulation

As discussed in the etalon scanning section, the etalon is piezoelectrically scanned over one order of interference in 128 steps. A complete scan typically takes around 23 seconds to complete. Each zone records its own spectra. Once phase and zone maps are consulted, each individual observation (exposure) is obtained by repeating multiple relatively rapid scans of the etalon, and co-adding the spectra obtained from each of these scans. Control software monitors the accumulating spectra during the exposure, and continues signal integration until the adequate signal to noise ratio is reached (on the average) across all zones. It also enforces a minimum number of scans per exposure to 4 scans under active auroral conditions and a maximum of 26 scans (takes around 10 *min*) during quiet conditions. An example of the spectra obtained from a single 630 *nm* airglow exposure is shown in Figures A.10 and A.11.

The real benefit of scanning FPS is that it resolves the ambiguity in non-scanned fringe images. Brightness at each pixel depends on three quantities - two angular coordinates and wavelength. A single static image (as recorded by traditional FPIs) only resolves variation in two dimensions and so must be ambiguous. Adding the scan introduces a third parameter and allows the ambiguity to be resolved.

A scanning FPS does not record continuous spectra. Discrete samples of the spectrum are obtained by scanning the etalon passband in wavelength and measuring the received intensity at each step. Any possible distortions due to spatial gradients in intensity across the sky are suppressed by co-adding a large number of short duration scans during each integration interval. On the other hand, the fixed plate etalon forms static fringes that are optically conjugate with the sky. The derived spectra from static fringe patterns are susceptible to distortions because of the modulation of static fringes in the presence of auroral intensity gradients across the sky.

The interference pattern recorded by the detector during each scan step is the modulated sky image in the form of interference fringes. Since the etalon scans over one order of interference, the interference fringes will sweep across every pixel in the field of view

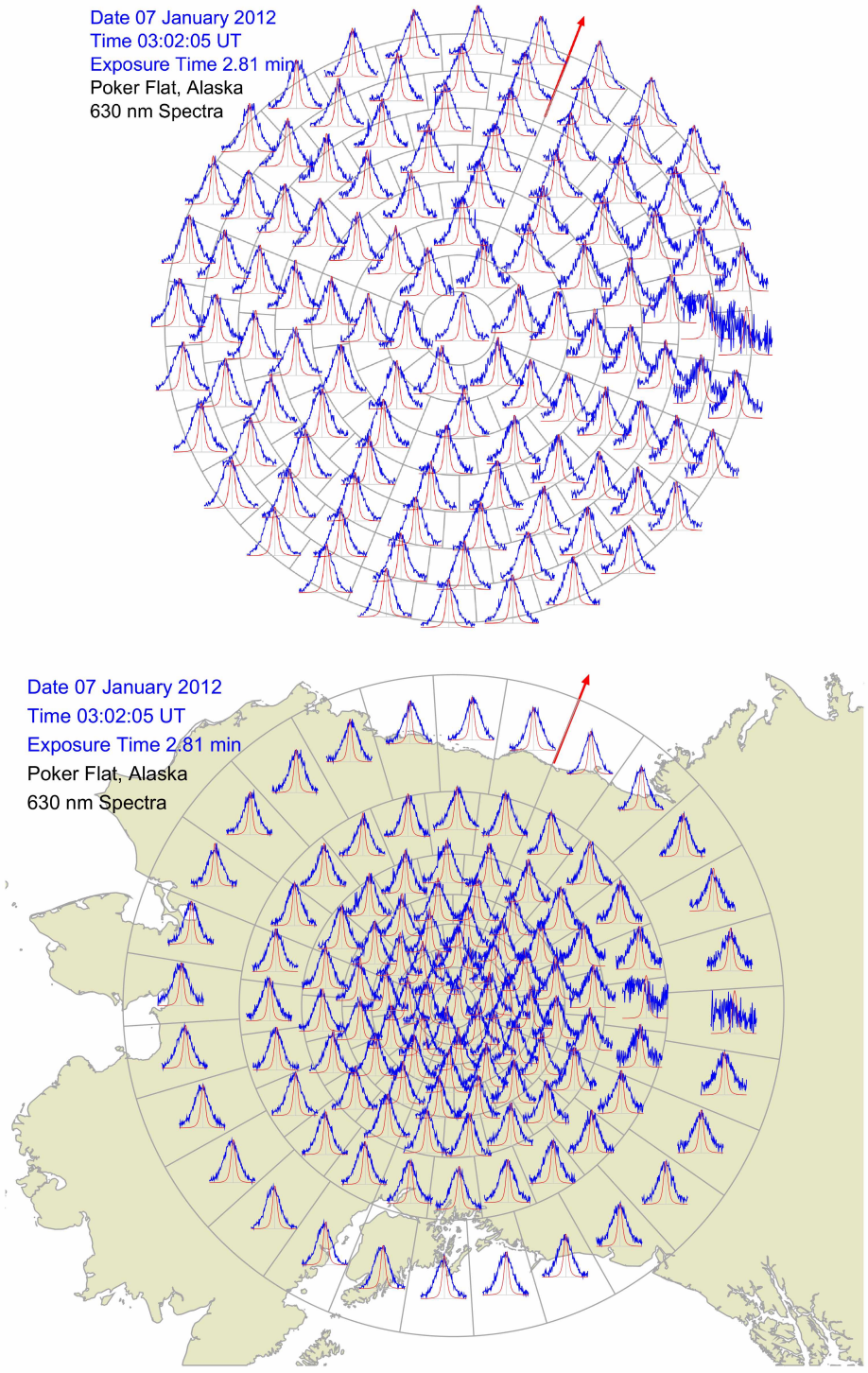

Figure A.10: Top panel shows normalized sky (blue) and calibration laser (red) spectra recorded at various zones on 07 January 2012. Bottom panel shows normalized sky and laser spectra when zone map is projected at 630 *nm* emission layer altitude ∼240 *km* (as viewed by a space-based observer). These spectra are obtained after an exposure of 2.81 *min*. The red arrow in each panel points toward the geomagnetic north. The distortion in the spectra in the zones on the right is due to contamination by moonlight.

over the course of a scan. If we combine all the interference images recorded by the detector during a complete scan, it will produce an unmodulated monochromatic image of the sky. While this product is not directly useful for Doppler spectroscopy, it does give an image of the auroral brightness over the same field of view and time interval that prevailed while the spectra were acquired, and so is useful as a supporting observation.

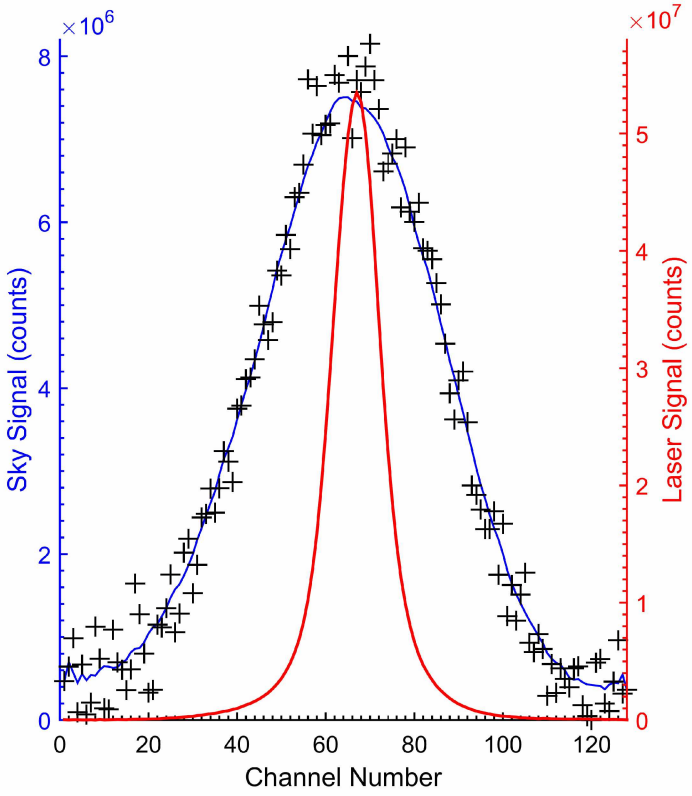

Figure A.11: Sky and laser spectrum from central zone (zone number 0) obtained on 07 January 2012. The crosses correspond to the observed sky spectrum, the blue curve is the smoothed sky spectrum, and the red curve is the laser spectrum.

A.8 Spectral Fitting of Emission Spectra

To produce estimates of Doppler shift and Doppler width, emission intensity and continuum background, the recorded spectra are fitted by an analytical function. The recorded spectra are (both sky and calibration laser) are subject to instrumental broadening due to the finite spectral passband of the instrument. The function that characterizes this broadening by the instrument is referred to as instrument function and denoted by

symbol I. It is calculated from the recorded laser spectrum. The comprehensive details of the spectral fitting algorithm used to fit observed emissions spectra are given in *Conde et al.* [2001]. The algorithm given in *Conde et al.* [2001] was basically developed for fitting Lidar backscatter spectra for which the signal was obtained by backscatter of a laser pulse, and there were contributions due to both aerosol and molecular scattering by several molecular species. Here we are only interested in a single "molecular" species, and the signal comes from passive emission rather than active backscatter. A brief discussion of *Conde et al.* [2001] algorithm in is given here.

As discussed in the etalon scanning section, a spectral scan is completed in a number of Q (=128) steps. At the end of each scan, we obtain a set of values $\{y_q\}$ which is the recorded spectrum. Here q varies from 0 to Q-1. The fitting algorithm models the recorded spectrum $\{y_q\}$ as a set of Q samples $\{s_q\}$ of the form:

$$s(\lambda) = \sum_{j=0}^{2} a_j S_j(\lambda) \tag{A.22}$$

where the coefficients a_j are the intensity of each of the three source terms $S_j(\lambda)$ and

$$S_o(\lambda) = 1 \qquad \textit{Continuum background} \tag{A.23}$$

$$S_1(\lambda) = I(\lambda) * \delta(\lambda - \lambda_o) \qquad \textit{Aerosol} \tag{A.24}$$

$$S_2(\lambda) = I(\lambda) * \sum_{k=0}^{K-1} q_k \, exp\left(- \left(\frac{\lambda - \lambda_o}{w_k(T)} \right)^2 \right) \quad \textit{Rayleigh backscattering} \tag{A.25}$$

$$\textit{contribution from K molecular species}$$

where $*$ denotes the convolution operator. Here $S_o(\lambda)$, $S_o(\lambda)$, and $S_o(\lambda)$ are the "basis functions" for the fitting function. $w_k(T)$ is the width of emission profile in wavelength units for the *kth* species which is a function of kinetic temperature (T). λ_o is the Doppler shifted peak wavelength of the emitting species moving with background. q_k are the predetermined relative contribution to the backscattering from *kth* molecular species, with the property

$$\sum_{k=0}^{K-1} q_k = 1 \tag{A.26}$$

So, total five parameters a_o, a_1, a_2, λ_o, and T are needed for fitting function.

In the case of FPIs, the signal comes from passive emission rather than active backscatter. This means, the aerosol term which describes the backscattering of radiations by aerosols, is not required and a_1 can be set to zero. Also, we measure airglow from only single atomic oxygen species, therefore $K = 1$ and $q_{k=0} = 1$. Thus Equation A.22 can be rewritten as:

$$s(\lambda) = a_o + I(\lambda) * a_2 \, exp\left(- \left(\frac{\lambda - \lambda_o}{w_k(T)} \right)^2 \right) \tag{A.27}$$

Then a conventional parameter χ^2 is used to find the degree to which the fitting model spectrum $\{s_q\}$ departs from the recorded spectrum $\{y_q\}$ and is given by:

$$\chi^2 = \sum_{q=0}^{Q-1} \frac{(y_q - s_q)^2}{\sigma_q^2} \tag{A.28}$$

where σ_q^2 is the variance of the qth element of the observed spectrum (y_q). The parameters $p = \{a_o, a_2, \lambda_o, T\}$ are selected such that they yield minimum χ^2. The best choice for $\{p_j\}$ should satisfy:

$$\frac{\partial \chi^2}{\partial p_j} = 0 \tag{A.29}$$

The algorithm solves analytically for a_o and a_2 while searching for best choices of λ_o and T.

A.9 Drift Correction

The above discussed spectral fitting algorithm provides the estimated 'peak positions' of the spectra in terms of channel numbers (between 0 and 127). The peak positions are calculated with respect to the first recorded calibration spectrum of the night for the corresponding zone. Since the phase map is only recorded at the beginning of the observation cycle of the night, any change in the plate separation (t) will bring change in the interference order of fringes on the detector. Therefore, any change in plate separation will change the peak positions of the spectra. Any 'drift' in the etalon plates (for example produced by thermal expansion of etalon components in response to variations in the ambient temperature) can be tracked by monitoring the peak positions of the calibration laser source spectra (assuming the laser itself is stable in wavelength throughout the entire night).

Suppose $M_L(z,T)$ is the laser peak position for zone $z(0z115)$ at time T and $M_L(z,T_o)$ is the first laser peak position of the night for zone z. Then the drift in laser peak position for zone z at time T is:

$$D(z,T) = M_L(z,T) - M_L(z,T_o) \tag{A.30}$$

The drift in sky spectra positions are corrected by subtracting drift $D(z,T)$ from the sky spectra peak positions. Since the drift $D(z,T)$ is valid for calibration laser source wavelength (say λ_o), it must be scaled before applying to the sky spectra obtained at wavelength λ. The drift corrected sky spectra peak positions are given by:

$$M_{sky\ corrected}(z,T) = M_{sky}(z,T) - D(z,T) \times \frac{\lambda_o}{\lambda} \tag{A.31}$$

A.10 Line-of-sight Wind Determination

To extract the line-of-sight (LOS) wind speed information from the drift corrected spectral peak positions, a reference peak position corresponding to zero Doppler shift (or zero Doppler baseline) is required. Zero Doppler baseline can be calculated from a stationary laboratory source emitting at the same wavelength at which observations from the sky are made. However, in the absence of a convenient laboratory source, zero Doppler baseline is obtained by using the spectra recorded from the station zenith (zone number 0). It is based on the assumption that the average vertical wind over the entire night is 0 $m.sec^{-1}$. The median of the drift corrected zenith peak position time series can be used as zero Doppler shift baseline. This median peak position value is then subtracted from the drift corrected peak positions from all zones.

According to the Doppler formula, changes in observed wavelength are related to changes in the speed (LOS wind speed) of the emitting source by

$$\Delta v = c\,\frac{\lambda - \lambda_o}{\lambda_o} \tag{A.32}$$

where λ_o is the wavelength of stationary source and λ is the wavelength when source is moving. Since the etalon scan is performed over one order of interference in 128 steps, this means the recorded spectra span one free spectral range in 128 channels. The nominal gap in etalon plates for all-sky SDI at Poker and Gakona is 18.6 mm. The wavelength span

of one free spectral range for normal incidence is (from Equation A.7)

$$\Delta\lambda = \frac{\lambda_o^2}{2\mu t} = \frac{(630 \times 10^{-9} m)^2}{2 \times 1 \times 18.6 \times 10^{-3} m} = 10.7 \times 10^{-12} m \tag{A.33}$$

μ=1 for air. $10.7 \times 10^{-12} m$ is the largest shift in 630 nm wavelength that can be resolved using an etalon with 18.6 mm gap. The shift in wavelength corresponding to the peak position $M_{sky\ corrected}(z, T)$ is:

$$\lambda - \lambda_o = \frac{10.7 \times 10^{-12} m}{128} \times M_{sky\ corrected}(z, T) \tag{A.34}$$

To calculate the Doppler LOS wind speed corresponding to the peak position $M_{sky\ corrected}(z, T)$, plug Equation A.34 into A.32:

$$\Delta v = 3 \times 10^8 \frac{m}{sec} \frac{10.7 \times 10^{-12} m}{128 \times 630 \times 10^{-9} m} \times M_{sky\ corrected}(z, T) = 39.8 \frac{m}{sec} M_{sky\ corrected}(z, T) \tag{A.35}$$

Equation A.35 is used to calculate the Doppler LOS wind speeds using drift corrected peak positions.

A.11 Vector Wind Fitting

The drift corrected Doppler LOS wind (derived in upper section) is a component of what is, in reality, a three component vector wind field. From a single LOS wind measurement from each zone of the sky spectrum, it is not possible to infer all the three components of the actual wind vector. However, by using some assumptions, it is possible to construct a horizontal vector wind field from every sky exposure. A vector wind fitting method (called monostatic wind fit) discussed in *Conde and Smith* [1998] is applied to construct two-dimensional vector wind field from a single station LOS wind data. This method is based on the wind estimation technique discussed in *Burnside et al.* [1981]. A brief discussion of the monostatic wind fit is given below. Figure A.12 shows the example zone map with total 115 zones. Each annulus of the zone map is centered about the station zenith. Zones are defined by the radius and centered on azimuthal angle θ_k. The radius of each annulus is given by zenith angle ϕ. The azimuthal angle θ_k is clockwise angle between $y - axis$ and horizontal projection of the LOS wind (shown in Figure A.12). The positive x and y directions are along the zonal and meridional directions respectively.

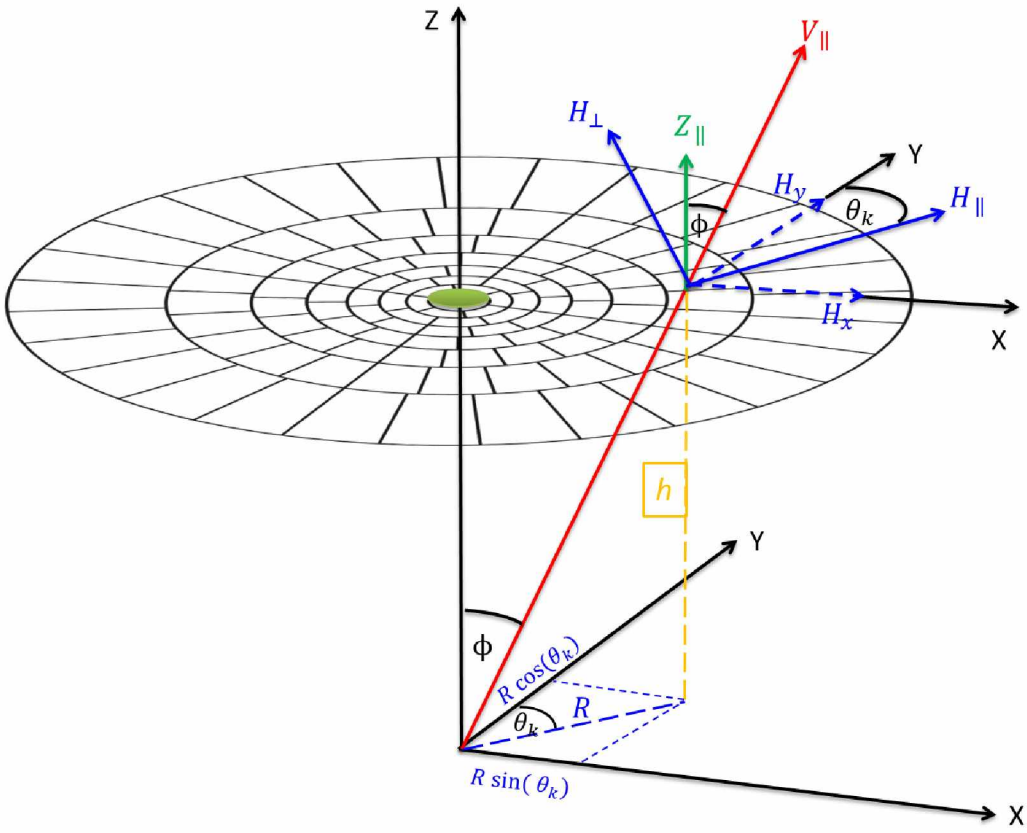

Figure A.12: Schematic layout of angles and vectors components used in the monostatic fitting algorithm. The details of angles and vectors components shown here is given in text.

Let $\{V_{\|}(\theta_k,\phi)\}$ be the set of LOS winds for a single exposure. The observed LOS wind by instrument is the combination of component of vertical wind ($Z_{\|}(\theta_k,\phi)$) and horizontal wind ($H_{\|}(\theta_k,\phi)$) along the LOS. Thus:

$$V_{\|}(\theta_k,\phi) = Z_{\|}(\theta_k,\phi)\,cos(\phi) + H_{\|}(\theta_k,\phi)\,sin(\phi) \tag{A.36}$$

The first assumption used in monostatic wind fit is that the vertical wind is constant across the entire region of sky viewed by the instrument. The LOS wind measured at central zone (station zenith) is the direct measure of the vertical wind.

$$Z_{\|}(\theta_k,\phi) = V_z = V_{\|}(\theta_1,0) \tag{A.37}$$

Now solving Equation A.36 for $H_{\|}(\theta_k, \phi)$ yields:

$$H_{\|}(\theta_k, \phi) = \frac{V_{\|}(\theta_k, \phi)\, cos(\phi) - V_z\, cos(\phi)}{sin(\phi)} \tag{A.38}$$

Since $V_{\|}(\theta_k, \phi)$ is known for every zone, $H_{\|}(\theta_k, \phi)$ can be directly calculated from it for every zone. The directly calculated $H_{\|}(\theta_k, \phi)$ preserves all of the features of the measured line-of-sight wind field. The horizontal wind velocity component parallel to the instruments LOS in *kth* azimuthal sector can be written in zonal and meridional components by:

$$H_{\|}(\theta_k, \phi) = H_x\, sin(\theta_k) + H_y\, cos(\theta_k) \tag{A.39}$$

where H_x and H_y denotes the spatially varying zonal and meridional wind fields. The total horizontal vector wind field is approximated by using first-order Taylor series expansion about the zonal and meridional components about the station zenith:

$$H_x = u_o + \left(\frac{\partial u}{\partial x}\right) x + \left(\frac{\partial u}{\partial y}\right) y \tag{A.40}$$

$$H_y = v_o + \left(\frac{\partial v}{\partial x}\right) x + \left(\frac{\partial v}{\partial y}\right) y \tag{A.41}$$

where x and y are the zonal and meridional distances from the station zenith to an observing zone located at (θ_k, ϕ). These horizontal distances from the origin to the location (θ_k, ϕ) can be written in terms of radial distance $R = h\, tan(\phi)$ by:

$$x = R\, sin(\theta) \tag{A.42}$$

$$y = R\, cos(\theta) \tag{A.43}$$

where h is the altitude of the emission layer. Plugging Equations A.40 to A.43 in Equation A.39 gives:

$$\begin{aligned} H_{\|}(\theta_k, \phi) = {} & u_o\, sin(\theta_k) + \left(\frac{\partial u}{\partial x}\right) R\, sin^2(\theta_k) + \left(\frac{\partial u}{\partial y}\right) R\, cos(\theta_k)\, sin(\theta_k) \\ & + v_o\, cos(\theta_k) + \left(\frac{\partial v}{\partial x}\right) R\, cos(\theta_k)\, sin(\theta_k) + \left(\frac{\partial v}{\partial y}\right) R\, cos^2(\theta_k) \end{aligned} \tag{A.44}$$

Using trigonometric identities:

$$sin(\theta)\, cos(\theta) = \frac{1}{2}\, sin(2\theta) \tag{A.45}$$

$$sin^2(\theta) = \frac{1}{2} - \frac{1}{2} cos(2\theta) \tag{A.46}$$

$$cos^2(\theta) = \frac{1}{2} + \frac{1}{2} cos(2\theta) \tag{A.47}$$

Plug in above identities into Equation A.44:

$$\begin{aligned} H_{\parallel}(\theta_k, \phi) = {} & u_o \, sin(\theta_k) + \left(\frac{R}{2}\right)\left(\frac{\partial u}{\partial x}\right)(1 - cos(2\theta_k)) + \left(\frac{R}{2}\right)\left(\frac{\partial u}{\partial y}\right) sin(2\theta_k) \\ & + v_o \, cos(\theta_k) + \left(\frac{R}{2}\right)\left(\frac{\partial v}{\partial x}\right) sin(2\theta_k) + \left(\frac{R}{2}\right)\left(\frac{\partial v}{\partial y}\right)(1 + cos(2\theta_k)) \end{aligned} \tag{A.48}$$

The observed horizontal LOS wind can be represented as a Fourier series expansion in θ_k:

$$H_{\parallel}(\theta_k, \phi) = a_o + \sum_{m=1}^{\frac{n}{2}-1} (a_m \, cos(m\theta_k) + b_m \, sin(m\theta_k) \tag{A.49}$$

where coefficients a_o, a_m, and a_o are given by:

$$a_o(\phi) = \frac{1}{n} \sum_{k=0}^{n-1} H_{\parallel}(\theta_k, \phi) \tag{A.50}$$

$$a_m(\phi) = \frac{2}{n} \sum_{k=0}^{n-1} H_{\parallel}(\theta_k, \phi) \, cos(m\theta_k) \tag{A.51}$$

$$b_m(\phi) = \frac{2}{n} \sum_{k=0}^{n-1} H_{\parallel}(\theta_k, \phi) \, sin(m\theta_k) \tag{A.52}$$

Comparing the coefficients of Equations A.49 and A.48:

$$a_o = \frac{R}{2}\left(\frac{\partial u}{\partial x} + \frac{\partial v}{\partial y}\right) \tag{A.53}$$

$$a_1 = v_o \tag{A.54}$$

$$b_1 = u_o \tag{A.55}$$

$$a_2 = \frac{R}{2}\left(\frac{\partial v}{\partial y} - \frac{\partial u}{\partial x}\right) \tag{A.56}$$

$$b_2 = \frac{R}{2}\left(\frac{\partial u}{\partial y} + \frac{\partial v}{\partial x}\right) \tag{A.57}$$

The series $\{H_{\parallel}(\theta_k, \phi)\}$ is calculated from Equation A.38 and the Fourier coefficients are calculated directly from it . This means at this stage, a_0, a_1, a_2, b_1, and b_2 are known. The background uniform wind field u_o and v_o are given directly by Equations A.54 and A.55 respectively. Now we have only three equations (A.53, A.56, and A.57) and four

unknowns (four partial derivatives). This means the LOS wind data from a single exposure of the instrument is not sufficient to calculate all the terms in the two Taylor series (Equations A.40 and A.41) and hence cannot determine the zonal and meridional wind components. It also means that both divergence ($\frac{\partial u}{\partial x} + \frac{\partial v}{\partial y}$) and vorticity ($\frac{\partial v}{\partial x} - \frac{\partial u}{\partial y}$) cannot be computed simultaneously from a single exposure [*Conde and Smith*, 1998].

In order to solve three equations, the assumption made in this work is that during a single exposure, the geomagnetic meridional winds does not vary much along the geomagnetic zonal direction which means we can set $\frac{\partial v}{\partial x} = 0$. This assumption is based on the analysis done in by *Burnside et al.* [1981]. He assumed that the meridional wind field is stationary in local time. Any variation in the meridional wind field is due to the rotation of the Earth moving the station underneath this wind field. In the auroral zone, wind fields are highly dynamical, and the zonal winds dominate most of the time. Although, this approximation will not always stand valid, our experience has shown that the meridional component along the zonal direction is least variable component compared to the others.

Substitute assumed $\frac{\partial v}{\partial x} = 0$ in Equation A.57 and solve for other gradients terms to get:

$$
\begin{aligned}
u_o &= b_1 \\
v_o &= a_1 \\
\frac{\partial v}{\partial x} &= 0 \\
\frac{\partial u}{\partial x} &= \left(\frac{a_o - a_2}{R}\right) \\
\frac{\partial u}{\partial y} &= \frac{2b_2}{R} \\
\frac{\partial v}{\partial y} &= \left(\frac{a_o + a_2}{R}\right)
\end{aligned}
$$

Now we have estimated the total horizontal wind field component parallel to the LOS. To estimate the total horizontal wind at each observation location, the estimated parallel component is to be added to the modelled perpendicular component. The perpendicular component can be easily constructed using estimated zonal and meridional components by:

$$H_{\perp}(\theta_k, \phi) = H_x \cos(180 - \theta_k) + H_y \cos(90 - \theta_k)$$

$$H_{\perp}(\theta_k, \phi) \;=\; H_y \; sin(\theta_k) \;-\; H_x \; cos(\theta_k) \tag{A.58}$$

Note that H_x and H_y components are calculated only to model perpendicular compo-

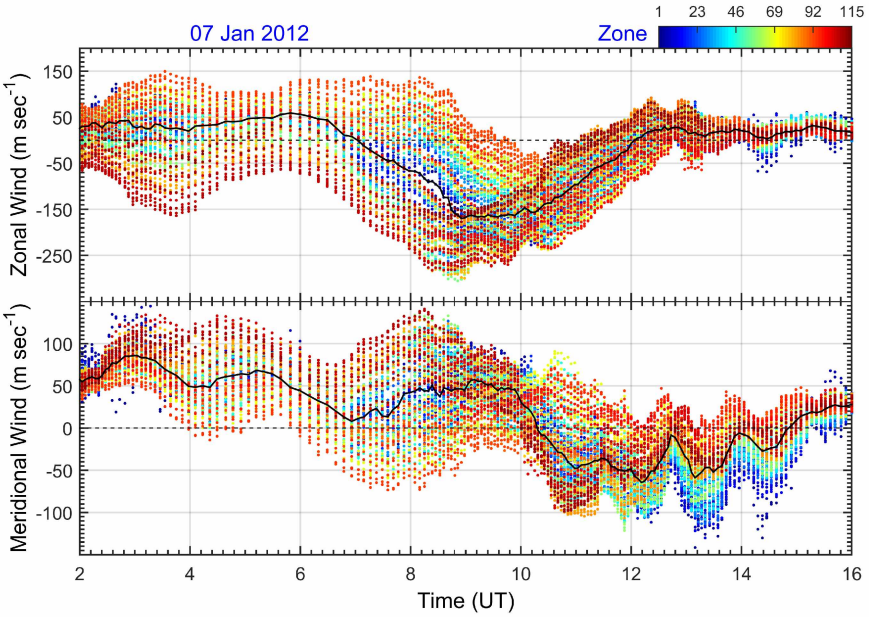

Figure A.13: An example of the F-region geographic zonal and meridional winds estimated using the monostatic wind fit analysis for the night of the 07 January 2012. The estimated wind components from different zone are assigned different colors. Each value in the black curve corresponds to the median wind component calculated from all 115 zones that contribute to a single exposure. The wind components presented here are derived using data from the SDI located at Poker Flat.

nent. Now, we have two components of the actual horizontal wind field: one is directly measured $H_{\parallel}(\theta_k, \phi)$ from the LOS wind which includes all of the features of the measured LOS wind field, and the other is modelled perpendicular component $H_{\perp}(\theta_k, \phi)$. By combining these two components, finally we can construct the "best estimates" of the zonal ($HH_x(\theta_k, \phi)$) and meridional components ($HH_y(\theta_k, \phi)$)of the actual wind field. Using the geometry presented in Figure A.12, the best estimates of the zonal and meridional components of the actual wind field are:

$$HH_x(\theta_k, \phi) \;=\; H_{\parallel}(\theta_k, \phi) \; sin(\theta_k) \;-\; H_{\perp}(\theta_k, \phi) \; cos(\theta_k) \tag{A.59}$$

$$HH_y(\theta_k, \phi) \;=\; H_{\parallel}(\theta_k, \phi)\, cos(\theta_k) \;+\; H_{\perp}(\theta_k, \phi)\, sin(\theta_k) \tag{A.60}$$

Note that it is not possible to fit vector horizontal wind in the central zone because we need at least four sectors in an annulus to at least estimate background terms (u_o and v_o) and six sectors in an annulus to estimate partial derivatives (refer to Equation A.49). So, we assign mean of the horizontal vector components calculated across the entire FOV to the central zone.

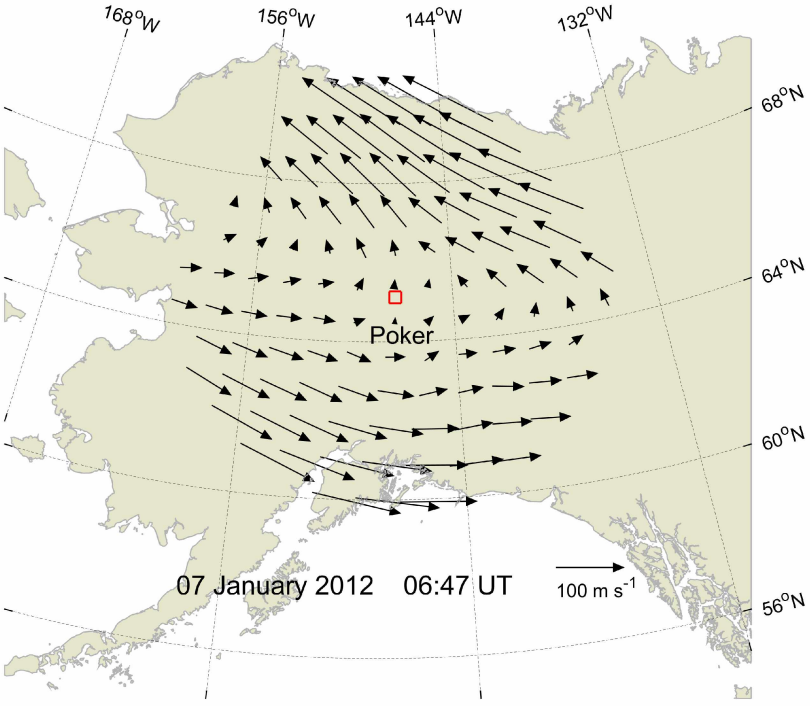

Figure A.14: An example of the spatially resolved horizontal vector wind field at F-region altitude, projected onto a geographic map of Alaska. The shown vector wind field is derived the exposure taken at 06:47 UT on 07 January 2012 by the SDI located at Poker Flat.

Figure A.13 shows an example of the F-region zonal and meridional winds estimated using the monostatic wind fit analysis for the night of the 07 January 2012.The estimated wind components (zonal and meridional) from each zone are color coded. Each value in the black curve corresponds to the median wind component calculated from all 115 zones that contribute to a single exposure. Figure A.14 shows an example of the spatially resolved horizontal vector wind field at F-region altitude.

A.12 References

Anderson, C. (2011), Optical remote sensing of local-scale thermospheric dynamics above Antarctica, *Thesis*.

Anderson, C., M. Conde, and M. G. McHarg (2012), Neutral thermospheric dynamics observed with two scanning Doppler imagers: 1. Monostatic and bistatic winds, *J. Geophys. Res. Sp. Phys.*, *117*(A3), A03,304, doi: 10.1029/2011ja017041.

Babcock, H. D. (1923), A study of the green auroral line by the interference method, *Astrophys. J.*, *57*, 209, doi: 10.1086/142747.

Burnside, R. G., F. A. Herrero, J. W. Meriwether, and J. C. G. Walker (1981), Optical observations of thermospheric dynamics at Arecibo, *J. Geophys. Res. Sp. Phys.*, *86*(A7), 5532–5540, doi: 10.1029/JA086iA07p05532.

Conde, M., and R. W. Smith (1995), Mapping thermospheric winds in the auroral zone, *Geophys. Res. Lett.*, *22*(22), 3019–3022, doi: 10.1029/95GL02437.

Conde, M., and R. W. Smith (1997), Phase compensation of a separation scanned, all-sky imaging Fabry Perot spectrometer for auroral studies, *Appl. Opt.*, *36*(22), 5441–5450, doi: 10.1364/AO.36.005441.

Conde, M., and R. W. Smith (1998), Spatial structure in the thermospheric horizontal wind above Poker Flat, Alaska, during solar minimum, *J. Geophys. Res.*, *103*(A5), 9471–9949, doi: 10.1029/97JA03331.

Conde, M., J. D. Craven, T. Immel, E. Hoch, H. Stenbaek-Nielsen, T. Hallinan, R. W. Smith, J. Olson, W. Sun, L. A. Frank, and J. Sigwarth (2001), Assimilated observations of thermospheric winds, the aurora, and ionospheric currents over Alaska, *J. Geophys. Res. Sp. Phys.*, *106*(A6), 10,493–10,508, doi: 10.1029/2000JA000135.

Conde, M. G., and M. J. Nicolls (2010), Thermospheric temperatures above Poker Flat, Alaska, during the stratospheric warming event of January and February 2009, *J. Geophys. Res. Atmos.*, *115*(D3), D00N05, doi: 10.1029/2010jd014280.

Hernandez, G. (1986), *Fabry-Perot Interferometers*, Cambridge Studies in Modern Optics, 360 pp., Cambridge University Press.

Jacka, F. (1985), Application of Fabry-Perot spectrometers for measurement of upper atmosphere temperatures and winds, *Int. Counc. Sci. Unions Middle Atmos. Handb.*, *13*, 19–40.

Shepherd, G. G. (2002), *Spectral Imaging of the Atmosphere*, vol. 82, 304 pp., Academic Press; 1 edition (August 20, 2002).

Vaughan, J. M. (1989), *The Fabry-Perot Interferometer: History, Theory, Practice and Applications (Optics & Optoelectronics)*, 86-20, 604 pp., Taylor & Francis Group.

Appendix B
Mesopause Temperature and Wind Determination Using Hydroxyl Nightglow Over Alaska by All-sky Scanning Doppler Imaging

B.1 Introduction

Neutral hydroxyl (OH) molecules are a minor constituent of Earth's lower and middle atmosphere. They are produced chemically in excited quantum states which are short-lived (metastable with a lifetime 10^{-3} *sec*) and collisionally deactivated or quenched at the altitudes below mesopause. But at the mesopause and above, the collision frequency is low enough that a significant fraction of the excited OH molecules survives long enough to undergo radiative relaxation and thus form an airglow layer. The mean altitude of OH airglow emissions layer is 87 *km* with a mean thickness of 8 *km* centered at the mesopause [*Baker and Stair*, 1988; *Offermann and Gerndt*, 1990; *Sivjee*, 1992; *Zhang and Shepherd*, 1999; *Liu and Shepherd*, 2006; *French and Mulligan*, 2010].

At the mesopause, the major constituents are N_2 and O_2 which together comprise 99% of the local number density; OH is only 10^{-9} of this. Despite being a minor constituent, OH is widely used as a mesospheric tracer. OH nightglow measurements in the Meinel band are extensively used as tools to study temperatures and dynamical processes such as gravity waves, planetary waves, and tides occurring at the mesopause height [*Takahashi et al.*, 1974; *Armstrong*, 1975; *Meriwether*, 1975; *Myrabø*, 1986; *Offermann and Gerndt*, 1990; *Sivjee*, 1992; *Hernandez et al.*, 1992a,b, 1993; *Hernandez and Roble*, 1995; *Fraser et al.*, 1993; *Scheer et al.*, 1994; *East et al.*, 1995; *Bittner et al.*, 2000]. The mesopause is the coldest part of the Earth's atmosphere, and a few modeling studies [e.g., *Roble and Dickinson*, 1989; *Golitsyn et al.*, 1996] have indicated that any increase in greenhouse gasses in the troposphere may enhance cooling of the already very cold upper mesosphere. This is due to the low collision frequency at high altitudes which cause greenhouse gasses to radiate the absorbed energy to space instead colliding with other atmospheric species and re-distributing the absorbed energy as heat. Thus, a long term monitoring of the mesospheric OH temperature may provide an indication of changes in the global greenhouse

gasses content in the troposphere. Many modeling studies have predicted that the impact of increases in greenhouse gasses would be stronger at high latitude mesosphere than at lower latitudes [*Roble and Dickinson*, 1989; *Rind et al.*, 1990; *Portmann et al.*, 1995; *Akmaev and Fomichev*, 1998, 2000]. The mesosphere is considerably hotter in winter than in summer. Its temperature varies between $\sim$150 *K* in summer to $\sim$250 *K* in winter. Noctilucent clouds forms around the same height as the mesopause and it is believed that the OH chemistry at polar latitudes plays an important role in their formation when temperatures fall to $\sim$150 *K* in summer. A study by *Thomas* [1996] showed that with increasing greenhouse gasses, increasing water vapor content and decreasing temperatures are expected to occur at upper mesospheric heights. There are various other properties that make OH an excellent mesospheric tracer, for example, determination of the atomic oxygen, ozone, and atomic hydrogen in the upper mesosphere that are very difficult to measure by other methods [*Sivjee*, 1992].

OH nightglow (vibrational-rotational emissions lines) which results from the exothermic hydrogen-ozone reaction, occurs in a number of bands. The intensity of each line in a band is very weak ($\sim$100 *Rayleigh*) which makes it hard to observe at high time resolution with an adequate signal to noise ratio for determining atmospheric parameters. The full description and nomenclature of OH emissions lines are given by [*Osterbrock and Martel*, 1992; *Osterbrock et al.*, 1996]. Out of various Meinel bands, 731 *nm* in the (8-3) band and 843 *nm* in the (6-3) band are the two most studied emission lines of OH nightglow. The 843 *nm* line emission brightness is approximately four times than that of the (8-3) band.

These emissions have long provided a well-established means of temperature measurements of the upper mesosphere. The most common technique of measuring OH rotational temperature is by comparing the emission intensities of two or more emission lines emitted by the transition between two different vibrational-rotational states of OH molecules. This approach is based on an assumption that the excited OH molecules are in thermal equilibrium with surrounding, and the rotational temperature of OH can be interpreted as kinetic atmospheric temperature. This technique has been used in many studies in both the southern and northern hemispheres [*Sivjee et al.*, 1987; *Scheer and Reisin*, 1990; *Scheer et al.*, 1994; *Takahashi et al.*, 1994; *Mulligan et al.*, 1995; *French et al.*, 2000; *In-*

nis and Conde, 2001; *Greet et al.*, 2002; *French and Klekociuk*, 2011]. Here, for measuring mesopause temperature, we used the Doppler width obtained with a high resolution all-sky Fabry-Perot spectrometer (which is an alternate approach). This approach is based on the assumption that the thermal kinetic energy distribution of emitting OH molecules is similar to that of the surrounding atmosphere.

In the past, narrow field Fabry-Perot spectrometers have been extensively used for remote sensing the mesopause wind and temperature fields using OH airglow. They obtain measurements in a number of directions across the sky, typically four or eight cardinal directions and zenith. For this study, we employed a high resolution all-sky wavelength scanning Doppler interferometer (SDI) to obtain spectra of the *P*-branch near infrared emissions from the OH (6,2) Meinel band at wavelength 843 *nm* (which is known as the $P_1(3)$ doublet emission line). Doppler widths and Doppler shifts of the recorded spectra were used to infer mesopause winds and temperatures [*Jacka*, 1985; *Rees et al.*, 1990; *Hernandez et al.*, 1992b; *East et al.*, 1995; *Greet et al.*, 1997]. This was the first time ever that the all-sky SDI technique was employed to study middle atmosphere temperatures and dynamics. The all-sky SDI technique enabled us to map mesopause winds and temperatures over a wide geographic region above Alaska. Due to nuclear spin of the OH molecules, OH emissions from the (6,2) Meinel band at 843 *nm* are subjected to lambda doublet splitting. The peaks of 843 *nm* doublet exist at 843.026 *nm* and 843.007 *nm*, which are only 19 *pm* apart (see Table 1 in *Greet et al.* [1997]). To avoid complications in the spectra due to the doublet structure, the etalon spacing was chosen carefully to make the two peaks actually fall on the top of each other when recorded by the instrument - which means we do not need to explicitly account for the doublet structure in our analysis. Superposing the lines also produces a small enhancement in signal/noise ratio for the recorded spectra, which is useful given the weak OH emission brightness. This technique is similar to the technique used by *Rees et al.* [1990] and *East et al.* [1995] for a fixed gap etalon instrument.

The purpose of this study is to present the first ever mesospheric wind and temperature data recorded with the all-sky SDI technique.

B.2 Hydroxyl Emissions

OH emissions are present in both dayglow and nightglow. The Bates-Nicolet process is the most widely accepted exothermic chemiluminescent reaction between atomic hydrogen and ozone for the production of excited OH molecules [*Bates and Nicolet*, 1950]:

$$O_3 + H \rightarrow OH\,(v \leq 9) + O_2 + 3.34\,ev \tag{B.1}$$

where is the vibrational state of OH molecule. The excited OH molecules in the higher vibrational levels ($v > 6$) have smaller lifetimes. Thermalization of excited OH (v=6) molecules is expected because of their longer radiative lifetimes (6-10 *ms*) and high collisional frequency at mesopause heights ($\sim 3 \times 10^4\,sec^{-1}$) [*Innis and Conde*, 2001]. The details of hydroxyl photochemistry are discussed in *McDade and Llewellyn* [1987]; *Walterscheid and Schubert* [1987]; *Walterscheid et al.* [1987].

B.3 Instrumentation and Data Analysis

The details of the all-sky SDI used in this study are described in *Anderson et al.* [2012a,b,c]. During the 2011-2012 winter season, an 843 *nm* OH filter with a bandwidth of 0.5 *nm* (on loan from Lancaster University, UK) was installed into the all-sky SDI located at Gakona, Alaska for remote sensing the mesopause wind and temperature fields. The observation cycle of this instrument also included 630 *nm* (red line auroral emission) and 557.7 *nm* (green line auroral emission) measurements. It uses a piezoelectrically separation scanned etalon with an aperture size of 150 *mm*. An individual scan over one order of interference was performed in 128 channels (steps) with the integration time of ~0.18 *sec* per step. A frequency stabilized He-Ne laser (632.8 *nm*) was used to measure intrinsic broadening that instrument introduces to the output signal (called instrument function). We deconvolved the instrument function from the 843 *nm* OH spectra, using the 632.8 *nm* laser profile as an instrument function.

The average intensity of the OH (6,2) Meinel band is ~400-600 *Rayleigh* [*Rees et al.*, 1990], which is much weaker than commonly observed auroral and airglow emissions from the thermosphere. Also, the detector's quantum efficiency for infrared 843 *nm* emission is only $\sim 50\%$ compared to $\sim 90\%$ for the visible spectrum. Thus, to get an adequate

OH sampling rate and signal to noise ratio, the full field of view (FOV) of the all-sky SDI was divided into only 43 software defined sub-fields (called zones) instead of our more typical scheme that uses 115 zones for the 557.7 *nm* and 630 *nm* emissions. Even at this spatial resolution, the average temporal resolution of the recorded OH data was around 10 *min*. High resolution Doppler spectra of the OH 843 *nm* were compiled from each of the 43 zones. The complete procedure to derive two-dimensional vector wind and scalar temperatures fields from the Doppler shifts and widths of the recorded spectra is discussed in *Conde and Smith* [1995, 1997, 1998]; *Anderson et al.* [2012a]. We used 557.7 *nm* emissions to test for any leakage through OH filter. The FOV of the all-sky SDI (full FOV ~80 degree) projected at 843 *nm* (~87 *km*) and 557.7 *nm* (~130 *km*) emission altitudes is depicted in Figure B.1, assuming planar geometry. The radius of coverage of 80 degree full FOV at mesopause and 557.7 *nm* emission layer altitude was 493 *km* and 737 *km* respectively.

B.4 Discussion

In this study, we used the hydroxyl airglow measurements recorded with the all-sky SDI located at Gakona. The instrument was run in a fully automatic mode for the whole observing season. The all-sky SDI OH observation cycle started on 09 Nov 2011 and ended on 08 May 2012 (early summer season). Total 153 nights of the OH data was recorded during this cycle with a total of 4245 individual exposures, including cloudy nights. On a cloudy night, the LOS wind information cannot be used to infer thermospheric winds because clouds scatter the emissions that come from the sky. This scattering does not change the wavelength of the signal; however angular information regarding the LOS is lost. Brownian motion in clouds cause negligible broadening of the Doppler spectra (private communication with Dr. Roger Smith). Therefore, the recorded spectra on a cloudy night can be used to infer temperatures without any trouble. The average temporal resolution of the data was ~10 min. Time series of the estimated mesopause temperatures and winds (zonal and meridional) are shown in Figure B.2 and Figure B.5 respectively. The data presented in these time series are the first ever mesospheric data obtained with the all-sky SDI technique.

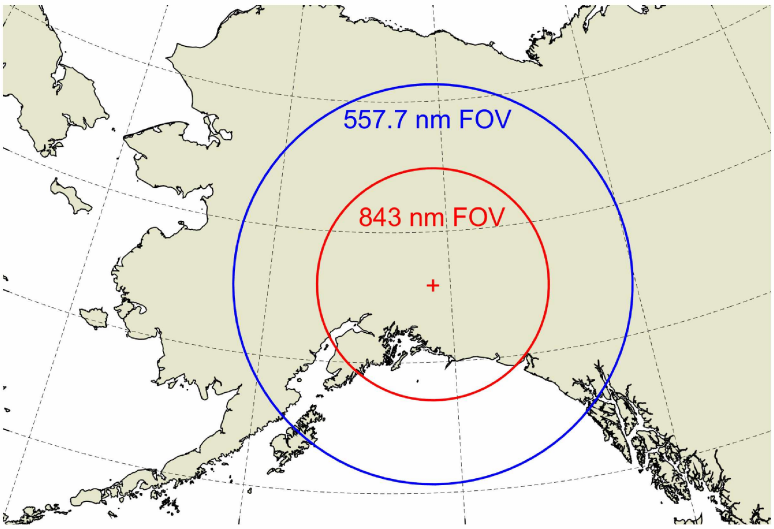

Figure B.1: Location of the SDI at Gakona (indicated by red plus) along with its full field of view projected at 87 *km* (shown in red) and 130 *km* (shown in blue) altitude above Alaska.

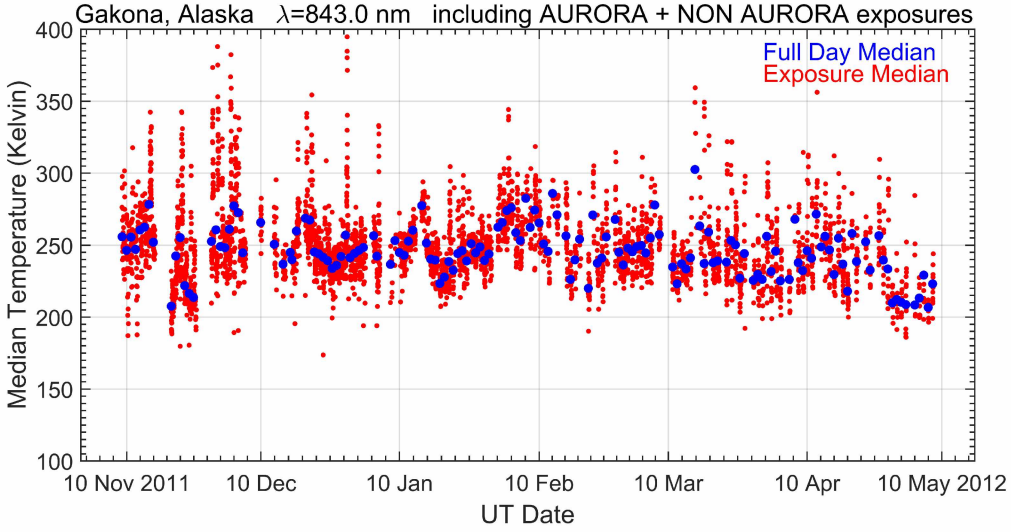

Figure B.2: Time series of median temperature estimates derived from all-sky OH spectra recorded at Gakona during the 2011-2012 observing season. Each temperature value represented in red is the median of all the temperatures estimated from a single all-sky exposure. Each temperature value represented in blue is the median of all the temperatures recorded on a single night. This plot includes all the data recorded during 201-2012 observing season.

Two temperatures are plotted in Figure B.2. One represents the median of the temperatures obtained from the 43 zones in each exposure (shown in red and called exposure median). Also shown is the median of all temperature measurements derived on a single day (shown in blue and called full day median). The full day median was calculated to show an overall trend in the estimated mesopause temperature. Exceptionally high temperatures ($> 400\ K$) were excluded from this study because they do not represent real mesospheric temperatures. The temperature series shows fluctuations in the estimated mesopause temperature. A possible reason for these fluctuations is the change in the emission source altitude. Almost half of the time, the median temperatures were higher than the normal expected 150-250 K temperature range of the mesopause (reason discussed later). The decrease in the full day median temperature from winter to early summer season was observed and this trend in temperature was expected because the winter mesopause is always warmer than the summer mesopause.

As discussed above, the estimated mesopause temperatures observed by the all-sky SDI were somewhat higher than the actual expected temperatures. The median of the whole temperature data is $\sim$246 K. The most probable reason for this overestimation is the auroral contamination in the observed OH spectra. This contamination was probably caused by the aurorally sensitive OI (^1D) emission line at 844.6 nm [*Greet et al.*, 1997] which is very close in the OH emissions 843 nm wavelength. We do not do measurements at 844.6 nm, but the intensity of 557.5 nm auroral emissions can be used as a proxy for the intensity of 844.6 nm emissions. To find if auroral contamination was present in our 843 nm observations, its emission intensity was compared with the 557.7 nm emission intensity from the lower thermosphere. Although, the observations at both wavelengths were in observation cycle of the SDI located at Gakona, the observation times were different. So, for intensity comparison, the 557.7 nm emission intensity was interpolated to the observational times at 843 nm. The SDI FOV projected at mesopause height ($\sim$87 km) was smaller than the FOV projected at 557.7 nm emission layer ($\sim$130 km), so only the first 87 zones of the 557.7 nm FOV were selected because they were well inside the 834 nm FOV. All the available 843 nm and 577.7 nm observations obtained during the 2011-2012 observation cycle were compared, including cloudy days (as shown in Figure B.3).

This comparison clearly shows increasing in OH emission intensity with increasing 557.7 *nm* emission intensity. This is a very strong indication that auroral emissions were leaking through the OH filter, causing contamination of the observed 843 *nm* spectra. This means, $P_1(3)$ airglow emission used here is subject to the auroral contamination at auroral lati-

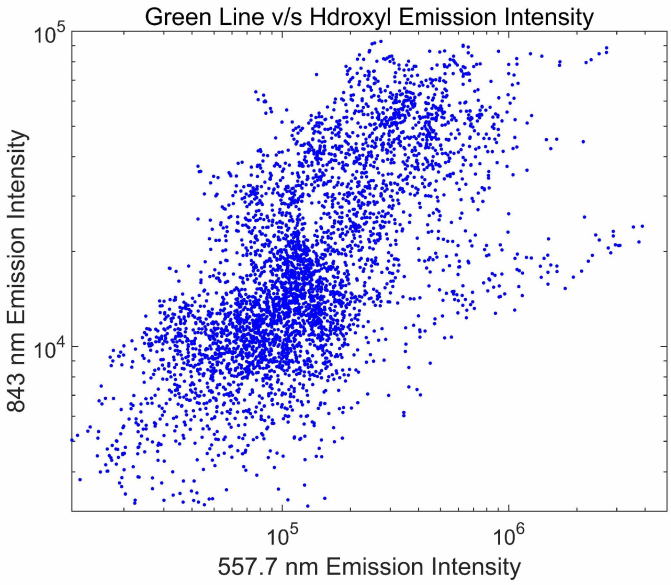

Figure B.3: Hydroxyl (843 *nm*) emission intensity recorded from the mesopause plotted against green line auroral (557.7 *nm*) emission intensity recorded from the lower thermosphere. Note that the units of emission intensity are arbitrary, and both axes are logarithmic in scale.

tudes, but it can offer most potential at the latitudes where only airglow emissions are observable. These auroral contaminations probably broaden the 843 *nm* Doppler spectra and hence lead to the elevation of estimated temperatures. The estimated increase was $\sim$50 *K*.

To extract useful temperature data without any auroral contamination, all the zones of each exposure recorded during the 2011-2012 observing season with possible auroral contamination were identified and removed. With this newly cleaned data, we again produced mesopause temperature time series for the whole season as shown in Figure B.4. There are some notable differences between the new temperature time series and the old temperature time series. Although the new temperature time series has a smaller num-

ber of data points compared to the original case, similar temperature oscillations are still present. There are now more number of data points toward the lower side of temperature. The median of aurorally cleaned data is ∼243 *K*. There are definitely improvements, but not so much as expected.

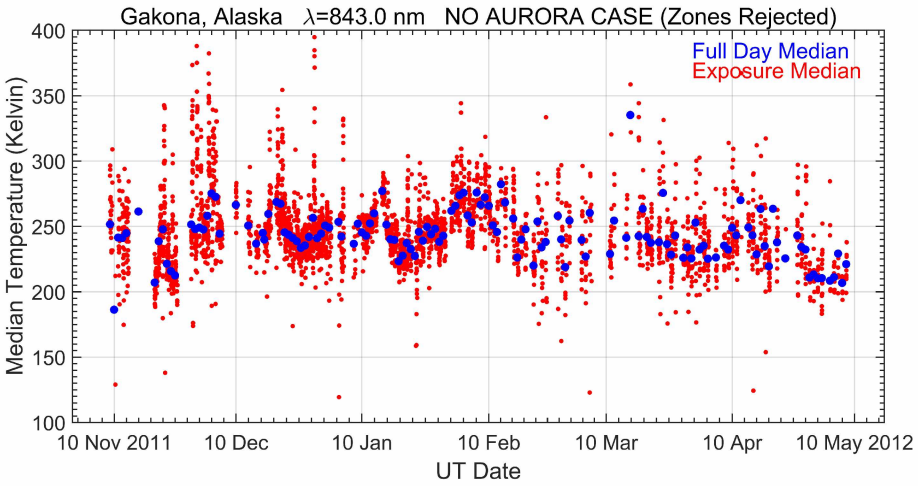

Figure B.4: As for Figure B.2, but excluding the zones in which aurora was present.

Another possible reason can be instrumental behavior at higher wavelengths. If a laboratory source at the wavelength same as the sky observations is present, then instrumental response at observational wavelength can be easily calculated. But, in our case, we used He-Ne laser at 632.8 *nm* to estimate the instrument function at 843 *nm*. As discussed in appendix A (section 2), the Airy function of an etalon is a function of wavelength and dependent on the reflectivity of the etalon plates. The etalon finesse is also a function of wavelength. As discussed in *Jacka* [1985] and *Greet* [1997], the instrument function is a convolution of aperture, defects in the etalon plates surfaces, and the Airy function. The only thing in the instrument function that varies with the incident wavelength and reflectivity of the etalon, is the Airy function. The Airy function at any wavelength can be easily calculated for a given reflective finesse. This means, for the best estimation of the instrument function at 843 *nm* wavelength, we require reflective finesse of the etalon plate at 843 *nm* and 632.8 *nm*. Consequently, any error in the given reflective finesse would lead to the estimation of slightly erroneous instrument function. A detailed discussion is presented in *Jacka* [1985] and *Greet* [1997]. At OH 843 *nm* wavelength, any ±1 change in the

reflective finesse would change the temperature by ± 10 *K* [*Greet*, 1997]. In our study, no attempt was made to include reflective finesse of the etalon while calculating scaling the instrumentation function from 632.8 *nm* to 843 *nm* wavelength. This could be another probable reason for enhanced temperatures, but verification needs to be done. An in-depth investigation of the reflective finesse of the etalon used in the Gakona instrument would be the next possible step. But, such an investigation is beyond the scope of this study.

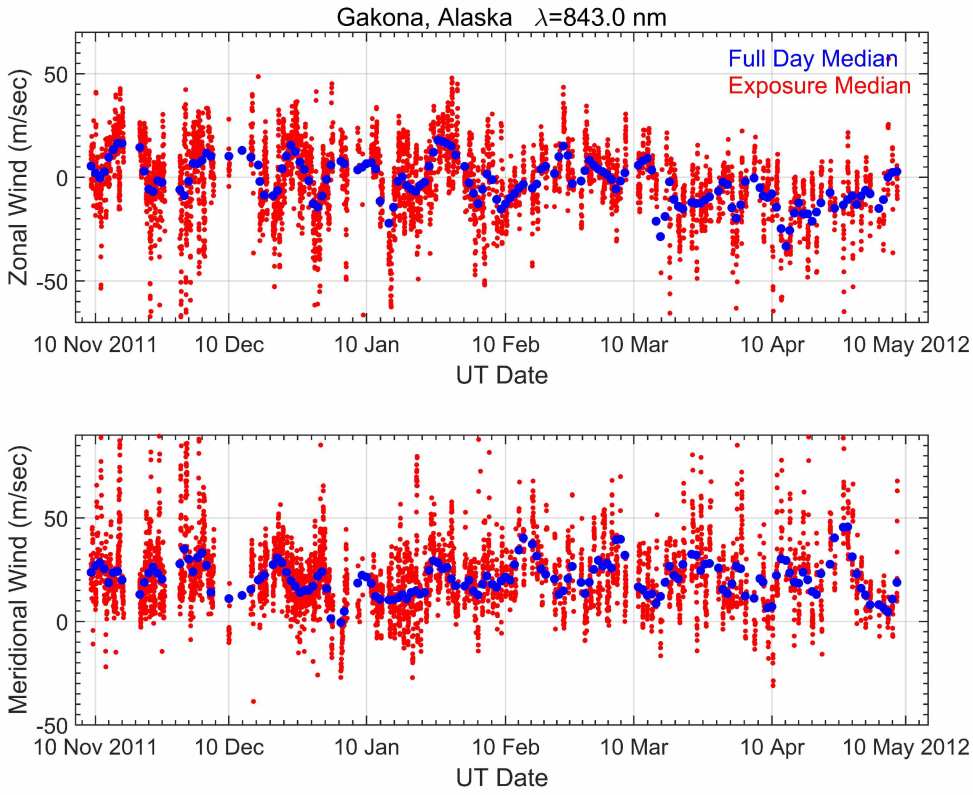

Figure B.5: Time series of the geomagnetic zonal (top panel) and meridional (bottom panel) wind components derived from all-sky OH spectra recorded at Gakona during the 2011-2012 observing season. In the top/bottom panel, each red value is the median of all zonal/meridional estimates from a single all-sky exposure and each blue value is the median of all zonal/meridional estimates recorded on a single night.

Figure B.5 shows time series of estimated wind components at mesopause heights above Gakona for the entire observing season. The zonal and meridional winds shown are aligned magnetic zonally (positive/negative toward magnetic east/west) and merid-

ionally (positive/negative toward magnetic north/south). Similar to the temperature series, exposure median and full day median were calculated as shown. The zonal winds were observed to be flowing more towards the magnetic south with shifting season from winter to early summer season. Meridional winds remained magnetic northward during the full observational cycle. Fluctuations were present in both zonal and meridional winds, but they were uncorrelated. There is strong possibility that the distortion of recorded OH spectra could have introduced errors in the estimated wind components. Nevertheless, the speed of the estimated wind components were comparable in magnitude to the typically 50-100 $m.sec^{-1}$ values published in various other OH studies [e.g., *Rees et al.*, 1990; *East et al.*, 1995].

The most important application of an all-sky SDI is that it can sample spectra from many locations across the sky simultaneously and enables us to construct two-dimensional fields of the required parameters (basically winds and temperatures), whereas conventional instruments provide only point measurements. Figure B.6 shows a spatially resolved horizontal vector wind field inferred from a single exposure that yielded 43 OH

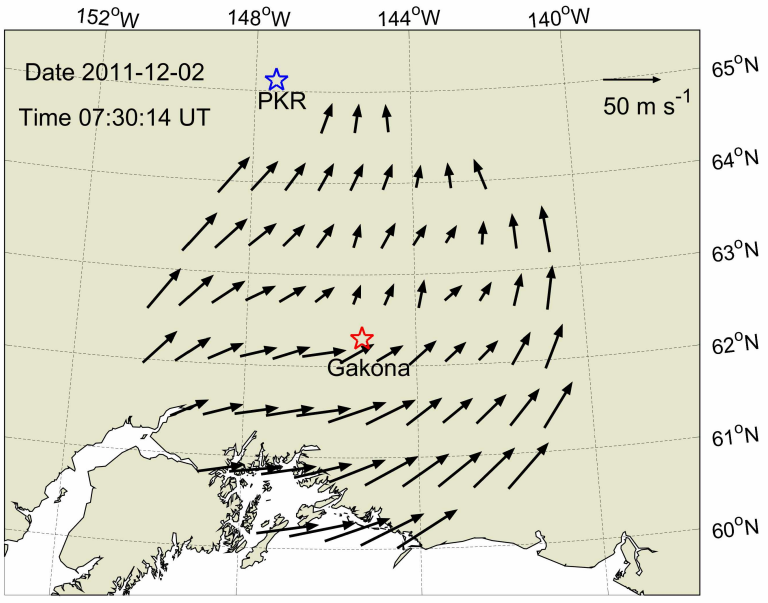

Figure B.6: An example of spatially resolved horizontal vector wind field estimated from OH Doppler spectra on an aurorally quiet night (02 Dec 2012). The wind field is mapped at mesopause height onto the geographic map of Alaska.

spectra. The central time of this exposure was 07:30:14 UT on the night of 02 Dec 2011. This selected night of the 02 Dec 2011 was an aurorally quiet night. The wind field shown is geographically mapped onto the map of Alaska. It is mapped at higher spatial resolution than the original data, due to interpolation.

As discussed earlier, auroral emissions were leaking through the filter, causing contamination on the recorded spectra. Nevertheless, it is entirely possible to obtain reasonable temperatures and winds by eliminating the time intervals from the recorded data when aurora was active. Another option is to use a filter with very narrow band to avoid the leakage of any undesired emission line.

B.5 Summary

Here, we have presented the mesopause wind and temperature data recorded at auroral latitudes with an all-sky SDI using $P_1(3)$ airglow emission from (6,2) Meinel band. This was the first time ever this all-sky SDI technique was employed to study middle atmospheric dynamics. The temperatures estimated with these data were higher than the range of normally observed mesopause temperatures. The comparison of $P_1(3)$ airglow emission intensity and the 557.7 nm emission intensity suggested that the auroral emissions were leaking through the OH filter which contaminated the OH airglow spectra. Another possible cause of temperature overestimation could be the scaling of instrument function from the calibration to source wavelength without including effects of wavelength variation in etalon reflective finesse. Nevertheless, the overall trend in the mesopause temperature from winter to early summer season was similar to that expected (higher in winter and lower in summer). Also, the magnitudes of estimated wind components were within in the expected range (0-100 $m.sec^{-1}$). These results show that this could be a promising new technique for studying middle atmospheric dynamics if used at wavelengths that are not easily contaminated by other emission sources. The data presented here are preliminary and require further validation before it could be used for detailed study of mesospheric dynamics.

B.6 References

Akmaev, R. A., and V. I. Fomichev (1998), Cooling of the mesosphere and lower thermosphere due to doubling of CO_2, *Ann. Geophys.*, *16*(11), 1501–1512, doi: 10.1007/s00585-998-1501-z.

Akmaev, R. A., and V. I. Fomichev (2000), A model estimate of cooling in the mesosphere and lower thermosphere due to the CO_2 increase over the last 3-4 decades, *Geophys. Res. Lett.*, *27*(14), 2113–2116, doi: 10.1029/1999GL011333.

Anderson, C., M. Conde, and M. G. McHarg (2012a), Neutral thermospheric dynamics observed with two scanning Doppler imagers: 1. Monostatic and bistatic winds, *J. Geophys. Res. Sp. Phys.*, *117*(A3), A03,304, doi: 10.1029/2011ja017041.

Anderson, C., M. Conde, and M. G. McHarg (2012b), Neutral thermospheric dynamics observed with two scanning Doppler imagers: 2. Vertical winds, *J. Geophys. Res.*, *117*(A3), A03,305, doi: 10.1029/2011JA017157.

Anderson, C., M. Conde, and M. G. McHarg (2012c), Neutral thermospheric dynamics observed with two scanning Doppler imagers: 3. Horizontal wind gradients, *J. Geophys. Res. Sp. Phys.*, *117*(5), doi: 10.1029/2011JA017471.

Armstrong, E. (1975), The influence of a gravity wave on the airglow hydroxyl rotational temperature at night, *J. Atmos. Terr. Phys.*, *37*(12), 1585–1591, doi: 10.1016/0021-9169(75)90038-0.

Baker, D. J., and A. T. Stair (1988), Rocket measurements of the altitude distributions of the hydroxyl airglow, *Phys. Scr.*, *37*(4), 611–622, doi: 10.1088/0031-8949/37/4/021.

Bates, D., and M. Nicolet (1950), The photochemistry of atmospheric water vapor, *J. Geophys. Res.*, *55*(3), 301–327.

Bittner, M., D. Offermann, and H. H. Graef (2000), Mesopause temperature variability above a midlatitude station in Europe, *J. Geophys. Res.*, *105*(D2), 2045, doi: 10.1029/1999JD900307.

Conde, M., and R. W. Smith (1995), Mapping thermospheric winds in the auroral zone, *Geophys. Res. Lett.*, *22*(22), 3019–3022, doi: 10.1029/95GL02437.

Conde, M., and R. W. Smith (1997), Phase compensation of a separation scanned, all-sky imaging Fabry Perot spectrometer for auroral studies, *Appl. Opt.*, *36*(22), 5441–5450, doi: 10.1364/AO.36.005441.

Conde, M., and R. W. Smith (1998), Spatial structure in the thermospheric horizontal wind above Poker Flat, Alaska, during solar minimum, *J. Geophys. Res.*, *103*(A5), 9471–9949, doi: 10.1029/97JA03331.

East, S., N. Meredith, M. Harris, D. Rees, V. Wickwar, I. K. Monson, and H. G. Muller (1995), First summer results on winds in the upper mesosphere derived from the 843 nm hydroxyl emissions measured from the Bear Lake Observatory, Utah, *J. Atmos. Terr. Phys.*, *57*(9), 995–1008, doi: 10.1016/0021-9169(94)00086-4.

Fraser, G. J., G. Hernandez, and R. W. Smith (1993), Eastward-moving 2-4 day waves in the winter Antarctic mesosphere, *Geophys. Res. Lett.*, *20*(15), 1547–1550, doi: 10.1029/93GL01707.

French, W. J. R., and A. R. Klekociuk (2011), Long-term trends in Antarctic winter hydroxyl temperatures, *J. Geophys. Res.*, *116*, D00P09, doi: 10.1029/2011JD015731.

French, W. J. R., and F. J. Mulligan (2010), Stability of temperatures from TIMED/SABER v1.07 (2002-2009) and Aura/MLS v2.2 (2004-2009) compared with OH(6-2) temperatures observed at Davis Station, Antarctica, *Atmos. Chem. Phys. Discuss.*, *10*(9), 21,547–21,565, doi: 10.5194/acpd-10-21547-2010.

French, W. J. R., G. B. Burns, K. Finlayson, P. A. Greet, R. P. Lowe, and P. F. B. Williams (2000), Hydroxyl (6-2) airglow emission intensity ratios for rotational temperature determination, *Ann. Geophys.*, *18*(10), 1293–1303, doi: 10.1007/s005850000260.

Golitsyn, G. S., A. I. Semenov, N. N. Shefov, L. M. Fishkova, E. V. Lysenko, and S. P. Perov (1996), Long-term temperature trends in the middle and upper atmosphere, *Geophys. Res. Lett.*, *23*(14), 1741, doi: 10.1029/96GL01592.

Greet, P. A. (1997), Mesospheric observations by high-resolution Fabry-Perot spectrometers: calibrations required for climate change studies, *J. Atmos. Sol. Terr. Phys.*, *59*(3), 281–294, doi: 10.1016/S1364-6826(96)00088-0.

Greet, P. A., W. J. R. French, G. B. Burns, P. F. B. Williams, R. P. Lowe, and K. Finlayson (1997), OH(6-2) spectra and rotational temperature measurements at Davis, Antarctica, *Ann. Geophys.*, *16*(1), 77, doi: 10.1007/s005850050581.

Greet, P. A., J. L. Innis, and P. L. Dyson (2002), Thermospheric vertical winds in the auroral oval/polar cap region, *Ann. Geophys.*, *20*(12), 1987–2001.

Hernandez, G., and R. G. Roble (1995), Thermospheric nighttime neutral temperature and winds over Fritz Peak Observatory: Observed and calculated solar cycle variation, *J. Geophys. Res.*, *100*(A8), 14,647, doi: 10.1029/95JA00565.

Hernandez, G., R. W. Smith, and J. F. Conner (1992a), Neutral wind and temperature in the upper mesosphere above South Pole, Antarctica, *Geophys. Res. Lett.*, *19*(1), 53–56, doi: 10.1029/91GL02957.

Hernandez, G., R. W. Smith, G. J. Fraser, and W. L. Jones (1992b), Large-scale waves in the upper-mesosphere at Antarctic high-latitudes, *Geophys. Res. Lett.*, *19*(13), 1347–1350, doi: 10.1029/92GL01281.

Hernandez, G., G. J. Fraser, and R. W. Smith (1993), Mesospheric 12-hour oscillation near South Pole, Antarctica, *Geophys. Res. Lett.*, *20*(17), 1787–1790, doi: 10.1029/93GL01983.

Innis, J. L., and M. Conde (2001), Thermospheric vertical wind activity maps derived from Dynamics Explorer-2 WATS observations, *Geophys. Res. Lett.*, *28*(20), 3847–3850, doi: 10.1029/2001GL013704.

Jacka, F. (1985), Application of Fabry-Perot spectrometers for measurement of upper atmosphere temperatures and winds, *Int. Counc. Sci. Unions Middle Atmos. Handb.*, *13*, 19–40.

Liu, G., and G. G. Shepherd (2006), An empirical model for the altitude of the OH nightglow emission, *Geophys. Res. Lett.*, *33*(9), L09,805, doi: 10.1029/2005GL025297.

McDade, I. C., and E. J. Llewellyn (1987), Kinetic parameters related to sources and sinks of vibrationally excited OH in the nightglow, *J. Geophys. Res.*, *92*(A7), 7643, doi: 10.1029/JA092iA07p07643.

Meriwether, J. W. (1975), High latitude airglow observations of correlated short-term fluctuations in the hydroxyl meinel 8-3 band intensity and rotational temperature, *Planet. Sp. Sci.*, *23*(8), 1211–1221, doi: 10.1016/0032-0633(75)90170-1.

Mulligan, F. J., D. F. Horgan, J. G. Galligan, and E. M. Griffin (1995), Mesopause temperatures and integrated band brightnesses calculated from airglow OH emissions recorded at Maynooth (53.2N, 6.4W) during 1993, *J. Atmos. Terr. Phys.*, *57*(13), 1623–1637, doi: 10.1016/0021-9169(94)00133-9.

Myrabø, H. (1986), Winter-season mesopause and lower thermosphere temperatures in the northern polar region, *Planet. Sp. Sci.*, *34*(11), 1023–1029, doi: 10.1016/0032-0633(86)90012-7.

Offermann, D., and R. Gerndt (1990), Upper mesosphere temperatures from OH-emissions, *Adv. Sp. Res.*, *10*(12), 217–221, doi: 10.1016/0273-1177(90)90399-K.

Osterbrock, D. E., and A. Martel (1992), Sky spectra at a light-polluted site and the use of atomic and OH sky emission lines for wavelength calibration, *Publ. Astron. Soc. Pacific*, *104*, 76, doi: 10.1086/132961.

Osterbrock, D. E., J. P. Fulbright, A. R. Martel, M. J. Keane, S. C. Trager, and G. Basri (1996), Night-sky high-resolution spectral atlas of OH and O_2 emission lines for echelle spectrograph wavelength calibration, *Publ. Astron. Soc. Pacific*, *108*, 277, doi: 10.1086/133722.

Portmann, R. W., G. E. Thomas, S. Solomon, and R. R. Garcia (1995), The importance of dynamical feedbacks on doubled CO_2-induced changes in the thermal structure of the mesosphere, *Geophys. Res. Lett.*, *22*(13), 1733–1736, doi: 10.1029/95GL01432.

Rees, D., A. Aruliah, T. J. Fuller-Rowell, V. B. Wickwar, and R. J. Sica (1990), Winds in the upper mesosphere at mid-latitude: First results using an imaging Fabry-Perot Interferometer, *Geophys. Res. Lett.*, *17*(9), 1259–1262, doi: 10.1029/GL017i009p01259.

Rind, D., R. Suozzo, N. K. Balachandran, and M. J. Prather (1990), Climate change and the middle atmosphere, part 1, the doubled CO_2 climate., *Am. Meteorol. Soc.*

Roble, R. G., and R. E. Dickinson (1989), How will changes in carbon dioxide and methane modify the mean structure of the mesosphere and thermosphere?, *Geophys. Res. Lett.*, *16*(12), 1441–1444, doi: 10.1029/GL016i012p01441.

Scheer, J., and E. R. Reisin (1990), Rotational temperatures for OH and O_2 airglow bands measured simultaneously from El Leoncito (31°48′S), *J. Atmos. Terr. Phys.*, *52*(1), 47–57, doi: 10.1016/0021-9169(90)90114-3.

Scheer, J., E. Reisin, J. Espy, M. Bittner, H.-H. Graef, D. Offermann, P. Ammosov, and V. Ignatyev (1994), Large-scale structures in hydroxyl rotational temperatures during DYANA, *J. Atmos. Terr. Phys.*, *56*(13-14), 1701–1715, doi: 10.1016/0021-9169(94)90005-1.

Sivjee, G. G. (1992), Airglow hydroxyl emissions, *Planet. Sp. Sci.*, *40*(l), 235–242.

Sivjee, G. G., R. L. Walterscheid, J. H. Hecht, R. M. Hamwey, G. Schubert, and A. B. Christensen (1987), Effects of atmospheric disturbances on polar mesopause airglow OH emissions, *J. Geophys. Res.*, *92*(A7), 7651, doi: 10.1029/JA092iA07p07651.

Takahashi, H., B. Clemesha, and Y. Sahai (1974), Nightglow OH (8,3) band intensities and rotational temperature at 23°S, *Planet. Sp. Sci.*, *22*(9), 1323–1329, doi: 10.1016/0032-0633(74)90051-8.

Takahashi, H., B. Clemesha, Y. Sahai, and P. Batista (1994), Seasonal variations of the mesopause temperature observed at equatorial (4°S) and low (23°S) latitude stations, *Adv. Sp. Res.*, *14*(9), 97–100, doi: 10.1016/0273-1177(94)90122-8.

Thomas, G. (1996), Global change in the mesosphere-lower thermosphere region: has it already arrived?, *J. Atmos. Terr. Phys.*, *58*(14), 1629–1656, doi: 10.1016/0021-9169(96)00008-6.

Walterscheid, R. L., and G. Schubert (1987), A dynamical-chemical model of tidally driven fluctuations in the OH nightglow, *J. Geophys. Res.*, *92*(A8), 8775, doi: 10.1029/JA092iA08p08775.

Walterscheid, R. L., G. Schubert, and J. M. Straus (1987), A dynamical-chemical model of wave-driven fluctuations in the OH nightglow, *J. Geophys. Res.*, *92*(A2), 1241, doi: 10.1029/JA092iA02p01241.

Zhang, S. P., and G. G. Shepherd (1999), The influence of the diurnal tide on the O(1S) and OH emission rates observed by WINDII on UARS, *Geophys. Res. Lett.*, *26*(4), 529–532, doi: 10.1029/1999GL900033.

Appendix C

Permission from Dr. John Meriwether to include Manuscript in Thesis

UNIVERSITY of ALASKA

Manbharat Dhadly <msdhadly@alaska.edu>

Fwd: Permission request

Manbharat Singh Dhadly <manbharatsingh@gmail.com> 8 November 2015 at 03:33
To: Manbharat Singh <msdhadly@alaska.edu>

---------- Forwarded message ----------
From: **John Meriwether** <john.meriwether@ces.clemson.edu>
Date: Mon, Nov 2, 2015 at 1:01 AM
Subject: Re: Permission request
To: Manbharat Singh Dhadly <manbharatsingh@gmail.com>

Hi Manbharat, congratulations on your successful defense!

Yes, you duo have my permission to use the paper as part of your dissertation manuscript.

Best wishes, ... John

--
John W. Meriwether
Professor of Physics
Department of Physics and Astronomy
208 Kinard Laboratory
Clemson University
Clemson, SC 29634-0978
E-mail meriwej@clemson.edu
https://sites.google.com/site/johnmeriwetherorg
864-656-0915